TECHNICAL UNIVERSITY OF MOLDOVA

JOURNAL OF ENGINEERING SCIENCE

Technical and applied scientific publication founded on 9 February 1995
Alternative title: Meridian ingineresc

2026

Vol. XXXIII (2)

ISSN 2587-3474
eISSN 2587-3482

TECHNICAL UNIVERSITY OF MOLDOVA (PUBLISHING HOUSE)
„TEHNICA UTM" (PRINTING HOUSE)

According to the Decision of the NAQAER No. 12 from 23.02.2024, JES is classified as B+ journal

Main subjects areas of the Journal of Engineering Science:

A. Industrial Engineering

- Mechanical Engineering and Technologies
- Applied Engineering Sciences and Management
- Materials Science and New Technologies
- Electrical Engineering and Power Electronics
- Light Industry, New Technologies and Design

B. Electronics and Computer Science

- Electronics and Communication
- Microelectronics and Nanotechnologies
- Biomedical Engineering
- Computers and Information Technology

C. Architecture, Civil and Environmental Engineering

- Architecture, Urbanism and Cadaster
- Civil Engineering and Management
- Energy Efficiency and New Building Materials
- Environmental Engineering

D. Food Engineering

- Food Technologies and Food Processes
- Food Industry and Management
- Biotechnologies, Food Chemistry and Food Safety

The structure of the journal corresponds to the classification of scientific publications: ***Engineering, Multidisciplinary.***

How to publish a paper:

1. Send the manuscript and information about the author to the **Editorial Board address:** jes@meridian.utm.md
2. Manuscripts are accepted only in English, by e-mail, in template file (www.jes.utm.md)
3. After a review, you will be notified of the editorial board's decision.
4. After the Journal has been published, we will send it to you immediately by mail.

Editor-in-Chief
Dr. hab. prof. univ. Viorel BOSTAN
Technical University of Moldova
viorel.bostan@adm.utm.md

Editorial Board

Abdelkrim Azzouz, Dr. Eng., Professor, Quebec University of Montreal, Canada
Adrian Gheorghe, PhD, Professor, Old Dominion University, Norfolk, Virginia, 23529, USA
Adrian Graur, PhD, Professor, University "Ștefan cel Mare", Suceava, Romania
Aurel-Mihail ȚÎȚU, PhD, Professor, "Lucian Blaga" University of Sibiu, Romania
Boris Gaina, Dr.hab., Professor, Acad. of the Academy of Sciences of Moldova
Camelia Vizireanu, Dr. Eng., Professor, "Dunarea de Jos" University of Galati, Romania
Cornel Ciupan, PhD, Professor, Technical University of Cluj Napoca, Romania
Cristoph Ruland, PhD, Professor, University of SIEGEN, Germany
Dimitr P. Karaivanov, PhD, Professor, University of Chemical Technology and Metallurgy, Sofia, Bulgaria.
Dumitru Mnerie, PhD, Professor, "Politehnica" University of Timișoara, Romania
Dumitru Olaru, PhD, Professor, Technical University "Gh. Asachi", Iași, Romania
Dumitru Țiuleanu, Dr. hab., Corr. Mem. of the Academy of Sciences of Moldova
Florin Ionescu, PhD, Professor, University Steinbes, Berlin, Germania
Gabriel Neagu, PhD, Profesor, National Institute for Research and Development in Informatics, Bucharest, Romania
George S. Dulikravich, PhD, Florida International University, U.S.A.
Gheorghe Badea, PhD in Engineering, Professor, Technical University of Civil Engineering Bucharest, Romania
Gheorghe Manolea, PhD, Professor, University of Craiova, Romania
Grigore Marian, PhD, Professor, Agrarian State University of Moldova, Chisinău, Republic of Moldova.
Hai Jiang, PhD, Professor, Department of Computer Science, Arkansas State University, U.S.A.
Heinz Frank, PhD, Professor, Reinhold Würth University, Germany
Hidenori Mimura, Professor, Research Institute of Electronics, Shizuoka University, Japan
Ion Bostan, Dr. hab., Professor, Acad. of the Academy of Sciences of Moldova
Ion Paraschivoiu, PhD, Professor, Universite Technologique de Montreal, Canada
Ion Rusu, Dr. hab., Professor, Technical University of Moldova
Ion Tighineanu, Dr. hab., Professor, Acad. of the Academy of Sciences of Moldova
Ion Vișa, PhD, Professor, University Transilvania of Brașov, Romania.
Laurențiu Slătineanu, PhD, Professor, Technical University „Gh. Asachi", Iași, Romania.
Lee Chow, PhD, Professor, University of Central Florida, USA
Leonid Culiuc , Dr. hab., Acad. of the Academy of Sciences of Moldova
Livia Nistor-Lopatenco, PhD, Associate Professor, Technical University of Moldova
Mardar Maryna, Doctor of Technical Science, Professor, Odessa National Academy of Food Technologies, Odessa, Ukraine
Natalia Tislinschi, PhD, Associate Professor, Technical University of Moldova
Oleg Lupan Dr. hab., Professor, Technical University of Moldova
Pavel Topală, Dr. hab., Professor, State University „Aleco Russo" from Bălți, Republic of Moldova
Peter Lorenz, PhD, Professor University of Applied Science Saar, Saarbrucken, Germania
Petru Cașcaval, PhD, Professor, "Gheorghe Asachi" Technical University of Iasi, Romania
Petru Stoicev, Dr. hab., Professor, Technical University of Moldova, Chisinau, Republic of Moldova
Polidor Bratu, PhD, Professor, president ICECON S.A., București, Romania
Radu Munteanu, PhD, Professor, Technical University of Cluj Napoca, Romania

Radu Sorin Văcăreanu, PhD, Professor, Technical University of Civil Engineering Bucharest, Romania
Rafał Gołębski, Dr., Associate Professor, Częstochowa University of Technology, Poland
Sergiu Zaporojan PhD, Professor, Technical University of Moldova
Spiridon Crețu, PhD, Professor, Technical University „Gh. Asachi", Iași, Romania.
Stanislav Legutko, PhD, Professor, Poznan University of Technology, Poland
Stefan Tvetanov, PhD, Professor, University of Food Technologies, Bulgaria
Ștefan-Gheorghe Pentiuc, PhD, Professor, University "Stefan cel Mare" of Suceava, Romania
Thierry Pauporté, PhD, Professor, Ecole Nationale Supérieure de Chimie de Paris, France
Thomas Luhmann, Dr. Eng., Professor, Jade University of Applied Sciences, Germany
Titu-Marius Bajenescu, Dr. Eng., Professor, Swiss Technology Association, Electronics Group Switzerland
Valentin Arion, PhD, Professor, Technical University of Moldova, Chișinău, Republic of Moldova
Valentina Bulgaru, PhD, Associate Professor, Technical University of Moldova, Chișinău, Republic of Moldova
Valeriu Dulgheru, Dr. hab., Professor, Technical University of Moldova, Chișinău, Republic of Moldova
Vasile Tronciu, Dr. hab., Professor, Technical University of Moldova, Chișinău, Republic of Moldova
Victor Ababii, PhD, Professor, Technical University of Moldova, Chișinău, Republic of Moldova
Victor Șontea, PhD, Professor, Technical University of Moldova, Chișinău, Republic of Moldova
Vilhelm Kappel, PhD, Institute of Research INCDIE ICPE-CA, Bucharest, Romania
Valentin Nedeff, PhD, Professor, "Vasile Alexandri" University of Bacău, Member of the Academy of Agricultural Sciences "Gheorghe Ionescu Șișești", Romania
Vladislav Resitca, PhD, Associate Professor, Technical University of Moldova, Chișinău, Republic of Moldova
Yogendra Kumar Mishra, Dr. hab., Kiel University, Germany
Yuri Dekhtyar, Dr.hab., Professor, Acad. of Latvian Academy of Sciences, Riga Technical University, Riga, Latvia

Responsible Editor
Dr. hab. Rodica STURZA
Editorial Board address: jes@meridian.utm.md

Editorial Production:
Dr. hab. Aliona Ghendov-Moșanu
Dr. Nicolae Trifan
Dr. Svetlana Caterinciuc
Dr. Rodica Cujba

CONTENT

A. Industrial Engineering

Gheorghe Bulai, Viorel Bostan, Lilia Rotaru, Tudor Bumbu — *Voice control system for piloting drones using artificial intelligence techniques*........ 7

Adriana Ursu, Igor Calmîcov, Viorel Cărbune — *Analysis of control architectures for unmanned aerial vehicles*....... 20

Mihail Popa — *ZnTe – Based of perovskite solar cells with inverted planar architecture*........ 32

Oleg Petrov — *Determining the location of overheating in an electrochemical battery*........ 46

B. Electronics and Computer Science

Gheorghe Gorceag, Oleg Lupan, Serghei Railean, Nicolai Ababii — *Optimization of the conformity assessment process for medical devices under conditions ensuring the evaluation of safety and performance parameters*........ 61

Rodica Bulai — *Lightweight RFID mutual authentication protocol providing untraceability*........ 71

C. Architecture, Civil and Environmental Engineering

Rodica Sirbu — *A geospatial framework for management of the integrated administration and control system (IACS) in the Republic of Moldova*........ 85

D. Food Engineering

Nadejda Botezatu, Ecaterina Covaci, Alexandra Arseni — *Assessment of the effects of temperature and thermal treatment duration on the stability of phenolic constituents in sweet extracts produced from Rara Neagră grape marc*........ 100

Viorica Bulgaru, Sorina Ropciuc, Iana Ciugureanu, Olga Smerea, Daniela Pauliuc, Natalia Netreba — *Structured oils in food systems: oleogels as sustainable alternatives to conventional solid fats*........ 113

CUPRINS

A. Industrial Engineering

Gheorghe Bulai, Viorel Bostan, Lilia Rotaru, Tudor Bumbu	*Sistem de control vocal pentru pilotarea dronelor utilizând tehnici de inteligență artificială*..	*7*
Adriana Ursu, Igor Calmîcov, Viorel Cărbune	*Analiza arhitecturilor de control pentru vehicule aeriale fără pilot .*	*20*
Mihail Popa	*Celule solare de perovskit pe bază de ZnTe cu arhitectură planară invertată*...	*32*
Oleg Petrov	*Determinarea localizării supraîncălzirii într-o baterie electrochimică*...	*46*

B. Electronics and Computer Science

Gheorghe Gorceag, Oleg Lupan, Serghei Railean, Nicolai Ababii	*Optimizarea procesului de evaluare a conformității dispozitivelor medicale în condițiile asigurării evaluării parametrilor de securitate și performanță*	*61*
Rodica Bulai	*Protocol RFID de autentificare reciprocă cu consum redus de resurse și asigurare a intrasabilității*	*71*

C. Architecture, Civil and Environmental Engineering

Rodica Sirbu	*Un cadru geospațial pentru managementul sistemului integrat de administrare și control (IACS) în Republica Moldova*	*85*

D. Food Engineering

Nadejda Botezatu, Ecaterina Covaci, Alexandra Arseni	*Evaluarea efectelor temperaturii și ale duratei tratamentului termic asupra stabilității constituenților fenolici din extractele dulci produse din tescovă de struguri Rara Neagră*.................................	*100*
Viorica Bulgaru, Sorina Ropciuc, Iana Ciugureanu, Olga Smerea, Daniela Pauliuc, Natalia Netreba	*Uleiuri structurate în sistemele alimentare: oleogeluri ca alternative sustenabile la grăsimile solide convenționale*................	*113*

Journal of Engineering Science *Vol. XXXIII, no. 2 (2026), pp. 7 - 19*
Fascicle *Industrial Engineering* *ISSN 2587-3474*
Topic *Applied Engineering Sciences and Management* *eISSN 2587-3482*

https://doi.org/10.52326/jes.utm.2026.33(2).01
UDC 004.8:004.934:629.735.33

VOICE CONTROL SYSTEM FOR PILOTING DRONES USING ARTIFICIAL INTELLIGENCE TECHNIQUES

Gheorghe Bulai[1*], ORCID: 0009-0002-1664-7856,
Viorel Bostan[1], ORCID: 0000-0002-2422-3538,
Lilia Rotaru[1], ORCID: 0000-0002-6578-418X,
Tudor Bumbu[2], ORCID: 0000-0001-5311-4464

[1]*Technical University of Moldova, 168 Stefan cel Mare blvd, MD2004,Chisinau, Republic of Moldova*
[2]*Moldova State University, 60 Alexei Mateevici Street, Chișinău, MD-2009, Republic of Moldova*
* Corresponding author: Gheorghe Bulai, *gheorghe.bulai@iis.utm.md*

Received: 05. 21. 2026
Accepted: 06. 17. 2026

Abstract. Voice control of drones is an innovation direction with high potential for many professional and social domains. This article analyzes the practical usefulness of a voice control system for drones based on an artificial intelligence model that runs locally, without an internet connection. The hybrid CNN+BiLSTM model is trained to recognize commands in Romanian and is deployed on the ESP-Drone platform with an ESP32-S2 microcontroller. Unlike commercial alternatives based on cloud infrastructure, the proposed solution runs entirely locally, eliminating latency and dependence on connectivity. The application domains with the greatest impact are examined, such as industrial inspections, search and rescue operations and precision agriculture, while also highlighting an often overlooked category of beneficiaries: people with motor disabilities, for whom voice control offers the possibility to pilot drones independently, without using their hands. The experimental results demonstrate a test accuracy of 99.4% and an end-to-end latency of 210–350 ms, confirmed under real flight conditions.

Keywords: *accessibility, voice control, human-machine interaction, BiLSTM, CNN, MFCC, neural networks, embedded systems, TinyML.*

Rezumat. Controlul vocal al dronelor este o direcție de inovare cu potențial ridicat pentru multe domenii profesionale și sociale. Acest articol analizează utilitatea practică a unui sistem de control vocal pentru drone bazat pe un model de inteligență artificială care rulează local, fără conexiune la internet. Modelul hibrid CNN+BiLSTM este antrenat să recunoască comenzi în limba română și este implementat pe platforma ESP-Drone cu un microcontroler ESP32-S2. Spre deosebire de alternativele comerciale bazate pe infrastructură cloud, soluția propusă rulează în întregime local, eliminând latența și dependența de conectivitate. Sunt examinate domeniile de aplicație cu cel mai mare impact, cum ar fi inspecțiile industriale, operațiunile de căutare și salvare și agricultura de precizie, evidențiind totodată o categorie de beneficiari adesea trecută cu vederea: persoanele cu dizabilități motorii, pentru care controlul vocal oferă posibilitatea de a pilota drone independent, fără a-și folosi mâinile.

Rezultatele experimentale demonstrează o precizie de testare de 99,4% și o latență end-to-end de 210–350 ms, confirmată în condiții reale de zbor.

Cuvinte cheie: *accesibilitate, control vocal, interacțiune om-mașină, BiLSTM, CNN, MFCC, rețele neuronale, sisteme integrate, TinyML.*

1. Introduction

In recent years, drones have seen accelerated market growth [1], evolving from devices intended for entertainment and multimedia applications to accessible platforms used in agriculture, technical inspections, logistics and emergency operations [2]. This rapid expansion exposes a fundamental limitation of the current control paradigm: the operator must use both hands for the remote controller, focusing their entire attention on maneuvering the device. In an industrial inspection scenario, an engineer who must simultaneously operate measuring equipment and pilot a drone faces an ergonomic constraint that is hard to solve with traditional solutions.

Voice control is a natural answer to this problem. The voice is the most intuitive human-machine interaction interface: it requires no prolonged training, leaves the hands free and can work under reduced visibility or operational stress. Recent advances in artificial intelligence, in particular the TinyML paradigm [3] (running machine learning models directly on embedded devices, without an internet connection), have made it possible to implement real-time voice recognition on affordable hardware [4].

The traditional remote controller with analog joysticks is a robust tool, but it implies an essential constraint: the operator cannot carry out any other manual activity while piloting the drone. Compared with the commercial DJI or Parrot solutions, which process voice commands in the cloud and do not support Romanian, the proposed system has an end-to-end latency of 210–350 ms, versus 500–1200 ms for cloud architectures [5], and runs entirely locally, including in areas without internet coverage. The system supports nine voice commands in Romanian (take off, land, forward, back, left, right, rotate left, rotate right and stop), enough coverage to perform all the fundamental movements of a quadcopter.

The usefulness of voice control appears in scenarios where the operator must be physically present, carry out parallel activities or act quickly. In industrial and critical-infrastructure inspections, the engineer can dictate observations and record data from a thermometer or a gas detector without interrupting piloting, thus removing a critical point of inefficiency. In search and rescue operations, a voice-controlled drone can be piloted by a rescuer who is simultaneously holding binoculars, a GPS or a safety rope; the local system performs the same regardless of telecommunication network coverage (GSM or internet), since communication with the drone takes place over a local WiFi network. In precision agriculture, a farmer can speak to the drone while manually examining plants or collecting soil samples. Voice control is also useful in tactical and security operations, as well as in cinematography, where the director can send simple commands (forward, rotate right, stop) directly to the drone.

An often overlooked application domain is accessibility for people with motor disabilities of the upper limbs. The traditional remote controller is practically inaccessible to people with paralysis or amputation of both upper limbs, and voice control removes this barrier: a person who can speak is able to pilot a drone with a system such as the one described in this paper. Concrete applications for this category of users include property surveillance, delivery of light objects inside the home, photography from inaccessible angles and participation in recreational activities on an equal footing with people without disabilities. Because the voice-recognition neural network is trained on the individual user's voice, the system also adapts to the pronunciation particularities of people with speech difficulties. Local operation removes the dependence on the internet connection, ensuring the system's availability under any conditions.

The main aim of the paper is to highlight the concrete domains where such a solution produces a real impact, including for people with motor disabilities, and to present the methodology for building a local voice control system for drones.

2. Materials and methods

This section presents the methodology for building the voice control system: the overall two-component architecture, the audio signal acquisition and processing chain together with the mathematical feature-extraction model, the architecture of the neural classification model and the communication protocol with the drone. For each stage, the components involved, the corresponding mathematical relations and their role in the processing chain are presented.

The architecture of the analyzed system is structured around two main components, the ground station (the operator's laptop) and the drone, which communicate over WiFi, without dependence on external infrastructure [6]. This conceptual separation is illustrated in Figure 1. This separation keeps the heavy computation, audio capture and neural inference, on the laptop, while the drone only receives ready-to-use flight commands. As a result, the drone needs no additional onboard hardware beyond its standard ESP32-S2 microcontroller, which keeps weight and cost low. The two components exchange data exclusively over a local WiFi link, so the system stays fully operational in areas without internet or cellular coverage. Because all model logic lives on the ground station, the recognition model can be retrained or replaced without any change to the drone firmware.

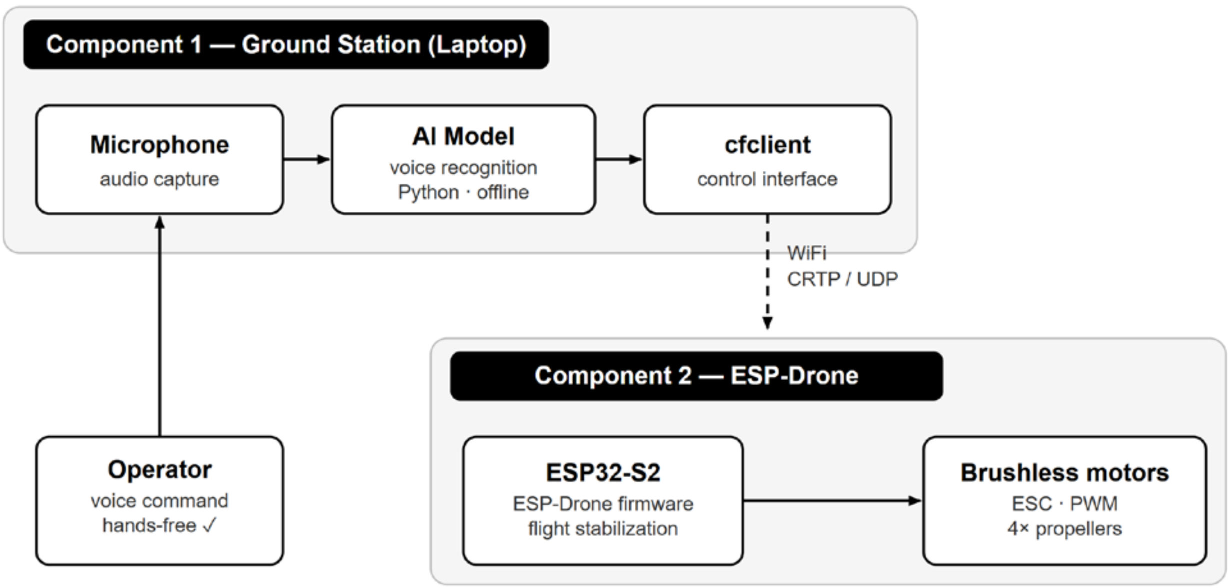

Figure 1. Conceptual architecture of the system: the ground station and the drone communicate over WiFi, without external infrastructure.

The ground station encompasses the entire voice-processing chain: capturing the audio signal through the microphone, preprocessing by extracting MFCC coefficients, inference of the CNN+BiLSTM artificial intelligence model and transmitting the resulting command over WiFi to the drone. This approach makes use of the computing resources of an existing laptop and removes the need for additional dedicated hardware. The ESP-Drone is equipped with the ESP32-S2 microcontroller, which receives the commands and translates them into control signals for the brushless motors, through electronic speed controllers (ESC), running the open-source ESP-Drone firmware derived from the Crazyflie project [6].

2.1. Audio signal acquisition and processing

The voice signal is captured by the microphone at a sampling rate of 16 kHz, in 2-second analysis windows. The complete processing flow, from signal capture to command execution on the drone, is shown in Figure 2 as a sequence diagram. The microphone sends the signal to the AudioFeatureExtractor component, which extracts the MFCC coefficients; these are passed to the CommandRecognizer component, which runs the CNN+BiLSTM network inference and, if the confidence score exceeds the set threshold, sends the command to the DroneController; the latter translates it into flight parameters and transmits it to the drone through CRTP packets over WiFi.

Sampling at 16 kHz is a deliberate compromise: it preserves the frequency range that carries the information of spoken commands while keeping the amount of data per window low enough for real-time processing on a standard laptop. The fixed 2-second window sets the maximum length of a command and gives the network a consistent input size, which simplifies both feature extraction and inference. The confidence threshold acts as a rejection mechanism: when no command is spoken, or when background noise dominates, the score stays low and the DroneController receives nothing, so the drone holds its current state instead of reacting to spurious input. Because each stage passes a compact representation to the next, the microphone hands over raw audio, the AudioFeatureExtractor a small feature matrix and the CommandRecognizer a single label, the data volume shrinks along the chain, which keeps the end-to-end latency within the range required for responsive control.

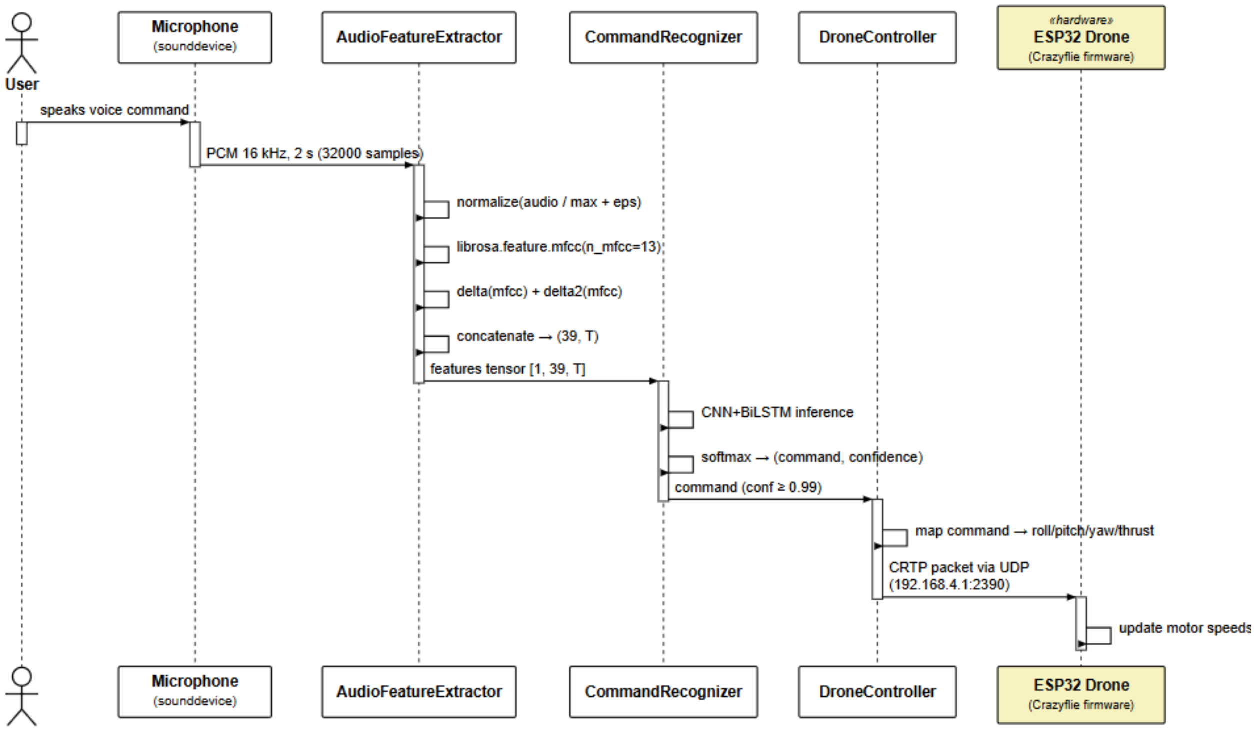

Figure 2. Sequence diagram of voice command processing.

The MFCC representation is preferred to the raw audio signal because it compresses the relevant spectral information of the human voice into a compact vector, significantly reducing the computational complexity of inference without loss of accuracy [7]. The coefficient extraction process, shown in Figure 3, goes through the following stages: pre-emphasis, framing, windowing, fast Fourier transform (FFT), Mel-scale filtering, log-energy computation and the discrete cosine transform (DCT).

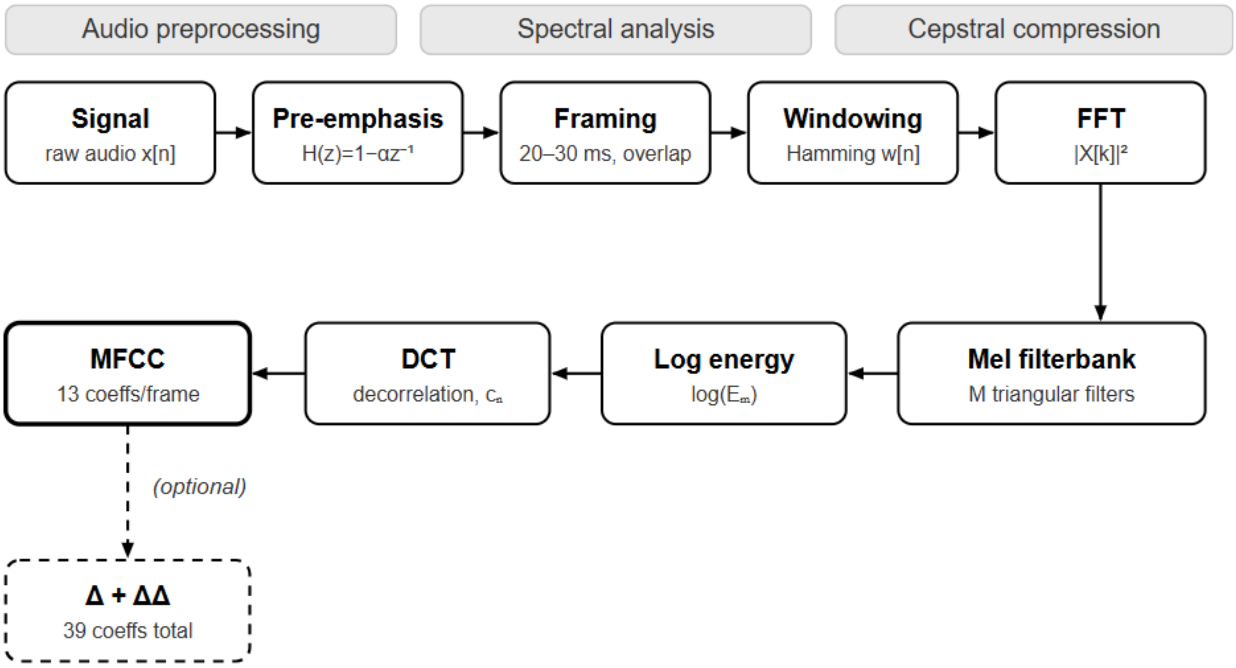

Figure 3. Mel-Frequency Cepstral Coefficients (MFCC) extraction pipeline.

The mathematical model of the extraction chain is described by relations (1)–(7), each stage playing a specific role in transforming the raw signal into a set of discriminative features. Pre-emphasis amplifies the high-frequency components of the signal $x[n]$, naturally attenuated in speech, balancing the spectrum and improving the signal-to-noise ratio for the upper formants; $\alpha \approx 0.97$ (Eq. (1)):

$$y[n] = x[n] - \alpha \cdot x[n-1] \tag{1}$$

The signal is then segmented into frames of 20–30 ms and weighted with a Hamming window $w[n]$, which reduces spectral leakage at the frame edges and ensures the continuity required for the Fourier transform; N is the number of samples in the frame (Eq. (2)):

$$w[n] = 0.54 - 0.46 \cdot cos\left(\frac{2\pi n}{N-1}\right) \tag{2}$$

For each frame, the power spectrum is computed through the discrete Fourier transform of the N samples, moving the signal from the time domain to the frequency domain, where voice information is more easily separable (Eq. (3)):

$$P[k] = \left|\sum_{n=0}^{N-1} x[n] \cdot w[n] \cdot e^{-j2\pi kn/N}\right|^2 \tag{3}$$

The linear frequencies f (in Hz) are converted to the perceptual Mel scale, which mimics the nonlinear frequency resolution of the human ear, finer at low frequencies, where the relevant voice information is concentrated (Eq. (4)):

$$m(f) = 2595 \cdot log_{10}\left(1 + \frac{f}{700}\right) \quad (4)$$

The energies resulting from the M triangular Mel filters are logarithmized, an operation that compresses the dynamic range, similar to human perception of sound intensity, and groups the energy into perceptually relevant bands; $H_m[k]$ is the response of filter m (Eq. (5)):

$$S_m = ln\left(\sum_{k=0}^{N-1} P[k] \cdot H_m[k]\right) \quad (5)$$

The discrete cosine transform decorrelates the log-energies and concentrates the information in the first coefficients, producing a compact feature vector; this yields the cepstral coefficients c_i, i = 0…12 (Eq. (6)):

$$c_i = \sum_{m=1}^{M} S_m \cdot cos\left(\frac{\pi \cdot i \cdot (m-0.5)}{M}\right) \quad (6)$$

To capture the temporal dynamics of speech (the speed and acceleration of spectral variation, essential for distinguishing commands), the delta coefficients Δc_t and, analogously, the accelerations $\Delta\Delta c_t$ are computed (Eq. (7)):

$$\Delta c_t = \frac{\sum_{n=1}^{K} n \cdot (c_{t+n} - c_{t-n})}{2 \cdot \sum_{n=1}^{K} n^2} \quad (7)$$

Each analysis window is thus transformed into a matrix of 39 coefficients (13 base MFCC, 13 delta and 13 delta-delta), which constitutes the input tensor of the neural network.

2.2. The CNN+BiLSTM neural model

Voice command recognition is treated as a multi-class classification problem: for a 2-second audio segment, the model assigns one of the nine labels corresponding to the commands, while recordings below the confidence threshold are rejected as background noise. The hybrid architecture was chosen because it combines the efficiency of convolutions in extracting local features from the spectral representation with the ability of LSTM networks to model long-term temporal dependencies [8]. The convolutional module consists of two successive Conv1d blocks (64 and 128 filters, kernel 5), each followed by ReLU activation, LayerNorm normalization and MaxPool1d subsampling, with Dropout (0.3). The output is passed to a recurrent module made of two stacked BiLSTM layers, with 256 hidden units per direction in the first layer (512 in total) and 128 in the second (256 in total), followed by temporal average pooling (global average pooling). The resulting vector passes through two fully connected layers with Dropout (0.3) for regularization; the last layer has nine outputs, one for each command.

The model was trained with the Adam optimizer (learning rate 0.001) and the CrossEntropyLoss objective. To improve robustness, the original set of about 1500 recordings was expanded through noise-based data augmentation [9], and an early stopping rule ended training when the validation accuracy stopped improving for ten consecutive epochs, which limited overfitting. Layer normalization was preferred over batch normalization because the small batch size and the variable length of the audio sequences make batch statistics unstable. The per-class behaviour of the trained model on the test set is summarized in the confusion matrix in Figure 4.

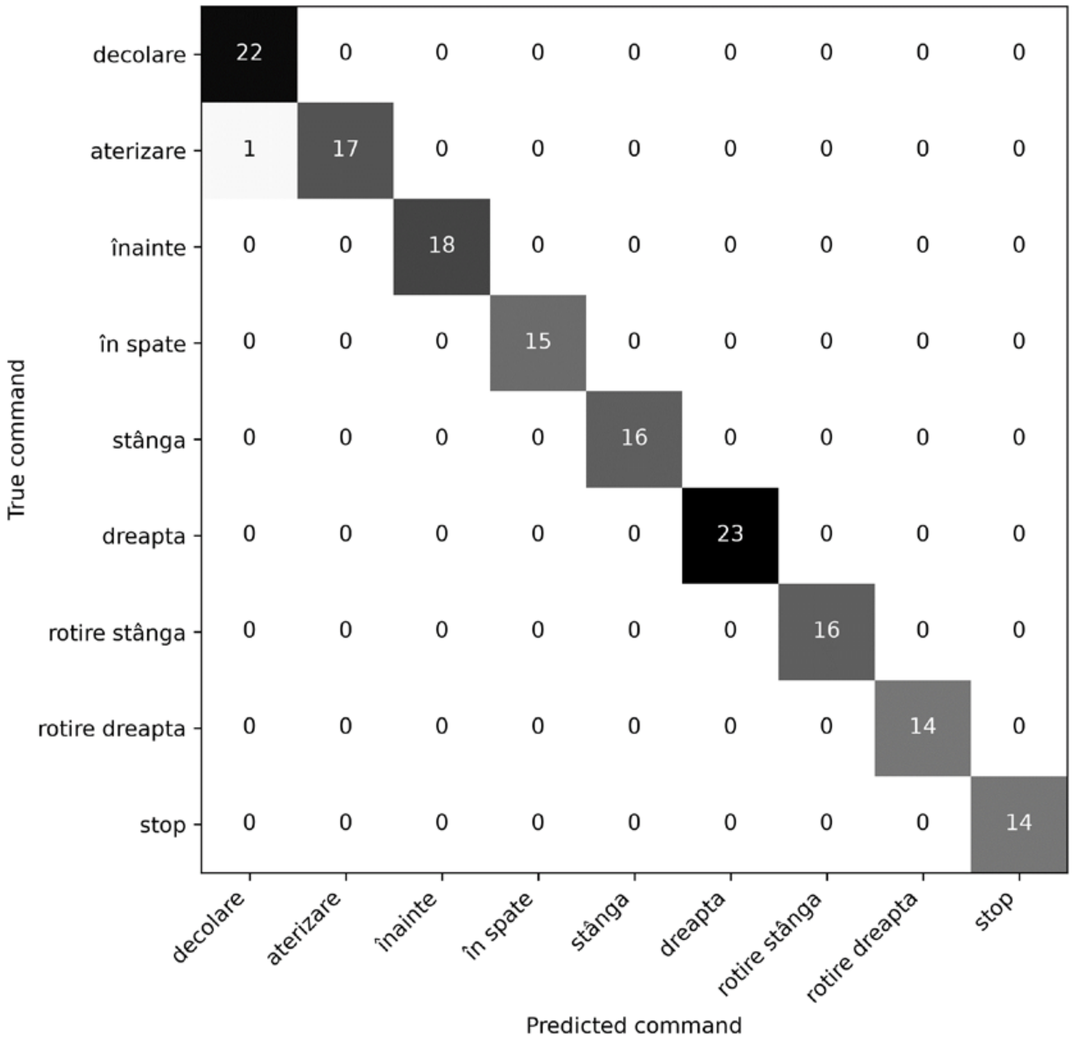

Figure 4. Confusion matrix of the CNN+BiLSTM model on the test set. Command labels are kept in Romanian, the language the model was trained on.

The matrix shows a near-diagonal structure: every command except one is recognized correctly, the single error being one ”*aterizare*” (LAND) sample predicted as ”*decolare*” (TAKE OFF), two short commands that begin with similar plosive sounds. No confusion appears between the compound commands and their short forms, for example ”*rotire stânga*” (ROTATE LEFT) is never mistaken for ”*stânga*” (LEFT), nor ”*rotire dreapta*” (ROTATE RIGHT) for ”*dreapta*” (RIGHT), which confirms that the stacked BiLSTM layers capture the temporal structure needed to separate them. The directional commands ”*înainte*” (FORWARD) and ”*în spate*” (BACK), which an operator might pronounce with overlapping vowels, are also kept apart without error. This balanced per-class behaviour, with no systematic weakness on any individual command, reflects the complementary roles of the convolutional stage, which extracts local spectral patterns, and the recurrent stage, which models how those patterns evolve in time. The complete layer-by-layer architecture that produces this behaviour is shown in Figure 5.

Figure 4 shows the full layer chain as implemented, from the sequence input of the 39 features to the softmax layer with nine outputs. The Deep Network Designer-style representation makes explicit the exact order of operations within each convolutional block (convolution, activation, normalization, subsampling, dropout) and how the two BiLSTM layers are chained before temporal aggregation.

Figure 5. CNN+BiLSTM model architecture.

This view was also used to check the consistency between the theoretical description and the actual model implementation.

2.3. Communication with the drone via the CRTP protocol

Communication between the laptop and the drone is carried out through the Crazyflie Real-Time Protocol (CRTP), a stateless real-time protocol that requires no handshake [10]. The 32-byte CRTP packets (1 header byte and 31 payload bytes) are transported through UDP datagrams to IP address 192.168.4.1, port 2390 of the drone, which acts as a WiFi access point. The measured communication latency is below 5 ms under normal conditions.

The recognized voice commands are translated into flight parameters (roll, pitch, yaw and thrust) and transmitted periodically to the drone. The take-off command initiates a progressive ramp-up of the thrust value over 2.4 seconds, avoiding abrupt movements, and a

3-second post-take-off immunity mechanism blocks accidental stop commands immediately after lift-off, preventing unintended landings caused by motor noise picked up by the microphone.

3. Case study

3.1. Software implementation and the state machine

The graphical interface, developed in Python with the CustomTkinter library, is structured into five functional sections: audio data collection, model training, validation, voice control and hardware configuration. The voice control section displays in real time the captured audio waveform, the recognized command and the associated confidence score, allowing the operator to monitor recognition quality. The code is organized according to clean architecture principles, with a clear separation of responsibilities between modules [11]. The complete implementation of the system is described in the authors' bachelor's thesis [12].

The transitions between the operating states of the drone controller (IDLE, CONNECTING, HOVER, MOVING, ROTATING and LANDING) are managed by a state machine, illustrated in Figure 6. From the IDLE state, starting voice control triggers the connection; a take-off command with high confidence brings the drone into the HOVER state, from which direction and rotation commands temporarily activate the MOVING and ROTATING states. Loss of the WiFi connection triggers an automatic transition to the IDLE state, with a controlled stop of the motors, ensuring predictable and safe behavior.

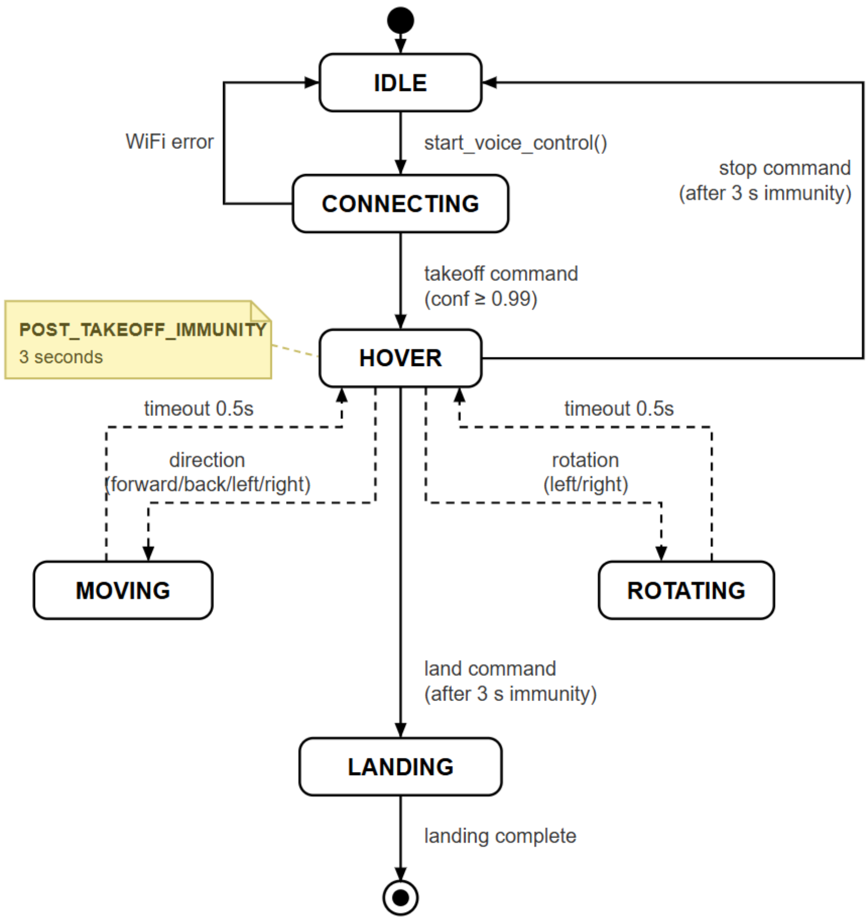

Figure 6. Drone controller state machine.

Organizing the controller as an explicit state machine guarantees that each command is interpreted only in the context where it is valid: a take-off command is ignored while the drone is already flying, and a direction command has no effect before take-off. After a movement, the MOVING and ROTATING states return to HOVER once the command ends, so the drone defaults to a stable hover rather than continuing an action indefinitely. The transition back to IDLE on connection loss is the central safety feature, since it prevents the drone from drifting under the last received command when communication drops. Because every transition is tied to a well-defined event, a voice command, a confidence threshold or a connection status, the behavior of the system remains deterministic and easy to predict, which is essential for safe operation near the operator.

This organization of the states guarantees that each voice command is interpreted only in the context in which it is valid, eliminating nondeterministic behaviors and increasing flight safety. For example, a stop command is accepted in HOVER, MOVING or ROTATING, but is ignored in IDLE or CONNECTING, where it has no meaning. The post-takeoff immunity window adds a further safety layer by blocking stop commands for three seconds after lift-off, preventing accidental landings caused by motor noise. Loss of the WiFi connection in any active state triggers a controlled transition back to IDLE, so the drone never remains in an undefined state when communication drops.

3.2. Experimental results

The system was evaluated under real flight conditions. The CNN+BiLSTM model reached an accuracy of 99.4% on the validation test set, and the measured end-to-end latency, from speaking the command to the drone's reaction, fell within the 210–350 ms range, compatible with real-time control. The latency of the CRTP communication layer remained below 5 ms. The main parameters and results of the system are summarized in Table 1.

Table 1

Parameters and performance of the voice control system

Parameter	Value
Recognized language	Romanian
Recognized voice commands	9
Sampling rate	16 kHz
Analysis window	2 s
MFCC coefficients per frame	39
Model architecture	CNN (2× Conv1d) + BiLSTM (512)
Dataset	~1500 samples
Test accuracy	99.4%
End-to-end latency	210 – 350 ms
CRTP communication latency	< 5 ms
Hardware platform cost	~40 USD

The values in Table 1 confirm that a low-cost platform (~40 USD) can support real-time local voice recognition, with an accuracy comparable to that of cloud-based commercial solutions, but without dependence on connectivity. To document the in-flight behavior, Figure 7 shows a sequence captured during voice operation of the drone.

Figure 7. Drone airborne while executing the voice command ”*înainte*” (*forward*).

The in-flight test confirms that the system works under real conditions: the “forward” command was recognized and sent to the drone with no perceptible delay, and the motion was controlled, with no abrupt attitude corrections. The post-take-off immunity window prevented accidental interpretation of a command during initial stabilization, which kept the flight stable throughout the sequence. Together with the values in Table 1, this shows that the system responds correctly to voice commands. Testing outdoors also exposed the system to conditions absent from the controlled recordings, such as wind noise and ambient park sounds, yet the command was still recognized on the first attempt, which suggests that the noise-based data augmentation helped the model generalize beyond the training environment. The operator kept both hands on the laptop throughout the maneuver, illustrating the hands-free interaction that motivates the whole approach: the drone was guided by voice alone, without any physical controller. The short, perceptible gap between speaking the command and the drone reacting stayed within the latency range reported in Table 1, confirming that local, offline processing is fast enough for responsive control. Taken together, the laboratory measurements and this field observation indicate that the system behaves consistently when it leaves the test environment.

4. Discussion

The results confirm the working hypothesis: a voice control system that runs entirely locally can achieve an accuracy and a latency compatible with real-time piloting, without depending on cloud infrastructure. The main advantages of the solution are fully local operation, the low cost of the platform, support for Romanian and adaptation to the individual user's voice, which makes it accessible even to people with speech difficulties.

The solution also has limitations. The vocabulary of nine commands covers the fundamental movements but restricts complex maneuvers; training on the individual voice increases accuracy but requires a data-collection stage for each new user; and the operating range is limited by the coverage of the local WiFi network. Compared with cloud architectures, the system reduces latency from 500–1200 ms to 210–350 ms and eliminates the dependence on the internet, at the cost of a more restricted vocabulary and a local training stage.

The identified development directions target continuous command recognition, vocabulary expansion and porting the TinyML model directly onto the drone, which would reduce latency below 100 ms and completely eliminate the need for a ground station. Periodic retraining on the user's voice could further improve accuracy in noisy environments.

5. Conclusions

The local voice control system for drones analyzed in this paper demonstrates that hands-free aerial piloting is a functional technical reality, experimentally validated with an accuracy of 99.4% and a latency compatible with real-time control. The solution removes the need for manual interaction between the operator and the drone and instead offers the possibility of full guidance through voice commands, keeping an optimal balance between performance, cost and independence from cloud infrastructure.

The practical impact appears on two complementary levels. On the professional level, voice control increases operator efficiency in industrial inspections, mountain rescue, agricultural monitoring and security operations, domains in which free hands are an operational necessity. On the social level, the system opens access to drone technology for people with motor disabilities of the upper limbs, giving them autonomy and the capacity to act. The open-source nature of the entire platform ensures the reproducibility and extensibility of the solution, including in resource-limited environments.

These results were obtained on a low-cost platform built around an ESP32-S2 microcontroller, which shows that the approach does not depend on specialized or expensive hardware and can be reproduced with widely available components. Because the recognition model runs entirely on the ground station, the system can be extended with new commands or adapted to a new user's voice without any change to the drone itself, which keeps the path open for future improvements. The main directions that follow from this work are enlarging the command vocabulary, moving the model directly onto the drone to remove the need for a ground station, and validating the system across more speakers and noisier environments. Taken together, the findings confirm that local, offline voice control is a practical and accessible way to pilot drones, with concrete benefits for both professional operators and users with motor disabilities.

Research Data Availability Statement: No new public datasets were created. The audio recordings used for training were collected by the authors and are not shared due to privacy considerations regarding the voice samples.

Acknowledgments. This work was carried out within the "Research on intelligent methods and effective means for monitoring forest, perennial and aquatic areas with the application of drones", 25.80012.5007.71SE. During the preparation of this manuscript, Gheorghe Bulai used Claude (Claude Opus 4.5, Anthropic) for translating the text from Romanian to English.

Contribution of authors.
Bulai Gheorghe: Conceptualization, Investigation, Methodology, Writing – original draft.
Viorel Bostan: Funding acquisition, Supervision, Project administration.
Rotaru Lilia: Investigation, Writing – editing.
Bumbu Tudor: Conceptualization, Supervision, Writing – review.

Conflicts of Interest. The authors declare no conflict of interest.

References

1. Pal, O.K., Shovon, M.S.H., Mridha, M.F. and Shin, J. (2024) In-depth review of AI-enabled unmanned aerial vehicles: Trends, vision, and challenges, Discover Artificial Intelligence, 4(1), 97. https://doi.org/10.1007/s44163-024-00209-1.
2. Valavanis, K.P. and Vachtsevanos, G.J. (eds.) (2015) Handbook of Unmanned Aerial Vehicles. Dordrecht: Springer Netherlands. https://doi.org/10.1007/978-90-481-9707-1.
3. Tsoukas, V., Gkogkidis, A., Boumpa, E. and Kakarountas, A. (2024) A review on the emerging technology of TinyM', ACM Computing Surveys, 56(10), pp. 1–37. https://doi.org/10.1145/3661820.
4. Di Leo, S., De Cicco, L. and Mascolo, S. (2025) Real-Time Speech-to-Text on Edge: A Prototype System for Ultra-Low Latency Communication with AI-Powered NLP, Information, 16(8), 685. https://doi.org/10.3390/info16080685.
5. Picovoice (2025) Speech-to-Text Latency: How to Read Vendor Claims. Available at: https://picovoice.ai (Accessed: May 2026).
6. Espressif Systems (2024) ESP-Drone Documentation – Get Started. Available at: https://docs.espressif.com (Accessed: March 2026).
7. Lyons, R.G. (2011) Understanding Digital Signal Processing. 3rd edn. Upper Saddle River, NJ: Prentice Hall.
8. Hochreiter, S. and Schmidhuber, J. (1997) Long Short-Term Memory, Neural Computation, 9(8), pp. 1735–1780. https://doi.org/10.1162/neco.1997.9.8.1735.
9. De Simone, G., Greco, A., Rosa, F., Saggese, A. and Vento, M. (2025) Context-aware data augmentation for enhanced speech command recognition in industrial environments, Scientific Reports, 15(1), 17445. https://doi.org/10.1038/s41598-025-01886-3.
10. Bitcraze AB (2024) CRTP – Communication with the Crazyflie. Available at: https://www.bitcraze.io (Accessed: March 2026).
11. Martin, R.C., Grenning, J., Brown, S. and Henney, K. (2018) Clean Architecture: A Craftsman's Guide to Software Structure and Design. Boston, MA: Prentice Hall.
12. Bulai, G. (2026) Voice Control System for Piloting Drones. Bachelor's thesis. Technical University of Moldova, Chișinău.

Citation: Bulai, Gh., Bostan, V., Rotaru, L, Bumbu, T. (2026). Voice control system for piloting drones using artificial intelligence techniques. *Journal of Engineering Science*. 2026, 33 (2), pp. 7-19. https://doi.org/10.52326/jes.utm.2026.33(2).01.

Publisher's Note: JES stays neutral with regard to jurisdictional claims in published maps and institutional affiliations.

Copyright:© 2026 by the authors. Submitted for possible open access publication under the terms and conditions of the Creative Commons Attribution (CC BY) license (https://creativecommons.org/licenses/by/4.0/).

Submission of manuscripts: jes@meridian.utm.md

Journal of Engineering Science *Vol. XXXIII, no. 2 (2026), pp. 20 - 31*
Fascicle *Industrial Engineering* *ISSN 2587-3474*
Topic *Applied Engineering Sciences and Management* *eISSN 2587-3482*

https://doi.org/10.52326/jes.utm.2026.33(2).02
UDC 629.7.05:681.5:004.8

ANALYSIS OF CONTROL ARCHITECTURES FOR UNMANNED AERIAL VEHICLES

Adriana Ursu*, ORCID: 0009-0003-4263-2444,
Igor Calmîcov, ORCID: 0000-0002-4017-3702,
Viorel Cărbune, ORCID: 0000-0002-1556-4453

Technical University of Moldova, Studentilor 9/7, Chișinău, 2045, Republic of Moldova
* Corresponding author: Adriana Ursu, *ursu.adriana@iis.utm.md*

Received: 05. 14. 2026
Accepted: 06. 17. 2026

Abstract. Unmanned aerial vehicles (UAVs) have become important components of modern systems for monitoring, inspection, mapping, and autonomous intervention. Their performance directly depends on the efficiency of the control systems and the architecture used for data processing, decision-making, and mission coordination. The paper presents a comparative analysis of the main control architectures used in UAV platforms: control with on-board processing (On-Board Control), hierarchical Master-Swarm architecture, and centralized systems based on a Ground Control System (GCS). It describes the operating principles of each architecture, the hardware and software components involved, advantages, limitations, and specific areas of application. The analysis highlights the impact of each solution on autonomy, scalability, resilience to communication loss, and real-time control performance. The results obtained show that On-Board Control systems offer superior autonomy and robustness, Master-Swarm architectures are intended particularly for the collaborative coordination of drone swarms, and GCS systems provide advanced capabilities for monitoring and centralized processing. Furthermore, current trends oriented towards hybrid architectures are highlighted, which combine the advantages of the three models to increase the level of autonomy, safety, and operational efficiency of modern UAV systems.

Keywords: *UAV, autonomous drone, control system, On-Board Control, Drone Swarm, Ground Control System, real-time control, autonomous navigation, drone swarm, operational autonomy, multi-agent systems, distributed control.*

Rezumat. Vehiculele aeriene fără pilot (UAV) au devenit componente importante ale sistemelor moderne de monitorizare, inspecție, cartografiere și intervenție autonomă. Performanța lor depinde direct de eficiența sistemelor de control și de arhitectura utilizată pentru procesarea datelor, luarea deciziilor și coordonarea misiunilor. Lucrarea prezintă o analiză comparativă a principalelor arhitecturi de control utilizate în platformele UAV: control cu procesare la bord (On-Board Control), arhitectura ierarhică Master-Swarm și sistemele centralizate bazate pe un Sistem de Control la Sol (GCS). Se descriu principiile de funcționare ale fiecărei arhitecturi, componentele hardware și software implicate, avantajele, limitele și domeniile specifice de aplicare. Analiza evidențiază impactul fiecărei soluții asupra autonomiei, scalabilității, rezistenței la pierderea comunicațiilor și performanței controlului în timp real. Rezultatele obținute arată că sistemele de Control la Bord oferă autonomie și robustețe superioare, arhitecturile Master-Swarm sunt destinate în special coordonării colaborative a roiurilor de drone, iar sistemele GCS oferă capabilități avansate de monitorizare și procesare centralizată. În plus, sunt evidențiate tendințele actuale orientate spre arhitecturi hibride, care combină avantajele celor trei modele pentru a crește nivelul de autonomie, siguranță și eficiență operațională a sistemelor UAV moderne.

Cuvinte cheie: *UAV, dronă autonomă, sistem de control, control la bord, roi de drone, sistem de control la sol, control în timp real, navigație autonomă, roi de drone, autonomie operațională, sisteme multi-agent, control distribuit.*

1. Introduction

Unmanned aerial vehicles (UAV), generically known as drones, represent aerial platforms capable of operating without a human crew on board, being controlled remotely or functioning autonomously through complex algorithms or artificial intelligence systems. Initially developed predominantly for entertainment, UAV technologies have experienced an exponential expansion in recent decades, particularly in the agricultural, commercial, research, and military sectors. Due to their versatility, low operational costs, and the ability to explore hostile or hard-to-reach environments without risking human lives, drones have become important tools in a wide range of applications. Currently, they are widely used in fields such as precision agriculture, critical infrastructure monitoring, emergency management, mapping and three-dimensional terrain modeling, environmental surveillance, and logistics [1].

Despite significant progress in the development of UAV platforms, designing control systems remains one of the most complex engineering challenges. The nonlinear character of flight dynamics, variations in aerodynamic parameters, uncertainties in mathematical models, and the influence of external disturbances require the development of robust and adaptive control strategies. Moreover, the integration of an increasing number of sensors, communication systems, and data processing algorithms leads to higher demands regarding the computational performance and reliability of on-board systems [2].

Current trends in UAV design aim to increase the degree of autonomy through the use of advanced control techniques and artificial intelligence algorithms. Thus, classical methods based on PID (Proportional-Integral-Derivative) control are supplemented or replaced by modern strategies, such as predictive control (MPC – Model Predictive Control), adaptive control, robust control, and machine learning methods [4, 5]. These approaches allow for improving navigation precision, optimizing energy consumption, and increasing the capacity to operate in complex and unstructured environments. They constitute, in essence, technological ecosystems of remarkable complexity, representing the convergence point of aerospace engineering, advanced electronics, systems theory, and applied computer science. Their fundamental purpose is to guarantee stable flight dynamics, high-precision navigation, and the autonomous or semi-autonomous execution of complex tasks, operating in dynamic and often unpredictable three-dimensional environments (subject to aerodynamic and meteorological disturbances).

In the context of modern applications, which include territory monitoring, mapping, precision agriculture, search and rescue operations, or autonomous deliveries, the requirements imposed on control systems are becoming increasingly complex. Depending on the operational requirements and the required degree of autonomy, the architecture of control systems can be implemented in different configurations. Thus, processing and decision-making can be performed directly on board the drone (On-Board Control) [4], can be coordinated via a main drone within multi-UAV systems (Master Drone) [7], or can be centrally managed by a Ground Control System (GCS) [8]. Each of these approaches presents specific advantages and limitations regarding communication latency, processing capacity, scalability, and the level of system autonomy. Analyzing these control architectures is very important for understanding how modern drones operate and for identifying optimal solutions based on the specific characteristics of each mission.

The problem addressed in this paper consists of the analysis and evaluation of control systems used for UAV platforms, focusing on the control mode, command architectures, and modern autonomous navigation methods [6]. The increasing complexity of missions performed by unmanned aerial vehicles requires the development of control systems capable of ensuring the safe, precise, and efficient operation of drones in dynamic and unpredictable environments. Traditional control systems, based exclusively on human operator intervention, are limited by communication latency, reduced real-time reaction capacity, and the difficulty of simultaneously managing a large number of aerial platforms. In this context, there is a need for advanced control architectures that allow for an increased degree of autonomy and adaptability for drones.

The main challenge lies in designing and integrating control architectures that ensure an optimal balance between system autonomy, communication reliability, processing capacity, and operational efficiency. The choice of how to organize local control on board the drone, coordinated via a main drone, or centrally managed via a ground control station directly influences the system's performance. Furthermore, the challenge is amplified by the need to maintain flight stability, synchronization among components, and resilience in the face of communication errors or unfavorable environmental conditions.

The objective of this paper is to analyze and compare the main control architectures used in UAV systems, with an emphasis on On-Board Control, hierarchical coordination through a Master Drone, and centralized management through a Ground Control System (GCS) [3, 6]. The paper aims to highlight the operating principles, advantages, and limitations of each approach, as well as to identify applicability domains based on operational requirements and the required level of autonomy. Through this analysis, the goal is to formulate conclusions regarding the efficiency and appropriateness of using different control models within modern drone systems.

2. Analysis of Control Architectures for UAV Platforms

The control system architecture represents one of the fundamental elements that determine the performance, degree of autonomy, and reliability of a UAV platform. The evolution of communication technologies, embedded systems, and artificial intelligence algorithms has led to the emergence of several models for organizing control, each optimized for specific operational scenarios. Among the most widely used architectures are On-Board Control, hierarchical coordination via a main drone (Master Drone Control), and centralized management through a Ground Control System (GCS).

2.1. On-Board Processing Control Architecture

The On-Board Control architecture is where all essential functions for flight control are executed by computing systems installed directly on the drone. This approach involves the integration of a flight control unit (Flight Controller), an on-board computer (Companion

Computer), and a set of sensors that provide information about the UAV's status and surrounding environment. Data from sensors are continuously analyzed to estimate the drone's position, speed, and orientation. Based on this information, control algorithms generate commands for the motors and control surfaces [4].

The diagram in Figure 1 presents the architecture of a closed-loop cascaded control system used for flight control of a drone or autonomous aircraft. Information flows from top to bottom for command execution, and measured data returns through a feedback loop to correct errors. The entire cycle repeats very rapidly (thousands of times per second) to maintain flight stability [5].

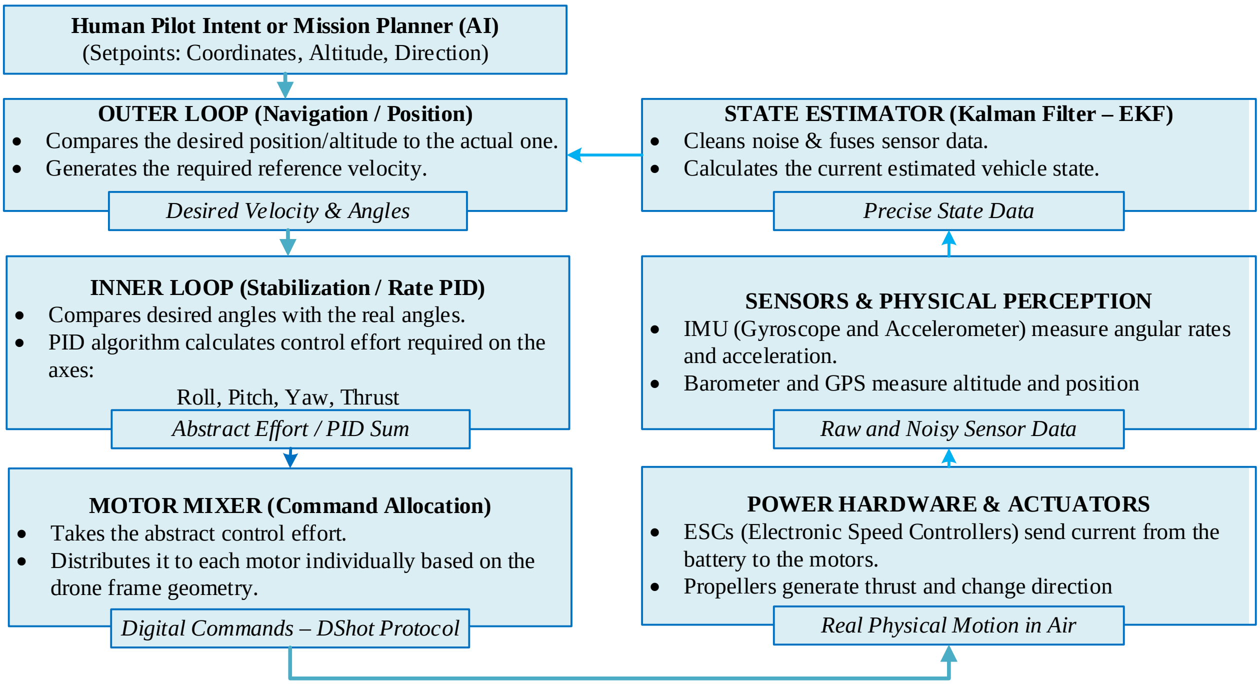

Figure 1. Architecture of an on-board processing control system for a drone.

1. The process begins with the actions of a human pilot or a mission planning application. This establishes the desired flight parameters, called setpoints, such as coordinates, altitude, and direction of travel. These values represent the objective that the control system must achieve.
2. The outer loop is responsible for navigation and positioning. It compares the desired position and altitude with the real position and altitude of the drone.
3. Based on this difference (control error), the system calculates the reference speed and angles needed to reach the desired position.
4. The output of the outer loop is transmitted to the inner loop, which handles the stabilization of the aircraft. This loop compares the desired angles with the actual angles of the drone. It uses PID (proportional-integral-derivative) control algorithms to calculate the required control action. This control is applied to the primary axes of motion, resulting in an abstract control action for each axis. This control action cannot be applied directly to the motors. Therefore, a motor mixer intervenes, transforming the abstract control commands and distributing them individually to each motor, taking into account the drone's frame geometry. Commands are sent as digital signals. Digital commands reach the ESCs (Electronic Speed Controllers), which control the current supplied by the battery to the motors and regulate the motors' rotation speed

[4, 5]. The motors rotate the propellers, which generate the necessary thrust for the drone to move through the air. In this stage, the actual physical motion of the drone occurs.

5. To understand the true state of the drone, the system uses multiple sensors such as a gyroscope, accelerometer, and barometer. Sensor data is raw and contains noise.
6. The sensory data is processed by the state estimator. It filters out noise from the data, combines information from different sensors, and calculates the drone's estimated state. The filtered data is transmitted back to the outer and inner control loops. The controller can compare the desired state with the real state, correct errors, and generate new commands. This process forms a closed control loop, which repeats continuously, usually between 1000 and 8000 cycles per second for drone control [4, 5]. Through this rapid updating, errors are corrected immediately, aircraft stability is maintained, and the vehicle can precisely execute navigation commands.

The on-board processing control architecture has several advantages. It does not need a continuous connection with a ground station for navigation, the drone is highly resistant to jamming attacks or accidental signal loss, decision-making time is minimal, and it is the only viable architecture for environments where GPS or radio signals are inaccessible. But it also has disadvantages, such as weight and energy consumption limiting available computing power; integrating high-performance processors and advanced sensors increases platform costs; and if the platform crashes and is destroyed, data processed and stored locally may be lost, not being transmitted in real-time to a secure database.

Due to its independence from external communication networks, this architecture dominates in applications deployed in isolated or heavily shielded environments. Areas of application for On-Board Control include autonomous navigation inside mines, sewer networks, or complex logistics warehouses, where a GPS signal is non-existent and maintaining a Data Link with the exterior is impossible. The drone relies entirely on local data processing and inertial positioning methods. Use in last-mile urban delivery scenarios, where zero latency in dynamic obstacle avoidance decisions (Sense and Avoid) is critical for safety. Space platforms sent to other planets, where the enormous latency of interplanetary communications makes real-time remote control impossible.

2.2. Master-Swarm Hierarchical Control Architecture

For missions requiring vast spatial coverage or operational redundancy, coordinated multi-agent systems are used. The Master-Swarm architecture reduces the individual complexity of drones by centralizing tactical intelligence at the level of a single aerial node. The Main Drone (Master) functions as a mobile aerial server. It has superior computing power and a more complex sensor suite. It handles generating global trajectories, obstacle avoidance, and dynamic target allocation.

The Subordinate Fleet (Swarm) are the component drones, which operate exclusively at the hardware level with simplified control loops. Their main task is maintaining a relative position compared to the Master drone or tracking velocity vectors transmitted by it. Communication is achieved via an ad-hoc network (FANET - Flying Ad-Hoc Network) [9]. The Master drone issues setpoint commands, and the local control loops of the swarm drones execute necessary corrections. This topology prevents radio frequency spectrum congestion and significantly reduces the fleet's production cost.

Figure 2 presents the architecture of a drone swarm system (master−swarm) used for coordination and autonomous execution of distributed missions. The system is controlled by the Ground Control System (GCS), which transmits mission objectives and monitors overall operation status through a long-range communication link. At the center of the architecture is the Master drone, responsible for mission planning, dynamic task allocation, global route calculation, and swarm health monitoring. It processes data received from drones in the network and transmits global commands to them.

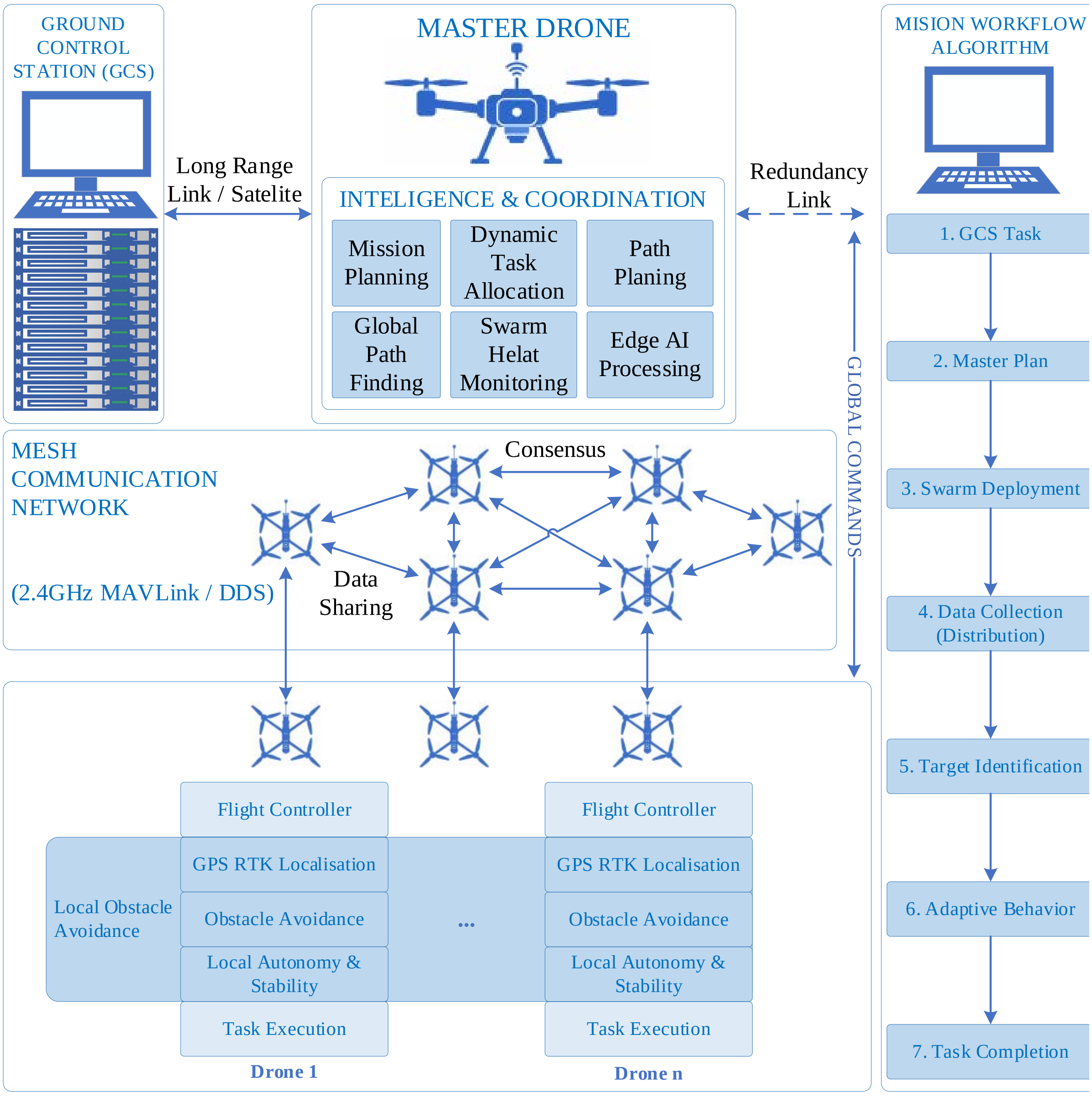

Figure 2. Architecture of a master-swarm drone system.

Drones in the swarm communicate with each other through a communication mesh network based on protocols such as MAVLink (Micro Air Vehicle Link) or DDS (Data Distribution Service) [7], which allows data sharing, routing through intermediate nodes, and achieving consensus between units. Each drone features a flight controller, RTK GPS localization system, obstacle avoidance sensors, and local autonomy modules, allowing it to execute tasks independently. The mission workflow includes stages such as task planning, swarm deployment, distributed data collection, target identification, and adaptive behavior depending on the situation [2]. This architecture allows for distributed coordination, scalability, and operational robustness in complex autonomous applications [1].

The Hierarchical Master-Swarm architecture, because it distributes tasks between an aerial command center and multiple executors, optimizing spatial coverage, has several advantages, such as:

- simultaneous monitoring of extensive areas;
- adding new drones to the swarm can be done with minimal software reconfiguration of the network topology;
- subordinate drones can be extremely simple and cheap, possessing only the hardware strictly necessary for flying and maintaining formation;
- the loss or failure of a drone in the swarm does not compromise the overall objective. The network automatically reconfigures to compensate for the missing node;

However, there are also disadvantages, such as:

- if the Master drone is destroyed or loses power, the entire swarm becomes inoperable or enters fail-safe mode, being unable to complete the mission;
- the system has high computational and algorithmic complexity;
- communication between drones is sensitive to radio spectrum congestion and requires considerable bandwidth over an area.

The ability to cover vast areas through efficient load balancing makes this architecture preferable for large-scale monitoring systems. Using swarms for simultaneous multispectral mapping of thousands of hectares of agricultural land. While the main drone creates a global map of water deficits or pest infections, the swarm drones perform parallel tasks, spraying pesticides only in affected areas. It is used for the rapid scanning of vast mountainous or maritime areas. Subordinate drones can scan the given area, and upon detecting a thermal anomaly (such as a lost person), the main drone would reorganize the swarm topology to focus monitoring efforts on that point. Another scenario could be analyzing the spread of forest fires or toxic chemical spills in real-time, minimizing human impact and reducing operating costs (losing a drone in a swarm does not stop the mission).

2.3 Ground Control Architecture

The Ground Control System (GCS) is a system where the control component is located on the ground, and the drone acts as a strict executor of commands received remotely. Communications management (Data Link) takes place through a bidirectional radio link, consisting of an uplink channel (navigation commands, parameter adjustments) and a downlink channel (detailed telemetry, real-time video stream). The human operator or the software installed on the GCS defines the route via waypoints, leaving the Flight Controller to manage exclusively the stabilization on the determined trajectory. An inherent vulnerability of architectures based on ground control stations (GCS) is the loss of the data link. For this reason, the architecture must include algorithms (safety protocols) to automatically initiate a return-to-home function. Upon detecting signal loss for a critical period (approximately 3 seconds), the drone automatically switches to strict On-Board mode to return to the launch point based on GPS coordinates stored at takeoff [8].

The diagram in Figure 3 presents the complete control cycle of a UAV, highlighting the information flow between the ground control station and the aerial vehicle, as well as the role of the drone's internal components. The system operates through two main types of communication links: control link (uplink) and telemetry and video (downlink). Initially, the operator uses a signal transmitter from the ground control station (GCS) to input flight control commands. These include parameters such as pitch, roll, yaw, throttle, or flight modes. Commands are transmitted to the drone via uplink.

The signal is received by the transceiver on board the drone, which transmits the data to the Flight Controller (FC), the central component responsible for stabilizing and coordinating all systems. The flight controller processes the received commands and uses information from the drone's sensors, such as the IMU (gyroscope and accelerometer), GPS, and barometer, to determine the vehicle's orientation and position [10]. Simultaneously, the drone transmits telemetry data to the control station via the MAVLink protocol, including information on battery level, GPS position, altitude, and drone orientation. Also, a video camera with a VTX (Video Transmitter) broadcasts the real-time video stream. This information forms the downlink, through which the operator receives visual and technical feedback about the drone's status [8]. Thus, a continuous cycle of control and monitoring is created, where commands are sent from the ground to the drone, and status and video data are returned to the operator for adjusting piloting and supervising the mission.

In the ground control system, the drone acts as a sensory relay and maneuver executor, but decision-making is outsourced to terrestrial servers or human operators. This allows running massive Machine Learning models on the Ground Control System or performing real-time photogrammetric processing, which is not possible to integrate onto a mobile platform [10]. This is essential in critical or emergency situations where final decision-making requires human judgment and adherence to strict flight safety regulations.

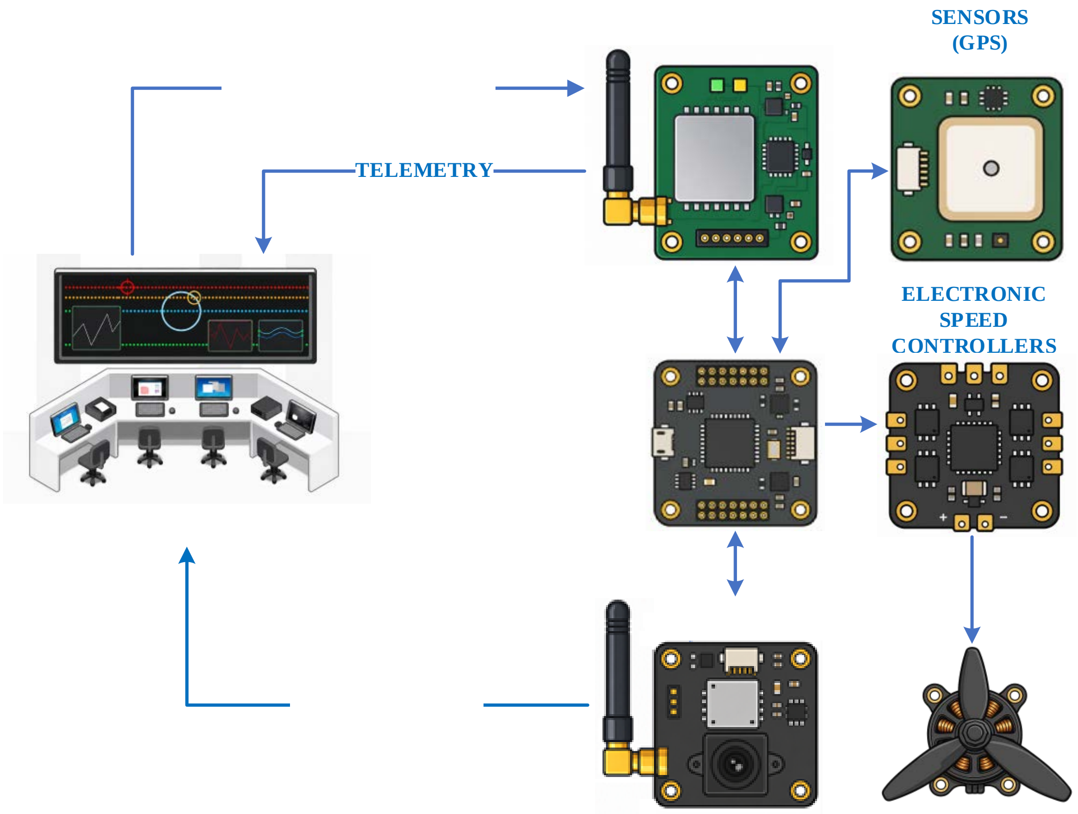

Figure 3. The control cycle between a drone and the ground station.

Shifting the computing load to the ground allows the drone to be physically lighter, and its computational and electronic characteristics to be simplified, resulting in enhanced maneuverability and longer flight times. However, this architecture also has several disadvantages. Any communication interruption, atmospheric interference, topographic shielding, or cyberattack on the communication channel can have a critical negative impact on the drone. The range is strictly dictated by the performance of ground antennas, except when using satellite communication systems, which introduce increased costs. The time required for data to be transmitted to the ground, processed, and a return command sent to the drone can cause instability in situations that require prompt actions.

When decision-making and big data analysis capabilities are more important than the mobility offered by remote UAV piloting architecture, the GCS architecture becomes the appropriate standard. This is used for monitoring oil and gas pipelines or high-voltage networks. Platforms navigate based on pre-established waypoints, transmitting terabytes of data (high-resolution photos, thermography) directly to terrestrial servers for immediate structural defect analysis. Another usage scenario for this architecture is high-precision terrain mapping with complex flight paths that require precise sensor calibration using the ground station control interface.

3. Comparative Analysis of UAV Control Architecture Performance

The comparative analysis of On-Board Control, Master Drone, and Ground Control System (GCS) architectures highlights that each control model is designed to meet different operational requirements and presents specific advantages and limitations, as seen in Table 1 [6]. From an autonomy perspective, the architecture based on on-board processing offers the best results. Because all critical decisions are made locally, the drone can continue the mission without relying on external communications. Master Drone type systems also offer a high level of autonomy, but their functioning depends on coordination between participating drones. Conversely, architectures based on a Ground Control System present a medium level of autonomy, as a significant part of the decision-making process is transferred to the ground control station.

Table 1

Comparative analysis of performances

Criterion	On-Board Control	Master Drone	GCS
Autonomy	Very high	High	Medium
Scalability	Low	High	Very high
Communication necessity	Minimal	Medium	Very high
Resilience to link loss	Very high	Medium	Low
Available computing power	Limited	Medium	Very high
Infrastructure cost	Medium	High	Very high
Real-time control	Excellent	Very good	Good

Regarding scalability, centralized systems and those based on hierarchical coordination are superior to local control. A single drone with on-board processing can efficiently execute individual missions, but simultaneously managing a large number of UAVs becomes difficult. The Master Drone architecture allows efficient coordination of drone groups by distributing tasks and organizing activities in a hierarchical structure. However, the highest scalability is offered by GCS systems, which can simultaneously monitor and control vast fleets of UAVs using high-performance IT infrastructures [3].

Analyzing communication dependency, it is observed that the On-Board Control architecture is the least dependent on the existence of a permanent communication link. This aspect represents a major advantage in applications deployed in isolated areas or in environments with electromagnetic interference. For the Master Drone architecture, communications are necessary for the continuous exchange of information between the leader and subordinate drones. GCS systems are the most dependent on communications, as the monitoring and command process relies on continuous data transfer between aerial platforms and the control center [3].

A criterion closely related to communications is resilience to communication link loss. Due to local processing, On-Board Control architectures are the most resistant to communication interruption. They can continue the mission or execute automatic fail-safe procedures without external support. In the Master Drone architecture, losing communication with the master drone can affect the coordination of the entire group, although modern redundancy mechanisms can mitigate this risk. GCS systems are the most vulnerable, as losing connection with the control station can significantly limit mission management capacity [6].

Regarding available computing power, GCS systems hold a dominant position. They benefit from high-performance servers and workstations that allow the implementation of complex artificial intelligence, video analysis, and mission optimization algorithms. Master Drone architectures offer intermediate computing capacity, as part of the processing is handled by the leader drone. For on-board control, computing power is limited by the dimensions, weight, and energy consumption of the equipment installed on the aerial platform [6].

Analysis of infrastructure costs indicates that GCS systems require the largest investments. Their implementation involves developing a complex infrastructure of communications, servers, management software, and operating stations. Master Drone-based architectures also involve high costs due to the complexity of coordination and redundancy mechanisms. On-board control presents moderate costs, as most functions are integrated directly into the UAV [3].

In terms of real-time control, the On-Board Control architecture provides the best performance. Local processing eliminates delays associated with data transmission and allows rapid reactions to environmental changes. Master Drone systems also offer very good performance, but response time can be influenced by information exchange between drones. In the case of GCS systems, performance depends on the quality and latency of communication channels.

Overall, the analysis highlights that the On-Board Control architecture is optimal for missions requiring high autonomy, rapid reaction, and independence from communications. The Master Drone architecture is best suited for the collaborative coordination of multiple UAVs and implementing smart swarm concepts. The Ground Control System architecture offers the best results in situations requiring centralized surveillance, simultaneous management of a large number of platforms, and the use of advanced computational resources. In practice, the current trend leans towards hybrid architectures that combine the advantages of all three models to achieve a superior level of autonomy, flexibility, and operational efficiency.

5. Conclusions

The analysis of control architectures for UAV platforms highlights that selecting a control solution depends directly on the mission's operational requirements, the required degree of autonomy, and available resources at the communication and processing infrastructure level. The architecture based on on-board processing (On-Board Control) offers the best performance in terms of autonomy, resilience to communication loss, and real-time control, being recommended for missions carried out in isolated environments or characterized by difficult communication conditions. The hierarchical Master-Swarm architecture allows the efficient coordination of a large number of drones and provides a high level of scalability, making it suitable for applications requiring distributed cooperation, monitoring over extensive areas, and simultaneous execution of multiple tasks. However, its functioning depends on maintaining the main node's integrity and the existence of efficient coordination and redundancy mechanisms. Systems based on a Ground Control System (GCS) have the most vastest computing resources and allow centralized monitoring of UAV operations, being appropriate for applications involving large data volumes, advanced processing, and in specific cases, can minimize or even completely reduce the need for human intervention in the decision-making process. The primary limitation of this approach is its high dependence on communication infrastructure and vulnerability to data link loss.

The comparative analysis performed demonstrates that there is no universal architecture for all use scenarios. The current trend in UAV system development is geared towards hybrid architectures integrating local processing, distributed coordination, and centralized management. This approach allows exploiting each model's advantages and contributes to increasing autonomy, operational safety, flexibility, and energy efficiency. Future research directions include the integration of distributed artificial intelligence technologies, use of 5G/6G communications and FANET (Flying Ad-Hoc Network) networks, developing adaptive mechanisms for switching between different control modes, and implementing collaborative swarm-type systems capable of operating autonomously in complex and dynamic environments [9].

Acknowledgments: This article was funded by the project: "Research on intelligent methods and effective means for monitoring forest, perennial and aquatic areas with the application of drones", 25.80012.5007.71SE at the stage of analysis of the field of study.

During the preparation of this article, the author Viorel Cărbune used Gemini3.1 Pro for translation into English. The authors reviewed and revised the result and assume full responsibility for the content of this publication.

Contribution of authors

Adriana Ursu: Conceptualization, Methodology, Investigation, Writing – original draft.
Igor Calmîcov: Investigation, Writing – editing.
Viorel Cărbune: Supervision, Investigation, Writing – editing.

Conflicts of Interest: The authors declare no conflict of interest.

References

1. Lizzio, F.F.; Capello, E.; Guglieri, G. (2022). 'A Review of Consensus-Based Multi-Agent UAV Implementations', *Journal of Intelligent & Robotic Systems*, 106, Article 43. DOI: 10.1007/s10846-022-01743-9;
2. Alenezi, M.; et al. (2024). 'Advancement Challenges in UAV Swarm Formation Control: A Comprehensive Review', *Drones*, 8(7), Article 320. DOI: 10.3390/drones8070320;

3. Cetinsaya, B.; Reiners, D.; Cruz-Neira, C. (2024). 'From PID to Swarms: A Decade of Advancements in Drone Control and Path Planning – A Systematic Review (2013–2023)', *Swarm and Evolutionary Computation*, 89, Article 101626. DOI: 10.1016/j.swevo.2024.101626;
4. Abbas, N.; Abbas, Z.; Zafar, S.; et al. (2024). 'Survey of Advanced Nonlinear Control Strategies for UAVs: Integration of Sensors and Hybrid Techniques', *Sensors*, 24(11), Article 3286. DOI: 10.3390/s24113286;
5. Wang, G.; Gu, C.; Li, J.; et al. (2023). 'Heterogeneous Flight Management System (FMS) Design for Unmanned Aerial Vehicles: Current Stages, Challenges, and Opportunities', *Drones*, 7(6), Article 380. DOI: 10.3390/drones7060380;
6. Zhang, Y.; Wang, X.; Li, H.; et al. (2024). 'Cooperative Motion Planning and Control for Aerial-Ground Autonomous Systems: Methods and Applications', *Progress in Aerospace Sciences*, 146, Article 101005. DOI: 10.1016/j.paerosci.2024.101005;
7. Xu, Z.; Liu, Y.; Wang, S.; et al. (2022). 'Algorithms and Applications of Intelligent Swarm Cooperative Control: A Comprehensive Survey', *Progress in Aerospace Sciences*, 135, Article 100869. DOI: 10.1016/j.paerosci.2022.100869;
8. Javaid, S.; Saeed, N.; Qadir, Z.; et al. (2023). 'Communication and Control in Collaborative UAVs: Recent Advances and Future Trends', *IEEE Transactions on Intelligent Transportation Systems*, 24, 5719–5739. DOI: 10.1109/TITS.2023.3248841;
9. Bertizzolo, L.; D'Oro, S.; Ferranti, L.; et al. (2020). 'SwarmControl: An Automated Distributed Control Framework for Self-Optimizing Drone Networks', *arXiv Preprint*, arXiv:2005.09781. DOI: 10.48550/arXiv.2005.09781;
10. Khan, M.A.; Kumar, N.; Mohsan, S.A.H.; et al. (2022). 'Swarm of UAVs for Network Management in 6G: A Technical Review', *arXiv Preprint*, arXiv:2210.03234. DOI: 10.48550/arXiv.2210.03234.

Citation: Ursu, A., Calmîcov, I., Cărbune, V. (2026). Analysis of control architectures for unmanned aerial vehicles. *Journal of Engineering Science*. 2026, 33 (2), pp. 20-31. https://doi.org/10.52326/jes.utm.2026.33(2).02.

Publisher's Note: JES stays neutral with regard to jurisdictional claims in published maps and institutional affiliations.

Copyright:© 2026 by the authors. Submitted for possible open access publication under the terms and conditions of the Creative Commons Attribution (CC BY) license (https://creativecommons.org/licenses/by/4.0/).

Submission of manuscripts: jes@meridian.utm.md

Journal of Engineering Science *Vol. XXXIII, no. 2 (2026), pp. 32 - 45*
Fascicle *Industrial Engineering* *ISSN 2587-3474*
Topic *Materials Science and New Technologies* *eISSN 2587-3482*

https://doi.org/10.52326/jes.utm.2026.33(2).03
UDC 621.383.51:620.92

ZnTe – BASED OF PEROVSKITE SOLAR CELLS WITH INVERTED PLANAR ARHITECTURE

Mihail Popa *, ORCID: 0009-0007-7903-3946

Technical University of Moldova, 168 Stefan cel Mare blvd., MD2004, Chisinau, Republic of Moldova
* Corresponding author: Mihail Popa, *mihail.popa@fiz.utm.md*

Received: 04. 14. 2026
Accepted: 05. 22. 2024

Abstract. This article presents applications of zinc telluride in perovskite solar cells. Devices in which the thin layer of ZnTe deposited by thermal evaporation is the only hole transport layer reached a maximum yield of about 2.14%, while those with hole transport layer consisting of PEDOT-PSS doped with ZnTe had a maximum efficiency of about 2.60%. Power conversion efficiency of approximately 7.40% was recorded in solar cells consisting of two hole transport layers, one of ZnTe and one of PEDOT-PSS. The maximum conversion yield of approximately 13.84% was recorded in devices, in which heterojunction was made from perovskite doped with ZnTe.

Keywords: *perovskite, zinc telluride, current density, voltage, fill factor, efficiency.*

Rezumat. Articolul prezintă aplicații ale telururii de zinc în celule solare cu perovskit. Dispozitivele în care stratul subțire de ZnTe depus prin evaporare termică este singurul strat de transport al găurilor au atins un randament maxim de aproximativ 2,14%, în timp ce cele cu strat de transport al găurilor constând din PEDOT-PSS dopat cu ZnTe au avut o eficiență maximă de aproximativ 2,60%. O eficiență de conversie a puterii de aproximativ 7,40% a fost înregistrată în celulele solare constând din două straturi de transport al găurilor, unul din ZnTe și unul din PEDOT-PSS. Randamentul maxim de conversie de aproximativ 13,84% a fost înregistrat în dispozitivele în care heterojoncțiunea a fost realizată din perovskit dopat cu ZnTe.

Cuvinte cheie: *perovskit, telurură de zinc, densitate de curent, tensiune, factor de umplere, eficiență.*

Abbreviations

ZnTe - Zinc telluride
ZnSe - Zinc selenide
ZnO – Zinc oxide
PEDOT-PSS – composite material where PEDOT (the conductive polymer) and PSS (polystyrene sulfonate).
$PC_{61}BM$ - [6,6]-phenyl-C_{61}-butyric acid methyl ester.
AFM - atomic force microscopy.
PCE - power conversion efficiency

1. Introduction

$A^{II}B^{VI}$ type semiconductor compounds have a wide range of optical and electrical properties and can become competitive materials in photovoltaic conversion and optoelectronic applications [1]. On the other hand, the structure and physical properties of the thin layers of these compounds greatly depend on the deposition method and the substrate temperature, the evaporation method and the deposition rate.

ZnTe is a binary semiconductor compound, type $A^{II}B^{VI}$, with the band gap average E_g = 2.26 eV at T = 300 K. Typically, zinc telluride crystallizes in cubic form (sphalerite, or "zincblende"), but can also be prepared as a hexagonal structure (wurtzite) [3].The compound, together with sulfides and selenides, belongs to the calcogenide category. In the form of thin layers it can be prepared by various methods such as thermal evaporation technique from one source [4] and two sources [5], electrodeposition [6, 7], epitaxial growth [8, 9], sputtering [1], molecular beam epitaxy [10], direct combination of Zn and Te in quartz ampoule [2, 11], pulsed-laser deposition [12].

Zinc telluride is an important material for photovoltaic applications. T. Tanaka et al. [13] presented the experimental results of the photovoltaic activity of the homojunction ZnTe from solar cells in which n-ZnTe layers are made by thermal diffusion of Al into p-ZnTe. W. Wang et al. [10] have grown n-ZnO/n-ZnSe/p-ZnTe structures on GaAs and GaSb and they demonstrated good rectifier diode qualities and good photovoltaic response. C. A. Wolden et al. [14] have prepared ZnTe buffer layers as posterior contact of CdTe solar cells and have significantly contributed to raising the efficiency of cells and to improving the stability of the module. N. G. Patel et al. [15] have demonstrated that the efficiency of p-ZnTe / n-CdSe type solar cells in thin layers strongly depends on the conditions of growth of the absorption layers and the window layers. P. Saikia et al. [16] have prepared ZnSe/ZnTe/CdTe/HgTe multijunction solar cells on tin oxide-coated glass substrate using the vacuum evaporation method and these structures have demonstrated the best photovoltaic parameters [2].

I believe that the ability of contemporary researchers to manufacture perovskite cells with a high filling factor is an important step towards assembling high-efficiency cells for commercial applications. Today, the number of researchers with perovskite solar cells with an efficiency of less than 15% is increasing [17]. J.Y. Jeng et al. showed solar cells similar to pervoskite $CH_3NH_3PbI_3$ / fullerene (C_{60}) planar - hybrid heterojunction with the following parameters V_{oc} = 0.60 V, J_{sc} = 10.30 mAcm^{-2}, *FF* = 0.63, *PCE* = 3.9% [18]. L. Etgar et al. reported obtaining hole conductor-free mesoscopic methylammonium lead iodide ($CH_3NH_3PbI_3$) perovskite / TiO_2 heterojunction solar cell with important photovoltaic characteristics: J_{sc} = 16.1 mA/cm^2, V_{oc} = 0.631 V, *FF* = 0.57 and *PCE* = 7.3% [19]. J.H. Im et al. have demonstrated highly efficient quantum-dot-sensitized solar cell based on perovskite $CH_3NH_3PbI_3$ with PCE = 6.54% [20]. M.M. Lee [21] presented a device with the structure FTO/TiO_2/$CH_3NH_3PbI_2Cl$/Spiro-OMeTAD/Ag and the most efficient device exhibited have photovoltaic characteristics: J_{sc} = 17.8 mAcm^{-2}, V_{oc} = 0.98 V, FF = 0.63 and η = 10.9 % [22]. N.J. Jeon et al. have discovered a solvent engineering technology for the preparation of extremely uniform perovskite layers and demonstrated a solution-processed perovskite solar cell with an energy conversion efficiency of about 16.5% [23]. Similar applications of thin layers of ZnSe, ZnTe and ZnS in perovskite solar cells have demonstrated M.E. Popa et al. [24 – 27].

Perovskite solar cells based on organic - inorganic halides [25] have aroused a special interest in research due to the increase of photovoltaic characteristics and the simpler way of preparation compared to other solar cells [28-37]. Replacing silicon with absorbent thin layers in such devices will greatly reduce the real cost of solar cells. The objectives of this paper are to present the experimental results of the use of thin layers of ZnTe and ZnTe powder in various variants of perovskite solar cells [25].

2. Materials and Methods

The lower electrodes of the solar cell were deposited from indium tin oxide (ITO) by etching on Corning 7059 glass [25], which had been initially ultrasonically cleaned in detergent, deionized water and acetone. The ITO layer served as cathode collecting holes.

The thin layer of ZnTe was subsequently deposited in vacuum as a hole transport layer by means of thermal evaporation. The mass of ZnTe powders with a purity of about 99.999% ranged from 15 to 32 mg. Substrate temperature was T_{sub} = 300 K, vacuum pressure - about 0.96 Pa, and electric power through the evaporator process was approximately 50 A.

The thickness of the ZnSe films was measured with the MII-4 interference microscope (Linnik type), the operation of which is based on the interference of fringes of equal thickness from the surface of the layer and the surface of the support. The DRON-3 diffractometer with MoKα radiation (λ = 0.710687 Å) was used to obtain X-ray diffractograms. The surface morphology of ZnTe thin layers was characterized by AFM.

The bulk heterojonction layer [25] was prepared of 80 μl of methylammonium lead iodide solution ($MAPbI_3$ = $CH_3NH_3PbI_3$) by the spin-coating method in two stages: after the first deposition the layer was rotated at a speed of 1000 rpm for 23 seconds, followed by a second deposition and a rotation at a speed of 4000 rpm for 30 seconds. 150 μl of toluene dropped in the 13th second [24].

The $PC_{61}BM$ (= PCBM) film was used as electron transport layer. It was deposited from the solution in the argon chamber by the spin-coating method at a rotational speed of 1000 rpm for 40 s [38]. The advantages of using $PC_{61}BM$ as an electron transport layer are: layers are deposited from the solution, their thickness can be adjusted, good electron transport properties in the deposited layers and the lack of need for additional heat treatment. Energetic direction of the holes and electrons is more favorable in this configuration, electrons move to a metal with small extraction work, and the holes move to material with large extraction work. Ag electrodes were deposited by thermal evaporation in a quasi-closed volume [24].

In another variant of perovskite solar cells the PEDOT-PSS layer doped with ZnTe powder was used as the hole transport layer, and the other layers were deposited analogously as in the first variant of solar cells [27]. The concentration of the powder in the mixture varied between 1.0 and 2.0 mg/ml. This was deposited from the solution by the spin-coating method for 60s at a rotational speed of 3000 rpm. Then followed a heat treatment in air for 10 minutes at a temperature of 150°C. Heat treatment time was measured with the stopwatch of a mobile phone.

The third type of perovskite solar cells had a two-layer structure (ZnTe + PEDOT-PSS) which fulfill the function of hole transport layer, and the other layers were deposited analogously as in the first variant of solar cells [25]. The ZnTe layer was deposited by thermal evaporation under conditions similar to those of the first type of solar cell, and the second layer of PEDOT-PSS was deposited by the spin-coating method under conditions similar to those of the second type of solar cells [39].

The last variant of solar cells uses as bulk heterojunction the perovskite layer $CH_3NH_3PbI_3$ doped with ZnTe powder, and the other layers were deposited similar into as in the first type of solar cells.

To measure the current density - voltage of solar cells dependencies, a closed box filled with nitrogen using simulated AM1.5G sun light was used, which was calibrated to 100 mW/cm^2 using an NREL tracking photodiode and a computer-controlled Keithley 2400 source unit [25]. The HITACHI S-3000N microscope was used for SEM measurements and the photovoltaic characteristics were measured at room temperature.

3. Results and Discussion

In Fig. 1 are presented two SEM images of a solar cell type ITO/PEDOT-PSS/$MAPbI_3$: ZnTe/$PC_{61}BM$/Ag after depositing the $PC_{61}BM$ fullerene layer. We notice that the surface of the cell is uniform, without perforations, but with some small spherical grains grown on the surface (about 3 μm in diameter) and elongated (3 to 5 μm in length) [24]. This uniform compact structure effectively blocks the recombination of charge carriers at the surface.

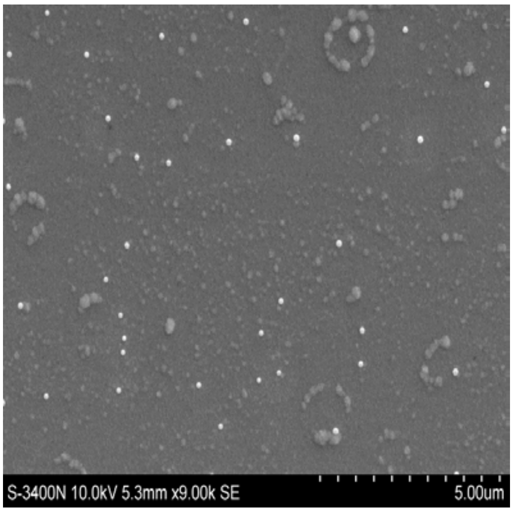

a)

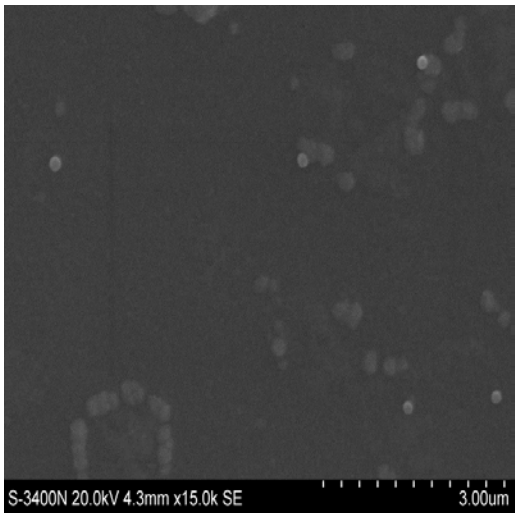

b)

Figure 1. The SEM images of surfaces of samples type ITO/PEDOT-PSS/$MAPbI_3$: ZnTe/$PC_{61}BM$/Ag.

Figure 2 (a) presents the schematic cross-section of the first variant of perovskite solar cells with inverted architecture described in this article, and the scheme of energy transitions in the layers of this solar cell are shown in Fig. 2 (b). Here the role of electron transport layer is fulfilled by the $PC_{61}BM$ film, and the role of hole transport layer - the ZnTe layer [25]. From this diagram we observe that the hole runs through the energy path -5.4 eV → -5.1 eV → -4.7 eV, and the electron runs through the energy path -3.9 eV → -4.3eV → -4.5 eV.

The output current of the photovoltaic cell is given by the relation [16, 40],

$$I = I_s \left[exp\left(\frac{q(V - IR_s)}{kT} \right) - 1 \right] - I_L, \tag{1}$$

where I_s and R_s are the diode saturation current and the series resistance of the respective cell. The fill factor that measures the quality of solar cells is determined by the relation [16, 40]

$$FF = \frac{I_m V_m}{I_{sc} V_{oc}}, \tag{2}$$

where I_m and V_m are the current and the voltage corresponding to the maximum power point P_{max} and I_{sc} and V_{oc} respectively short-circuit current and open-circuit voltage. An important parameter is the power conversion efficiency (*PCE*) of the solar cell, which is defined as the ratio from the output power (electricity) and the input power (the light) and can be calculated by the equation [16, 40]:

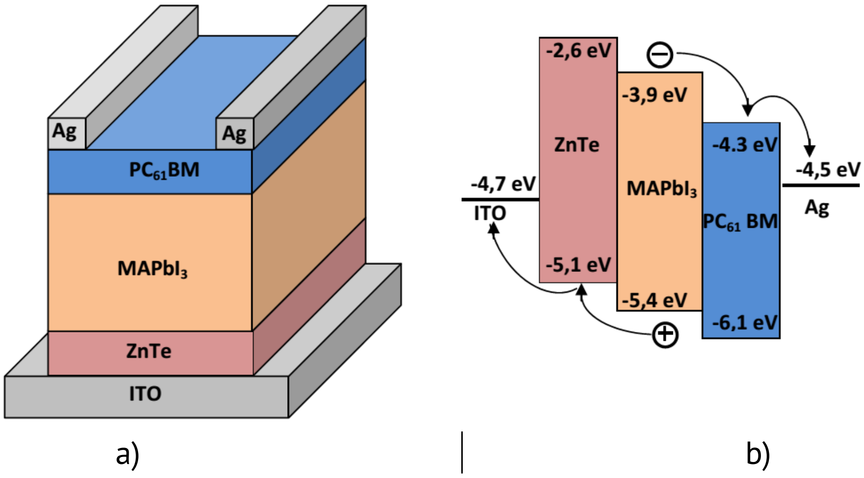

Figure 2. (a) Device structure of first type of solar cells;
(b) The energy diagram of first type of solar cell.

$$PCE = \eta = \frac{P_{output}}{P_{input}} = FF\frac{I_{sc}V_{oc}}{P_{input}}. \tag{3}$$

Typically, the "inverted" planar structure has a V_{oc} and a high *FF*, which are indicators that this structure has favorable electrical contacts and that the charges are efficiently collected on electrodes within this structure.

The *J-U* dependencies and the photovoltaic parameters of the solar cells with the ITO/ZnTe/$MAPbI_3$/PCBM/Ag structure are presented in Fig. 3 and Table 1 [25].

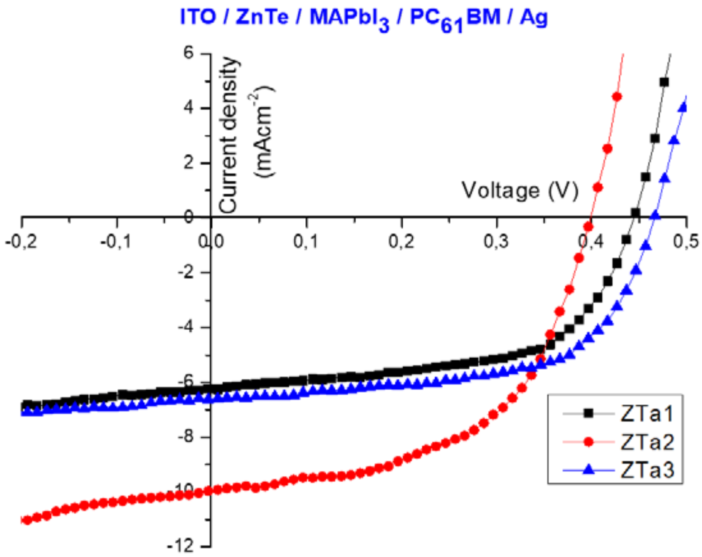

Figure 3. Current density – voltage characteristics of first type of solar cells.

The experimental curves were constructed according to the thickness of the ZnTe layer deposited on the ITO, and the photovoltaic parameters analyzed were open circuit voltage (V_{oc}), short-circuit current (J_{sc}), fill factor (*FF*) and power conversion efficiency (*PCE*). For the cell with a ZnTe layer thickness of about d = 20 nm, the electrical dependence ZTa1 was obtained with the following characteristics: V_{oc} = 0.44 V, J_{sc} = - 6.24 mA/cm^{-2}, *FF* = 59.48 %, *PCE* = 1.66 %. For the device with the thickness of the ZnTe layer of about d = 33 nm, the ZTa2 curve was obtained, in which the hysteresis of the curve increased to the value J_{sc} = -9.98 mA/cm^{-2}, and V_{oc} decreased to 0.39 V. For the solar cell with the ZnTe layer thickness of d = 48 nm the ZTa3 curve was obtained, which is very close to the form of the initial *J-U* dependency ZTa1 [25].

Table 1

Photovoltaic parameters of first type of solar cells

Devices	d_{ZnTe} (nm)	U_{oc} (V)	J_{sc} (mA/cm^2)	FF (%)	PCE (%)
ZTa1	20	0.44	-6.24	59.48	1.66
ZTa2	33	0.39	-9.98	54.19	2.14
ZTa3	48	0.46	-6.62	61.14	1.88

Low values of the power conversion efficiency is probably due to mainly the small displacement of the ZnTe valence band to the perovskite valence band and probably due to low crystallinity and high roughness of the surface of the ZnTe layer. Thus, the ZnTe layer with the function of hole transporting layer did not improve charge transport, but probably created increased contact resistance.

For the best ITO/ZnTe/$MAPbI_3$/PCBM/Ag solar cell the characteristic *J-U* was measured to the forward lighting (at decrease of voltage) and reverse lighting (at increase of voltage) (Fig. 4). From Table II we notice that at reverse scanning V_{oc} decreases from 0.390 V to 0.386 V, J_{sc} decreases from 9.98 mAcm^{-2} to 9.61 mAcm^{-2}, *FF* is reduced from 54.19 % to 51.49 % and *PCE* decreases from 2.14 % up to 2.02 %.

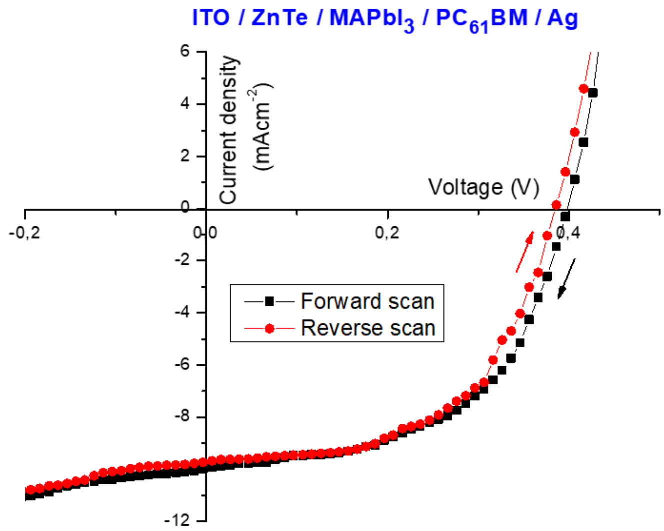

Figure 4. Forward and reverse J-U characteristics of ZTa2 device (d_{ZnTe} = 33 nm).

Table 2

Parameters of of ZTa2 solar cell (d_{ZnTe} = 33 nm) with forward and reverse scanning

Directions of scanning	U_{oc} (V)	J_{sc} (mA/cm^2)	FF (%)	PCE (%)
forward	0.390	-9.98	54.19	2.14
reverse	0.386	-9.61	51.49	2.02

The structure and morphology of a ZnTe layer deposited on the ITO electrode and the glass support was investigated. In the XRD diffractogram (Fig. 5.a) three diffraction peaks (111), (200) and (311) were identified in ASTM and ICDD data sheets for ZnTe, which demonstrates that the studied layers are polycrystalline and have a zinc blend structure with a strong orientation of the crystalites with the planes (111), (200) and (311) parallel to the surface of the support. The AFM image of the ZnTe thin layer surface is shown in Fig. 5.b. It is noted that the sample has small crystalites, grooved perpendicular to the support, in the form of "scales" with similar dimensions (length about 0.08 - 0.1 μm, width about 0.04 - 0.06 μm). The image of Fig. 5.c demonstrates that the thickness of the ZnTe layer is about 33 nm and has a surface roughness of about 3 - 5 nm.

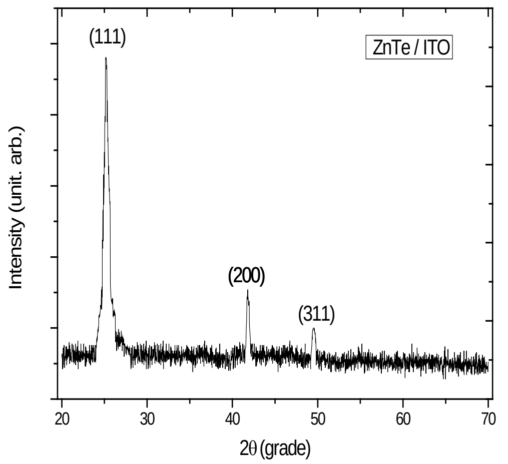

a)

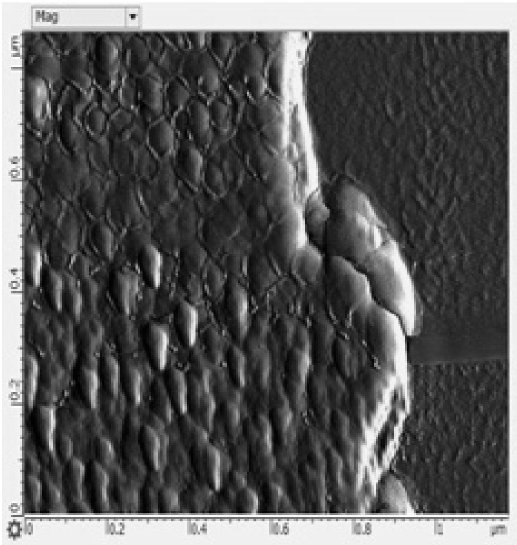

b)

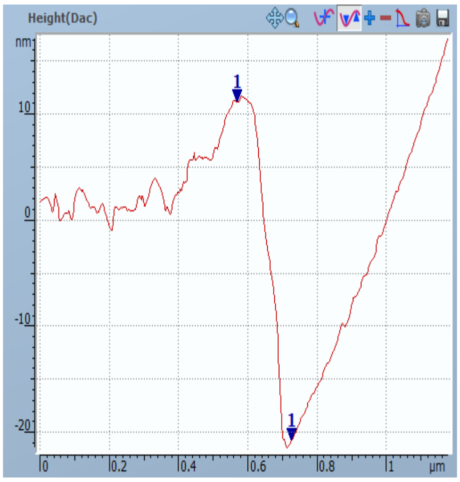

c)

Figure 5. (a) XRD image confirming the crystalline structure of the ZnTe layer: b) AFM image of the ZnTe layer deposited on ITO/glass,c) AFM image to measure the height of ZnTe layer deposited on ITO/glass.

The modification of hole transport layer in order to increase of the power conversion efficiency of solar cells it was achieved by doping the PEDOT: PSS solution with the ZnTe powder. The concentration of the powder in the solution ranged from 1.2 - 2.0 mg/ml.

Fig. 6 presents the current density - voltage dependencies of solar cells with ITO/PEDOT-PSS: ZnTe/$MAPbI_3$/PCBM/Ag structure, and Table 3 represents the parameters of the respective cells. For the ZTb1 solar cell with the concentration n = 1.2 mg/ml of ZnTe in PEDOT-PSS, the experimental curve with the following characteristics was obtained: V_{oc} = 0.58 V, J_{sc} = - 5.64 mA/cm^2, FF = 43.94%, PCE = 1.43%. The hysteresis of the ZTb4 curves, with the concentration n = 1.8 mg/ml of ZnTe in PEDOT-PSS, increased continuously reaching the values J_{sc} = - 9.27 mA/cm^2 and V_{oc} = 0.69 V, which corresponds to the maximum value of PCE = 2.56 %. For solar cells with a concentration n > 1.8 mg/ml of ZnTe in PEDOT-PSS the hysteresis becomes lower than in the previous cell, and the energy efficiency decreases continuously.

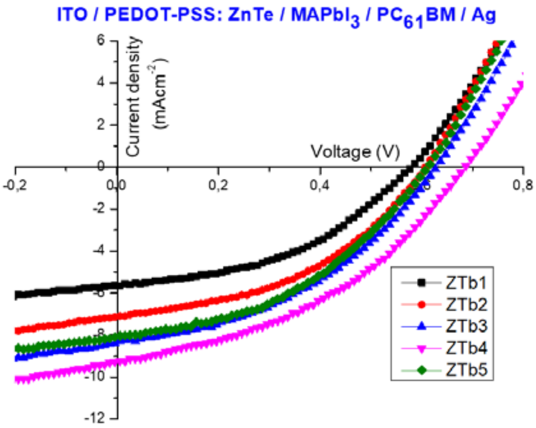

Figure 6. J-U curves of the second type of solar cells.

Table 3

Photovoltaic parameters of the second type of solar cells [25]

Devices	*n (mg/ml)*	U_{oc} *(V)*	J_{sc} *(mA/cm*^{2}*)*	*FF (%)*	*PCE (%)*
ZTb1	1.2	0.58	-5.64	43.94	1.43
ZTb2	1.4	0.60	-7.14	43.32	1.88
ZTb3	1.6	0.63	-8.40	40.94	2.15
ZTb4	1.8	0.69	-9.27	40.31	2.56
ZTb5	2.0	0.62	-8.10	41.50	2.07

Fig. 7 and Table IV show small deviations in *J-U* characteristic at forward lighting (at decreasing of voltage) and reverse lighting (at increasing the voltage) of the best solar cell type ITO/PEDOT-PSS:ZnTe/$MAPbI_3$/PCBM/Ag.

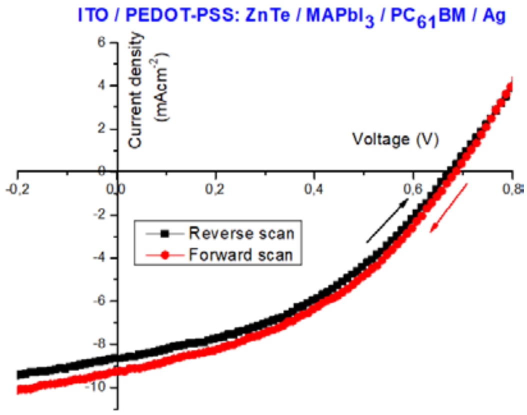

Figure 7. Forward and reverse J-U characteristics of ZTb4 device (n = 1.8 mg/ml).

Table 4

Parameters of of ZTb4 solar cell (n = 1.8 mg/ml) with forward and reverse scanning

Directions of scanning	U_{oc} *(V)*	J_{sc} *(mA/cm*^{2}*)*	*FF (%)*	*PCE (%)*
forward	0.69	-9.27	40.31	2.56
reverse	0.67	-8.63	40.16	2.38

To increase the efficiency of hole transport layer a third variant of solar cells was prepared in which two layers of p-type conduction were deposited: a ZnTe film obtained by quasi-closed thermal evaporation, the thickness of which was measured after each deposition, and the second layer of PEDOT-PSS obtained by the spin-coating method.

Fig. 8 presents the most representative J-U curves of solar cells with ITO/ZnTe / PEDOT: PSS/MAPbI$_3$/PCBM/Ag structure, which were analyzed according to the thickness of the ZnTe layer deposited on the ITO, and their energy quantities are indicated in Table V. The ZTc1 solar cell has the thickness of the ZnTe layer equal to 20 nm and the characteristic current density - voltage has the following photovoltaic parameters: V_{oc} = 0.94 V, J_{sc} = 12.73 mA/cm^2, *FF* = 59.87% and *PCE* = 7.14%. The ZTc2 device with a ZnTe layer thickness of about 33 nm has a significantly higher short-circuit current value of about 19.16 mA/cm^2, and an open circuit voltage of less than 0.78 V. The hysteresis of the ZTa3 solar cell, with a ZnTe layer thickness equal to 48 nm, decreases, and the characteristic current density - voltage moves upwards, perpendicular to the current density axis. In all perovskite solar cells with ZnTe as the electron transport layer from Fig. 8 a *PCE* > 7% was obtained [25].

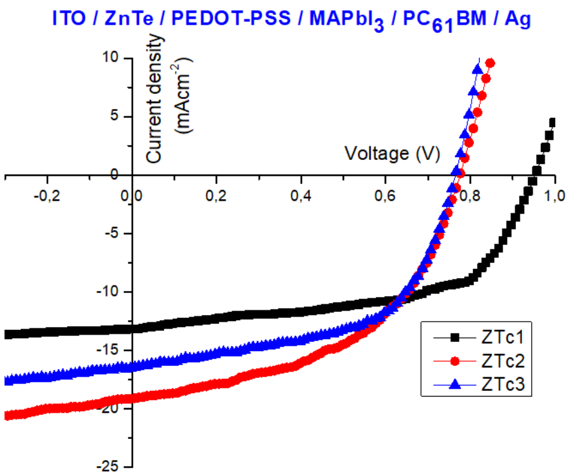

Figure 8. Current density – voltage characteristics of *the* third type of solar cells.

Table 5

Photovoltaic parameters of the third type of solar cells

Devices	d_{ZnTe} (nm)	U_{oc} (V)	J_{sc} (mA/cm^2)	*FF* (%)	*PCE* (%)
ZTc1	20	0.94	-12.73	59.87	7.14
ZTc2	33	0.78	-19.16	49.71	7.40
ZTc3	48	0.77	-16.52	56.38	7.14

The energy diagram of recent solar cells is shown in Fig. 9. It is noticed that this structure significantly simplifies the movement of the holes from the perovskite to the ITO electrode by making smaller jumps, in a cascade, between close energy levels (from 5.4 eV to 5.2 eV and then from 5.1 eV to 4.7 eV). This probably explains the increase in the PCE value of those cells compared to other solar cells.

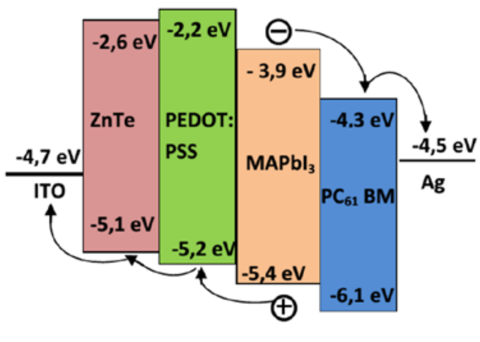

Figure 9. The energy diagram of the third type of solar cells.

J-U characteristic of ZTc2 device at reverse illumination presented a smaller hysteresisthan the forward illumination (Fig. 10). From Table 6 we note that at reverse scanning V_{oc} decreases from 0.78 V to 0.70 V, J_{sc} increases from 19.16 mAcm^{-2} to 19.63 mAcm^{-2}, *FF* decreases from 49.71 % to 48.11 % and PCE declines 7.40 % to 6.67 %.

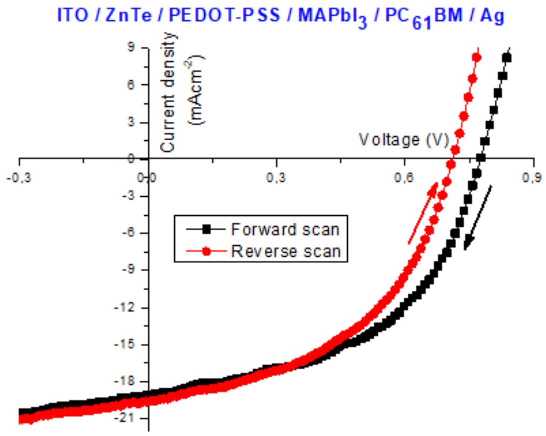

Figure 10. Forward and reverse J-U characteristics of ZTc2 device (d_{ZnTe} = 33 nm).

Table 6

Parameters of ZTc2 solar cell (d_{ZnTe} = 33 nm) with forward and reverse scanning

Directions of scanning	U_{oc} (V)	J_{sc} (mA/cm^2)	FF (%)	PCE (%)
forward	0.78	-19.16	49.71	7.40
reverse	0.70	-19.63	48.11	6.67

By doping the perovskite solution ($CH_3NH_3PbI_3$) with the ZnTe powder in the bulk heterojonction layer, the fourth variant of solar cells was obtained. In the solar cells with the best photovoltaic characteristics the concentration of the powder in the solution varied between 1.2 - 1.8 mg/ml. The mode of deposition of this layer was the same as in the case of depositing the pure layer of perovskite. Other layers-components of the solar cells were prepared analogously to the ZTal – ZTa3 samples.

The J-U dependencies of solar cells with ITO/PEDOT: PSS/$MAPbI_3$: ZnTe/PCBM/Ag structure are represented in Fig. 11, and the photovoltaic parameters of the respective solar cells are presented in Table 7. For the solar cell in which the concentration of ZnTe in $MAPbI_3$ is n = 1.2 mg/ml, the ZTd1 curve was obtained with the following characteristics: V_{oc} = 0.95 V, J_{sc} = 15.52 mA/cm^{-2}, *FF* = 61.56%, *PCE* = 9.05%. Increasing the concentration of ZnTe to n = 1.4 mg/ml it is observed that the open circuit voltage remains practically constant, and the hysteresis of the current density-voltage curve increases to the value of short-circuit current of about 24.97 mA/cm^2, and the value maximum *PCE* = 13.84%. If the concentration of ZnTe in $CH_3NH_3PbI_3$ increases even more than in the ZTd2 solar cell, the energy efficiency of the solar cells decreases continuously, because the V_{oc} and *FF* values decrease [25].

Table 7

Photovoltaic parameters of the fourth variant of solar cells

Devices	n (mg/ml)	U_{oc} (V)	J_{sc} (mA/cm^2)	FF (%)	PCE (%)
ZTd1	1.2	0.95	-15.52	61.56	9.05
ZTd2	1.4	0.95	-24.97	58.53	13.84
ZTd3	1.6	0.92	-25.97	51.92	12.36
ZTd4	1.8	0.86	-27.04	39.36	9.12

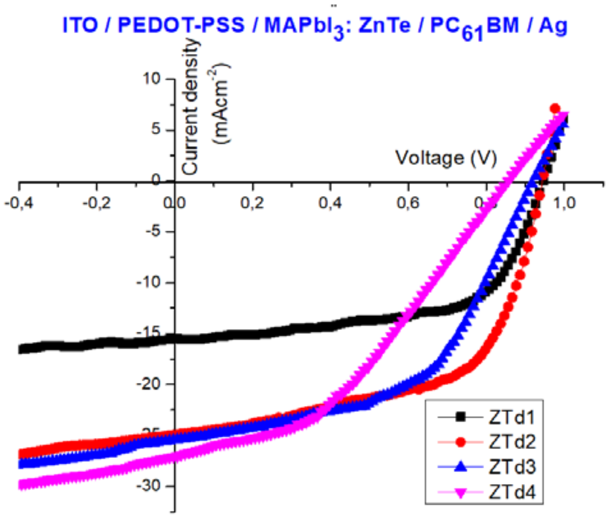

Figure 11. Current density – voltage characteristics of the fourth variant of solar cells.

Fig. 12 represents the current density - voltage dependencies for the most efficient ZTd2 solar cell. A direct scan of the solar cell the J-U dependence revealed the following parameters: V_{oc} = 0.95 V, J_{sc} = 24.97 mA/cm^2, FF = 58.53 %, PCE = 13.84 %, and at the reverse scan V_{oc} = 0.91 V, J_{sc} = 24.96 mA/cm^2 , FF = 55.38 % and PCE = 13.32 % (Table 8).

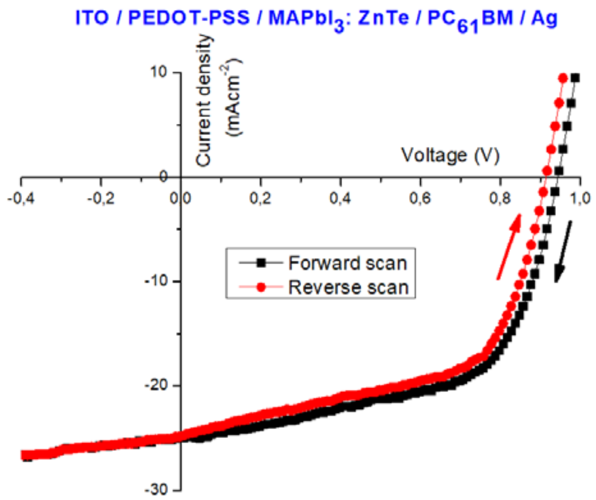

Figure 12. Forward and reverse J-U characteristics of ZTd2 device (*n = 1.8 mg/ml*).

Table 8

Parameters of ZTd2 solar cell (n = 1.8 mg/ml) with forward and reverse scane

Directions of scane	*U_{oc} (V)*	*J_{sc} (mA/cm^2)*	*FF (%)*	*PCE (%)*
forward	0.95	-24.97	58.53	13.84
reverse	0.91	-24.96	55.38	13.32

5. Conclusions

The paper demonstrated the experimental results obtained in the preparation and investigation of perovskite solar cells in which ZnTe performed the function of hole transport layer. The highest power conversion efficiency PCE ≈ 7.40% was detected in ITO/ZnTe/PEDOT-PSS/$MAPbI_3$/PCBM/Ag devices with an open circuit voltage V_{oc} ≈ 0.777 V, a filling factor FF ≈ 0.50 and with a short-circuit current J_{sc} ≈ - 1.02 mA/cm^2. By doping perovskites with ZnTe solar cells with the structure ITO/PEDOT-PSS/$CH_3NH_3PbI_3$: ZnTe/PC_{61}BM/Ag were obtained with the best photovoltaic characteristics: PCE = 13.84%, V_{oc} = 0.947 V, FF = 59% and J_{sc} = - 24.97 mA/cm^2.

References

1. Bellakhder H, Debbagh F, Outzourhit A, Bennouna A, Brunel M, Ameziane E (1997) Characterization of Te/Zn/Te … multilayers deposited by RF-sputtering, Sol. Energy Mater. Sol. Cells, 45(4), 361-368. https://doi.org/10.1016/S0927-0248(96)00083-9
2. Aqili A, Ali Z, Maqsood A (2000) Optical and structural properties of two-soursed evaporated ZnTe thin films, Applied Surface Science, Vol. 167, Issues 1-2, p. 1-11 DOI: 10.1016/S0169-4332(00)00498-0
3. Haynes WM, Eds., (2011), CRC Handbook of Chemistry and Physics, 92nd ed., CRC Press.
4. Aboraia AM, Ahmad M, Abdel Wahab EA, Shokry Hassan H., Shaaban ER (2015) Structural and optical properties of ZnTe thin films induced by plasma immersion O – ion implantation. Int. J. New. Hor. Phys. 2(1), 11-20. http://dx.doi.org/10.12785/ijnhp/020103
5. Aqili A, Ali Z, Maqsood A. (2000) Optical and structural properties of two-sourced evaporated ZnTe thin films. Applied Surface Science, 167 (1-2), 1-11. DOI:10.1016/S0169-4332(00)00498-0
6. Ishizaki T, Ohtomo T (2004) Structural, optical and electrical properties of ZnTe thin films electrochemically deposited from a citric acid aqueous solution, Journal of Physics D: Applied Physics 37(2), 255-261. DOI:10.1088/0022-3727/37/2/014
7. Murali KR, Rajkumar PR, (2006) Characteristics of pulse plated ZnTe films, Journal of materials science. Materials in electronics 17(5), 393-396. DOI: 10.1007/s10854-006-7476-1
8. Matsumoto T, Ishida T (1984) Chemical vapor deposition of zinc chalcogenides using elemental source materials, Journal of Crystal Growth, 67(1), 135-140. DOI:10.1016/0022-0248(84)90142-8
9. Guo Q, Nada M, Ding Y, Tanaka T, Nishio M (2010) Low-temperature buffer layer effects on the quality of ZnTe epilayers grown on sapphire substrates. J. Appl. Phys., 107, 123525-1 - 123525-5. https://doi.org/10.1063/1.3452356
10. Wang W, Phillips J, Pan X. (2011). ZnO/ZnSe/ZnTe Heterojunctions for ZnTe - Based Solar Cells, J. Electron. Mater. 40(8), 1674-1678. DOI:10.1007/s11664-011-1641-x
11. Pal U, Saha S, Chaudhuri AK, Rao V, Banerjee HD (1989) Some optical properties of evaporated zinc telluride films, J. Phys. D: Appl. Phys. 22(7), 965-970. DOI:10.1088/0022-3727/22/7/014
12. Erlacher A, Ambrico M, Perna G, Schiavulli L, Ligonzo T, Jaeger H., Ullrich B, Erlacher A (2005) Absorption and photoconductivity properties of ZnTe thin films formed by pulsed-laser deposition on glass, Appl. Surf. Sci. 248(1-4), 402-405. https://doi.org/10.1016/j.apsusc.2005.03.041
13. Tanaka T, Yu KM, Stone PR, Beeman JW, Dubon OD, Reichertz LA, Kao VM, Nishio M, Walukiewicz W (2010). Demonstration of homojunction ZnTe solar cells, J. Appl. Phys., 108(2), 024502-1 – 024502-2 DOI:10.1063/1.3463421
14. Wolden CA, Abbas A, Li J, Diercks DR, Meysing DM, Ohno TR, Beach JD, Barnes TM, Walls JM (2016) The roles of ZnTe buffer layers on CdTe solar cell performance, Sol. Energy Mater. Sol. Cells, 147, 203-210. https://doi.org/10.1016/j.solmat.2015.12.019
15. Patel NG, Panchal CJ, Makhija KK, Patel PG, Patel SS (1994) Fabrication and characterization of ZnTe/CdSe thin film solar cells, Crystal Research and Technology, 29(2), 247-251. https://doi.org/10.1002/crat.2170290214
16. Saikia P, Saikia PK, Saikia (2011) Fabrication and characterization of ZnSe/ZnTe/ CdTe/ HgTe multijunction solar cell, Optoelectron. Adv. Mat. 5(3), 204-207.
17. Yella A, Heiniger LP, Gao P, Nazeeruddin MK, Gratzel M (2014) Nanocrystalline Rutile Electron Extraction Layer Enables Low-temperature Solution Processed Perovskite Photovoltaics with 13,7 Efficiency, Nanoletters, vol. 14, Issue 5, pag. 2591-2596 DOI: 10.1021/nl500399m
18. Jeng JY, Chiang YF, Lee MH, Peng SR, Guo TF, Chen P, Wen TC (2013) $CH_3NH_3PbI_3$ perovskite / fullerene planar - heterojunction hybrid solar cells, Adv. Mater., 25(27), 3727-3732 DOI: 10.1002/adma.201301327
19. Etgar L, Gao P, Xue Z, Peng Q, Chandiran AK, Liu B, Nazeeruddin MK, Grätzel M (2012) Mesoscopic $CH_3NH_3PbI_3/TiO_2$ Heterojunction Solar Cells, J. Am. Chem. Soc., 134(42), 17396. DOI: 10.1021/ja307789s
20. Im JH, Lee CR, Lee JW, Park SW, Park NG (2011) 6.5% efficient perovskite quantum-dot-sensitized solar cell, Nanoscale, 3, 4088-4093, https://doi.org/10.1039/C1NR10867K
21. Lee MM, Teuscher J, Miyasaka T, Murakami T, Snaith HJ (2012) Efficient hybrid solar cells based on mesosuperstructured organometal halide perovskites, Science, 338(6107), 643-647. DOI: 10.1126/science.1228604
22. Giorgi G, Yamaschita K, Zero-dipole molecular organic cations in mixed organic–inorganic halide perovskites: possible chemical solution for the reported anomalous hysteresis in the current–voltage curve measurements, Nanotechnology, vol. 26, Nr. 44, DOI: 10.1088/0957-4484/26/44/442001

23. Jeon NJ, Noh JH, Kim YC, Yang WS, Ryu S., Seok S.I, (2014) Solvent engineering for high-performance inorganic-organic hybrid perovskite solar cells, Nat. Mater, 13(9), 897-903. DOI: 10.1038/nmat4014
24. Popa M, Zakhidov A, Tiginyanu I (2018) Perovskite solar cells with ZnS as electron transport layer, Proceedings of Romanian Academy, series A, vol. 19, No. 4, p. 559-566. https://www.repository.utm.md/bitstream/handle/5014/10900/Proc_of_theRomanian_Academy_2018_N4_p559_566.pdf?isAllowed=y&sequence=1
25. Popa ME (2019), Applications of Chalcogenides as Hole Transport Layers and Dopants in Perovskite Solar Cells, In Proceedings of 4th International Conference on Nanotechnologies and Biomedical Engineering, September 18–21, 2019, Chisinau, Moldova, p. 177-180. https://link.springer.com/book/10.1007/978-3-030-31866-6
26. Popa ME (2019), Applications of Chalcogenides as Electron Transport Layers and Doping Materials in Perovskite Solar Cells, In Proceedings of 4th International Conference on Nanotechnologies and Biomedical Engineering, September 18–21, 2019, Chisinau, Moldova, p. 173-176 https://link.springer.com/book/10.1007/978-3-030-31866-6
27. Popa ME (2020), Current-voltage characteristics of ZnSe-based Perovskite solar cells with inverted planar architecture, Journal of Optoelectronics and Advanced Materials, vol. 22, No. 7-8, p. 371 – 378, https://joam.inoe.ro/articles/current-voltage-characteristics-of-znse-based-perovskite-s-olar-c-ells-with-inverted-planar-architecture/fulltext
28. Stranks SD, Eperon GE, Grancini G, Menelaou C, Alcocer MJP, Leijtens T, Herz LM, Petrozza A, Snaith HJ (2013) Electron-Hole Diffusion Lengths Exceeding 1 Micrometer in an Organometal Trihalide Perovskite Absorber, Science, 342 (6156), 341-344. DOI: 10.1126/science.1243982
29. Yin WJ, Shi T, Yan Y (2014) Unique properties of halide perovskites as possible origins of the superior solar cell performance, Adv. Mater., 26(27), 4653-8. DOI: 10.1002/adma.201306281
30. Yin WJ, Shi T, Yan Y (2015) Superior Photovoltaic Properties of Lead Halide Perovskites: Insights from First-Principles Theory, J. Phys. Chem. C, 119(10), p. 5253–5264 DOI:10.1021/jp512077m
31. Bidikoudi M., Stathatos E (2024) Chalcogenides in Perovskite Solar Cells with a Carbon Electrode: State of the Art and Future Prospects, Nanomaterials, 14(22), 1783. DOI: 10.3390/nano14221783
32. Wang C, Nie R, Dai Y, Tai H, Zhu B, Zhao L, Wu Y, Guo W, Seok SI (2024**)** Enhancing the Inherent Stability of Perovskite Solar Cells through Chalcogenide-Halide Combinations. Energy Environ. Sci. , 17, 1368–1386, DOI: 10.1039/D3EE03612J
33. Njema, GG, Kibet JK, (2025) A Review of Chalcogenide-Based Perovskites as the next Novel Materials: Solar Cell and Optoelectronic Applications, Catalysis and Future Perspectives, Next Nanotechnol. , 7, 100102. DOI: 10.1016/j.nxnano.2024.100102
34. Agresti A, Giacomo FD, Pescetelli S, Carlo AD (2024) Scalable Deposition Techniques for Large-Area Perovskite Photovoltaic Technology: A Multi-Perspective Review, Nano Energy, 122, 109317. DOI:10.1016/j.nanoen.2024.109317
35. Rehman UU, Sahar KUl, Mahmood K, Hussain E, Wang CM (2025) Exploring the potential of non-toxic chalcogenide based perovskite solar cells: Performance analysis and insights, Inorganic Chemistry Communications, Volume 174, Part 1, 113923 https://doi.org/10.1016/j.inoche.2025.113923
36. Shimul A I, Khan M A, Rayhan A, Ghosh A (2025), Machine Learning-Based Optimization and Performance Enhancement of $CH_3NH_3SnBr_3$ Perovskite Solar Cells with Different Charge Transport Materials Using SCAPS-1D and wxAMPS, Advansed Theory and Simulations, DOI: 10.1002/adts.202500182
37. Saadat M, Amiri O (2024), Chalcogenide perovskites for solar energy applications: The role of Sn substitution in $BaZrS_3$-based photovoltaic devices, Inorganic Chemistry Communications, 168, 112977, DOI: 10.1016/j.inoche.2024.112977
38. Wada H, Kuwayama C, Hiroshiba N, Koike K, Kawaha M, (2026) Characterization of VO_2 thin films deposited on flexible ultrathin glass via MOD, Materials Letters, Volume 403, 139374, https://doi.org/10.1016/j.matlet.2025.139374
39. Shorok E, Bedir Y, Mohy Eldin AAE (2021) Efficiency enhancement of intermediate band solar cell using front surface pyramid grating, Optical and Quantum Electronics, vol. 53, nr. 360, https://link.springer.com/article/10.1007/s11082-021-03007-6
40. Sze SM (1981) Physics of Semiconductor Devices, 2nd Ed., John Wiley and Sons, New York

Citation: Popa., M. (2026). ZnTe – Based of perovskite solar cells with inverted planar arhitecture. *Journal of Engineering Science*. 2026, 33 (2), pp. 32-45. https://doi.org/10.52326/jes.utm.2026.33(2).03.

Publisher's Note: JES stays neutral with regard to jurisdictional claims in published maps and institutional affiliations.

Copyright:© 2026 by the authors. Submitted for possible open access publication under the terms and conditions of the Creative Commons Attribution (CC BY) license (https://creativecommons.org/licenses/by/4.0/).

Submission of manuscripts: jes@meridian.utm.md

Journal of Engineering Science *Vol. XXXIII, no. 2 (2026), pp. 46 - 60*
Fascicle *Industrial Engineering* *ISSN 2587-3474*
Topic *Electrical Engineering and Power Electronics* *eISSN 2587-3482*

https://doi.org/10.52326/jes.utm.2026.33(2).04
UDC 621.355:681.586:536.5

DETERMINING THE LOCATION OF OVERHEATING IN AN ELECTROCHEMICAL BATTERY

Oleg Petrov* ORCID: 0000-0003-4791-2384

Technical University of Moldova, Department of Transport, 9/8 Studentilor Street, block of study nr. 6, MD-2045 Chisinau, Republic of Moldova
* Corresponding author: Oleg Petrov, *oleg.petrov@tran.utm.md*

Received: 04. 25. 2026
Accepted: 05. 28. 2026

Abstract. This paper presents a device and a method for early warning of the risk of thermal runaway in electrochemical batteries. The effectiveness of the proposed system was assessed using mathematical modeling applied specifically to the battery module of the Audi e-tron. Modeling of prismatic cell overheating and calculation of instantaneous operating modes were performed in Excel Microsoft 365. The results, presented in analytical graphs, demonstrate the ability of the system to detect battery cell overheating, which confirms both the operability of the device and the reliability of the method. The proposed solution is especially suitable for improving the safety of lithium-ion, nickel-cadmium and other multi-cell battery systems during operation, as well as for integration into new battery modules. Main applications: monitoring cell temperature in a multi-cell battery module; early warning of thermal runaway risk in a multi-cell battery module; providing emergency alerts in case of immediate and obvious thermal runaway danger.

Keywords: *Thermal runaway, multi-cell battery module, cell overheating detection, thin film thermistor, temperature monitoring, multi-cell battery thermal modeling.*

Rezumat. Această lucrare prezintă un dispozitiv și o metodă pentru avertizarea timpurie a riscului de fuga termică în bateriile electrochimice. Eficacitatea sistemului propus a fost evaluată folosind modelarea matematică aplicată specific modulului bateriei Audi e-tron. Modelarea supraîncălzirii celulelor prismatice și calculul modurilor de funcționare instantanee au fost efectuate în Excel Microsoft 365. Rezultatele, prezentate în grafice analitice, demonstrează capacitatea sistemului de a detecta supraîncălzirea celulelor bateriei, ceea ce confirmă atât operabilitatea dispozitivului, cât și fiabilitatea metodei. Soluția propusă este potrivită în special pentru îmbunătățirea siguranței sistemelor de baterii litiu-ion, nichel-cadmiu și alte sisteme multicelulare în timpul funcționării, precum și pentru integrarea în module de baterii noi. Aplicații principale: monitorizarea temperaturii celulelor modulului bateriei multicelular; avertizare timpurie a riscului de fuga termică modulului bateriei multicelular; furnizarea de alerte de urgență în caz de pericol imediat și evident de fuga termică.

Cuvinte cheie: *Fuga termică, modul baterie multicelular, detectarea supraîncălzirii celulelor, termistor cu peliculă subțire, monitorizarea temperaturii, modelare termică a bateriilor multicelulare.*

Abbreviations The following abbreviations are used in this manuscript:

ISC Internal short circuit
CAN BUS A controller area network bus (CAN bus) is a vehicle bus standard designed
to enable efficient communication primarily between electronic control units (ECUs).
CANduino v4.0 Arduino-compatible development board designed for those working on automotive systems: the Canduino, with a built-in CAN bus.
LED A light-emitting diode (LED) is a semiconductor device that emits light when current flows through it.
GND is a reference point in a circuit from which voltage is measured
NTC stands for Negative Temperature Coefficient

1. Introduction

Thermal runaway in lithium-ion, nickel-cadmium, and other types of electrochemical energy storage devices is a phenomenon characterized by a chain of exothermic reactions within the battery. It is usually caused by an internal short circuit caused by defects or aging of the cell.

However, the most common cause is overheating, often caused by charging current flowing through a cell that has already reached full charge while other battery cells have not yet completed the charging process. In an overheated cell, exothermic reactions dramatically increase the internal temperature, which accelerates electrochemical activity and leads to excessive heat generation. This increase in temperature causes the release of flammable gases, an increase in internal pressure, and expansion of the outer casing, which can lead to an explosion and fire of the entire battery [1]. In three out of four cases, a fire breaks out during the charging phase **[**2]. Highlighting the importance of monitoring of battery cells.

Several technologies are known to prevent thermal runaway:

- Ultrasonic detection, which provides dynamic feedback on structural changes inside the cell for early warning systems;
- Detection of gas released during electrolyte decomposition using gas sensing devices to monitor chemical reactions;
- Voltage sensing using alternating topologies and multiple sensors to monitor terminal voltage of individual lithium-ion cells;
- Temperature monitoring is a fundamental method that allows real-time detection of abnormal increases in internal temperature [3].

Gas analyzers and ultrasonic scanning can detect electrolyte decomposition, signalling the onset of thermal runaway and cell failure. Voltage monitoring is a simple and reliable method for diagnosing internal short circuits (ISCs), especially when overcharging is a factor [4]. However, parallel connection of cells in battery modules complicates individual cell measurements. In addition, measuring internal resistance and voltage alone may not provide timely detection of thermal runaway [5].

Given these limitations, temperature monitoring is considered the most fundamental method for preventing thermal runaway [3]. Stopping the heating before the electrolyte decomposes can avoid battery destruction. However, both temperature monitoring and voltage monitoring require multi-wire circuits, which increases the system cost and reduces reliability. Common temperature sensors such as thermistors, thermocouples, and analog-to-digital sensors have disadvantages such as low detection accuracy and sensitivity to the environment.

One of the known thermal runaway warning devices [6] involves the use of temperature-sensitive tape sensors that melt when overheated. These disposable tapes must be replaced after activation, which makes them impractical due to labor-intensive and unreliable operation. Therefore, safety management methods and systems for electrochemical devices continue to evolve.

Based on the above, the objective of this work is to investigate the performance of the proposed thermal runaway risk early warning system [**7**], in particular, in the temperature monitoring mode of the battery module cells in the electrochemical battery system of the Audi e-tron [8].

2. Model for Studying of the proposed Overheated Cell Detection and Early Warning System for the Audi e-tron Electrochemical Battery Module

Electrochemical battery modules, in particular those used in electric vehicles, may differ in the number and shape of individual cells. To select the appropriate type and resistance parameters of flexible thin-film sensors, as well as the iterative selection of a constant resistance resistor for the proposed overheated cell detection system of the electrochemical battery module [8], it is necessary to study the operating modes of the system using a mathematical model. This study allows optimizing the device parameters for a specific battery module.

However, to develop a universal algorithm and test the corresponding software module for use in various types and configurations of batteries, a physical prototype is required - a test bench. This section presents a model of the proposed cell overheated detection and early warning system [7], specially adapted for the Audi e-tron electrochemical battery module [8].

The schematic diagram of the proposed overheated cell detection system is shown in Fig. 1.

The diagram includes the following components:

- Sensor unit (1): Consists of a flexible thin-film sensor (2) with a high-temperature nonlinear resistance coefficient. Identical sections (10) of which are attached to the corresponding cells of the electrochemical module of the battery.
- Control unit (3) includes:
  - controller (4) based on CANduino v4.0;
  - constant resistance resistor (5);

Alarm unit (6) includes: LED indicator (7) and buzzer (8).

This configuration provides thermal contact between each section of the sensor and the housing of the corresponding cell, covering two equal groups of cells inside the module.

The electrical connections of the proposed overheated cell detection system are as follows:

- one end of the flexible thin-film sensor (2) is connected to the +5 V voltage source of the controller (4) via the electrical conductor (11);
- the other end of the sensor is connected to the analog input A7 of the controller (4) via the electrical conductor (12);
- the constant resistance resistor (5) is connected between the ground contact (GND) and the analog input A7 of the controller (4);

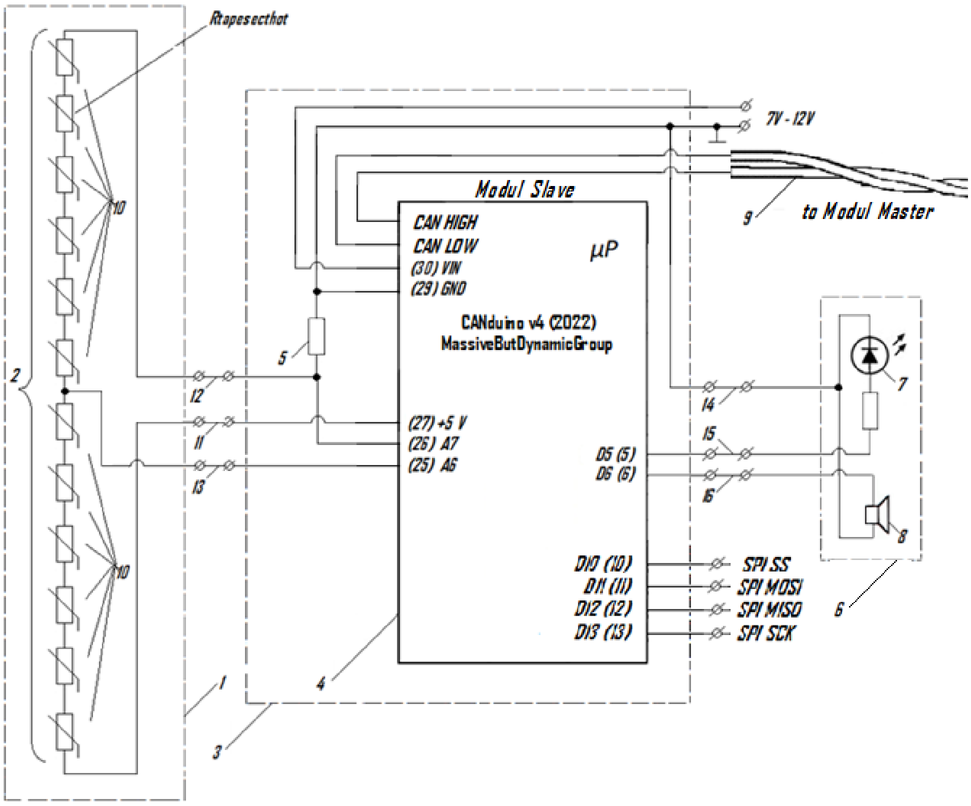

Figure 1. Overheated cell detection system in a twelve-cell lithium-ion battery module of the Audi e-tron [8].

- the midpoint of the sensor film is connected to the analog output A6 of the controller (4) via the electrical conductor (13);
- the +5 V DC output of the controller (5) is connected to the common power supply wire of the alarm unit (6) via the electrical conductor (14);
- the LED indicator (7) of the alarm unit (6) is connected to the digital output D2 of the controller (4) via the electrical conductor (15);
- the control output of the controller (4) is connected to the buzzer (8) of the alarm unit (6) via the electrical conductor (16).

3. Selection of sensors and controller for the system for determining the location and early warning of overheating in the battery module of electrochemical batteries

For monitoring the prismatic cells in the Audi e-tron lithium-ion battery module [8], a flexible thin-film sensor is considered the most suitable option. This type of sensor enables more reliable thermal contact across a larger surface area of the battery elements. However, such sensors are not yet commercially available.

Interest in flexible thin-film sensors stems from a series of successful experimental studies conducted by Tsung-Shine Ko et al. at the Department of Electronic Engineering, National Changhua University of Education, Taiwan [9]. Their research demonstrated that bulk thin-film $MoxW_{1-x}S_2$ has significant potential as a thermal sensor, and its future production is anticipated.

Since this promising material is still in the experimental phase and not yet manufactured, the characteristics of the NTC thermistor 1AE103R44T5A - produced by North Star Sensors, LLC [10] - are used to model the behavior of sections (10) of the flexible thin-film sensor (2). The specifications of the NTC thermistor 1AE103R44T5A are presented in Table 1.

Table 1

NTC thermistor characteristics

Part Number	**Resistance at25 °C,R_{25},** (kΩ)	**Temperature Tolerance,** **(°C)**	**R/T Curve**	**25 °C / 85°C ß**	**Recommended Measurement Current,** (µA)
1AE103R44T5A	10	± 0.5 from 0 to 70	44	3978	< 50

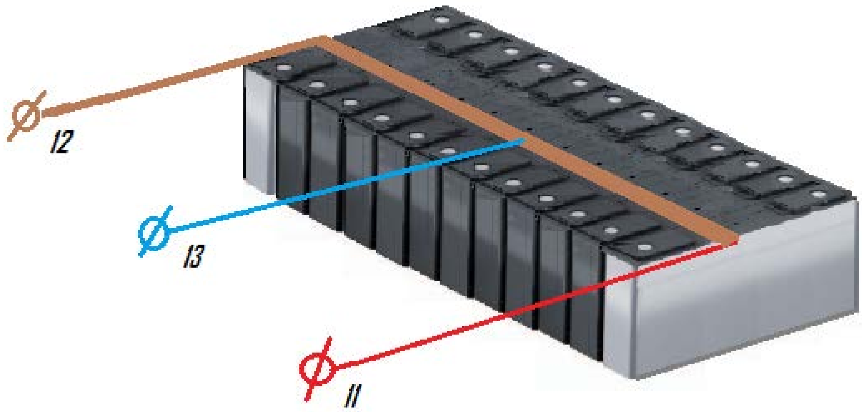

Figure 2. Prismatic lithium-ion battery (cell) module with flexible thin-film sensor.

Further research by Tianqi Yang et al. (2025) [11] examined temperature distributions in prismatic battery modules approaching thermal runaway. Their findings revealed that the highest temperatures occur at the top of the prism, between the cell poles. Based on these findings and recommendations [12], flexible thin-film sensors for detecting cell overheating in the twelve-cell prismatic lithium-ion battery module of the Audi e-tron [8] can be arranged as shown in Fig. 2. Let us consider the operation of the overheating detection system as applied to this module (Fig. 2).

Table 2

CANduino v4.0 Technical Specifications

Specification	**Parametr**
Microcontroller	ATmega328PA
Operating Voltage Cell modules	5 V
Input Voltage Range	7 V – 12 V
Digital I/O Pins	14 (6 with PWM)
Analog Input/Output Pins	8 (ADC channels)
Maximum current	40 mAh from one output
Flash memory	32 kb
Interface	SPI & CAN with USB Type-C
CAN controller / transceiver	MCP25625
Analog pins measure voltage with an accuracy	of 0,005 V

Since no publicly available information exists regarding the type of controller used in the Audi e-tron GT Quattro battery module, the CANduino v4 [12] is selected as the controller for the battery control unit (4). The technical specifications of the CANduino v4, designed by MassiveButDynamic in Germany, are provided in Table 2 [13].

The CANduino v4 interface supports CAN V2.0B with a speed of 1 Mbit/s and can be used to communicate with the master battery control processor via a twisted pair CAN Bus.

According to these data, we will accept the supply voltage of the sensor unit Ussupply = 5 V. In this case, the voltage of the midpoint of the flexible thin-film sensor, in the absence of overheated cells, will be Utest = 2.5 V.

4. Methodology for determining the location and early warning of overheating in the module of an electrochemical battery

To monitor the average temperature of the module cells and improve the accuracy of detecting when an overheated cell reaches the thermal runaway risk threshold, we calculate the voltage drop Utape across a constant resistor Rconst. This voltage drop varies as the resistance Rtape of the flexible thin-film sensor circuit changes in response to cell temperature fluctuations.

We use the RESISTANCE RATIO Rt/R25 ratio from the NORTH STAR SENSORS CURVE 44 specification to calculate the change in resistance of the flexible thin-film sensor sector [10]. We enter the calculation results in Table 3. To measure the average temperature of the module cells, we plot the dependence of the voltage drop on the resistance of the constant value Rconst in the flexible thin-film sensor circuit when the temperature Thotcell of the module cells changes, which increases from 20 °C to 100 °C.

To do this, we calculate the equivalent resistance Rtapeeqw of flexible thin-film sensor 2, consisting of ns = 12 sectors (Fig. 2), using formulas (1) and (2), taking into account the change in temperature:

$$\text{Rtapeeqw} = \sum_{i=1}^{ns} \text{Rtapesect (i)} \quad (1)$$

Current IC flowing in the resistance Rconst of a constant resistor 5 (Fig. 3):

$$\text{IC} = \text{Ussupply} / (\text{Rtapeeqw} + \text{Rconst}) \quad (2)$$

Let's calculate Utape, the value of the voltage drop as a function of the change in the operating temperature of the module cells:

$$\text{Utape} = \text{IC} \bullet \text{Rconst} \quad (3)$$

The calculations will be performed under the condition that the supply voltage of the flexible thin-film sensor will be equal to Ussupply = 5.0 V, the resistance of the sector of the flexible thin-film sensor at 25 °C (thermistor) will be R25 = 10 kΩ, the resistance of the constant-value resistor will be equal to Rconst = 1.4 kΩ. The calculation results are presented in Table 3 and in the graph of Fig. 3.

Table 3

Dependence of the voltage Utape on the temperature of the thin-film sensor Ttape

Ttape, (°C)	**20**	**40**	**60**	**80**	**100**
Ω RATIO **Rt/R25**	1.24927	0.53266	0.24869	0.12554	0.06784
Rtapesecthot, (kΩ)	12.493	5.327	2.487	1.255	0.678
Ic, (mA)	0.0330	0.0765	0.160	0.304	0.524
Utape, (V)	0.0463	0.1072	0.2241	0.4251	0.7337

Let us assume that the overheated cell has a thermal contact with the sector Rtapesecthot in the right part of the flexible thin-film sensor from the midpoint. Let us calculate the absolute value of the voltage deviation $dUtest_{20\ °C}$, that is, the modulus of the difference Utest voltage of the midpoint of the flexible thin-film sensor (in the absence of overheated cells) and $Utape_{20\ °C}$ of the midpoint voltage of the flexible thin-film sensor at the operating temperature of the module cells Tcelloper = 20 °C, when the resistance of each sector of the flexible thin-film sensor does not change and is $Rtapesect_{20\ °C}$ = 12.493 kΩ, except for the resistance of the sector Rtapesecthot in the right half of the thin-film sensor in contact with the cell, the temperature Thotcell of which increases from 20 °C to 100 °C.

We will calculate the absolute value of the voltage deviation $dUtest_{20\ °C}$ using the formula:

$$dUtest_{20\ °C} = ABS\ (Utest - Utape_{20\ °C}) \tag{4}$$

The voltage $Utape_{20\ °C}$ of the midpoint of the flexible thin-film sensor as a function of Thotcell with a change in the resistance of the sector Rtapesecthot in the right half of the thin-film sensor in contact with the cell, the temperature of which Thotcell increases from 20 °C to 100 °C, is determined by the formula:

$$Utape_{20\ °C} = Rrightside_{20\ °C} \bullet Itape_{20\ °C} \tag{5}$$

The resistance $Rrightside_{20\ °C}$ as a function of Thotcell of the right half of the flexible thin-film sensor at a module cell temperature of 20 °C with a change in the resistance of the sector Rtapesecthot as a function of Thotcell in the right half of the thin-film sensor is determined by the formula:

$$Rrightside_{20\ °C} = Rtapesect_{20\ °C} \bullet (ns/2 - 1) + Rtapesecthot \tag{6}$$

The current of the flexible thin-film sensor $Itape_{20\ °C}$ with a change in the resistance $Rtape_{20\ °C}$ of the flexible thin-film sensor as a function of Thotcell is determined by the formula:

$$Itape_{20°C} = Ussupply / Rtape_{20°C} \tag{7}$$

The total resistance of the flexible thin-film sensor $Rtape_{20\ °C}$ as a function of Thotcell is determined by the formula:

$$Rtape_{20°C} = Rrightside_{20°C} + Rleftside_{20°C} \tag{8}$$

The resistance of the left half of the flexible thin-film sensor $Rleftside_{20°C}$ at a module cell temperature of 20 °C is determined by the formula:

$$Rleftside_{20°C} = Rtapesect_{20°C} \bullet ns /2 \tag{9}$$

The calculation results are presented in Table 4 and in the graph of Fig. 4.

Table 4

Dependence of the deviation of the voltage of the midpoint of the dUtest sensor when one cell in the module overheats

Thotcell, (°C)	**20**	**40**	**60**	**80**	**100**
$dUtest_{20\ °C}$, (V)	0.000	0.126	0.179	0.203	0.214
$dUtest_{40\ °C}$, (V)	-	0.000	0.116	0.170	0.196

We repeat the calculation using formulas (4) - (9) at Tcelloper = 40 °C, when the resistance of each sector of the flexible thin-film sensor does not change and is $Rtapesect_{40°C}$

= 5.327 kΩ, and the temperature of which Thotcell in the right half of the thin-film sensor in contact with the cell increases from 40 °C to 100 °C.

The calculation results are presented in Table 4 and in the graph of Fig. 4.

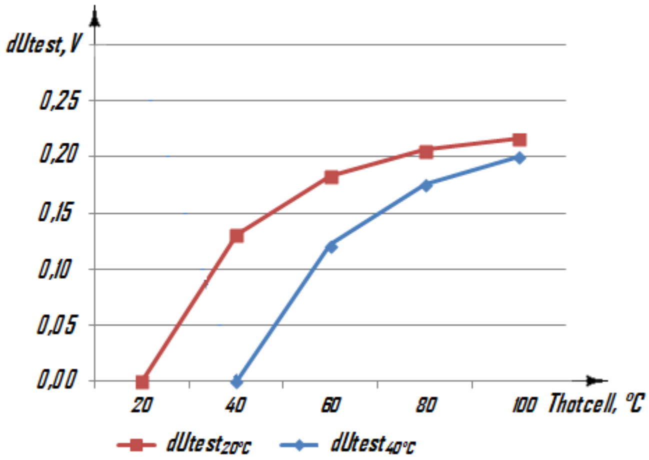

Figure 4. Dependence of the deviation of the midpoint voltage of the dUtest sensor when one cell in the module overheats at a temperature of the remaining cells of 20 °C or 40°C.

The graphs in Fig. 4 show that for practical application it is necessary to find a method for processing the results of measuring the midpoint voltage of the sensor to increase the accuracy.

One possible method may be to reduce the curves of the deviation of the midpoint voltage of the sensor dUtest to the temperature threshold point of the risk of develop-ing thermal runaway of the battery module cell. For this purpose, we use the value of the voltage drop Utape on the constant-value resistor Rconst, measured when deter-mining the average temperature of the module cells using a flexible thin-film sensor (Fig. 3).

We will compose a sum consisting of the absolute value of the difference between the test voltage Utest and the potential dUtape of the midpoint of the flexible thin-film sensor, and add to it the voltage drop Utape on the constant-value resistor obtained when calculating the average temperature of the module cells and obtain the value of dUtest':

$$dUtest' = ABS\ (Utest - dUtest) + Utape \quad (10)$$

Let us calculate the change in $dUtest'_{20\,^{\circ}C}$ when the temperature of the overheated cell Tcellhot changes from 20 °C to 100 °C using formula (5) for an average temperature of the module cells of 20 °C.

Let us calculate the change in $dUtest'_{40\,^{\circ}C}$ when the temperature of the overheated cell Tcellhot changes from 40 °C to 100 °C for an average temperature of the module cells of 40 °C. The calculation results are given in Table 5. The graph in Fig. 5 is constructed based on the calculation results.

Table 5

Change in $dUtest'_{40^{\circ}C}$ with change in temperature of superheated cell Tcellhot

Specification	**Parametrs**				
Thotcell, (°C)	20	40	60	80	100
$dUtest'_{20^{\circ}C}$ by $Ttape_{20^{\circ}C}$, (V)	0.046	0.174	0.228	0.253	0.264
$dUtest'_{40^{\circ}C}$ by $Ttape_{40^{\circ}C}$, (V)	-	0.107	0.228	0.284	0.311

The intersection point of the curves of the deviation of voltage dUtest'$_{60\ °C}$ of the flexible thin-film sensor midpoint during overheating of one of the module cells in Fig. 5 is determined by the value of the voltage drop Utape on the constant-value resistor Rconst.

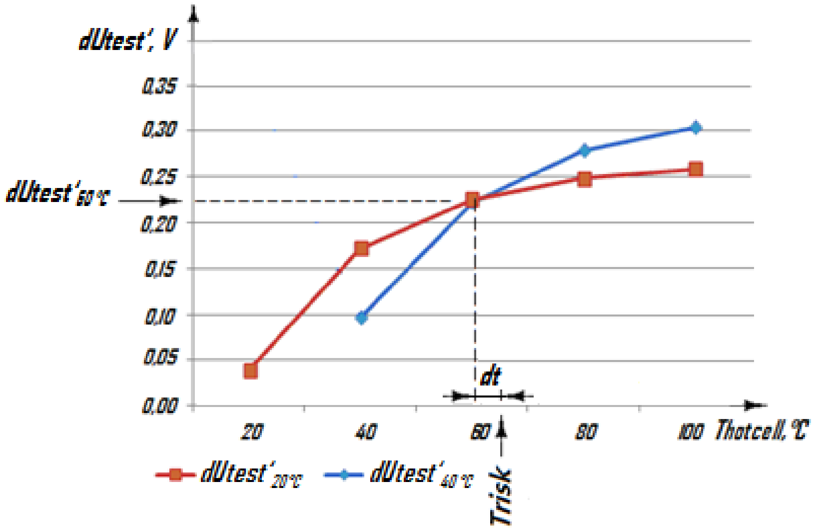

Figure 5. Corrected deviation of voltage dUtest' of the flexible thin-film sensor midpoint during overheating of one of the module cells at the temperature of the remaining 20 °C or 40 °C.

Thus, to bring the curves together at the required overheating temperature of one of the module cells, it is necessary to iteratively select the parameters of the constant value resistor Rconst on a mathematical model created by means of Excel Microsoft 365. The convergence of the curves in Fig. 5 allows one to set the threshold of the temperature of the risk of thermal runaway of the overheated module cell, uniform in value for any operating temperature of the remaining module cells. How-ever, to control the occurrence of the thermal runaway hazard of an overheated cell in a module, it is impossible to set a single temperature threshold at any operating temperature of the remaining cells in the module, since the curves diverge when the temperature of the overheated cell rises above the thermal runaway risk threshold Fig. 5.

Therefore, the algorithm provides for checking the efficiency of cooling the battery module and, if as a result of the measures taken, the temperature of the overheated cell decreases, the thermal runaway risk signal will be disabled, and if the temperature of the overheated cell, measured after the reaction time Treact, is higher than the risk temperature threshold Trisc, the sound signal warning about the danger of thermal runaway of the cell is activated. Where Treact is the time for the module temperature to decrease by 1°C at the maximum cooling mode.

It is advisable to study the practical application of the system for determining the location and early warning of thermal runaway of a lithium-ion battery on a model. The diagram is shown in Fig. 1. It is proposed to use the CANduino v4.0 microprocessor, which is equipped with an analog-to-digital converter (ADC), as a controller.

The A0-A5 contacts of the CANduino v4.0 microprocessor are used to read ana-log voltages. The ADC converts the voltage into bits that the microprocessor can understand. The ADC of this microprocessor has a 10-bit resolution, which means that it can represent the analog voltage with 1024 digital levels. [14]. The analog pins A0-A5 measure the voltage with an accuracy of dPv = 0.005 V (Table 1). Let us determine the accuracy in degrees with which the ADC can determine the cell surface temperature using a flexible thin-film sensor Ttape when the cell temperature changes from 40°C to 60°C. Let us plot the ratio of the ordinate to the abscissa of the graph in Fig. 3, based on the data in Table 2:

$$(Utape_{60\ °C} - Utape_{40\ °C}) \text{ is related to } (Ttape_{60\ °C}\ Ttape_{40\ °C}) \text{ as} \qquad (11)$$
$$dPv \text{ is related to } dPg$$

Let's substitute the values and determine the measurement accuracy in degrees – dPg:

$$dPg = 0.005\ V \bullet (60°C - 40°C) / (0.2241V - 0.1072\ V) \qquad (12)$$
$$dPg = 0.86\ °C$$

The analog outputs A0–A5 can measure the cell temperature with an accuracy of dPg = 0.86 °C, which allows the use of the CANduino v4.0 microprocessor for building a test bench, as well as for the battery module temperature monitoring system.

5. Determination of Temperature Thresholds for the Risk and Danger of Thermal Runaway in Lithium-Ion Batteries

Thermal runaway in lithium-ion batteries is typically divided into three stages:

- Self-heating stage: 50 -140 °C;
- Runaway stage: 140 - 850 °C;
- Termination stage: 850 °C down to ambient temperature.

Some literature sources indicate that the mass melting temperature of the separator begins around 140 °C [5]. $LiFePO_4$ batteries can typically operate in a temperature range of -20 °C to 60 °C (-4 °F to 140 °F), but optimal performance is achieved at temperatures of 0 °C to 45 °C (32 °F to 113 °F) [15].

The exothermic reaction before thermal runaway of the battery is mainly caused by the decomposition and regeneration of the anodic solid electrolyte interface (SEI). Researchers Jin, C. et al. (2024) [16] found that SEI can start to decompose above 70 °C. Therefore, the decomposition of the anode SEI can be considered as the beginning of the thermal runaway of the battery, which the proposed system should not allow. The exact decomposition temperature of the anode SEI is related to the chemistry of the specific battery, the thickness of the SEI and the state of the SOC [5], so for each specific application of the proposed system it should be taken into account when setting the thermal runaway risk threshold.

Research by Kisseler, N. et al. (2024) [17] showed that in large-format high-energy prismatic battery cells, the temperature difference between the internal temperature and the external surface temperature of the cell can reach 1.8 °C during cycling under natural convection conditions, even at low charging currents of 0.25 °C, which are likely to be significantly higher at higher charging currents.

Based on this, we adopt a correction for the temperature difference between the internal temperature and the external surface temperature of the cell equal to dt = 5 °C for the cells of the module under consideration.

Taking into account the correction dt, we set the thermal runaway risk temperature threshold of the battery module cell Trisk = 60 °C. By iteratively selecting the resistance of the resistor of constant value Rconst, we achieve the intersection of the curves of the voltage deviation dUtest' of the midpoint of the flexible thin-film sensor, when one of the module cells is overheated, at a point with a temperature equal to Trisk = 60 °C (at a temperature of the remaining cells of 20 °C and, accordingly, 40 °C). In Fig. 5, the dashed line shows that for any operating temperature of the cells of the module under consideration, the value of the temperature threshold for the overheated one will correspond to the same calculated voltage dUtest' = 0.225 V, at the actual temperature of the overheated cell Thotcell = 65 °C.

6. Operating algorithm of the system for determining the location and early warning of overheating in the battery module

The operating algorithm of the system for determining the location and early warning of overheating of the battery module is shown in Fig. 6. Before the start of the operation of the early warning system and determining the location of overheating of the electrochemical battery module, the data of the battery module in question are entered into the memory of the slave controller CANduino Slave v4 for monitoring by the proposed system:

Initialization

S10 : The following constants are assigned:

Urisk : Calculated voltage threshold for thermal runaway risk
Udngr : Calculated voltage threshold for thermal runaway danger
Utest : Test voltage, equal to half of Ussupply
Flag : Timer activation flag, initialized as Flag = 0
ns : Number of sensor sections in the battery module
Treact : Time required by the cooling system to reduce the module temperature by 1 °C in forced mode

Additionally, the data from Table 2 - representing the dependence of Utape on cell temperature Ttape - are stored in the controller’s memory.

Temperature Measurement

S20: To determine average module temperature:

Apply Ussupply = 5 V from Controller (4) to one end of the flexible thin-film sensor (2)
Connect the other end to GND via constant resistor (5)
Disconnect pin A6, connect pin A7 to the ADC, and read Utape
Use Table 2 to determine Ttape, the average module temperature

Iterative Monitoring Loop

S30: Decrement variable i = i − 1

S40: Using the digitalWrite(A7, 0) function, set ground GND on pin A7 of controller (4).

S50: Measure the voltage dUtest of the midpoint of flexible thin-film sensor (2) on wire (13) using the analog-to-digital converter of analog input A6 of controller (4) of battery control unit (3). Calculate the magnitude of the difference modulus Utest of the test voltage and dUtest of the midpoint voltage of flexible thin-film sensor (2), then add the value Utape of the voltage drop at the beginning of the constant resistor (7) and assign to constant dUtest'.

S60: Compare the obtained value dUtest with the threshold value Urisk of the thermal runaway risk voltage, if it is less, then go to S50 to perform the next cycle, if it is greater than or equal to Urisk, then go to S90.

S70: Decrement i = i − 11

S80: If i = 0, return to S20; if i ≠ 0, go to S40.

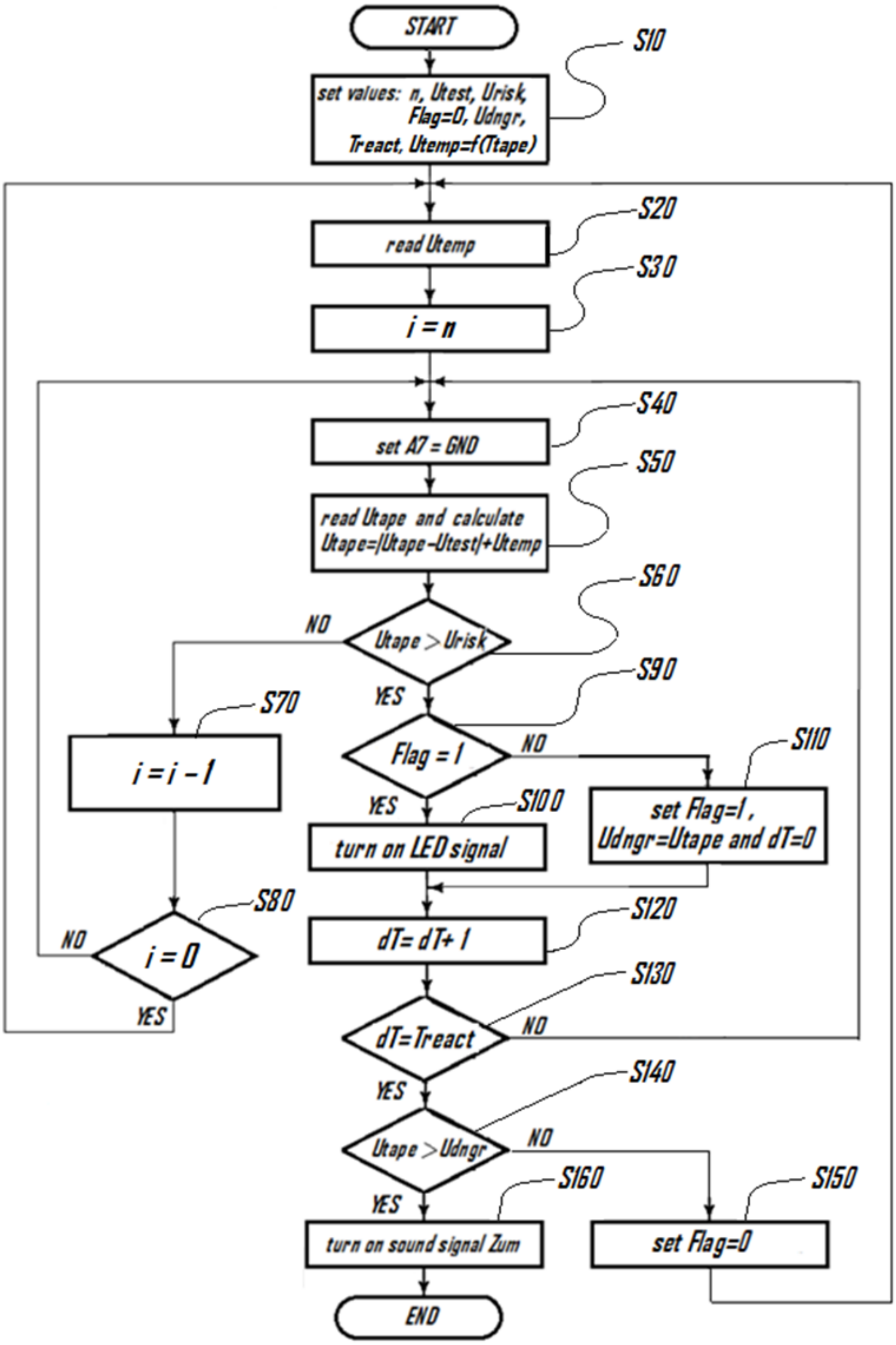

Figure 6. Algorithm of operation of the system for determining the location and early warning of overheating in the battery module.

Response Logic

S90: Check Flag = 1.

- If true, go to S100
- If false, go to S110

S100: Activate LED indicator and send signal to the battery regulation control unit to:

- Turn on cooling fans at full power
- Halt charging/discharging of the module or entire battery

S110: Assign: Flag = 1, Udngr = Utape, dT = 0
S120: Assign to the variable dT = dT + 1
S130: Compare dT = Treact. proceed to S140; otherwise, return to S40
S140: Compare dUtest' > Udngr
 If true, go to S160
 If false, go to S150
S150: Assign: Flag= 0 and go to S20.
S160: Activate buzzer (8) and send signal to the battery regulation control unit to:
 Trigger the active fire extinguishing system for the module or entire battery

8. Results

Audi, like most manufacturers, monitors the temperature, current and voltage of each cell to protect against thermal runaway, and intervenes if necessary. The pro-posed technical solution reduces the number of wires for monitoring the cell temperature by almost an order of magnitude, and also increases the accuracy of determining the average temperature of the module cells and reduces the effect of the operating temperature on the accuracy of determining the temperature threshold at which the operation of the cell is associated with the risk of thermal runaway.

9. Conclusion

This paper presents a system for monitoring the temperature of battery module cells using flexible thin-film thermistors. The system is designed to ensure that the accuracy of detecting an overheated cell remains unaffected by temperature variations in the other cells within the module.

To investigate the proposed temperature monitoring system, a basic application diagram of the system for monitoring a real electric vehicle battery module was developed. The operating modes of the system were analyzed using mathematical modeling of the conditions under which cell overheating occurs.

The technical outcomes of the proposed monitoring system include:

- Early detection of an overheated cell in an electrochemical battery module-prior to the onset of cell degradation-enabling timely signaling of both risk and danger associated with thermal runaway if the temperature rise is not mitigated.
- Precise identification of the moment when a cell reaches the critical temperature threshold, beyond which continued operation poses a risk of thermal runaway, independent of the overall temperature of the module.
- Cost reduction in components and electrical connections, achieved by using flexible thin-film sensors instead of individual sensors for each cell.
- Sustained monitoring capability after the temperature of the overheated cell drops below the thermal runaway hazard threshold.

Data Availability Statement The battery data used in this paper are from the public source. No new data were created in this study.

Note Article editing was done using Microsoft 365 Copilot artificial intelligence.

Funding: This research received no external funding.

Acknowledgments During the preparation of this manuscript/study, the author used Excel Microsoft 365 to perform calculations and plot graphs. The author have reviewed and revised the output and accept full responsibility for the content of this publication.

References

1. Finegan, D.P., Darcy, E., Keyser, M., Tjaden, B., Heenan, T.M.M., Jervis, R. *et al.* (2017) Characterising thermal runaway within lithium-ion cells by inducing and monitoring internal short circuits, *Energy & Environmental Science*, 10, pp. 1377–1388.
2. Schmiedeberg, I. (2024) *Drei Viertel aller Brände entstehen in der Ladephase*. Presseinformation, Institut für Schadenverhütung und Schadenforschung e.V., Kiel, Germany. Available at: https://www.bsbrandschutz.de/news/drei-viertel-aller-braende-entstehen-in-der-ladephase-4087710.html.
3. Shi, P., Zhu, H., Dong, X. and Hai, B. (2025) Research Progress on Thermal Runaway Warning Methods and Fire Extinguishing Technologies for Lithium-Ion Batteries, *World Electric Vehicle Journal*, 16(2), 81. https://doi.org/10.3390/wevj16020081.
4. Gao, W., Li, X., Ma, M., Fu, Y., Jiang, J. and Mi, C. (2020) Case Study of an Electric Vehicle Battery Thermal Runaway and Online Internal Short Circuit Detection, *IEEE Transactions on Power Electronics*. Available at: https://www.researchgate.net/publication/343343110.
5. CM Batteries (2024) *What Is Lithium Battery Thermal Runaway?* Available at: https://cmbatteries.com/what-is-lithium-battery-thermal-runaway/.
6. *Battery Thermal Runaway Early Warning Method*. Chinese Patent CN111370784B, published 13 May 2022. Available at: https://patents.google.com/patent/CN111370784B.
7. Petrov, O. (2025) *Sistem pentru determinarea locației și avertizare timpurie a supraîncălzirii într-un banc de baterii electrochimice și metodă de utilizare a acestuia*. Cerere de brevet AGEPI, Republica Moldova, Nr. s 2025 0045, depusă la 19 May 2025.
8. George, M. (2024) *Audi Electric Car Battery: Revolutionizing Green Travel*. Available at: https://electriccarwiki.com/audi-electric-car-battery-2/.
9. Ko, T.-S., Lin, E.-T., Huang, X.-W., Wu, P.-T. and Yang, Y.-L. (2022) High-Temperature Coefficient of Resistance in MoxW1−xS2 Thin Film, *Applied Sciences*, 12, 5110. https://doi.org/10.3390/app12105110.
10. North Star Sensors, LLC (2025) *1AE103R44T5A NTC Thermistor*. Available at: https://www.northstarsensors.com/nss-store/1ae103r44t5a.
11. Yang, T., Xu, H., Xie, C., Xu, L., Liu, M., Chen, L., Xin, Q., Zeng, J., Zhang, H. and Xiao, J. (2025) A Thermal Runaway Protection Strategy for Prismatic Lithium-Ion Battery Modules Based on Phase Change and Thermal Decomposition of Sodium Acetate Trihydrate, *Batteries*, 11(5), 198. https://doi.org/10.3390/batteries11050198.
12. Aufranc, J.-L. (2022) CANduino v3 – A Microchip ATmega168PA Board with CAN Bus, Arduino Nano Form Factor, *CNX Software – Embedded Systems News*, 16 July 2022.
13. Massive Group (2025) *CANduino v4 – ATmega328P with CAN-Bus*. Available at: https://www.tindie.com/products/massivegroup/canduino-v4-atmega328p-with-can-bus/.
14. Circuito.io (2025) *An Introduction to Arduino Uno Pinout*. Available at: https://www.circuito.io/blog/arduino-uno-pinout/.
15. Murden, D. (2024) *LiFePO4 Battery Operating Temperature Range: Safety, Precautions, and Common Mistakes*. Eco Tree Lithium. Available at: https://ecotreelithium.co.uk/news/lithium-iron-phosphate-battery-operating-temperature-range/.
16. Jin, C., Sun, Y., Wang, H., Zheng, Y., Wang, S., Rui, X., Xu, C., Feng, X., Wang, H. and Ouyang, M. (2022) Heating power and heating energy effect on the thermal runaway propagation characteristics of lithium-ion battery module: Experiments and modeling, *Applied Energy*, 312, 118760.
17. Kisseler, N., Hoheisel, F., Offermanns, C., Frieges, M., Heimes, H. and Kampker, A. (2024) Monitoring of Thermal Runaway in Commercial Prismatic High-Energy Lithium-Ion Battery Cells via Internal Temperature Sensing, *Batteries*, 10, 41. https://doi.org/10.3390/batteries10020041.
18. DK Testing Equipment (Hangzhou) Co., Ltd. (2025) *Li-Ion Cell Grading Tester DT50W*. Available at: https://dk-tester.com/products/li-ion-cell-grading-tester-dt50w.

Citation: Petrov, O. (2026). Determining the location of overheating in an electrochemical battery. *Journal of Engineering Science*. 2026, 33 (2), pp. 46-60. https://doi.org/10.52326/jes.utm.2026.33(2).04.

Publisher's Note: JES stays neutral with regard to jurisdictional claims in published maps and institutional affiliations.

Copyright:© 2026 by the authors. Submitted for possible open access publication under the terms and conditions of the Creative Commons Attribution (CC BY) license (https://creativecommons.org/licenses/by/4.0/).

Submission of manuscripts: jes@meridian.utm.md

Journal of Engineering Science *Vol. XXXIII, no. 2 (2026), pp. 61 - 70*
Fascicle *Electronics and Computer Science* *ISSN 2587-3474*
Topic *Biomedical Engineering* *eISSN 2587-3482*

https://doi.org/10.52326/jes.utm.2026.33(2).05
UDC 615.47:006.83:620.1

OPTIMIZATION OF THE CONFORMITY ASSESSMENT PROCESS FOR MEDICAL DEVICES UNDER CONDITIONS ENSURING THE EVALUATION OF SAFETY AND PERFORMANCE PARAMETERS

Gheorghe Gorceag *, ORCID: 0000-0002-4470-8014,
Oleg Lupan, ORCID: 0000-0001-7193-5530,
Serghei Railean, ORCID: 0000-0001-5478-4363,
Nicolai Ababii, ORCID: 0000-0001-5046-8611

Technical University of Moldova, 168 Ștefan cel mare blvd., Chisinau, Republic of Moldova
* Corresponding author: Gheorghe Gorceag, *gheorghe.gorceag@mib.utm.md*

Received: 04. 05. 2026
Accepted: 05. 12. 2026

Abstract. Periodic verification through examinations and laboratory testing represents a technical operation that can ensure an adequate level of performance and safety of medical devices. This verification ensures the assessment of general safety, electrical safety, functionality, alarm control, and, most importantly, the performance parameters of medical devices. In order to establish a service system intended for the periodic conformity assessment of medical devices, it was necessary to identify new methodological approaches. This methodology is based on the cost–effectiveness ratio, ensuring the application of a minimum set of non-destructive methods in accordance with standards, while guaranteeing an appropriate level of performance and safety of medical devices.

Keywords: *medical devices, periodic conformity assessment, periodic inspection, non-destructive testing, standards, safety, performance, reliability, efficiency, quality.*

Rezumat. Verificarea periodică prin examinări și încercări de laborator reprezintă operațiunea tehnică ce poate garanta nivelul adecvat al performanțelor și siguranței dispozitivelor medicale. Această verificare asigură evaluarea securității generale, a securității electrice, a funcționalității, a controlului alarmelor și, cel mai important, controlul parametrilor de performanță a dispozitivelor medicale. Pentru a institui un sistem de servicii destinat evaluării periodice a conformității dispozitivelor medicale, a fost necesară identificarea unei noi metodologii. Metodologie, care are la bază raportul cost-eficiență, prin care se asigură îndeplinirea setului minim de metode nedistructive conform standardelor, cu garantarea nivelului corespunzător de performanță și securitate al dispozitivelor medicale.

Cuvinte-cheie: *dispozitive medicale, evaluarea periodică a conformității, verificare periodică, metode nedistructive, standarde, securitate, performanță, siguranță, eficiență, calitate.*

1. Introduction

In order to ensure the functionality and practical applicability of the system for periodic conformity assessment of medical devices, based on the established regulatory framework, it was necessary to develop specific procedures for the periodic verification of medical devices in accordance with the Nomenclature approved by the Annex to Government Decision No. 966/2017 "On the approval of the Regulation regarding the periodic verification of medical devices placed into service and in use" [1, 2, 3].

In this context, it was necessary to determine a methodology for selecting non-destructive testing methods from applicable standards, based on a cost–efficiency ratio, in order to ensure an appropriate level of performance and safety of medical devices.

Considering that the verification interval is 24 months, it was also necessary to take into account the allocation of financial resources for periodic verification activities, in order to ensure the continuity of this process by medical institutions. Furthermore, consideration was given to the time required to perform periodic verification, in order to avoid prolonged downtime of medical devices, as well as to the human, material, and financial resources required for this purpose.

Based on these considerations, the requirements of standards applicable to medical devices at the manufacturing stage were researched and analyzed, with the aim of identifying the methods within those standards that would form the basis for the specific verification procedures.

Standards include both destructive and non-destructive methods, which are fully applied at the manufacturing stage, particularly during the conformity assessment. However, for the periodic verification medical devices that have already been placed into service and are in use, and which have undergone conformity assessment at the time of manufacture, it is evident that only non-destructive methods can be applied [4, 5].

A particularly complex task consisted in the study, identification, and establishment of a minimum set of methods capable of ensuring the safety and quality of medical devices by verifying general safety, electrical safety, and performance parameters, taking into account all the aforementioned aspects [6–9].

Accordingly, the methods selected from the standards applicable to medical devices at the manufacturing stage were incorporated into the specific procedures for periodic verification, which derive from the general procedure for periodic verification. These must correspond to the needs of the healthcare system, ensuring compliance with safety and performance parameters of medical devices, while also taking into account technological developments and international best practices in the field.

2. Phasing of the periodic verification process

Were studied standards for all 29 types of medical devices, in accordance with the Nomenclature approved by the Annex to Government Decision No. 966/2017 "On the approval of the Regulation regarding the periodic verification of medical devices placed into service and in use", for the purpose of developing and approving specific procedures for periodic verification.

As an example, in order to determine the methodology for developing a specific procedure for periodic verification, was selected, the electrocardiograph.

The development of a specific procedure for periodic verification was based on several stages, namely:

At the first stage, harmonized European standards adopted as Moldovan standards concerning general safety, electrical safety, and performance requirements were analyzed and selected. For example, for electrocardiographs: *Standard SM EN 60601-1-8, SM EN 60601-1-8/A1/AC "Medical electrical equipment – Part 1-8: General requirements for basic safety and essential performance – Collateral standard: General requirements, tests and guidance for alarm systems in medical electrical equipment and medical electrical systems"* [10]; *Standard SM EN 62353 "Medical electrical equipment – Recurrent test and test after repair of medical electrical equipment"; Standard SM SR EN 60601-1 "General requirements for basic safety and essential performance"* [11]*; Standard SM EN 60601-2-25 "Medical electrical equipment – Part 2-25: Particular requirements for the basic safety and essential performance of electrocardiographs"* [12]*; Standard SM EN 60601-2-51 "Medical electrical equipment – Part 2-51: Particular requirements for safety, including essential performance, of recording and analyzing single-channel and multi-channel electrocardiographs"* [13]; *Standard SM EN 60601-2-47 "Medical electrical equipment – Part 2-47: Particular requirements for safety, including essential performance, of ambulatory electrocardiographic systems"* [14].

Subsequently, the terminology and definitions used were examined and studied in order to ensure the correct interpretation of the specific procedure for periodic verification, in accordance with the regulatory framework in the field of medical devices. At the same time, it has been established that, in order to perform periodic verification of all types of medical devices, the following are required: *medical device testers, simulators, connection cables, measuring instruments (multimeters), as well as computers equipped with software for data acquisition and processing* [15].

Furthermore, in accordance with standard provisions, prior to initiating periodic verification, environmental conditions must be confirmed, specifically: *ambient temperature between (15–35) °C and relative humidity between (45–75) %* [15].

Another mandatory condition is that only specialists who have undergone safety training and are familiar with the operating documentation of the medical device are allowed to perform the verification.

Subsequently, for the same type of medical device, taking as an example: the electrocardiograph, all non-destructive methods specified in the standards were studied and analyzed in order to establish a minimum set of methods capable to ensure the performance and safety parameters.

Accordingly, the identification and analysis of methods from the standards were carried out in stages, namely:

- ✓ methods related to general safety;
- ✓ methods related to electrical safety;
- ✓ methods related to device performance.

After preparing the medical device for periodic verification through examination and testing, as described above, before verifying electrical safety and performance parameters, the device must first be tested for general safety.

Thus, according to standard SM SR EN 60601-1, from the perspective of general safety for electrocardiographs, the following methods requiring examination and testing were identified:

- ✓ classification of medical devices;
- ✓ instability during transport;
- ✓ interruption of power supply/mains supply to the medical device;

- ✓ mains-connected parts, components, and their arrangement;
- ✓ legibility of markings;
- ✓ marking on the exterior and interior of the device or applied parts [10–14].

Specific to electrocardiographs, for conformity control based on the requirements of standards SMV EN 60601-1-1 and SMV EN ISO 9919, methods for visual inspection and functional testing were established as necessary, namely:

Visual inspection:

- ✓ intact housing (no missing components);
- ✓ intact connectors;
- ✓ intact buttons;
- ✓ intact display;
- ✓ sensor condition;
- ✓ interconnection cable condition.

Functional verification:

- ✓ display brightness;
- ✓ self-test functionality;
- ✓ functional buttons;
- ✓ presence of alarm sound;
- ✓ presence of battery;
- ✓ detection of missing sensor or interconnection cable [10–14].

Requirements regarding the verification of sealing and marking elements related to the device housing and connection cables were studied and subsequently selected.

For the periodic verification of electrical safety parameters of the electrocardiograph, Standard SM SR EN 60601-1 was studied, and essential methods related to electrical operation were selected. Accordingly, for electrically powered medical devices, including electrocardiographs, the following methods are relevant:

- ✓ measurement of supply voltage;
- ✓ power consumption;
- ✓ earth leakage currents;
- ✓ patient leakage currents;
- ✓ enclosure leakage currents;
- ✓ auxiliary leakage currents;
- ✓ insulation resistance [10–14].

Furthermore, according to Standard SMV EN 60601-2-51, specific to electrocardiographs, several methods for periodic verification related to performance parameters were studied and identified, for example:

- ✓ requirements for amplitude measurement;
- ✓ requirements for waveform interval and duration;
- ✓ requirements for stability under noise conditions;
- ✓ minimum configuration requirements;
- ✓ calibration signal;
- ✓ sensitivity accuracy;
- ✓ internal filters;
- ✓ noise level;
- ✓ high-frequency response;
- ✓ low-frequency response;

- ✓ recording speed [10−14].

Using the methodology described above, periodic verification methods were identified and established from the standards applicable to electrocardiographs. Similarly, standards for all types of medical devices included in the approved Nomenclature were studied in order to develop specific procedures for periodic verification.

3. Measurement of the time required for periodic verification

In accordance with the stages of the general procedure for periodic verification, the time required for electrocardiograph verification was measured and estimated, as presented in Table 1.

Table 1

Time required for the periodic verification of the electrocardiograph

Nr. d/o	Title of the works related to periodic verification		Time (hours)
1.	**Receipt and analysis of the request for performing periodic verifications**		**0,10**
	1.1	registration of the testing request	0,05
	1.2	preparation of test and examination sheets for recording results	0,05
2.	**Preparation of the medical device for testing**		**0,05**
3.	**Performing examinations and testing of parameters**		**2,20**
	3.1	general safety parameters	0,15
	3.2	of the alarm system	0,00
	3.3	electrical safety	0,55
	3.4	performance	1,10
4.	**Preparation of the inspection report**		**0,20**
	5.1	transfer of data from the test sheet and completion of the report	0,15
	5.2	conclusions and remarks on the medical device	0,05
5.	**Issuance of the inspection certificate based on the report**		**0,10**
Total			**3,05**

Accordingly, the time required for the periodic verification of the electrocardiograph is approximately 3.05 hours.

Similarly, the time required to perform periodic verification was measured and estimated for another 8 types of medical devices from the Nomenclature, namely:

patient monitor;
pulse oximeter;
infusion pump;
artificial ventilation device (ventilator);
external defibrillation device (defibrillator);
electrosurgical unit (electro coagulator);
neonatal incubator;
neonatal resuscitation table.

The time required for periodic verification consists of the totality of activities aimed at evaluating general safety parameters, alarm system parameters, electrical safety, and performance.

At the same time, it was observed that the time required to verify electrical safety parameters is approximately the same for electrically powered medical devices. Similarly, the time required to verify general safety parameters is nearly identical across all types of medical devices. The difference is mainly determined by the time required to assess performance parameters (Figure 1).

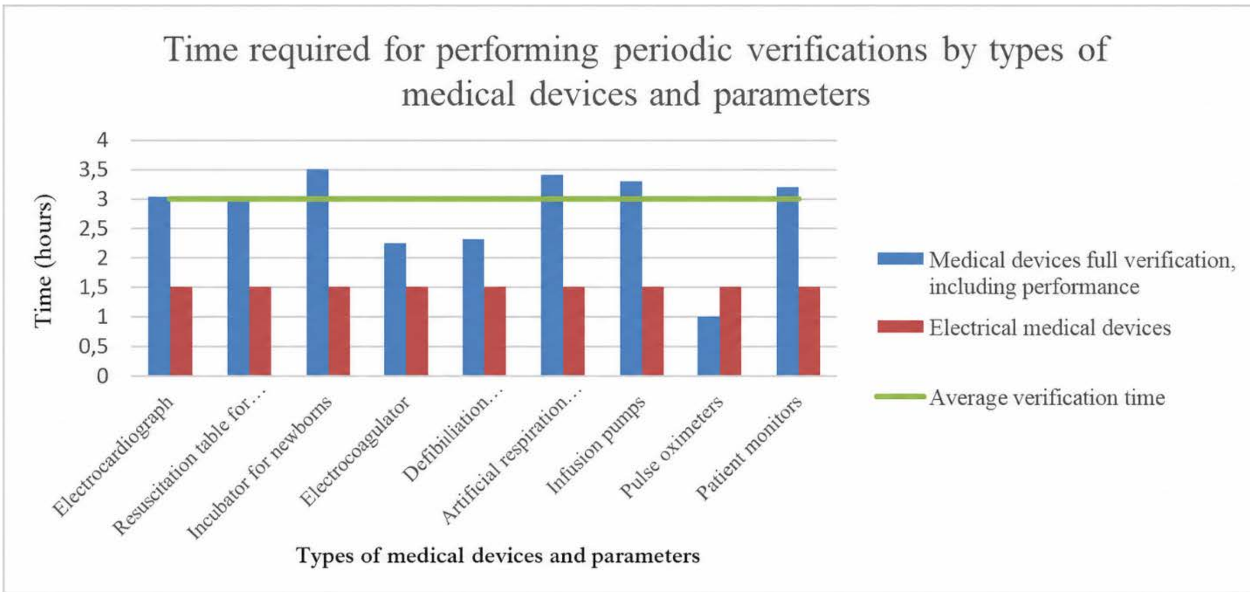

Figure 1. Time required for performing periodic verifications by types of medical devices and parameters.

Furthermore, based on the 9 types of medical devices selected for estimating the verification time, representing approximately one-third of the total number of device types in the Nomenclature, the total time required for the periodic verification of the entire inventory of medical devices was estimated.

Based on the calculated data, it was determined that the average time required for the periodic verification of a single medical device is approximately 3 hours (Figure 1). This represents a considerable amount of time, implying higher costs for medical institutions, given the hourly labor cost associated with periodic verification services.

At the same time, the measured average time of approximately 3 hours indicates a prolonged downtime of medical devices during the verification process.

4. Optimization of the time required for the periodic verification

In the context of the estimated time of approximately 3 hours for the periodic verification of medical devices, which was found to be quite high, it became necessary to review and reduce this duration, but not at the expense of confirming the conformity of device parameters. This required determining the minimum set of methods for periodic verification of general safety, electrical safety, and performance parameters.

To obtain a clearer overview of all medical devices subject to periodic verification, information was extracted from the Medical Devices Management Information System (SIMDM) regarding the units of medical devices available in medical institutions for the 9 selected types [7].

Based on the number of medical devices, the total time required for their periodic verification was estimated, as shown in Table 2.

Table 2

Estimation of the total time required for the periodic verification of medical devices according to the units extracted from SIMDM

Nr. d/o	**Name of the type of medical device**	**Quantity** (units)	**Time required for the periodic verification of a medical device** (hours)	**Time required for the periodic verification of all medical devices** (hours)
1.	Electrocardiographs	2678	3,05	8167
2.	Neonatal resuscitation tables	123	3,00	369
3.	Neonatal Incubators	202	3,50	707
4.	Electrosurgical units (electro coagulators)	376	2,25	846
5.	Defibrillation resuscitation devices	799	2,30	1837
6.	Artificial ventilation devices	1468	3,40	4991
7.	Infusion pumps	3091	3,30	10200
8.	Pulse oximeters	1618	1,00	1618
9.	Patient monitors	2226	3,20	7123
10.	Electrically powered medical devices	50000	1,50	75000

The calculation of the total time required for the periodic verification of all medical devices at the national level indicates that approximately 75,000 hours would be needed, equivalent to 3,125 days of 24 hours each. Considering standard 8-hour working days in accordance with the Labor Code of the Republic of Moldova, and the fact that a maximum of 2,000 working hours per year is estimated, the periodic verification of 9 types of medical devices at the national level (*including electrically powered devices*) would require 9,375 working days, that is, over 26 years.

It should also be noted that the lifespan of a medical device varies between 5 and 10 years, and only rarely reaches 15 years, during which the device must remain safe, effective, and of high quality. Therefore, the evaluation of performance and safety must be ensured within the device’s lifespan, which further emphasizes the need to optimize verification time.

For further analysis, the same type of medical device, the electrocardiograph, was used. Thus, the periodic verification of all electrocardiographs at the national level would require 8,167 hours, equivalent to more than 4.2 working years, a very long duration that necessitated identifying solutions to reduce this timeframe.

The viable solution consisted in reviewing the number of methods identified from standards and establishing a minimum set of methods for verifying general safety, electrical safety, and performance parameters.

In this regard, a working group within the Ministry of Health (*including representatives from the Ministry of Health, the Medicines and Medical Devices Agency, the Technical University of Moldova, the Conformity Assessment Bodies as well as biomedical engineers and other specialists*) aimed to establish the minimum set of methods for periodic verification [6].

Accordingly, the verification time was measured and estimated in such a way as to allow the confirmation of device conformity within its operational lifespan, thereby ensuring the provision of safe, effective, and high-quality medical devices within the healthcare system.

As a result, for the electrocardiograph, out of 12 performance parameter methods, 5 methods were selected.

Similarly, the minimum set of methods was established for each type of medical device, forming the basis for the development of specific procedures for periodic verification, which were subsequently approved by Order of the Ministry of Health. Thus, based on the established methods, a draft Order was developed for the approval of 29 specific procedures for the periodic verification of medical devices put into service and in use [2, 3].

Following the development of this draft, the Order of the Ministry of Health, Labor and Social Protection No. 30 of January 12, 2018 was approved, which endorses the specific procedures for periodic verification of medical devices, and was published in the Official Gazette on February 23, 2018.

With the approval of these procedures, it can be stated that a new system for periodic verification has been successfully created and implemented, representing an important step for the healthcare system of the Republic of Moldova. Currently, the regulatory framework is fully applicable, enabling periodic verification of medical devices at the national level.

5. Conclusions

The development of periodic verification methods for medical devices is based on the requirements set out in the standards applicable at the manufacturing stage.

The approval of specific procedures for periodic verification represented the final stage in the creation and implementation of the new system for periodic verification of medical devices in the Republic of Moldova.

With the approval of these procedures, it can be firmly stated that the new system for periodic verification of medical devices has been fully established, representing an essential and highly significant step for the national healthcare system. The conformity assessment of medical devices, through which compliance with safety and performance parameters is confirmed, contributes to increasing the safety and quality of medical services within the healthcare system.

Currently, the entire regulatory framework governing periodic verification of medical devices has been approved, and the mechanism is functional and applicable to all public healthcare institutions in the country.

All medical institutions in the country (approximately 400) are required to ensure the periodic verification of medical devices for 29 types, in accordance with the nomenclature and mechanism approved by Government Decision No. 966/2017 on the approval of the Regulation concerning the periodic verification of medical devices that have been put into service and are in use.

Based on the results obtained, the following recommendation can be formulated:

The new system for periodic conformity assessment of medical devices has been successfully implemented at the national level. At the same time, the list of medical devices subject to mandatory periodic verification may be expanded in order to cover a broader range of medical devices used within the healthcare system of the Republic of Moldova.

Acknowledgments The study was supported by the State Program LIFETECH "Innovations in Biomedical Engineering: Advanced Technologies and Applications for Data Acquisition, Processing and Analysis" No. 020404 at Technical University of Moldova.

Conflict of interest: I declare the absence of a conflict of interest.

References

1. Law No. 102 of 9 June 2017 on Medical Devices (2017). Official Gazette of the Republic of Moldova, No. 244–251, Art. 389.
2. *Draft Government Decision for the Approval of the Regulation on the Periodic Verification of Medical Devices* (2017). Public Consultations. Available at: https://www.cna.md/public/files/rapoarte_expertiza/Proiect-verif-dispoz-medic5877d.pdf (Accessed: 21 April 2026).
3. Draft Order Regarding the Approval of Specific Procedures for Periodic Verification of Medical Devices Put into Operation and in Use (2023). Available at: https://particip.gov.md/ro/document/stages/proiectul-de-ordin-cu-privire-la-aprobarea-procedurilor-specifice-de-verificare-periodica-a-dispozitivelor-medicale-puse-in-functiune-si-aflate-in-utilizare/4544 (Accessed: 21 April 2026).
4. Regulation (EU) 2017/745 of the European Parliament and of the Council of 5 April 2017 on Medical Devices, Amending Directive 2001/83/EC, Regulation (EC) No 178/2002 and Regulation (EC) No 1223/2009 and Repealing Council Directives 90/385/EEC and 93/42/EEC (Text with EEA Relevance) (2017). Official Journal of the European Union, L117, pp. 1–175.
5. Regulation (EU) 2017/746 of the European Parliament and of the Council of 5 April 2017 on In Vitro Diagnostic Medical Devices and Repealing Directive 98/79/EC and Commission Decision 2010/227/EU (Text with EEA Relevance) (2017). Official Journal of the European Union, L117, pp. 176–332.
6. *Ministry of Health of the Republic of Moldova* (2026). Available at: https://ms.gov.md/ (Accessed: 21 April 2026).
7. *Agency for Medicines and Medical Devices – Medical Devices Section* (2026). Available at: https://amdm.gov.md/ro (Accessed: 21 April 2026).
8. *Essential Principles of Safety and Performance of Medical Devices and IVD Medical Devices (Edition 2)* (2024). International Medical Device Regulators Forum (IMDRF). Available at: https://www.imdrf.org/sites/default/files/2024-04/IMDRF%20GRRP%20WG%20N47%20%28Edition%202%29.pdf (Accessed: 21 April 2026).
9. *Technical Guidance Series (TGS): Guidance on Test Method Validation for In Vitro Diagnostic Medical Devices* (2017). WHO Prequalification Diagnostic Assessment Programme, World Health Organization. Available at: https://iris.who.int/bitstream/handle/10665/258971/WHO-EMP-RHT-PQT-TGS4-2017.04-eng.pdf?sequence=1 (Accessed: 21 April 2026).
10. IEC 60601-1-8:2020. Medical Electrical Equipment—Part 1-8: General Requirements for Basic Safety and Essential Performance—Collateral Standard: General Requirements, Tests and Guidance for Alarm Systems in Medical Electrical Equipment (2020). Consolidated Version. ISBN 9782832287200. Available at: https://www.iso.org/standard/41986.html (Accessed: 21 April 2026).
11. SM SR EN 60601-1:2010. Aparate Electromedicale. Partea 1: Cerinţe Generale de Securitate de Bază şi Performanţe Esenţiale (2010).
12. SM EN 60601-2-25:2016. Aparate Electromedicale. Partea 2-25: Cerinţe Particulare de Securitate de Bază şi Performanţe Esenţiale pentru Electrocardiografie (2016).
13. SMV EN 60601-2-51:2010. Aparate Electromedicale. Partea 2-51: Cerinţe Particulare de Securitate, Inclusiv Performanţe Esenţiale, pentru Electrocardiografie cu Înregistrare şi Analizare Mono şi Multicanal (2010).
14. SM EN 60601-2-47:2015. Aparate Electromedicale. Partea 2-47: Cerinţe Particulare de Securitate, Inclusiv Performanţe Esenţiale, pentru Sisteme de Electrocardiografie Ambulatorie (2015).
15. Best Practice Guidance for the Submission of Technical Documentation under Annex II and III of Medical Device Regulation (EU) 2017/745 (2022). Team-NB. Available at: https://www.team-nb.org/wp-content/uploads/2022/10/Team-NB-PositionPaper-BPG-TechnicalDocEU-MDR-2017-745-V1-20221005.pdf (Accessed: 21 April 2026).

Citation: Gorceag, Gh., Lupan, O., Railean, S., Ababii, N. (2026). Optimization of the conformity assessment process for medical devices under conditions ensuring the evaluation of safety and performance parameters. *Journal of Engineering Science*. 2026, 33 (2), pp. 61-70. https://doi.org/10.52326/jes.utm.2026.33(2).05.

Publisher's Note: JES stays neutral with regard to jurisdictional claims in published maps and institutional affiliations.

Copyright:© 2026 by the authors. Submitted for possible open access publication under the terms and conditions of the Creative Commons Attribution (CC BY) license (https://creativecommons.org/licenses/by/4.0/).

Submission of manuscripts: jes@meridian.utm.md

Journal of Engineering Science *Vol. XXXIII, no. 2 (2026), pp. 71 - 84*
Fascicle *Electronics and Computer Science* *ISSN 2587-3474*
Topic *Computers and Information Technology* *eISSN 2587-3482*

https://doi.org/10.52326/jes.utm.2026.33(2).06
UDC 621.396.663:004.056:003.26

LIGHTWEIGHT RFID MUTUAL AUTHENTICATION PROVIDING UNTRACEABILITY

Rodica Bulai *, ORCID: 0009-0003-1898-2575

Technical University of Moldova, 168 Stefan cel Mare blvd., MD2004, Chisinau, Republic of Moldova
* Corresponding author: Rodica Bulai, *rodica.bulai@ati.utm.md*

Received: 04. 16. 2026
Accepted: 05. 27. 2026

Abstract. The widespread deployment of low-cost RFID tags raises significant security and privacy concerns, since tags with limited computational resources cannot support strong cryptographic primitives, while backward and forward untraceability have become essential requirements for modern RFID protocols. We hypothesize that a lightweight authentication scheme based on pseudo-random number generators (PRNGs) and short-term session keys can provide a broad spectrum of security properties without relying on costly primitives. The purpose of this study is to design and analyze such a mutual authentication protocol for RFID systems. Two variants of the protocol are constructed - one optimized for limited tag computational power and one minimizing data transmission - using one-time pad encryption keyed by PRNG output, timestamps for replay-attack protection, and a refreshable forward/backward key sub-chain. The resulting protocol withstands replay, denial-of-service, tag and server impersonation attacks, and guarantees information privacy, location privacy, and both backward and forward untraceability. We conclude that even weak primitives such as linear or non-linear feedback shift registers can be safely used as the underlying PRNG, which makes the protocol particularly well suited to low-cost RFID deployments.

Keywords: *attack, traceability, computer security, cryptography, privacy, protocol, RFID system.*

Rezumat. Utilizarea pe scară largă a etichetelor RFID de cost redus generează probleme semnificative de securitate și confidențialitate, deoarece etichetele cu resurse de calcul limitate nu pot susține semnale criptografice puternice, iar imposibilitatea de urmărire a devenit o cerință esențială pentru protocoalele RFID moderne. A fost formulată ipoteza, că o schemă de autentificare de tip ușor, bazată pe generatoare de numere pseudo-aleatorii (PRNG) și chei de sesiune pe termen scurt poate oferi un spectru larg de proprietăți de securitate fără a recurge la primitive costisitoare. Scopul lucrării a constat în proiectarea și analiza unui astfel de protocol de autentificare mutuală pentru sisteme RFID. Sunt construite două variante ale protocolului - una optimizată pentru etichete cu putere de calcul redusă, iar cealaltă pentru minimizarea volumului de date transmise - folosind cifrare cu cheie unică (one-time pad) generată de PRNG, marcaje de timp pentru protecția împotriva atacurilor de tip replay și un lanț reînnoibil de sub-chei înainte/înapoi. Protocolul rezultat rezistă la atacuri replay, de refuz al serviciului, de impersonare a etichetei și a serverului, asigură confidențialitatea informației și a localizării, precum și imposibilitatea de urmărire înainte și

înapoi. S-a constatat că registrele cu deplasare cu reacție liniară sau neliniară pot fi utilizate în siguranță ca funcție PRNG subiacentă, ceea ce face protocolul deosebit de convenabil pentru implementări RFID de cost redus.

Cuvinte cheie: *atac, trasabilitate, securitate informatică, criptografie, confidențialitate, protocol, sistem RFID.*

1. Introduction

Radio Frequency Identification (or RFID for short) has developed at a fast pace, as different security properties emerged from the need to defend against a wave of attacks on deployed protocols. Replying to a reader query with the identifier of the tag began to be viewed as an invasion of privacy due to the possibility of obtaining sensitive information through back-door channels, and was soon replaced with a masking of some sort of the reply. Location traceability became a problem allowing unauthorized readers to track persons based on replies to bogus queries. As in most security protocols, replay attacks and denial of service attacks were considered as threats as soon as the complexity of the protocol increased and the adversary model was granted more power.

Many identification and authentication protocols for RFID systems have been proposed so far. One distinction between them is usually made by the computational power of the tag. Tags with good computational capabilities can implement protocols based on strong cryptographic primitives, such as public-key schemes built on elliptic curve cryptography [1], [2], [3] or symmetric schemes based on AES [4]. More recent constructions rely on physically unclonable functions (PUFs) [5], [6], [7], [8] and have been analyzed in connection with formal privacy models [9]; a broader classification of RFID authentication approaches is given in [10]. Such designs, however, can be too costly to be adopted in most retailer operations which are envisioned as major applications of the RFID technology. A large amount of research has therefore been dedicated to designing RFID authentication protocols based on hash functions and hash function chains [11], [12], [13], as well as on pseudo-random functions and random number generators [14], [15], [16].

Lightweight and ultra-lightweight authentication protocols for RFID systems only require to perform primitive operations such as random number generation, arithmetic bit-wise operations, cyclic redundancy code checksum, or even light hash or pseudo-random functions. Representative ultra-lightweight constructions include the EMAP, M2AP and Gossamer protocols [17], [18], [19], as well as minimalist and human-assisted approaches [20], [21], [22]. More recent proposals target specific application domains such as healthcare, the Internet of Vehicles and mobile commerce [23], [24], [25], [26], or build on contemporary block-cipher primitives [27]. Critical analyses of the security and traceability properties of such schemes are provided in [28], [29], [30], [31]. There is a widespread view that the lightweight and ultra-lightweight authentication protocols will be the best candidate technology for securing the future low-cost RFID systems.

In the rest of the paper we shall focus on lightweight RFID systems. Most low-cost tags have no protection of memory, allowing a strong adversary to read the entire state of the tag at some point, effectively cloning it (given the opportunity). As such, backward traceability, or the ability of an adversary to deduce past states of the tag based on the current state, became an issue, and protocols were designed to resist such attacks by updating the tag's internal state in a manner reproducible by the server and synchronizing upon a successful authentication. One of the most recent security concerns was formally introduced and studied in [14], namely forward traceability. Intuitively, one would desire an adversary to be unable to deduce future states of the tag based on the present one. Although it is unclear whether this concern was raised by the need for tags to securely change hands (perfect ownership transfer), forward untraceability and perfect ownership transfer were introduced together in [14], along with a protocol that provides them under an assumption.

Security models have been proposed for powerful RFID systems that can classify the level of privacy obtained by them [32], [33]. Recent extensions of these models address adversaries with temporary state disclosure capabilities [34]. Unfortunately, such formal models are missing for (ultra-) lightweight RFID systems. This is why many papers propose lightweight RFID schemes for which security and privacy issues are studied ad hoc, as in [35], [36], [37]. A structured and rather detailed discussion on security concerns in lightweight RFID protocols can be found in [15].

Structure of the paper This paper is structured into six sections. The present section is an introductory one, while the following overviews some related work and draws up our contributions. Two variants of the protocol are described in the third section and their privacy and security properties are inferred in the fourth. Prospective applications for the protocol are analyzed in the fifth section. Conclusions are drawn in the final section..

2. Contributions and Related Work

In this paper we propose a lightweight mutual authentication protocol for RFID, based on a generic pseudo-random number generator (PRNG) and short-term (or rather session) keys. The protocol we propose enjoys a large spectrum of security properties, ranging from protection against low-level attacks (replay attacks and DoS) to attacks mountable by strong adversaries (backward and forward traceability), under a set of assumptions. Another characteristic of the protocol is that it tries to alleviate the computational requirements imposed on the tag as much as possible, shifting most responsibilities to the server.

Moreover, the generic PRNG used in our protocol can be instantiated in various ways, depending on the computational capabilities of the tag and the probabilistic security a deployer desires. For instance, one could use lightweight hash functions, block ciphers, linear feedback shift registers (LFSR) or non-linear feedback shift registers (NLFSR), all resulting in the same level of security considering ideal primitives.

Instead of relying on complex cryptographic primitives, most of the messages exchanged in the protocol we propose are the result of the application of a one-time pad encryption, with keying material provided by a generic pseudo-random number generator. A similar approach was suggested by [38], where a pseudo-random number generator was used together with a shared key for sequence synchronization. The protocol did not take into consideration forward traceability concerns and the data on the tag was static, allowing an adversary that would recover the shared key from the tag to monitor all future communication.

Location privacy and backward untraceability are a direct consequence of the use of a forward key chain for encrypting communication from the tag to the server. Similar approaches were suggested in [13], [14]. Unlike similar approaches, which relied on the server being able to recognize the key chain used to encrypt data and identify the tag, we chose to use the links in our forward key chain (which are basically chained outputs of a pseudo-random number generator) for encryption only, using a temporary or session key to identify the tag, leading to faster queries and eliminating the need for the server to keep a copy of the forward key chain, reducing storage requirements. The session key is refreshed on each successful authentication to prevent forward traceability.

In order to prevent forward traceability, our protocol used a similar technique to that presented in [14], which adopted a backward key chain, but instead of precomputing the whole chain before deployment, small fragments of a chain (or rather sub-chains) are used and refreshed on each successful authentication, along with the tag identifier, the seed for the pseudo-random number generator and the session key. This refreshing of the tag's state represents a probabilistic evolution, a complementary operation to updating said state in a deterministic way. Similar techniques were used in [14], [15], [39]. Communication from the server to the tag is encrypted using links of the backward key sub-chain, recognizable by the tag and the old session key.

In order to prevent desynchronization, our protocol retains, for each tag, both the values known to be on the tag on the last successful authentication and the new values generated to prevent forward traceability. This doubling up of the authentication data is a common feature for RFID protocols, best represented in the work of [12], [14], [15], [40].

Replay attacks are thwarted by the introduction of timestamps. While other protocols [14], [15] suggest the use of nonces, in an attempt to unburden the tag from any time-consuming computations, we chose to use a timestamp generated by the reader and that will be later checked by the server.

In fact, many features of the protocol were motivated by the desire to minimize the tag's required capabilities. Instead of providing a fresh seed that would be later used by the tag to extract various new elements, all elements are computed on the server and provided to the tag. Similarly, a single pseudo-random function is assumed to be computable. Note that, given a proper relaxation of the notion of pseudo-random number generator or pseudo-random function, one could deploy instances of the protocol described in this paper by using non-linear feedback shift registers (or NLFSRs for short) or even linear feedback shift registers (LFSRs). Although many authors advise against LFSRs due to the ease of their analysis, considering that the seed is constantly being refreshed and the outputs are used exclusively as keying material, it is the authors' belief that deploying an instance based on LFSRs might be considered appropriately secure. Nevertheless, the model does allow for stronger pseudo-random functions to be deployed, and the choice of a particular function should be carefully made to comply with required security parameters. In a sense, this paper introduces a family of identification protocols, instances of which might be suitable for a wide range of applications.

The use of NLFSRs was considered for RFID as far as 2003 [41], and pseudo-random number generators were used as a primary security mechanism for many protocols, including [16], [38], [42], although this frequently lead to weaknesses such as those exposed in [43]. For a more detailed discussion on RFID protocols in general, the reader is referred to [44].

3. Using PRNGs and Short-term Keys for RFID

The protocol we propose comes in two variants, the former requiring less computational power from the tag, while the latter minimizes data transmission.

Notation and nomenclature Throughout the remainder of this section, some terms and notation conventions will be used. A *chain* refers to a sequence generated by a PRNG, while a *sub-chain* is used to denote a continuous part of a chain of significantly reduced dimension.

Link is used to denote a single element in either a chain or sub-chain. Conventional notations that we use are enumerated below:

- $x \ll k$ denotes the circular left shift of the bit string x by k positions;
- $x \oplus y$ is used to denote the bitwise exclusive or of the bit strings x and y;
- $f^0(x)$ is the identity function;
- $f^{k+1}(x) = f(f^k(x))$, for all $k \geqslant 0$.

3.1. A Protocol for Limited Tag Computational Power

The description of our protocol follows three steps: basic assumptions, initialization, and the authentication protocol.

Assumptions. In the construction of our protocol, we assume the following:

- The server and the trusted readers communicate through a secure channel;
- The reader and the tag communicate via an unsafe channel (wireless, radio frequency channel) that can suffer from eavesdropping or interference from a malicious third party;
- An intruder could attempt to impersonate the tag in order to misdirect an honest reader;
- An intruder could attempt to impersonate a reader to obtain information from a tag;
- An intruder could attempt to impersonate the server while impersonating a reader by responding with a message constructed to resemble a valid reply from the server;
- An intercept-then-invalidate attack is highly unlikely to be successful;
- A strong adversary could obtain the state of a tag at a given moment.

The enumeration above describes the setting taken into consideration when designing the protocol below. To summarize, the third party in the communication (the server) is considered trusted by default and in turn will only reply to trusted readers, reducing the problem of the authentication process to the reader-tag communication.

Initialization. Upon deployment, one should assume that the server has access to a cryptographic hash function (denoted from here on out by h) and a pseudo-random number generator (denoted by f) which would require a seed of truly random bits. This pseudo-random number generator could also be a linear or a non-linear feedback shift register considering an appropriate relaxation of the notion.

The important aspect regarding f is that given a random seed it can produce keying material for a one-time pad and that its output is seemingly random. The function *f* is also expected to be easily computable by each tag.

The server maintains a database of tag information, some of which would be present on the tag itself and could be recognized upon receiving a relayed query from the reader. For each tag, the server stores the following values:

- Two identification tokens denoted ID_{old} and by ID_{new};
- Two tag identifiers denoted $TID_{old} = h(ID_{old})$ and $TID_{new} = h(ID_{new})$;
- Two session keys denoted SK_{old} and SK_{new};
- Two backward key sub-chains, comprised of the following links: $f^i(BKL_{old})$ and $f^i(BKL_{new})$ for all $0 \leqslant i \leqslant 4$;
- Some data relevant to the tag, denoted *Data*, which does not play any role in the authentication process.

A tag is expected to store the following data:

- A tag identifier denoted *TID*;
- A session key denoted *SK*;
- A forward key link denoted *FKL* (which constitutes the seed for the function *f* to generate keying material);
- A terminal backward key link denoted *TBKL*.

The correlation between tag and server data is enforced by the following process. When registering a tag, the vendor generates *ID*, computes $TID = h(ID)$, chooses at random a session key *SK* and stores the last two on the tag and all of them in the database in ID_{new}, TID_{new} and SK_{new} respectively. It then randomly chooses a backward key link *BKL* and stores it in BKL_{new} iterates the function *f* four times, storing the resulting values in their respective place in the new backward key sub-chain. The fifth application of the f function generates a value to be stored on the tag in the *TBKL* variable. The *FKL* variable on the tag is also initialized with a random value.

Authentication. The following steps describe the communication process in this protocol. For simplicity, denote the tag by T, the reader by R and the server by S.

1. R queries T by transmitting a timestamp τ.

2. T responds by transmitting to R the message $M_1=SK \oplus f(FKL)$, $M_2=f(f(FKL) \oplus \tau) \oplus TID$

At the end of this step, T updates *FKL* to $f^2(FKL)$.

3. R appends τ to the message received from the tag and forwards it to S via a secure channel.

4. Upon receiving the above message, S performs the following actions:

(a) Check freshness of the message by comparing τ to local time.

(b) For some row, extract $\alpha_{new} = SK_{new} \oplus M_1$ and $\beta_{new} = f(\alpha_{new} \oplus \tau) \oplus M_2$

If $\beta_{new} = TID_{new}$, then move the data from the new columns to the old ones and continue to sub-step (c). Otherwise, extract $\alpha_{old} = SK_{old} \oplus M_1$ and $\beta_{old} = f(\alpha_{old} \oplus \tau) \oplus M_2$

If $\beta_{old} = TID_{old}$, then continue to sub-step (c). Otherwise, if there are rows remaining, perform the current sub-step on the following row. If no more rows exist, halt and send R an error message.

(c) T being identified (by the values marked by either new or old), S does the following

- Chooses a random *ID'* and stores it in ID_{new}
- Computes $TID' = h(ID')$ and stores it in TID_{new}
- Chooses a random session key *SK'* and stores it in SK_{new}
- Chooses a random forward key link *FKL'*
- Chooses a random backward key link *BKL'*, computes $f^i(BKL')$ for all $0 \leqslant i \leqslant 4$, and stores the resulting values in the corresponding columns of the backward key sub-chain marked by new
- Computes the messages $M_3 = SK_{old} \oplus BKL_{old}$, $M_4 = f(BKL_{old}) \oplus TID'$, $M_5 = f^2(BKL_{old}) \oplus SK'$, $M_6 = f^3(BKL_{old}) \oplus FKL'$, $M_7 = f^4(BKL_{old}) \oplus f^5(BKL')$
- Sends M_3, M_4, M_5, M_6, M_7, *Data* to R

5. Upon receiving the message from S, R extracts *Data* and forwards M_3, M_4, M_5, M_6, and M_7 to T.

6. Upon receiving the message from R, T extracts $\gamma = SK \oplus M_3$ and computes $f^5(\gamma)$. If $f^5(\gamma) \neq TBKL$, the tag halts. Otherwise, T refreshes its state as follows:

- Stores $f(\gamma) \oplus M_4$ in the variable *TID*.
- Stores $f^2(\gamma) \oplus M_5$ in the variable *SK*.

- Stores $f^3(\gamma) \oplus M_6$ in the variable *FKL*.
- Stores $f^4(\gamma) \oplus M_7$ in the variable *TBKL*.

This concludes the description of the proposed protocol.

3.2. Minimizing Data Transmission

Slightly raising the computational capabilities of the tag yields a modified protocol that minimizes the number of messages exchanged between parties. For brevity, we choose to enumerate only the changes that have to be made to the protocol in order to minimize data transmission.

1. In the initialization process, the two backward key sub-chains stored in the server's database are comprised of the links $f^i(BKL_{old})$ and $f^i(BKL_{new})$ for $0 \leqslant i \leqslant 2$, while the tag will hold $TBKL = f^3(BKL_{new})$

2. In the authentication process:

(a) Sub-step (c) of the fourth step is replaced by:

- Choose a random backward key link BKL', compute $f^i(BKL')$ for all $0 \leqslant i \leqslant 2$, and store the resulting values in the corresponding columns of the backward key sub-chain marked by new
- Choose a random *ID* and store it in ID_{new}
- Compute $TID' = h(ID')$ and store it in TID_{new}
- Compute $SK' = f(f^3(BKL') << 1)$ and store it in SK_{new}
- Compute M_3, M_4 and M_5 by $M_3 = SK_{old} \oplus BKL_{old}$, $M_4 = f(BKL_{old}) \oplus TID'$, $M_5 = f^2(BKL_{old}) \oplus f^3(BKL')$
- Send *M3*, *M4*, *M5*, *Data* to R

(b) The fifth step becomes: Upon receiving the message from S, R extracts *Data* and forwards M_3, M_4 and M_5 to T.

(c) The final step becomes: Upon receiving the message from R, T extracts $\gamma = SK \oplus M_3$ and computes $f^3(\gamma)$. If $f^3(\gamma) \neq TBKL$, the tag halts. Otherwise, T refreshes its state as follows:

- Stores $f(\gamma) \oplus M_4$ in the variable *TID*.
- Stores $f^2(\gamma) \oplus M_5$ in the variable *TBKL*.
- Stores $f(TBKL << 1)$ in the variable *SK*.
- Stores $f(SK << 1)$ in the variable *TBKL*.

Throughout this description, the circular shifting to the left by one position can be replaced with any simple combination of shifting, splitting and recombination that the tag and the server agree upon and can reproduce separately. The first version of the protocol requires less computations to be done by the tag at the cost of two extra messages on the confirmation step, while at the same time providing strong randomness to the refreshed data. In turn, the second version reduces the number of messages on the confirmation step at the cost of the tag having to perform an extra operation (or set of operations) to refresh its internal state. Depending on the implementation, the fact that three separate variables on the tag are derived from the same source of supposedly truly random bits in a deterministic way might expose the second version to some attacks.

4. Security and Privacy

We discuss in this section the basic security properties our protocol enjoys.

Information privacy. Typically, a tag would respond to a query by providing an identifier that would further be used by an authorized reader to extract more information from the database. Although this strategy might be suitable for most situations, when dealing with sensitive data it poses some concerns. For instance, an unauthorized reader might make use of some back-channel or some other source of information to obtain data on the tag bearer. The protocol described in the previous section avoids this by encrypting the identifier with a session key shared with the server before replying to the reader.

Location privacy. Another possible threat posed to a tag bearer is unauthorized location tracking. If, somehow, an unauthorized reader can correlate responses to queries to some tag identity, then it can successfully track said tag without having to access server data. This type of attack is thwarted in our protocol by the use of a pseudorandom number generator as a source of keying material for one-time pad encryption of messages exchanged between parties, at the same time allowing the server to recover the seed of the sequence due to the fact that it possesses the session key.

Tag impersonation. An intruder might try to impersonate a tag in a communication with a reader. However, a weak intruder has a negligible chance of issuing a valid response to a query without knowing the current session key. This does not change the fact that a strong intruder might be able to clone a tag by completely mimicking its internal state.

Replay attack. The tag has no way of checking the freshness of the timestamp τ issued by the reader performing the query (maintaining current time is somewhat of a stretch for RFID tag technology and practically infeasible for tags without a battery). However, the timestamp does reach the server and will be subsequently checked (initially upon retrieval) and verified for tampering (by the combination of the first and second part of the relayed message), protecting the server from replay attacks.

DoS attack. A denial of service attack in this scenario would aim to permanently desynchronize the server and the tag, by changing the internal state of the tag to be unrecognizable by the server or by tampering with the terminal backward key link in order to make the server unrecognizable for the tag.

Due to the unlikeliness of the success of an intercept-then-invalidate attack on the confirmation step of the authentication process and considering the assumption that the channel between the reader and the server is secure, an adversary could mount such an attack by gaining knowledge of both the backward key sub-chain leading to the terminal backward key link on the tag and the current session key. Supposing the session key and the terminal backward key link could be obtained, the backward key sub-chain itself must be computed by inverting the pseudo-random function used for generating it. The computational hardness of inverting said function renders this attack impractical.

Even so, an intruder capable of cloning a tag can desynchronize the authentic one successfully by either sequential impersonations leading to database updates or a single successful authentication, followed by a server impersonation due to the knowledge of the backward key subchain inferred from the reply.

Backward traceability. Due to the fact that on every successful authentication the tag's internal state is completely refreshed, one would expect to be able to trace a tag backward at most between two successful authentications. Even supposing the entire internal state is recovered, tracing the tag's action backwards is a challenging attack. Knowledge of the current seed for the pseudo-random function could represent an advantage, especially in the case of linear and non-linear feedback shift registers, which are periodical. An attacker could cycle through an entire period to discover past values of the root and trace back the failed transactions since the last authentication. This data should not be considered relevant, as failed transactions are most likely results of the actions of an intruder, rendering the gained knowledge useless.

Forward traceability. Supposing an intruder manages to recover the internal state of a tag and instead of impersonating it to desynchronize it from the database decides to track it. This strategy is feasible, as long as the intruder does not miss a single successful authentication, which would result in a complete refresh of the tag's internal data. If he observers the entire process, he can deduce the new state of the tag by following the protocol. Missing the final step of a successful authentication leads to a blind update of the tag's data from the intruder's perspective.

Server impersonation. Suppose an intruder gained access to the internal state of a tag, it could attempt to impersonate the server in order to desynchronize it permanently. One of the attacks is described in a previous paragraph, the other is sketched below.

For linear and non-linear feedback shift registers, and intruder could take advantage of the periodic nature of the function, computing forward values until reaching the starting point again. Doing this for the TBKL variable and already knowing the tag's state, the intruder would basically possess enough information to impersonate the server and possibly desynchronize the tag. A costly operation, making this attack highly unlikely to succeed. Also note that an attacker would have a small window of opportunity for deploying this attack, namely before a successful authentication, in which case the internal state of the tag would be completely refreshed.

5. Prospects

This section introduces some prospective applications of our general protocol, considering different instantiations of the pseudo-random number generator used as a cryptographic primitive. As previously pointed out, this generic notion can take on multiple interpretations as a result of various interpretations. While strong security might require the use of block ciphers or hash functions to simulate this randomness, weaker security demands make room for a wider array of cryptographic primitives, including linear and non-linear feedback shift registers.

These are of particular interest to RFID technology due to their efficient hardware implementation and seemingly simple computation. In light of these arguments, the authors believe a discussion on the advantages and disadvantages of each approach is in order. From now on, two categories will be considered - the strong primitives and the weak primitives, depending on the computational effort an adversary has to put in to invert the underlying function of the pseudo-random number generator.

An underlying function for a PRNG will be considered *a strong primitive* if it requires the same amount of effort for each step backward. That is to say, an adversary attempting to invert the underlying function could not gain a consistent computational advantage by trying to guess a value further back in the sequence. Intuitively, this would imply the presence of some probabilistic choice one would have to make at each backward step.

Alternatively, an underlying function for a PRNG will be considered *a weak primitive* if a single backward step would require virtually as much effort as any fixed number of steps backward. That is to say, an adversary attempting to trace the PRNG backwards would gain a significant advantage by trying to guess values further back in the sequence. Intuitively, this would imply that the underlying function is injective.

5.1. Strong primitives

Strong primitives are best represented by hash functions. The fact that they map a given set to a significantly smaller one makes backward traceability infeasible even in the absence of a refresh from the server. Their impact on an adversary possessing both the session key and the terminal backward key link trying to impersonate the server is limited. However, an adversary in possession of said secret material can easily recover the whole state of the tag effectively cloning it, exposing two other available DoS attacks described in the previous section, making this advantage arguably unimportant.

Implications on backward traceability. Even considering an adversary possessing an oracle for the inverse of a hash function, said adversary would still be faced with the problem of choosing the appropriate former value used as the seed out of the set of values in the inverse. Given a function that hashes inputs of $n + t$ bits to outputs of n bits, an adversary possessing an oracle for the inverse would have to make a choice between $O(2^t)$ values given a somewhat uniformly distributed hash function. One problem with using hash functions is that a single application would not yield such results, as the outputs would have to be extended to $n + t$ bits to be further used either as keying material or as the seed for the following values in the forward key chain. Instead, $1 + \left\lceil \frac{t}{n} \right\rceil$ consecutive applications could be combined in a deterministic way, reproducible by the server, to output a sequence of appropriate length. This, in turn, would complicate things further for an adversary trying to recover past states of the tag, consolidating backward untraceability.

Impact on performance. Having to perform multiple iterations of the same function for a single forward step in the key chain has a massive performance impact on the tag. The overall authentication scheme becomes slower and harder to implement on tags with limited resources. A reasonable alternative for more powerful tags, the authors would however advise against such deployments, as a discussion on backward traceability in the previous section argued that any data recoverable would be limited to the failed communications spanning to the last successful authentication, which by themselves could be considered irrelevant and possibly compromised data, as failed authentications are a strong indicator of outside interference.

5.2. Weak primitives

Weak primitives are injective by contrast to strong primitives. Considering ideal primitives, trying to guess the previous key link based on the current one is as hard as trying to guess any prefix of the current link in the chain. Weak primitives that could successfully be deployed as underlying functions for the PRNG in our protocol include block ciphers, LFSRs and NLFSRs. Arguably, these primitives could be used in the construction of a hash function, yielding strong primitives. The authors, however, advise against this, as no significant advantage would be gained.

Implications on backward traceability. As previously sketched during the discussion on backward traceability from the previous section, given a weak primitive, an adversary could successfully recreate the past states of the tag spanning to the last successful authentication. Note that block ciphers are also periodical due to the fact that they are bijective and that their domain is the same as their co-domain, so the same argument works for block ciphers as well.

Impact on performance. The fact that a single iteration of the underlying function yields the following number in the PRNGs sequence is a great improvement to the previous model with respect to performance, as all computations are greatly reduced when generating keying material and seeds for future iterations of the PRNG. It is the authors' opinion that our protocol encourages the deployment of weak primitives.

6. Conclusions

Backward and forward untraceability are fundamental security properties for RFID protocols, given that most low-cost tags have no way of securing data stored on them, allowing a strong adversary to read their entire internal state.

The first protocol to provide backward and forward untraceability, along with a mechanism for perfect ownership transfer and other desirable security properties, is the one in [14]. It is based on the OSK protocol [13], which at the time performed rather well, allowing a maximum number of failed authentications that were backward untraceable based on a precomputed forward key chain. The idea in [14] is to refresh the tag data through some form of shared randomness involved in every successful transaction. To avoid desynchronization, data is doubled up in the backend database by retaining both newly generated values and the last known values to be held by the tag. Also, to thwart server impersonation attempts, a backward key chain is used to authenticate the server to the tag in the confirmation step, rendering a mutual authentication protocol. Three pseudo-random functions are considered, and implementations are suggested based on block ciphers rather than hash functions to allow cheaper deployments on RFID tags.

Most influential to our paper was the work in [15], which, besides having a properly structured identification of possible threats (concerning both privacy and security) addressed some performance issues regarding [14] and other prominent protocols at the time [12], [16], [38], [40]. The protocol in [15] assures both information and location privacy, while at the same time covering some of the attacks a weak adversary might perform (tag impersonation, replay attacks, denial of service) and stronger attacks, which assume an adversary capable of cloning tags (backward and forward traceability and server impersonation). The security properties are obtained under some assumptions much like the ones we made regarding the environment in which our protocol should be deployed.

We provided two variants of a protocol for RFID mutual authentication using generic PRNGs. Both variants enjoy desirable security properties such as resilience against replay and DoS attacks, server and tag impersonation and backward and forward traceability. The major privacy concerns in RFID (information and location privacy) are also covered. As to the two variants of the protocol, the former is designed to work with tags having a limited computational power, while the latter would take advantage of the increased computational power of a tag to minimize data transmission.

The generic PRNG can be instantiated in various ways, all classifiable as either weak or strong primitives. Most representative for strong primitives are hash functions, while block ciphers, LFSRs and NLFSRs are considered equally weak in our analysis. Furthermore, based on our findings, we can infer that our protocol encourages the use of weak primitives, as stronger ones offer no significant advantage.

Acknowledgments: The author is grateful to Prof. Ferucio Laurentiu Ţiplea and Prof. Ion Bolun for fruitful discussions on the security and privacy of RFID authentication protocols, which have shaped the ideas presented in this work.

Conflicts of Interest: The authors declare no conflict of interest.

References

1. Batina L, Guajardo J, Kerins T, et al (2006) An elliptic curve processor suitable for RFID tags. https://www.researchgate.net/publication/220337092_An_elliptic_curve_processor_suitable_for_RFID-tags. Accessed 16 April 2026
2. Batina L, Guajardo J, Kerins T, et al (2007) Public-key cryptography for RFID-tags. In: Proceedings of the Fifth IEEE International Conference on Pervasive Computing and Communications Workshops. pp 217–222
3. Lee YK, Sakiyama K, Batina L, Verbauwhede I (2008) Elliptic-curve-based security processor for RFID. IEEE Trans Comput 57:1514–1527. https://doi.org/10.1109/TC.2008.148
4. Feldhofer M, Dominikus S, Wolkerstorfer J (2004) Strong authentication for RFID systems using the AES algorithm. In: Joye M, Quisquater J-J (eds) Cryptographic Hardware and Embedded Systems – CHES. Lecture Notes in Computer Science, vol 3156. Springer, pp 357–370
5. Ţiplea FL, Andriesei C, Hristea C (2020) Security and privacy of PUF-based RFID systems. In: Cryptography - Recent Advances and Future Developments. IntechOpen, London, pp 1–23. https://doi.org/10.5772/intechopen.94018
6. Ţiplea FL, Hristea C (2021) Practically efficient RFID scheme with constant-time identification. In: Proceedings of the 18th International Conference on Security and Cryptography (SECRYPT), Vol. 1. SciTePress, pp 495–506. https://doi.org/10.5220/0010544804950506
7. Ţiplea FL, Hristea C (2021) PUF protected variables: a solution to RFID security and privacy under corruption with temporary state disclosure. IEEE Trans Inf Forensics Secur 16:999–1013. https://doi.org/10.1109/TIFS.2020.3027147
8. Hristea C, Ţiplea FL (2020) Privacy of stateful RFID systems with constant tag identifiers. IEEE Trans Inf Forensics Secur 15:1920–1934. https://doi.org/10.1109/TIFS.2019.2953398
9. Ţiplea FL (2022) Narrow privacy and desynchronization in Vaudenay's RFID model. Int J Inf Secur 21:563–575. https://doi.org/10.1007/s10207-021-00569-0
10. Pantelić G, Bojanić S, Tomašević V (2009) Authentication protocols in RFID systems. In: Zhang Y, Kitsos P (eds) Security in RFID and Sensor Networks. Auerbach Publications, pp 99–120
11. Avoine G, Oechslin P (2005) A scalable and provably secure hash-based RFID protocol. In: Third IEEE International Conference on Pervasive Computing and Communications Workshops. pp 110–114
12. Henrici D, Muller P (2004) Hash-based enhancement of location privacy for radio-frequency identification devices using varying identifiers. In: Proceedings of the Second IEEE Annual Conference on Pervasive Computing and Communications Workshops. pp 149–153
13. Ohkubo M, Suzuki K, Kinoshita S (2003) Cryptographic approach to "privacy-friendly" tags. In: RFID Privacy Workshop.https://www.researchgate.net/publication/2926255_Cryptographic_Approach_to_Privacy-Friendly_Tags. Accessed 16 April 2026
14. Lim CH, Kwon T (2006) Strong and robust RFID authentication enabling perfect ownership transfer. In: Ning P, Qing S, Li N (eds) Information and Communications Security. Lecture Notes in Computer Science, vol 4307. Springer, pp 1–20
15. Song B, Mitchell CJ (2008) RFID authentication protocol for low-cost tags. In: Proceedings of the First ACM Conference on Wireless Network Security. pp 140–147
16. Weis SA, Sarma SE, Rivest RL, Engels DW (2004) Security and privacy aspects of low-cost radio frequency identification systems. In: Hutter D, Müller G, Stephan W, Ullmann M (eds) Security in Pervasive Computing. Lecture Notes in Computer Science, vol 2802. Springer, pp 201–212
17. Peris-Lopez P, Hernandez-Castro JC, Estevez-Tapiador JM, Ribagorda A (2006) EMAP: an efficient mutual-authentication protocol for low-cost RFID tags. In: Meersman R, Tari Z, Herrero P (eds) On the Move to Meaningful Internet Systems. Lecture Notes in Computer Science, vol 4277. Springer, pp 352–361
18. Peris-Lopez P, Hernandez-Castro JC, Estevez-Tapiador JM, Ribagorda A (2006) M2AP: a minimalist mutual-authentication protocol for low-cost RFID tags. In: Ma J, Jin H, Yang LT, Tsai JJ-P (eds) Ubiquitous Intelligence and Computing. Lecture Notes in Computer Science, vol 4159. Springer, pp 912–923
19. Peris-Lopez P, Hernandez-Castro JC, Estevez-Tapiador JM, Ribagorda A (2009) Advances in ultralightweight cryptography for low-cost RFID tags: Gossamer protocol. In: Chung K-I, Sohn K, Yung M (eds) Information Security Applications. Springer, pp 56–68
20. Juels A (2005) Minimalist cryptography for low-cost RFID tags (extended abstract). In: Blundo C, Cimato S (eds) Security in Communication Networks. Lecture Notes in Computer Science, vol 3352. Springer, pp 149–164

21. Juels A, Weis SA (2005) Authenticating pervasive devices with human protocols. In: Shoup V (ed) Advances in Cryptology – CRYPTO. Lecture Notes in Computer Science, vol 3621. Springer, pp 293–308
22. Vajda I, Buttyán L (2003) Lightweight authentication protocols for low-cost RFID tags. In: Second Workshop on Security in Ubiquitous Computing – Ubicomp 2003. https://www.researchgate.net/publication/2930099_Lightweight_Authentication_Protocols_for_Low-Cost_RFID_Tags. Accessed 16 April 2026
23. Chander B, Gopalakrishnan K (2022) A secured and lightweight RFID-tag based authentication protocol with privacy-preserving in telecare medicine information system. Comput Commun 191:425–437. https://doi.org/10.1016/j.comcom.2022.05.002
24. Khorasgani AA, Sajadieh M, Yazdani MR (2022) Novel lightweight RFID authentication protocols for inexpensive tags. J Inf Secur Appl 67:103191. https://doi.org/10.1016/j.jisa.2022.103191
25. Kumar S, Banka H, Kaushik B, Sharma S (2021) A review and analysis of secure and lightweight ECC-based RFID authentication protocol for internet of vehicles. Trans Emerg Telecommun Technol 32:e4354. https://doi.org/10.1002/ett.4354
26. Mala H, Aghili SF (2019) Security analysis of an ultra-lightweight RFID authentication protocol for m-commerce. Int J Commun Syst 32:e3837. https://doi.org/10.1002/dac.3837
27. Xiao L, Xu H, Zhu F, et al (2020) SKINNY-based RFID lightweight authentication protocol. Sensors 20:1366. https://doi.org/10.3390/s20051366
28. Alavi SM, Baghery K, Abdolmaleki B, Aref MR (2015) Traceability analysis of recent RFID authentication protocols. Wirel Pers Commun 83:1663–1682. https://doi.org/10.1007/s11277-015-2469-0
29. Chien HY, Huang CW (2007) Security of ultra-lightweight RFID authentication protocols and its improvements. SIGOPS Oper Syst Rev 41:83–86
30. Chien HY, Huang CW (2010) A lightweight authentication protocol for low-cost RFID. J Signal Process Syst 59:95–102
31. Piramuthu S (2007) Protocols for RFID tag/reader authentication. Decis Support Syst 43:897–914. https://doi.org/10.1016/j.dss.2007.01.003
32. Hermans J, Peeters R, Preneel B (2014) Proper RFID privacy: model and protocols. IEEE Trans Mob Comput 13:2888–2902. https://doi.org/10.1109/TMC.2014.2314127
33. Vaudenay S (2007) On privacy models for RFID. In: Proceedings of the Advances in Cryptology 13th International Conference on Theory and Application of Cryptology and Information Security, ASIACRYPT. Springer, Berlin, Heidelberg, pp 68–87
34. Ţiplea FL, Hristea C, Bulai R (2022) Privacy and reader-first authentication in Vaudenay's RFID model with temporary state disclosure. Comput Sci J Moldova 30(3):335–359
35. Burmester M, De Medeiros B (2008) The security of EPC Gen2 compliant RFID protocols. In: Proceedings of the 6th International Conference on Applied Cryptography and Network Security. Springer, Berlin, Heidelberg, pp 490–506
36. Ţiplea FL (2014) A lightweight authentication protocol for RFID. In: Kotulski Z, Ksiezopolski B, Mazur K (eds) Cryptography and Security Systems – Third International Conference. Communications in Computer and Information Science, vol 448. Springer, pp 110–121
37. Năstase GD, Ţiplea FL (2015) On a lightweight authentication protocol for RFID. In: Bica I, Naccache D, Simion E (eds) Innovative Security Solutions for Information Technology and Communications – SECITC. Lecture Notes in Computer Science, vol 9522. Springer, pp 212–225
38. Molnar D, Wagner D (2004) Privacy and security in library RFID: issues, practices, and architectures. In: Proceedings of the 11th ACM Conference on Computer and Communications Security. pp 210–219
39. Dimitriou T (2005) A lightweight RFID protocol to protect against traceability and cloning attacks. In: First International Conference on Security and Privacy for Emerging Areas in Communications Networks. pp 59–66
40. Chien HY, Chen CH (2007) Mutual authentication protocol for RFID conforming to EPC Class 1 Generation 2 standards. Comput Stand Interfaces 29:254–259. https://doi.org/10.1016/j.csi.2006.04.003
41. Weis SA (2003) Security and privacy in radio-frequency identification devices. MS Thesis, Massachusetts Institute of Technology, Cambridge, MA
42. Duc DN, Park J, Lee H, Kim K (2006) Enhancing security of EPCglobal Gen-2 RFID tag against traceability and cloning. In: Proc SCIS, Hiroshima, Japan. p 97
43. Yeh KH, Lo NW (2010) Improvement of two lightweight RFID authentication protocols. Inf Assur Secur Lett 1:6–11. https://www.mirlabs.org/iasl/volume_1/IASL_Vol_1_Paper_2.pdf. Accessed 16 April 2026

44. Zhang Y, Kitsos P (2009) Security in RFID and Sensor Networks, 1st edn. Auerbach Publications, Boston. https://www.researchgate.net/publication/326990799_Security_in_RFID_and_sensor_networks. Accessed 16 April 2026

Citation: Bulai, R. (2026). Lightweight RFID mutual authentication providing untraceability. *Journal of Engineering Science*. 2026, 33 (2), pp. 71-84. https://doi.org/10.52326/jes.utm.2026.33(2).06.

Publisher's Note: JES stays neutral with regard to jurisdictional claims in published maps and institutional affiliations.

Copyright:© 2026 by the authors. Submitted for possible open access publication under the terms and conditions of the Creative Commons Attribution (CC BY) license (https://creativecommons.org/licenses/by/4.0/).

Submission of manuscripts: jes@meridian.utm.md

Journal of Engineering Science *Vol. XXXIII, no. 2 (2026), pp. 85 - 99*
Fascicle *Architecture, Civil and Environmental Engineering* *ISSN 2587-3474*
Topic *Architecture, Urbanism and Cadaster* *eISSN 2587-3482*

https://doi.org/10.52326/jes.utm.2026.33(2).07
UDC 528.8:332.3:004.65

OPEN ACCESS

A GEOSPATIAL FRAMEWORK FOR MANAGEMENT OF THE INTEGRATED ADMINISTRATION AND CONTROL SYSTEM (IACS) IN THE REPUBLIC OF MOLDOVA

Rodica Sirbu *, ORCID: 0000-0001-7892-8747

Technical University of Moldova, 168 Stefan cel Mare blvd., Chisinau, MD-2004, Republic of Moldova
* Corresponding author: Rodica Sirbu, *rodica.sirbu@icg.utm.md*

Received: 04. 18. 2026
Accepted: 05. 28. 2026

Abstract. The paper proposes a methodology and a validation framework for the development and implementation of the Land Parcel Identification System (LPIS) in the Republic of Moldova. The main purpose of the paper is to analyze the theoretical and technological foundations of the IACS and LPIS systems in the European Union countries, as well as to present the existing context and the possibilities for its development and implementation in the Republic of Moldova. The research aims to highlight how geospatial technologies contribute to the efficiency of land administration and the optimization of decision-making processes in priority areas, such as agriculture. The objectives of the paper include, among others, examining the fundamental concepts related to the IACS system, analyzing the role of existing spatial data and modern spatial technologies in monitoring land. At the same time, a design exercise for physical blocks delimitation was carried out, taking into account the existing data in the national spatial data infrastructure and the existing regulatory framework in the Republic of Moldova, adapted to specific institutional and operational requirements. The research methodology is based on the critical analysis of the specialized literature, international/European regulations and standards relevant to the field. At the same time, specialized platforms and programs were used in the research, such as the QGIS software, as well as other modern GIS solutions, which facilitated the practical understanding of the processes of integration, administration and analysis of spatial data. The principal limitations of this work arise from its predominantly conceptual research approach, in the absence of full access to official data sets and institutional resources, since these are regulated by the legal framework, cooperation agreements, spatial data sharing protocols, also the need to protect the confidential data of landowners.

Keywords: *Land Parcel Identification System (LPIS), Geographic Information Systems (GIS), remote sensing, orthophoto, QGIS.*

Rezumat. Lucrarea propune o metodologie și un cadru de validare pentru dezvoltarea și implementarea Sistemului de Identificare a Parcelelor Funciare (LPIS) în Republica Moldova. Scopul principal al lucrării este de a analiza fundamentele teoretice și tehnologice ale sistemelor IACS și LPIS în țările Uniunii Europene, precum și de a prezenta contextul existent și posibilitățile de dezvoltare și implementare a acestuia în Republica Moldova. Cercetarea își propune să evidențieze modul în care tehnologiile geospațiale contribuie la eficiența administrării terenurilor și la optimizarea proceselor decizionale în domenii prioritare, precum agricultura. Obiectivele lucrării includ, printre altele, examinarea conceptelor fundamentale legate de sistemul IACS, analiza rolului datelor spațiale existente și al tehnologiilor spațiale moderne în monitorizarea terenurilor. A fost realizat un exercițiu de proiectare pentru delimitarea blocurilor fizice, luând în considerare datele existente în infrastructura națională de date spațiale și cadrul de reglementare existent în Republica Moldova, adaptat cerințelor instituționale și operaționale specifice. Metodologia cercetării se bazează pe analiza critică a literaturii de specialitate, a reglementărilor și standardelor internaționale/europene relevante domeniului. În același timp, în cercetare au fost utilizate platforme și programe specializate, cum ar fi software-ul QGIS, precum și alte soluții GIS moderne, care au facilitat înțelegerea practică a proceselor de integrare, administrare și analiză a datelor spațiale. Principalele limitări ale acestei lucrări decurg din abordarea sa predominant conceptuală a cercetării, în absența accesului deplin la seturi de date oficiale și resurse instituționale, deoarece acestea sunt reglementate de cadrul legal, acorduri de cooperare, protocoale de partajare a datelor spațiale, precum și de necesitatea protejării datelor confidențiale ale proprietarilor de terenuri.

Cuvinte cheie: *sistem de identificare a parcelelor funciare (LPIS), sisteme informaționale geografice (GIS), teledetecție, ortofotografie, QGIS.*

1. Introduction

Current developments regarding the processing, storage and use of spatial data and their use in various fields, including agricultural land information management, have undergone fundamental changes. Furthermore, innovative and integrated methods are meant to support the development and modernization of agriculture, through more efficient and transparent administration. A suitable example at EU level is Integrated Administration and Control System (IACS), which comprises a variety of interconnected digital elements, technology, institutions and databases (Figure 1). It also integrates two key geospatial subsystems: the Land Parcel Identification System (LPIS) and the Geospatial Application (GSA). The LPIS identifies agricultural lands eligible for payments under the EU Common Agricultural Policy (CAP) within designated areas. In IACS terminology, these areas are called reference parcels. Each reference parcel can consist of several agricultural parcels, which are the main spatial units represented in the GSA geodata [1].

Beyond this, one of the important framework that regulates and supports the agricultural sector within the Union is the Common Agricultural Policy [3, 4], and according to information published by the European Commission, it represents one of the most important and oldest common policies, implemented since 1962, with the main aim of supporting farmers, ensuring food security and, at the same time, the sustainable development of rural areas. Thus, the IACS represents a current, administrative and informational mechanism developed within this complex framework, first introduced in 1992 by the European Union with the aim of managing, monitoring and controlling direct payments granted to farmers [5]. This system has the role of ensuring the correct and transparent distribution of agricultural funds, by verifying the eligibility of beneficiaries and the land areas for which financial support is requested. The IACS system is based on the use of electronic registers and databases that store information relating to agricultural activity, land parcels used for agricultural purposes and subsidy applications submitted by farmers.

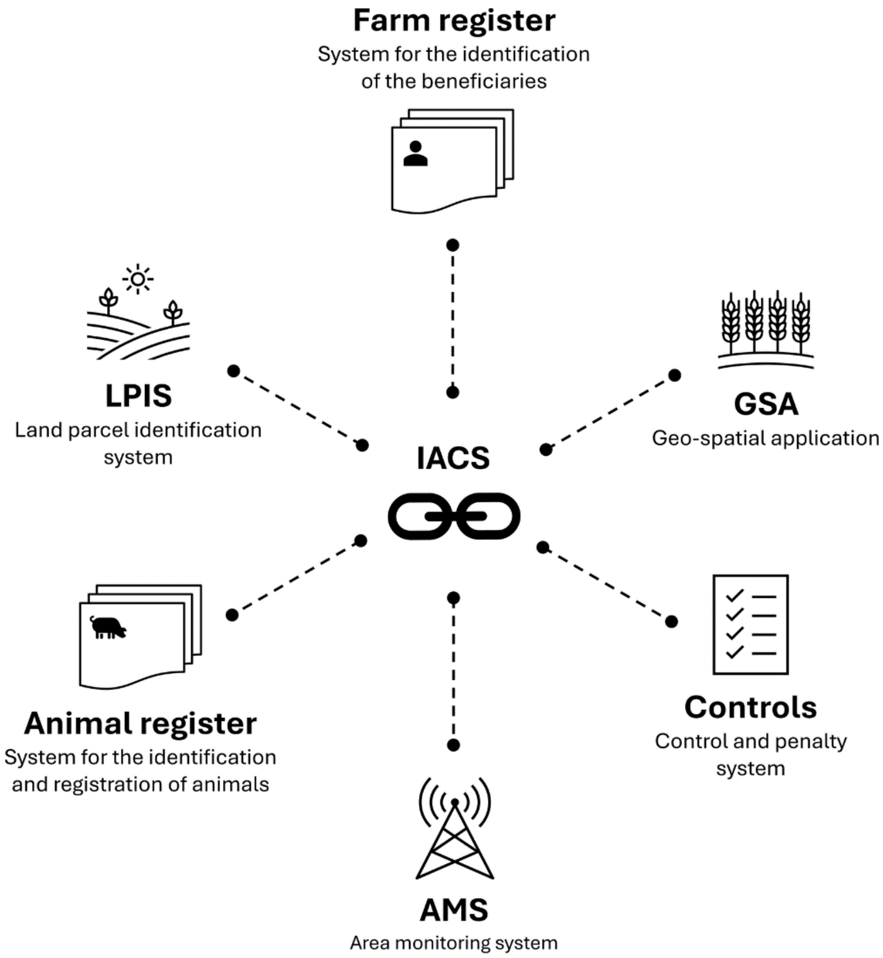

Figure 1. Overview of the digital components, systems and databases that make up IACS.
Source: Jänicke, C., Petersen, KA, Schmidts, P. et al. [2].

By correlating and analyzing this data, the system allows for the precise identification of agricultural areas, verification of compliance with eligibility criteria, etc. In this context, it should be noted that the Republic of Moldova obtained the status of candidate country for accession to the European Union in October 2024. The process of negotiating accession chapters requires compliance with community norms in all areas, including Chapter 11, Agriculture and Rural Development. This chapter requires, among other things, the implementation of a functional Integrated Administration and Control System (IACS), which allows for the management of direct payments to farmers and the verification of the compliance of subsidy applications [6].

The fundamental geospatial component of IACS is the LPIS, which is an agricultural parcel identification system based on high-resolution orthoimagery, which allows the unique location, precise delimitation and measurement of areas eligible for payments. According to Regulation (EU) 2021/2116 Art. 66-68 [7], each Member State adopting the system must establish and maintain an LPIS based on reference maps or cadastral data, complemented by modern remote sensing techniques. More specifically, the specific regulatory framework of this approach includes the following reference acts:

1. Commission Delegated Regulation (EU) 2022/1172 of 4 May 2022 supplementing Regulation (EU) 2021/2116 of the European Parliament and of the Council with regard to the integrated administration and control system in the common agricultural policy and the application and calculation of administrative penalties for conditionality [8], Articles 2-4,

laying down detailed rules on the LPIS, including the definition of the reference parcel, the minimum mandatory attributes and the quality requirements for spatial data;
2. Commission Implementing Regulation (EU) 2022/1173 of 31 May 2022 laying down rules for the application of Regulation (EU) 2021/2116 of the European Parliament and of the Council with regard to the integrated administration and control system in the common agricultural policy [9], Articles 8, 10, 12 lay down the technical rules for the implementation of IACS, including the requirements for LPIS quality control and data acquisition;
3. International standard ISO 19157:2013. Geographic information - Data quality [10], used as a reference for quality control of spatial data produced for the implementation of IACS;
4. Directive 2007/2/EC of the European Parliament and of the Council of 14 March 2007 establishing an Infrastructure for Spatial Information in the European Community (INSPIRE) [11], which ensures the creation, existence and interoperability of spatial data and metadata;
5. Law No. 254/2016 on the national spatial data infrastructure [12], which regulates, develops and implements policies in the field of spatial data infrastructure in the Republic of Moldova;
6. Law No. 71/2023 on subsidies in agriculture and the rural environment [13], which regulates the duties in this fields;
7. Technical Guidelines on IACS Spatial Data Sharing - Part 2 – Interoperability [1], which details information regarding Land Parcel Identification System (LPIS) and Geospatial Aid Application (GSAA), data models and solutions to address the lack of harmonisation of GSAA datasets in Europe, which is, among other considerations, the main obstacle to the interoperability of spatial datasets of IACS.

The list of normative acts, technical specifications and standards that contribute to the development of this integrated system can continue, because in the implementation, official information will be accessed from several state registers and geographic information systems (parcels, administrative boundaries, land cover, roads, water bodies, rivers, utility networks etc.) being designed to be interactive, for the permanent update of information. At the same time, the national framework already indicates certain technological aspects in regard to systems' development, including the creation of a technological solution compatible with the common government technological solutions and platforms, namely MCloud and MConnect, or the principles that must be taken into account such as: legality, division of the architecture into levels, expandability, security by design, modularity and scalability, etc.

The system will also include administrative and technical control mechanisms that allow permanent updating of data regarding agricultural land use and the changes' monitoring at the farm level. Through these functions, IACS contributes to increasing the efficiency of the agricultural payments administration process, reducing errors and fraud, and strengthening transparency in the management of funds for the agricultural sector.

2. Materials and methods

The research on the implementation of a Geographic Information Systems (GIS) framework for the efficient management of the Integrated Administration and Control System (IACS) in the Republic of Moldova is based on an interdisciplinary approach, which combines specific methods to the fields related to geoinformatics, land administration, spatial analysis and information systems management.

STAGE I
- analysis of scientific literature on the implementation of IACS and the use of GIS technologies;
-examination of European IACS management models;
- analysis of the national regulatory framework on agricultural land administration, subsidizing and monitoring of agricultural holdings in the Republic of Moldova.

↓

STAGE II
- identification of spatial data sources for the creation of physical blocks: existing orthophotomaps (or satellite images with specific requirements (art. 68 of Regulation (EU) 2021/2116); satellite images; cadastral data; administrative boundaries, etc.;
- analysis of data availability (network services, agreement, protocol, etc.).

↓

STAGE III
- proposals for the processing process: data georeferencing, spatial consistency checking, elimination of topological errors, standardization of coordinate systems (Moldref99, ISO 19111:2019) integration of spatial databases;
- conceptual modeling of the system through UML diagrams, LPIS UML model, INSPIRE Generic Conceptual Model, OGC 06-103r4, information flow.

↓

STAGE IV
- development of the attribute table or completion of the database, ISO 19118:2011 Geographic information - Encoding;
- development of proposals regarding the GIS programs and applications used: for creation, storage, collection, distribution of spatial data (QGIS, PostGresSQL, QGISCloud, Qfield. GeoPackage as alternative encoding, etc.)

↓

STAGE V

- development of proposals for spatial analysis methods in the process of developing and implementing IACS in the Republic of Moldova: spatial overlay analysis, proximity analysis, analysis of land use changes, classification of agricultural areas.

↓

STAGE VI
- highlighting the principles of inspection of quality assessment: eligibility conditions, reference data acquisition procedure, reference data processing, comparison between declaration and reality, ISO 19157:2013 Geographic information
- data quality analysis (art. 3 of EU Regulation (EU) 2022/1172) - data quality element - completeness, logical consistency, positional accuracy, etc.

Figure 2. Methodology applied for the study.
Source: prepared by the author.

The proposed methodology aims to assess the current structure of IACS, identify the limitations of existing administration and control processes, design an integrated GIS framework, test spatial analysis and monitoring functionalities, formulate recommendations for optimizing administrative and agricultural control processes This system supports the authorities in making strategic decisions and contributes to the sustainable development of the agricultural sector. Thus, at the moment, the Government of the Republic of Moldova has adopted GD No. 597/2024, by which the "Farmers' Registry" Information System was established as a component part of IACS, strengthening the legal and digital framework necessary for the management of subsidies, transparency of public funds and modernization of agriculture [9] and is in the process of developing the Government's decision on the approval of the IACS concept. The research is of an applied nature and uses both quantitative and qualitative methods, and in more detail, the addressed methodology is presented in Figure 2.

Also methodology is based on the realities and spatial data existing in the Republic of Moldova. At the same time, it is important to clarify with reference to two important terms, namely: Declared area (or requested area), which is the area declared by the beneficiary as eligible for payment within a certain unit amount. The declared area can be applied both to individual parcels and at the farm level. Therefore, the declared area excludes any areas well known/recorded as permanently ineligible, included in the outer perimeter of a requested parcel; Eligible area, being the area corresponding to the number of hectares for which all the conditions related to a requested unit amount have been met. The eligible area can be applied both to individual parcels and at the farm level, depending on the criteria submitted for the creation of the data set [14].

3. Results

The proposals made in this paper start from the assumption that the Republic of Moldova has been administering and managing the Farmers' Register for several years and the Ministry of Agriculture and Food Industry (MAIA) is responsible for the administration, maintenance and development of the system, being the official owner of the Farmers' Register [13]. The Agency for Intervention and Payments for Agriculture (AIPA) manages farmers' data and coordinates the application of subsidies, ensuring the fairness and transparency of the allocation of funds. It works in collaboration with other public institutions and is integrated with the MConnect interoperability platform, which facilitates the data exchange between the different registers and government entities. There is also a similarity in the scope of application between certain types of LPIS and GSA elements and the types of elements of the following INSPIRE spatial data themes, or in national terms, Law 254/2016 [12]:
1) Annex I: Cadastral parcels (CP): similarity (in specific cases, coincidence) between reference parcel (ReferenceParcel) and LPIS cadastral parcel (CadastralParcel - CP) INSPIRE element types.
2) Annex II: Land Cover (LC): similarity between the LPIS Landscape Feature and the INSPIRE Land Cover Unit (LC) element types.
3) Annex III: Land Use (LU): similarity between LPIS Agricultural Area (AgriculturalArea) and Existing Land Use Object (ExistingLandUseObject - LU) INSPIRE element types. Thus, there is similarity between the GSA element type of Agricultural Parcel (AgriculturalParcel) and Existing Land Use Object (ExistingLandUseObject - LU) INSPIRE element types. Accordingly, these similarities allow new INSPIRE-compliant LC/LU datasets to be derived from LPIS/GSA datasets and existing INSPIRE-compliant CP datasets to be reused to generate LPIS datasets.

Therefore, in order to develop the space component in IACS, spatial data modeling and creation is the process by which real-world objects and phenomena are transformed into a digital form usable in GIS systems. Within the framework of data modeling and analysis activities for the development of LPIS in the Republic of Moldova, it is recommended to use the free and open-source specialized software – QGIS [15], intended for visualization, processing and manipulation of raster (Fig. 3) and vector (Figure 4) spatial data.

The implementation of the LPIS in the Republic of Moldova involves the development of a geospatial infrastructure capable of managing, updating and controlling agricultural areas eligible for the administration of agricultural subsidies within the IACS system.

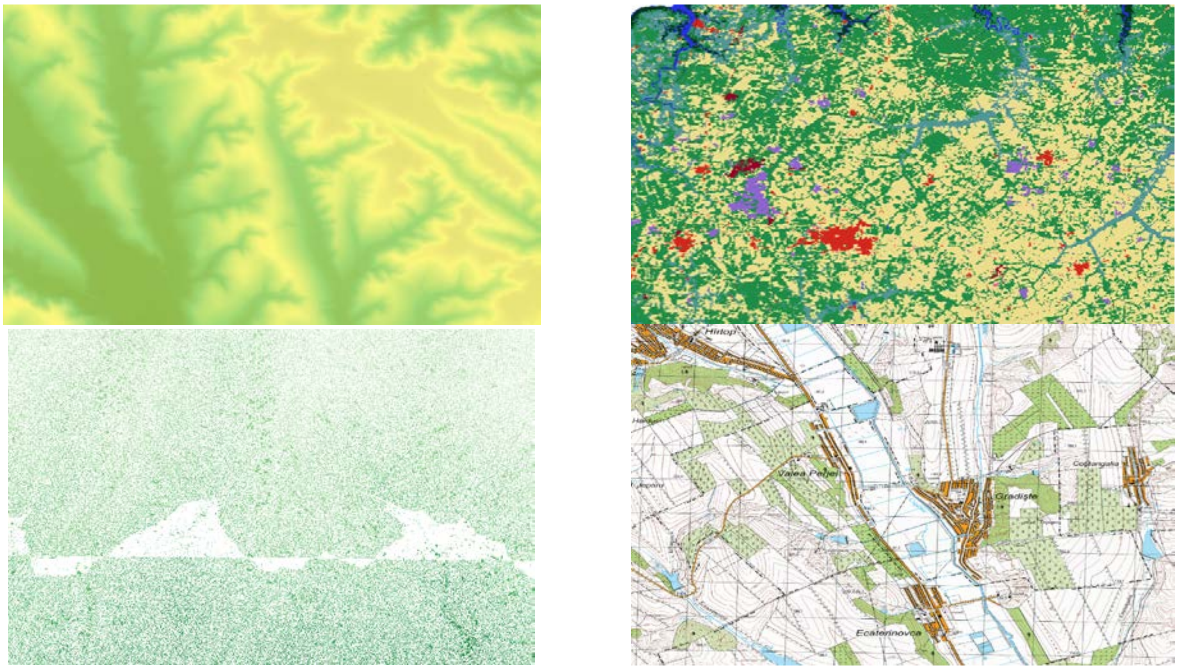

Figure 2. Viewing and managing raster data used to create new data.
Source: developed by the author based on data from GEODATA.

Thus, an important role in this process is played by the classification of cadastral information referring to land, administrative boundaries, addresses, digital terrain model, orthophoto with a resolution of at least 50 cm for the last year, land cover, etc., but also the integration of spatial data and the use of modern GIS and remote sensing technologies for the analysis of multi and hyperspectral images for crop mapping, vegetation indicators, etc.

It should be noted that land cover mapping plays an essential role in providing the necessary information for many areas, including the implementation of IACS in the Republic of Moldova, territorial planning, environmental management, agricultural activities and natural resource management. As a solution for this process, the Google Earth Engine [16, 17] is proposed, which can have an essential role in mapping agricultural crops and land cover for the LPIS development, due to its capacity to process large satellite and spatial data. Google Earth Engine allows the use of images from various archives such as Google Earth Engine Data Catalog [18], European Space Agency Sentinel-1 and Sentinel-2, NASA Landsat, which can be used for delimiting agricultural plots, identifying crop types, automatically classifying agricultural areas, and periodically updating maps. At the same time, it must be taken into account that for good data accuracy a resolution of ≤ 0.5 m is required.

Therefore, the use of open-source solutions reduces implementation costs and provides flexibility in data management and updating. It is also recommended to use in the system design the use of network services (WMS, WFS) or modern APIs [20] and other interoperability standards that facilitate data exchange between institutions and the automation of verification and monitoring processes of agricultural areas. For the creation of spatial data management, it is proposed to use the GeoPackage format, which allows storing in a single file the geometry and attributes associated with agricultural parcels (data collection date, name/surname of the engineer who collected the data, land cover, classifier, etc.). Also, for the management of large amount of spatial data and the performance of advanced queries, the PostgreSQL database [21] with the PostGIS spatial extension can be used.

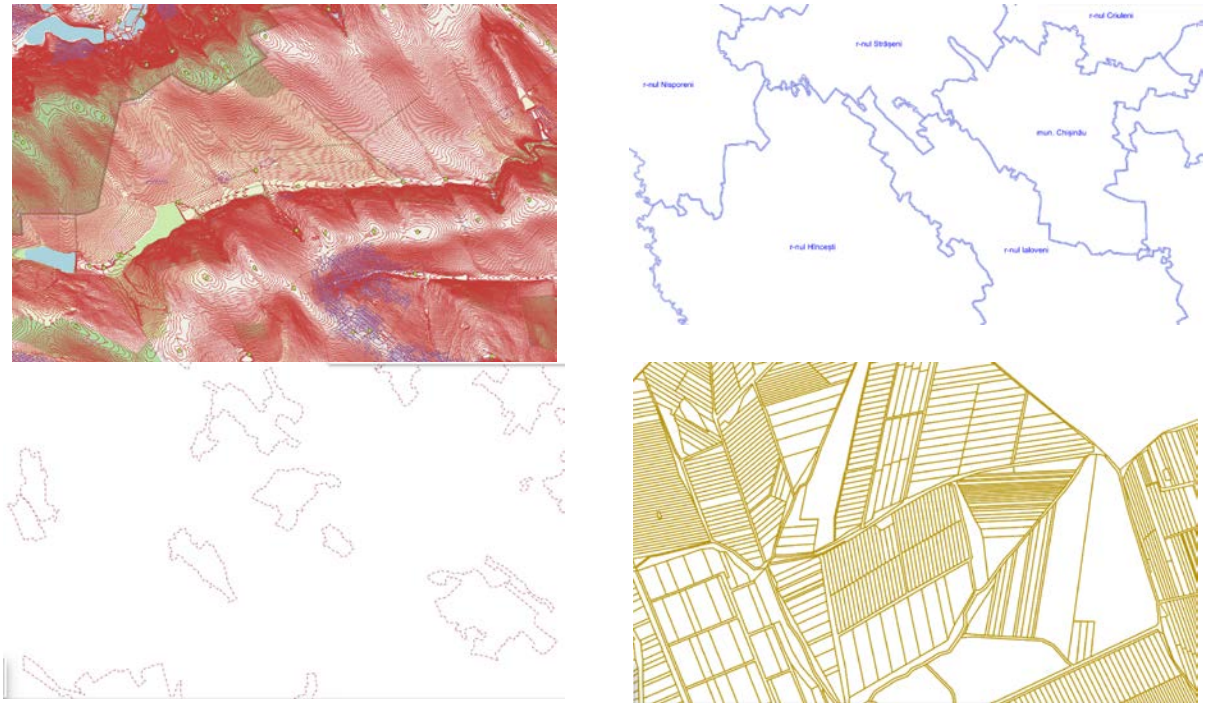

Figure 4. Viewing and managing vector data used to create new data.
Source: developed by the author based on data from GEODATA [19].

The use of open-source solutions reduces implementation costs and allows the development of a flexible and interoperable system. It is also important to choose a GIS infrastructure that ensures data interoperability and the integration of diverse sources, such as satellite images, cadastral data and field information.

Thus, the relationship between physical blocks, agricultural parcels and other data in the system is defined as follows: the physical block represents the reference cartographic unit, and the agricultural parcel represents the area declared by the farmer within this physical block. For the exercise of analyzing the possibilities and realities of the Republic of Moldova, QGIS software was used, an open-source geographic information system, which allowed the processing, analysis and visualization of spatial data. The management and storage of geospatial information was carried out through the GeoPackage database, chosen due to its advantages compared to traditional formats (such as Shapefile), offering a single integrated file, support for multiple layers and better data consistency.

As for the data sources, among others, orthophoto 2020 was used, which constituted the main basis for the interpretation and delimitation of land units. Although the use of annually updated orthophotomaps is recommended for the operational implementation of the LPIS, these data were used in the case study as a support for spatial analysis and methodological example. Additionally, the reference data from Public Institution Real Estate Cadastre [23] was used, which provided a basic cadastral framework for correlating and verifying the geometry of physical blocks. These data allowed a easier recognition between cadastral information and visual interpretation of land cover, contributing to increased accuracy of the process of spatial units' delimitation and validat [25].

For the purpose of implementing the LPIS in the Republic of Moldova, each Reference Parcel receives a unique classification according to the European Land Cover Groups nomenclature. The classification is carried out based on photointerpretation of orthoimages, supplemented where necessary with auxiliary data (Sentinel-2, CORINE Land Cover, cadastral data).

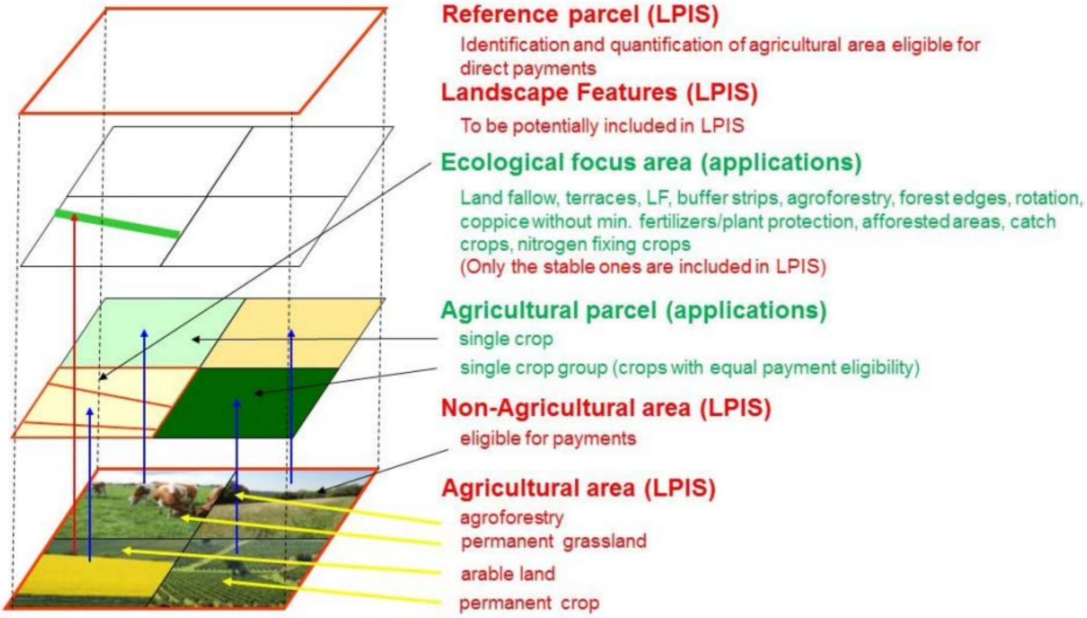

Figure 4. Conceptual structure of the LPIS system and classification of agricultural land use within INSPIRE.

Source: [1].

Table 1

LCG categories and classification criteria for LPIS

LCG code	Full name	Definition and identification criteria
AL	Arable Land	Areas used for annual or crop rotation, without permanent vegetation. Including cereals, technical crops (e.g., sunflower, soybean, beet), vegetables, land left fallow or temporarily uncultivated (less than 5 years). They are recognizable on the orthophotomap by their uniform appearance, traces of agricultural work and the presence of crops.
PC	Permanent Crops	Areas occupied by perennial plantations that produce fruits, nuts, grapes or flowers and that remain on the same plot for at least 5 years. Includes vineyards, orchards (apple, plum, cherry, walnut), horticultural nursery and fruit shrub crops. Identified by regular alignments and constant spacing between rows.
PG	Permanent Grassland	Land covered with perennial herbaceous vegetation (grasses and forage plants), which has not been part of the crop rotation for at least 5 years. A minimum vegetation cover of 20% is required. Includes pastures, hayfields and meadows in meadow or mountain areas.
N	Non-eligible	Areas that cannot benefit from direct agricultural payments. This includes forests (over 0.5 ha and with a canopy cover greater than 20%), buildings and infrastructure, permanent waters, degraded lands (severe erosion, salinization), landfills, mining operations, industrial areas etc.

Source: developed by the author based on [22].

It should be noted that, for the delimitation of parcels, there are already methodologies developed according to each approach. For example, in the case physical blocks, are represented as continuous area of agricultural land, delimited by stable features in the terrain, such as roads, rivers, forests, fences or settlements. A physical block can include one or more agricultural parcels, several farmers and different crops. It is important to note that not all land areas are mapped within the LPIS system, and there are clear exclusion rules (Table 1).

Table 2

Examples of some exclusion rules for physical blocks delimitation

Non-eligible areas	Exclusion threshold	Identification method	Observations
Roads, access roads, ditches	Width greater than 2 m	Determination on orthophoto plane at scale 1:2000	Completely removed from the RP; roads with a width of ⩽ 2 m are considered an integral part of the RP
Groups of trees and shrubs	Area greater than 300 m²	Crown contouring on RGB images	Isolated specimens or small groups (⩽ 300 m²) remain included in the RP
Water surfaces (lakes, ponds, basins)	Area over 100 m²	Contour tracing on orthophoto plane	Narrow and elongated watercourses are treated similarly to roads (if they exceed 2 m in width)
Artificial constructions and arrangements	Total exclusion (100%)	Identification on orthophoto map and based on cadastral data	Any building is removed from the RP, regardless of size
Cliffs and rock outcrops	Area greater than 100 m²	Visual analysis based on texture in images	Areas without a layer of agricultural soil, with rock on the surface
Material warehouses, silos	Total exclusion (100%)	Visual interpretation + cadastral verification	Includes all fixed structures intended for storage

Source: Prepared by the author.

Thus, within the IACS and LPIS, the rules for delimiting physical blocks establish which areas are not considered eligible and, therefore, are not included in the agricultural contour used for granting payments. Although there may be slight variations between Member States, the general principles of the European Union are common. In this respect, the main categories of areas excluded are: buildings, concrete yards and platforms, roads, parking lots, quarries, industrial land, as well as areas permanently covered by water, compact forests, dense scrub, permanent forest vegetation, cliffs, ravines and marshes. Linear elements that exceed the permitted limits, such as wide hedges, canals, internal roads wider than 2 m and forest curtains, are also excluded, as they are not considered part of the eligible agricultural area. The exclusion rules derive mainly from the documentation of the European Commission, namely the CAP/IACS regulations, the LPIS system, the JRC (Joint Research Centre) technical guides.

4. Results and Discussions

The IACS is the fundamental IT architecture through which EU Member States administer direct payments to farmers and check the compliance of subsidy applications and comprises the following main components, defined in Regulation (EU) 2021/2116:

- the geospatial component that ensures the unique identification, location and measurement of eligible agricultural areas. The LPIS uses Reference Parcels (RP) as basic units, each RP having location, eligible area (MEA), classification (LCG) and associated metadata attributes;

- the geospatial application through which farmers graphically submit payment applications, indicating agricultural parcels on the digital map. GSA is based directly on LPIS data and the most recent orthoimages;
- the area monitoring system through remote sensing (Copernicus Sentinel-1 and Sentinel-2 satellites), which permanently verifies the declared agricultural activity on parcels (AMS - Area Monitoring System);
- the system of checks by continuous monitoring, which partially replaces physical on-site inspections with analyses based on satellite and remote sensing data (CbM - Checks by Monitoring);

Thus, the LPIS constitutes the foundation on which all other IACS components are built. The quality and accuracy of LPIS data directly determine the efficiency of the entire agricultural payment system. To create a real example of delimitation of physical blocks, cadastral sectors 5501102 and 5501103 from Ialoveni district were selected (Fig. 5). The choice of these sectors was based on the existence of compact agricultural areas, the diversity of land use types and the presence of natural and artificial boundaries easily identifiable on orthophotos and satellite images. To create the working layer, a new Shapefile (.shp) vector layer was designed within the QGIS application, using polygon geometry (Layer → Create Layer → New Vector Layer → Polygon). The choice of polygon geometry is justified by the fact that physical blocks and agricultural parcels represent spatially delimited areas, which require precise storage of boundaries and attributes associated with them, including the area.

Since the initial phase of the project opted for the use of vector data of type .shp, four separate layers were created, each having a distinct role in the organization and management of spatial information. Separating the data into individual layers facilitates the digitization, topological verification and subsequent management of the information within the spatial database. Thus, the following Land Cover Group (LCG) layers were defined and used, corresponding to the classification used within the LPIS (Table 1).

Figure 5. Creating layers according to LCG categories and classification criteria for LPIS.

Source: prepared by the author.

Since the data used were, in many cases, unclear or insufficiently precise for the correct delimitation of physical blocks and LPIS parcels, it was necessary to use additional geospatial data sources and satellite images. For this purpose, platforms and services such as ArcGIS Satellite, Bing Maps Satellite, OpenStreetMap, as well as QGIS plugins such as QuickMapServices and Send2GE (Fig. 6) were used. These tools were used to better understand the real situation on the ground and to compare information from different cartographic sources and satellite images. The integration of multiple image sources allowed for a clearer identification of the boundaries of agricultural parcels, roads, canals, forest curtains, built-up areas and other stable elements used for the delimitation of physical LPIS blocks. In some cases, the available orthophoto images had strong shadows, low resolution or seasonal differences in vegetation, which made it difficult to correctly interpret agricultural areas. By comparing images from different sources, it was possible to reduce digitization errors and obtain a more accurate delimitation of agricultural land.

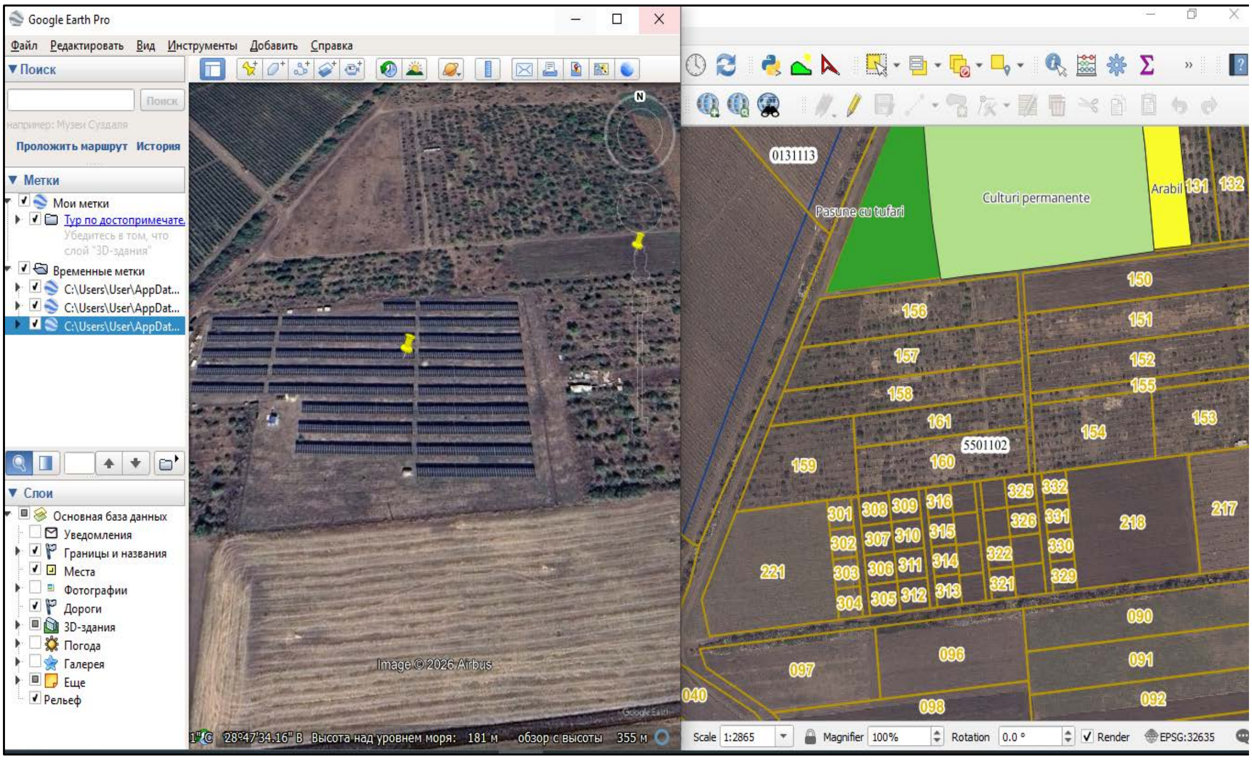

Figure 6. Use of SENT2GE plugin for current field analysis.

Source: prepared by the author.

In the context of implementing a modern agricultural monitoring and spatial data management system within an LPIS system, it is proposed to use the QField application as a solution for automating and optimizing field activities. QField is an open-source mobile application developed for working directly with projects created in QGIS. The application allows the use in the field of the same spatial layers, forms, symbols and rules defined in the main GIS project, without the need for complex data conversion. This approach facilitates the continuity of the workflow between the office stage and the field activity. Implementing the mentioned solution would allow the automation of several essential processes, such as:

1. direct collection and updating of geospatial data in the field;
2. editing the boundaries of agricultural parcels and physical blocks;
3. automatic topological validation of geometry;

4. completing personalized digital forms for each plot;
5. capturing GPS coordinates in real time;
6. attaching georeferenced photos;
7. automatic synchronization with the central database;
8. verifying mandatory attributes and reducing data entry errors;
9. offline operation in areas without internet connection;
10. integration of satellite images and orthophotos for rapid verification of land use.

In the implementation of an LPIS system in the Republic of Moldova, the use of the QField application could represent an effective solution for the digitalization and automation of agricultural monitoring processes, contributing to increasing data quality, reducing human errors and streamlining the control and updating activities of the spatial database. For the centralized storage and management of spatial information, the project used a PostgreSQL relational database together with the PostGIS extension. This solution allows for the efficient management of large volumes of geospatial data, the execution of complex spatial queries and simultaneous access of multiple users to the same database.

For the web visualization component of spatial data, the QGIS Cloud platform is proposed, which allows for the rapid publication of projects created in QGIS directly on the internet. Through this platform, maps can be accessed from the browser, without installing a program or an additional solution.

An important advantage of the platform is the possibility of rapid data updates. For example, if an operator changes the delimitation of a parcel in the database, the change can automatically appear on the web map. In addition, QGIS Cloud allows the display of satellite images and orthophotos, useful for checking agricultural land and identifying crops. The platform also supports services such as WMS and WFS, which allow the connection and exchange of data between different GIS systems. Projects can also be managed centrally, which facilitates collaboration between multiple institutions or users involved in managing the LPIS system.

For example, physical blocks and agricultural parcels delimited in QGIS can be exported to an interactive web map, where the user can select a parcel and view information such as the parcel code, area or crop type. At the same time, different thematic layers can be activated or deactivated for easier analysis of agricultural land. By using the qgis2web plugin, the LPIS project becomes more accessible and user-friendly, as spatial data can be consulted directly from the browser, contributing to improving the monitoring and management of agricultural land.

5. Conclusions

The paper showed that spatial reference data from the Republic of Moldova must be the main component of the LPIS implementation. The integration of multiple data sources, such as orthophotos, cadastral data and satellite images, allows obtaining a real and updated picture of the situation on the ground, reducing errors and increasing the accuracy of delimitation.

It was also demonstrated that the use of open-source GIS technologies and remote sensing tools plays an important role in the modernization of the system. Applications such as QGIS, PostgreSQL/PostGIS, QField and QGIS Cloud offer the possibility to manage, analyze and visualize spatial data in an efficient, flexible and accessible way and should be considered in IACS development and implementation in Republic of Moldova. At the same time, the use of Sentinel satellite images and spatial analysis methods allows for continuous monitoring of agricultural lands and rapid updating of information according to changes in the field.

For the implementation and operation of the LPIS system in the Republic of Moldova, the following main recommendations can be stated:

- Orthophoto should be updated every two years, which is used as the main basis for the operational implementation of the LPIS;
- PostGIS-type spatial databases, for managing large volumes of data and performing advanced queries;
- GeoPackage format used for storing and managing spatial data, due to the advantage of keeping the geometry and associated attributes in a single file;
- Implementation of the QField application in the field, for collecting, validating and updating spatial data and images in real time;
- QGIS Cloud platform, for publishing and accessing GIS projects online.

References

1. Martirano, G. and Toth, K. (2023) Technical Guidelines on IACS Spatial Data Sharing - Part 2 – Interoperability, Publications Office of the European Union, Luxembourg. doi:10.2760/646422, JRC132427. Accessed 7 March 2026
2. Jänicke, C., Petersen, K.A., Schmidts, P. et al. (2025) Field and farm-level data on agricultural land use for the European Union. Sci Data 12, 1050. https://doi.org/10.1038/s41597-025-05210-6. Accessed 7 March 2026
3. European Commission. Common Agricultural Policy – Overview. https://agriculture.ec.europa.eu/common-agricultural-policy/cap-overview_ro. Accessed 11 March 2026
4. European Commission. Supporting farmers and food security in the EU. https://agriculture.ec.europa.eu/overview-vision-agriculture-food/vision-agriculture-and-food_en?prefLang=ro. Accessed 15 March 2026
5. European Union. Integrated Administration and Control System (IACS) – overview. https://agriculture.ec.europa.eu/common-agricultural-policy/financing-cap/assurance-and-audit/managing-payments_ro. Accessed 15 March 2026
6. National Program for the Accession of the Republic of Moldova to the European Union for 2025-2029. https://old.gov.md/ro/advanced-page-type/2025-2029-national-programme-accession-republic-moldova-eu. Accessed 20 March 2026
7. Regulation (EU) 2021/2116 of the European Parliament and of the Council of 2 December 2021 on the financing, management and monitoring of the common agricultural policy and repealing Regulation (EU) No 1306/2013. https://eur-lex.europa.eu/legal-content/RO/TXT/PDF/?uri=CELEX:32021R2116. Accessed 20 March 2026
8. Commission Delegated Regulation (EU) 2022/1172 of 4 May 2022 supplementing Regulation (EU) 2021/2116 of the European Parliament and of the Council with regard to the integrated administration and control system in the common agricultural policy and the application and calculation of administrative penalties for conditionality. https://eur-lex.europa.eu/legal-content/RO/TXT/?uri=CELEX:32022R1172. Accessed 14 March 2026
9. Commission Implementing Regulation (EU) 2022/1173 of 31 May 2022 laying down rules for the application of Regulation (EU) 2021/2116 of the European Parliament and of the Council with regard to the integrated administration and control system in the common agricultural policy. https://eur-lex.europa.eu/legal-content/ro/TXT/?uri=CELEX%3A32022R1173. Accessed 14 March 2026
10. ISO 19157:2013 Geographic information-Data quality. https://www.iso.org/standard/32575.html. Accessed 14 March 2026
11. Directive 2007/2/EC of the European Parliament and of the Council of 14 March 2007 establishing an Infrastructure for Spatial Information in the European Community (INSPIRE). https://eur-lex.europa.eu/legal-content/RO/TXT/?uri=CELEX:32007L0002. Accessed 14 March 2026
12. Law No. 254/2016 on the national spatial data infrastructure. https://www.legis.md/cautare/getResults?doc_id=150082&lang=ro. Accessed 12 May 2026
13. Law No. 71/2023 on subsidies in agriculture and the rural environment. https://www.legis.md/cautare/getResults?doc_id=149490&lang=ro#. Accessed 12 May 2026

14. Overview of the IACS quality assessment in 2024, Union level methodology. https://apia.org.ro/wp-content/uploads/2025/01/3.Union_Level_Methodology_2024_v3_0-Document-de-lucru-de-la-JRC_.pdf . Accessed 12 May 2026
15. The specialized software - QGIS. https://docs.qgis.org/3.44/en/docs/about/preamble.html. Accessed 20 May 2026
16. Google Earth Engine. https://earthengine.google.com/. Accessed 20 May 2026
17. SÎRBU, R., CUJBĂ, V. (2025). Advanced geoinformation systems. Methodological guide for practical and laboratory work, Chișinău, 172 p., ISBN 978-9975-3702-1-9. https://repository.utm.md/handle/5014/34915. Accessed 20 May 2026
18. Earth Engine Data Catalog. https://developers.google.com/earth-engine/datasets. Accessed 24 April 2026
19. Geodata. https://geodata.gov.md/_v/2026060518/#/. Accessed 24 April 2026
20. APIs for the Web. https://ogcapi.ogc.org/, Accessed 24 April 2026
21. PostgreSQL.https://www.postgresql.org/. Accessed 24 April 2026
22. Şîmşek, Fatīh Fehmī & Durduran, S. (2022). Land cover classification using Land Parcel Identification System (LPIS) data and open source Eo-Learn library. Geocarto International. 38. 19. 10.1080/10106049.2022.2146760. Accessed 24 April 2026
23. Land (cadastral parcels) WMS visualization service. https://geoportalinds.gov.md/geonetwork/srv/eng/catalog.search#/metadata/c64ef8f4-9cd6-49cb-a500-0bd12c9ce16c. Accessed 24 April 2026
24. INSPIRE Good Practice: GeoPackage encoding of INSPIRE datasets. https://github.com/INSPIRE-MIF/gp-geopackage-encodings/blob/main/spec/GeoPackage_Good_Practice_initiation_fiche.md. Accessed 24 April 2026

Citation: Sărbu, R. (2026). A geospatial framework for management of the integrated administration and control system (IACS) in the Republic of Moldova. *Journal of Engineering Science*. 2026, 33 (2), pp. 85-99. https://doi.org/10.52326/jes.utm.2026.33(2).07.

Publisher's Note: JES stays neutral with regard to jurisdictional claims in published maps and institutional affiliations.

Copyright:© 2026 by the authors. Submitted for possible open access publication under the terms and conditions of the Creative Commons Attribution (CC BY) license (https://creativecommons.org/licenses/by/4.0/).

Submission of manuscripts: jes@meridian.utm.md

Journal of Engineering Science | | *Vol. XXXIII, no. 2 (2026), pp. 100 - 112*
Fascicle | *Food Engineering* | *ISSN 2587-3474*
Topic | *Food Technologies and Food Processes* | *eISSN 2587-3482*

https://doi.org/10.52326/jes.utm.2026.33(2).08
UDC 663.26:664.8:547.56

OPEN ACCESS CC BY

ASSESSMENT OF THE EFFECTS OF TEMPERATURE AND THERMAL TREATMENT DURATION ON THE STABILITY OF PHENOLIC CONSTITUENTS IN SWEET EXTRACTS PRODUCED FROM RARA NEAGRĂ GRAPE MARC

Nadejda Botezatu*, ORCID: 0009-0006-6897-6220,
Ecaterina Covaci, ORCID: 0000-0002-8108-481,
Alexandra Arseni, ORCID: 0009-0002-0166-4215

Technical University of Moldova,168 Stefan cel Mare Blvd., Chisinau, Republic of Moldova
* Corresponding author: Nadejda Botezatu, *nadejda.botezatu@enl.utm.md*

Received: 05. 20. 2026
Accepted: 06. 19. 2026

Abstract. Sweet red grape pomace represents a valuable source of anthocyanins, polyphenols, and flavonoids. Heating affects the content of biologically active compounds. However, well-controlled thermal processing can contribute to their preservation. The aim of this study was to provide a detailed presentation of the degradation of biologically active compounds during heating, as well as to describe their thermal behavior. The study was based on the preparation and investigation of hydroalcoholic extracts acidified with citric acid obtained from unfermented sweet red grape pomace of the Rara Neagră grape variety, harvest year 2025. Following thermal treatment within the studied temperature range (80−140°C, 7−30 min), the total phenolic content of the acidified Rara Neagră extracts decreased from 50.67 mg GAE/g DW to 17.98 mg GAE/g DW. The total anthocyanin content remained almost constant. In contrast, the experimental results highlighted a decrease in the content of monomeric anthocyanins. Analysis of the absorption spectra revealed the highest stability at 80−100°C and rapid degradation at 120−140°C. The stability observed at 80−100°C indicates that these compounds can withstand moderate food-processing operations (pasteurization and short-term thermal treatments). Therefore, the obtained results are of direct importance for the food industry and for the valorization of wine industry by-products.

Keywords: *grape pomace, Rara Neagră, thermal treatment, anthocyanins, polyphenols, antioxidant compounds, by-product valorization, food processing.*

Rezumat. Tescovina dulce de struguri roșii reprezintă o sursă valoroasă de antociani, polifenoli și flavonoide. Încălzirea influențează asupra conținutului de compuși biologic activi. Însă o procesare termică bine controlată poate contribui la menținerea lor. Scopul acestui studiu a fost de-a oferi o prezentare detaliată a degradării compușilor biologic activi în timpul încălzirii, precum și de a descrie comportamentul termic al acestora. Studiile s−au bazat pe prepararea și studierea extractelor hidro-alcoolice acidulate cu acid citric din tescovina nefermentată dulce de struguri roșii Rara Neagră, anul recoltei 2025. În urma tratamentului termic în intervalul de temperaturi studiat (80−140°C, timp 7−30 minute), conținutul total de substanțe fenolice din extractele acidulate de Rara Neagră a scăzut de la 50,67 mg EAG/g s.u. până la 17,98 mg EAG/g s.u. Conținutul de antociani a rămas aproape constant. În schimb, rezultatele experimentale au evidențiat o diminuare a conținutului de antociani monomeri. În urma realizării spectrelor de absorbție s–a observat o stabilitate maxima la 80–100 °C și o degradare rapida la 120–140 °C. Stabilitatea la 80–100°C indică faptul că acești compuși pot rezista unor procese tehnologice alimentare moderate (pasteurizare, tratamente termice de scurtă durată). Prin urmare rezultatele obținute au o importanță directă pentru industria alimentară și valorificarea subproduselor vitivinicole.

Cuvinte–cheie: *tescovină, Rara Neagră, tratare termică, antociani, polifenoli, compuși antioxidanți, valorificarea subproduselor, procesarea alimentelor.*

1. Introduction

Sweet grape pomace represents a valuable source of biologically active compounds, particularly anthocyanins, polyphenols, and flavonoids, recognized for their antioxidant properties [1]. These compounds contribute to the neutralization of many reactions involved in the onset of oxidative stress and numerous chronic diseases. The antioxidant activity of phenolic compounds is based on their ability to donate hydrogen atoms or electrons, stabilizing free radicals and interrupting oxidative chain reactions. They can also act through complementary mechanisms, such as chelation of metal ions or inhibition of oxidative enzymes. In the case of anthocyanins, for example, antioxidant efficiency is influenced by chemical structure, particularly by the number and position of hydroxyl groups, as well as by the stable molecular form in an acidic medium [1,2].

In recent times, diets rich in antioxidant compounds or based on functional foods have become increasingly promoted in public health sectors, due to their potential to reduce the incidence of cancer and other chronic diseases, considered leading causes of mortality. In addition to nutritional value itself, food contributes significantly to protecting the body against numerous pathologies, reinforcing the concept of functional food and nutraceuticals [3]. The development of an interdisciplinary link in food research integrating natural compound chemistry, food science, and nutrition allows for more detailed information on the chemical composition of food products, changes induced by industrial processing, and the bioavailability of bioactive compounds. Plant-based food sources are recognized as being extremely rich in substances with beneficial health effects [3]. For example, anthocyanins are natural pigments responsible for the red, violet, and blue hues of numerous plant products, recognized for their antioxidant properties and beneficial health effects [4]. The main challenge preventing the use of these compounds as alternatives to synthetic additives is their limited stability, particularly at high pH values and elevated temperatures. However, compared to other natural colorants (betalains, carotenoids, chlorophylls), anthocyanins show better thermal stability, which justifies the need for further applied research in this area. Academic interest in studying biologically active compounds is directed toward validating beneficial health effects, such as antioxidant, anti-inflammatory, anti-obesity, antidiabetic, antitumoral, anti-ulcer, and neuroprotective activities [5, 6].

Since most plant-based foods are subjected to heat treatments before consumption, to inhibit microbial growth, remove water, or inactivate enzymes, heating influences the content of biologically active compounds. Thermal stability experiments are generally carried out by treating extracts at different temperatures and for varying periods of time, after which the total or individual residual content is determined [6]. To reduce the degradation of biologically active compounds during thermal processing of foods containing these compounds, appropriate formulation of thermal conditions is necessary so that product quality is not affected [7, 8]. Since the antioxidant activity of these compounds also depends on their total content, well-controlled thermal processing can contribute to maintaining or even improving antioxidant properties, due to the formation of other compounds with antioxidant activity [9] as a result of heat-induced reactions.

The aim of this study was to provide a detailed and updated overview of the molecular mechanisms and kinetics of degradation of biologically active compounds during heating, as well as to describe their thermal behavior.

2. Materials and Methods

2.1. Materials for research

The studies were based on the preparation and investigation of extracts from unfermented sweet red grape pomace of Rara Neagra, harvest year 2025. The red Rara Neagra grapes were brought from the Stefan Voda region, Purcari commune, and processed technologically in the micro-winemaking section of the Department of Oenology and Chemistry.

The pomace was dried to dryness at a temperature of 55 ± 2°C, in oven BOV-T30C ground with an electric mill Bosch KM13 and used for obtaining the study extract. The solvent used for extraction was ethyl alcohol at 60% acidified with citric acid. Acidification of the medium with citric acid is an efficient and eco-friendly technique for the recovery of bioactive compounds from pomace [10]. Citric acid, used to adjust the pH to acidic values (approximately pH 3.0), promotes the degradation of plant cell walls and increases the diffusion of phenolic compounds and anthocyanins [11] into the extraction medium.

The experimental extraction regime included 12 hours with periodic agitation at temperatures of 40 ± 2°C. After extraction, the hydro-alcoholic samples were filtered and stored in the dark at 20 ± 1°C. Subsequently, the extracts were heat-treated at temperatures of 80, 100, 120 and 140 ± 5°C for 7, 14, 21 and 30 minutes at the Oenological Research Center, Faculty of Food Technology, UTM.

Reagents. The Folin–Ciocalteu reagent Merck (Darmstadt, Germany), gallic acid 98%, 2,2-diphenyl-1-picrylhydrazyl (DPPH) 90 %, sodium carbonate (Na_2CO_3) powder 99.5 %, ethanol (C_2H_5OH) 98%, sodium hydroxide (NaOH) solution 33% and hydrochloric acid (HCl) 37.5% were obtained from Sigma-Aldrich. All other chemicals were analytical reagent grade.

2.2 Research methods

For the pH value the InoLab pH 7110 was employed. Dry substance content was established using ATAGO Pocket refractometer PAL-1.

Evaluation of Chromatic Characteristics

Before spectrophotometric analysis, the extract samples were subjected to centrifugation at 2000 rpm for 15 min. The absorbance values were subsequently recorded at 420, 520, and 620 nm using a T80 UV–VIS spectrophotometer and 1 mm optical path cuvettes. These wavelengths are associated with the yellow, red, and blue-violet regions of the visible spectrum and provide information regarding the color characteristics of anthocyanin-containing extracts [12].

The absorbance measurements obtained at the three selected wavelengths were used to calculate the chromatic parameters according to equations (1) and (2). These parameters allowed the evaluation of color intensity and hue, providing insight into the changes in pigment composition and color stability induced by thermal treatment.

$$\text{Color intensity: } I_c = A_{420} + A_{520} + A_{620} \quad (1)$$

$$\text{Hue color: } H_c = \frac{A_{420}}{A_{520}} \quad (2)$$

where: A_{420} – absorbance at 420 nm;

A_{520} – absorbance at 520 nm;

A_{620} – absorbance at 620 nm.

Summary appreciation of phenolic compounds

For the determination of total phenolic content, 1 cm³ of extract diluted at a ratio of 1:5 was transferred into a 100 cm³ volumetric flask. Subsequently, 50 cm³ of distilled water, 5 cm³ of Folin–Ciocalteu reagent, and 20 cm³ of 20% sodium carbonate solution were added. The mixture was brought to volume with distilled water and homogenized thoroughly. After an incubation period of 30 min, the absorbance was measured at 750 nm using 10 mm path-length cuvettes, with distilled water serving as the blank [12].

When the measured absorbance deviated significantly from the target value of approximately 0.3 absorbance units, the analysis was repeated using an adjusted dilution factor to obtain readings within the optimal analytical range. The concentration of total phenolic compounds was determined from a calibration curve prepared with gallic acid standards (0–500 mg/L). Results were expressed as milligrams of gallic acid equivalents per gram of dry weight of grape pomace extract (mg GAE/g DW).

Determining anthocyanin content

For the determination of anthocyanin content, 3 cm³ of clarified extract was transferred into a 25 cm³ pycnometer. Subsequently, 12.5 cm³ of rectified ethanol adjusted to pH 1.2 and three drops of concentrated hydrochloric acid were added. The mixture was then diluted to the calibration mark with distilled water and thoroughly homogenized by vigorous shaking. After centrifugation at 1500 rpm for 15 min, the absorbance of the content was recorded at 520 nm using a 1 mm path-length cuvette, with distilled water serving as the blank reference [12].

The concentration of anthocyanins was subsequently determined using the equation presented below:

$$C_{ant} = 1056.7\,A \quad (3)$$

where: A – absorbance of sample;

1056.7 – transfer coefficient, established for malvidin-3-glucoside isolated from grape skins.

Determination of monomeric pigments using the pH differential method (pH 1.0 and pH 4.5)

The concentration of monomeric anthocyanins was determined using the pH differential method, based on the reversible structural transformation of anthocyanin pigments under different pH conditions according [13]. The method is based on the structural transformation of anthocyanin-like monomeric pigments depending on pH. At pH 1.0, pigments exist predominantly in the colored flavylium cation form, while at pH 4.5, they are converted to a colorless hemiketal form. The difference in absorbance between the two pH values is proportional to the concentration of monomeric pigments. For this method the preparation of two separate dilutions of the same sample is necessaire:

Sample Preparation: two dilutions of the same sample were prepared using buffer solutions of different pH values:

- pH 1.0 potassium chloride buffer;
- pH 4.5 sodium acetate buffer.

Typically, 0.5 mL of sample was mixed with 4.5 mL of the corresponding buffer solution, resulting in a 1:10 dilution ratio. The dilution factor was adjusted when necessary, according to the color intensity of the sample. The diluted samples were thoroughly mixed and allowed to equilibrate for 15–20 min at room temperature in the absence of light to ensure complete pigment stabilization.

Spectrophotometric Measurements: the absorbance of each solution was measured using a UV–VIS spectrophotometer at:

- 520 nm, corresponding to the maximum absorbance wavelength of anthocyanin pigments;
- 700 nm, used to correct for sample turbidity and light scattering effects.

Mathematical calculations: the absorbance values for each pH condition were calculated according to equations (4) and (5):

$$A_{pH1} = (A_{520} - A_{700})_{pH1} \tag{4}$$

$$A_{pH4.5} = (A_{520} - A_{700})_{pH4.5} \tag{5}$$

The net absorbance attributable to monomeric anthocyanins was then calculated as:

$$A = A_{pH1} - A_{pH4.5} \tag{6}$$

The concentration of monomeric anthocyanins, expressed as cyanidin-3-glucoside equivalents per liter of extract, was calculated using equation (7):

$$C = \frac{A \times MW \times DF \times 1000}{\varepsilon \times l} \tag{7}$$

where: C - monomeric anthocyanin concentration (mg/L);

A -net absorbance of samples;

MW – molecular weight of cyanidin-3-glucoside (449.2 g/mol);

DF – dilution factor;

ε – molar absorptivity coefficient (26,900 $L \cdot mol^{-1} \cdot cm^{-1}$);

l – optical path length of the cuvette (cm).

3. Results and discussions

The dry matter content of the acidified hydroalcoholic extract of Rara Neagra, calculated in %, was 29.8 ± 0.05, and the pH value was 3.28 ± 0.01.

From the absorption spectra included in Fig.1, maximum stability was observed at 80 to 100 °C and rapid degradation at 120 to 140 °C. The relative stability in the temperature range 80 to 100°C (nearly constant absorbance) is explained by the fact that in this temperature range, most anthocyanins and polyphenols were in a zone of relative thermal stability, their degradation was slow. Additionally, pigmentation effects (interactions between anthocyanins and other polyphenols) may have been present in the pomace extracts, stabilizing the color and absorbance. The decrease in absorbance at 120 and 140°C is explained by the degradation of anthocyanins, polymerization reactions, and degradation of flavonoids, resulting in a visibly decreased absorbance of the samples [14]. All at once the absorbance of the untreated control samples was lower, the most likely explanation is that heat treatment increased the content of anthocyanins in a soluble and detectable state in the extracts.

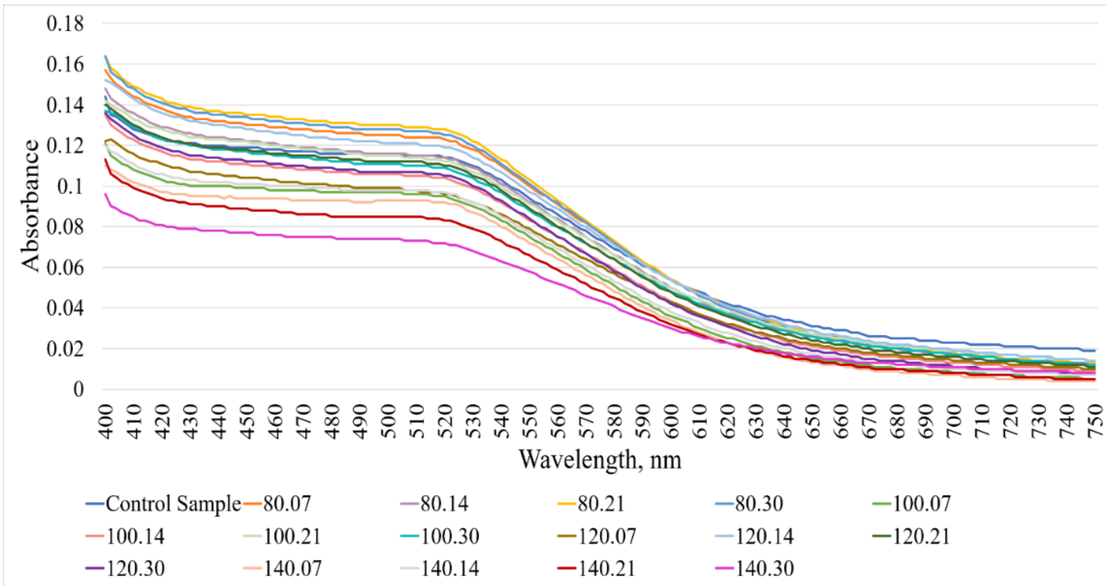

Figure 1. Absorption spectra of the studied extracts (dilution factor 50), temperature range (80–140°C), duration (7–30 minutes).

Following heat treatment in the studied temperature range (80–140°C, duration 30 minutes), the total phenolic content of the acidified Rara Neagra extracts decreased from 50.67 mg GAE/g DW to 17.98 mg GAE/g DW. As can be observed in Fig. 2, with the increase in temperature from 80°C to 140°C and treatment time from 0 to 30 minutes, a percentage reduction of total polyphenol content in the extract of up to 35.49% was observed. In the study conducted by Daniela Serea [15], a percentage reduction of total polyphenol content in the extract of up to 45.45% was observed, which is explained by the longer heat treatment duration and the different grape variety.

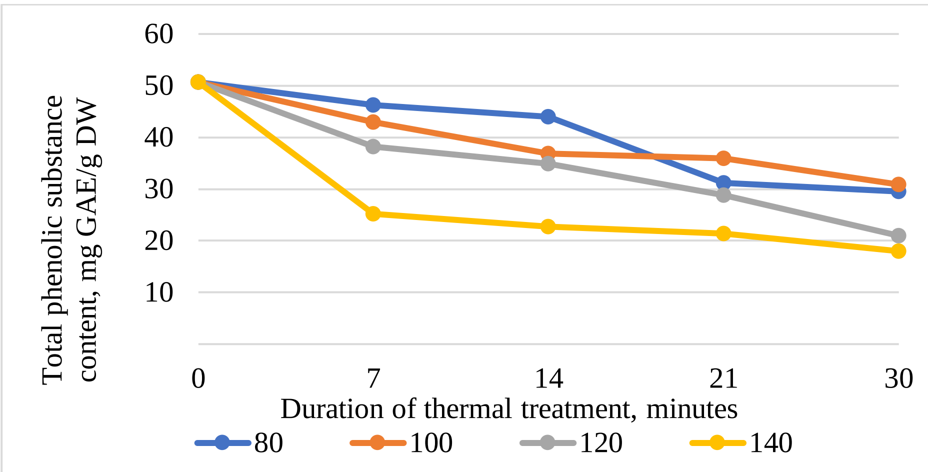

Figure 2. Influence of heat treatment (7, 14, 21 and 30 min) on total phenolic content of Rara Neagra extracts at different temperatures (80, 100, 120 and 140 °C).

The decrease in the total phenolic compound content observed in sweet red grape pomace extracts acidified with citric acid can be explained by thermal degradation processes, oxidation, and structural transformations of phenolic compounds [16]. High temperatures and prolonged treatment duration favored the formation of reaction products, such as quinones and polymeric compounds, which were no longer efficiently detected by the spectrophotometric methods used. Although the acidic medium contributed to partial stabilization of these compounds, it was unable to prevent their degradation under severe thermal conditions.

When determining the anthocyanin content, it was observed that they remained nearly constant (Fig. 3). This is explained by the fact that the hydroalcoholic extracts, being acidified with citric acid, created favorable conditions for anthocyanins. At pH acid (2.5– 3.5), the flavylium form dominated, being the most thermally and oxidatively stable [17]. Another important factor was the fact that pomace extracts are rich in polyphenols, sugars, and organic acids, which could interact with anthocyanins through pigmentation mechanisms. These interactions contributed to color stabilization and protection of anthocyanins against thermal degradation. In addition, the presence of acylated anthocyanins, known for their superior thermal stability, may have contributed to maintaining the total concentration under heating conditions.

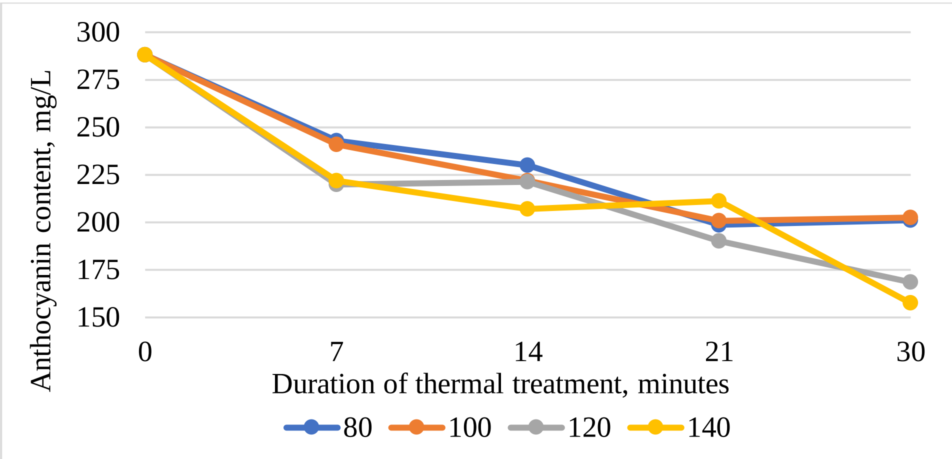

Figure 3. Anthocyanin content in Rara Neagra extracts at experimental condition.

Heating can increase the value determined by the pH differential method, as this method quantifies only anthocyanins that respond reversibly to pH change and exhibit characteristic absorption [13]. In untreated extracts, anthocyanins may be associated with tannins and polysaccharides, upon heating, these associations can be partially broken, making the anthocyanins more accessible.

Experimental results revealed a decrease in the monomeric anthocyanin content of sweet red grape pomace extracts acidified with citric acid, with increasing temperature from 80 to 140 °C and heating time from 7 to 30 minutes (Fig. 4). This behavior can be explained by the high sensitivity of monomeric anthocyanins to elevated temperatures, which accelerate their thermal degradation, hydration, and structural transformation processes [18]. Although the acidic medium contributed to stabilizing anthocyanins in the flavylium form, the protective effect of citric acid became insufficient at high temperatures and prolonged heating durations. In addition, polymerization and condensation reactions with other phenolic compounds may have led to a reduction of the monomeric anthocyanin fraction and to the formation of more complex and thermally stable pigments.

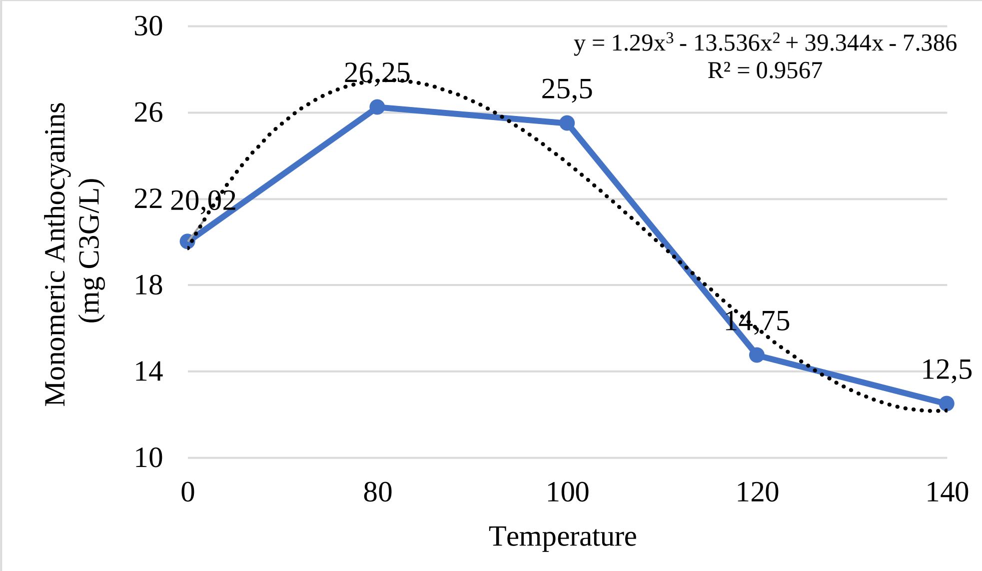

Figure 4. The dynamic of monomeric anthocyanin content in the studied experimental samples.

Based on the mean values calculated from all samples, a graph of the dependence of monomeric anthocyanin content on temperature was constructed (Fig. 4). It was observed that the maximum stability of anthocyanin monomers was between 80 °C and 100 °C, at 120°C, rapid degradation began, and at 140°C, significant destruction occurred. The relatively high stability of monomeric anthocyanins observed at 80–100°C may be attributed to the acidic conditions of the extract, which favor the predominance of the flavylium cation form, known to be the most stable anthocyanin structure.

The trend analysis revealed a temperature-dependent biphasic behavior of monomeric anthocyanins. Moderate heating (up to 80 °C) promoted anthocyanin release and increased their concentration, reaching a maximum value of 26.25 mg C3G/L. Further temperature elevation induced a progressive decline, suggesting thermal degradation, oxidation, and condensation reactions leading to the transformation of monomeric anthocyanins into more stable polymeric pigments. The high coefficient of determination (R^2 = 0.9567) confirms the strong relationship between temperature and anthocyanin content.

In addition, the presence of other phenolic compounds may contribute to pigment stabilization through copigmentation interactions. At 120°C, thermal energy became sufficient to accelerate the hydrolysis and structural transformation of anthocyanins, resulting in the formation of less stable chalcone and colorless degradation products. At 140°C, extensive degradation occurred due to the combined effects of thermal cleavage of anthocyanin molecules, oxidation reactions, and the breakdown of glycosidic bonds. These processes lead to substantial losses of monomeric anthocyanins and a significant reduction in their stability.

In the study conducted by Daniela Serea [15], the same pattern of monomeric anthocyanin degradation with increasing temperature and time is characteristic, from 25 mg C3G/L in the control to 5 mg C3G/L, while in our case from 20 mg C3G/L in the control to 12.5 mg C3G/L. Şelale Yalçınöz et al. [19], also demonstrated that the degradation of monomeric anthocyanins increases progressively during heating, meaning that significant reductions in monomeric anthocyanin content occur with increasing processing temperature, only they studied the anthocyanins in pomegranate juice.

The color hue remained relatively constant because the acidic medium created by citric acid acidification continued to stabilize the flavylium cationic form of the anthocyanins remaining in the system (Fig. 5). Under low pH conditions, the equilibrium between the different structural forms of anthocyanins was shifted toward the predominantly red forms, limiting major changes in chromatic tone.

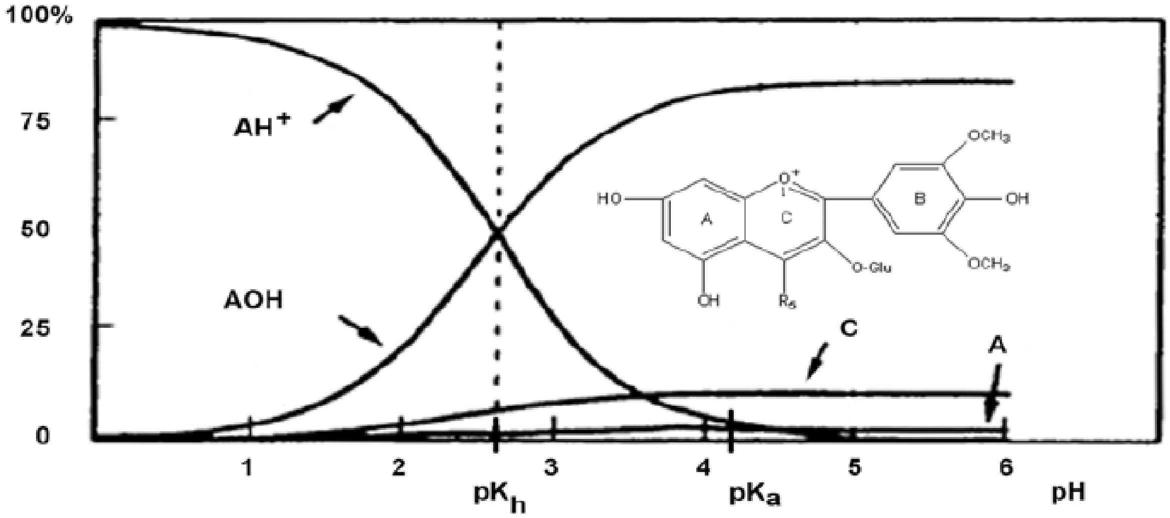

Figure 5. The distribution of anthocyanin structural forms as a function of pH.

The experimental pH value was 3.28, so the system was located close to the transition region around pK_h (~3.0). This indicates an intermediate equilibrium state: a significant fraction of anthocyanins remained in the colored forms (AH^+ and partially quinonoidal forms).

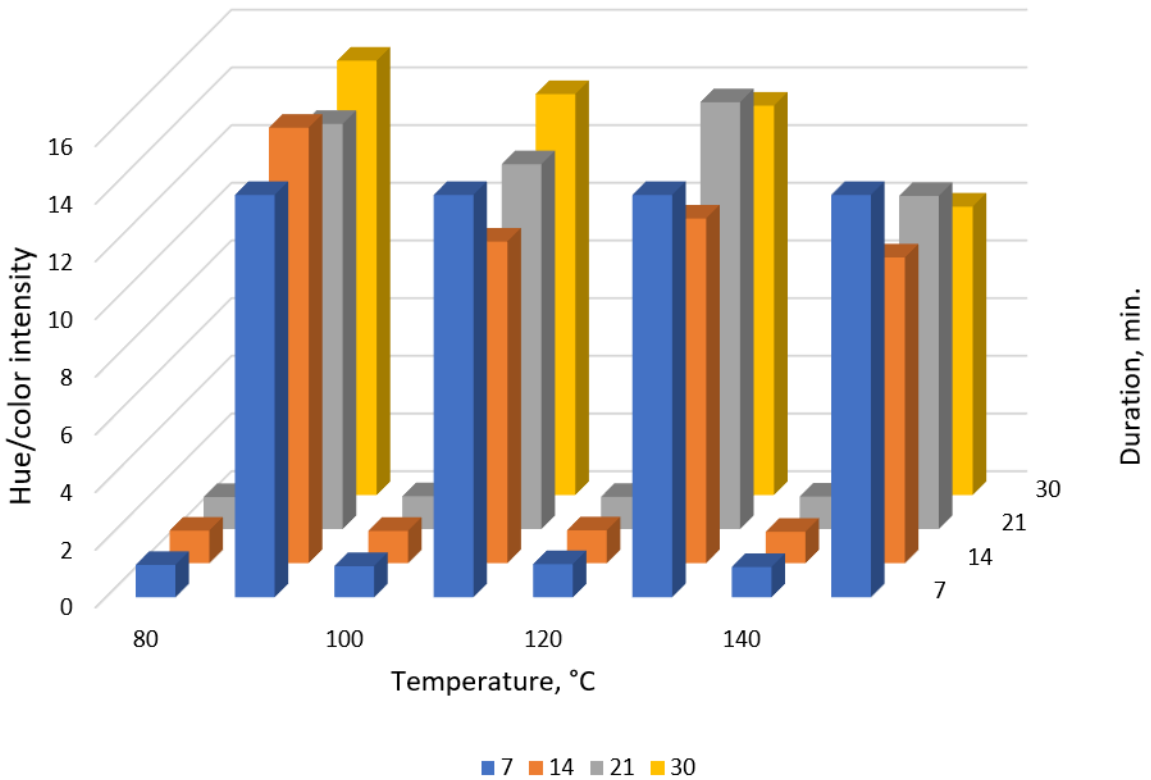

Figure 6. Influence of heat treatment (7, 14, 21 and 30 min) on color intensity and hue of Rara Neagra extracts at different temperatures (80, 100, 120 and 140 °C).

According to the anthocyanin structural equilibrium diagram (Fig. 5), the pH value of the investigated extracts (pH 3.28) was located slightly above pKh, where the flavylium cation (AH^+) and the hydrated hemiketal form (AOH) coexist in dynamic equilibrium.

Under these conditions, hydration of the flavylium cation becomes significant, leading to a partial conversion of the colored anthocyanin species into the nearly colorless hemiketal form. Consequently, the proportion of AH^+ decreases, resulting in a reduction of color intensity, while the hue remains relatively stable. At pH 3.28, the formation of quinonoidal bases and chalcone structures is still limited, since these transformations become more pronounced at higher pH values approaching pKa.

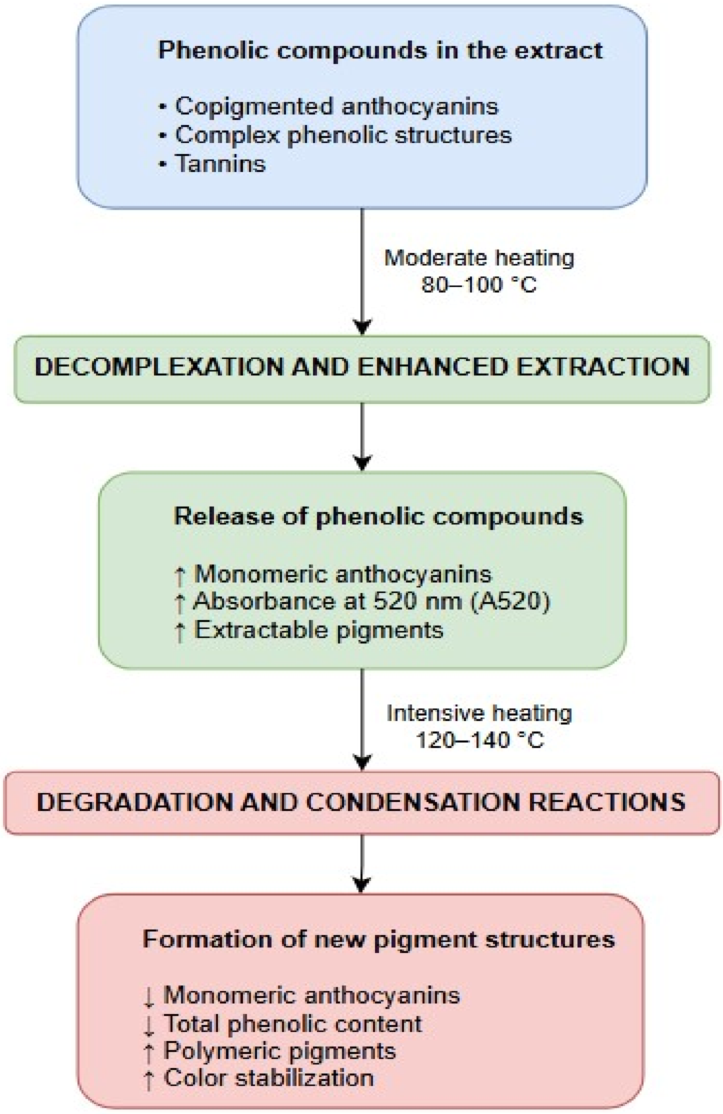

Figure 7. The comparative analyzes of the stages of Rara Neagra extracts.

Thus, even as the total concentration of coloring pigments decreases, the relative proportion of compounds responsible for the red color remained sufficiently stable so that the hue did not undergo significant variations (Fig. 6). The heat treatment simultaneously affected the release of anthocyanins and intensification of the red color as well as the appearance of minor chemical transformations of phenolic compounds that increased absorbance at 420 nm [20]. Therefore, although the color became more intense, the ratio between yellow and red components increased slightly, leading to higher color hue values compared to the untreated control sample.

The reduction in color intensity indicated a decrease in the concentration of colored monomeric forms of anthocyanins, as a result of thermal degradation accelerated by increasing temperature and heating duration (Fig. 6). At high temperatures, anthocyanins underwent hydration reactions, opening of the flavylium nucleus, and conversion to less colored or even colorless forms, leading to a decrease in specific absorbance and consequently to a reduction in the chromatic intensity of the extract [21].

At 140°C, the decrease in color intensity was approximately 47%, a result consistent with the findings reported by Turturică et al. [18], who observed a reduction in color intensity of up to 60% at 120°C. These results indicate that the system under study falls within the same range of accelerated degradation, characterized by pronounced thermal breakdown of anthocyanin compounds at elevated temperatures.

Therefore, as a result of the experimental study, a conceptual model of the structural and functional transformations that occurred in the studied sweet red grape pomace extracts during heat treatment can be demonstrated (Fig. 7). In the initial state, the extract contained pigmented anthocyanins, complex phenolic compounds, and tannins, in a relatively stable molecular system. [22].

At moderate temperatures (80–100°C), heating favored decomplexation processes and the release of bioactive compounds from the plant matrix, leading to an increase in monomeric anthocyanin content and intensification of absorbance at 520 nm. The increase in temperature in the 120–140°C range resulted in predominance of thermal degradation and condensation processes of phenolic compounds. Under these conditions, a reduction in the monomeric anthocyanin fraction and total phenolic content was observed, concurrent with the formation of thermally more stable polymeric pigments [23].

4. Conclusions

Sweet red pomace represents a valuable source of natural bioactive compounds. The obtained results demonstrated that thermal processing of acidified hydroalcoholic extracts from sweet red grape pomace enhanced anthocyanin availability and improved chromatic characteristics, as evidenced by increased absorbance at 520 nm, color intensity, and monomeric anthocyanin content. The experimental results demonstrating the stability of anthocyanins in an acidified hydroalcoholic medium suggest the possibility of using the extracts as natural food colorants. Stability at 80–100°C indicates that these compounds can withstand moderate food processing conditions (pasteurization, short heat treatments). Degradation at 120–140°C shows that intense technological processes (severe sterilization, prolonged heat treatments) can reduce the functional and colorant value of the extracts.

The treatments temperature initiated the chemical reactions, while time only finalizes transformations already begun, this is why there are small differences between 7 and 30 minutes, but very visible differences between 80°C and 140°C. Overall, the combination of thermal treatment and acidic conditions proved effective in improving the technological and functional quality of grape pomace extracts intended for valorization as natural colorant. Therefore, the obtained results have direct importance for the food industry and the valorization of wine by-products.

Acknowledgments: The research was supported by Institutional Project, subprogram 02.04.05 Optimizing food processing technologies in the context of the circular bioeconomy and climate change, Bio-OpTehPAS, being implemented at the Technical University of Moldova.

Contribution of Authors

Nadejda Botezatu: Conceptualization, Methodology, Investigation, Resources, Data curation, Formal analysis, Writing – original draft preparation.

Ecaterina Covaci: Software, Methodological guidance, Validation, Supervision, Conceptual discussion, Writing – review & editing, Project administration.

Alexandra Arseni: Software, Investigation, Visualization.

Conflicts of Interest: The authors declare no conflict of interest. The funders had no role in designing the study; collecting, analyzing, or interpreting data; writing the manuscript; or deciding to publish the results.

References

1. Balea SS, Pârvu AE, Pârvu M, Vlase L, Dehelean CA, Pop TI (2020) Antioxidant, anti-inflammatory, and antiproliferative effects of Vitis vinifera L. var. Fetească Neagra and Pinot Noir pomace extracts. Front. Pharmacol 11:990. https:// doi: 10.3389/fphar.2020.00990
2. Almanza-Oliveros A, Bautista-Hernandez I, Castro-Lopez C, Aguilar-Zarate P, Meza-Carranco Z, Rojas R, Michel M, Cristian G, Martinez-Avila G (2024) Grape Pomace—Advances in Its Bioactivity, Health Benefits, and Food Applications. Foods 13:580. https:/ / doi: 10.3390/foods13040580
3. Teresa Abreu T, Luís C, José S, Teixeira J, Rosa Perestrelo R (2025) Unveiling potential functional applications of grape pomace extracts based on their phenolic profiling, bioactivities, and circular bioeconomy. Biomass Conversion and Biorefinery 15:31491–31506. https://doi.org/10.1007/s13399-025-06578-6
4. Ghendov-Mosanu A, Cojocari D, Balan G, Patras A, Lung I, Soran ML, Opri O, Cristea E, Sturza R (2022) Chemometric Optimization of Biologically Active Compounds Extraction from Grape Marc: Composition and Antimicrobial Activity. Molecules 27(5) :1610. https:// doi.org/10.3390/molecules27051610.
5. Wittenauer J, Mäckle S, Sußmann D, Schweiggert-Weisz U, Carle R (2020) Inhibitory effects of polyphenols from grape pomace extract on collagenase and elastase activity. Fitoterapia 101:179–187. https:// doi: 10.1016/j.fitote.2015.01.005
6. Karastergiou A, Gancel AL, Jourdes M, Teissedre PL (2024) Valorization of Grape Pomace: A Review of Phenolic Composition, Bioactivity, and Therapeutic Potential. Antioxidants 13(9):1131. https://doi: 10.3390/antiox13091131
7. Peixoto CM, Dias MI, Alves MJ, Calhelha RC, Barros L, Pinho SP, Ferreira IC (2018) Grape pomace as a source of phenolic compounds and diverse bioactive properties Food Chemistry 253:132–138. https:// doi: 10.1016/j.foodchem.2018.01.163
8. Patras A, Brunton NP, O'Donnell C, Tiwari BK (2019) Effect of thermal processing on anthocyanin stability in foods. Trends in Food Science & Technology 21(1): 3–11. https:// doi: 10.1016/j.tifs.2009.07.004.
9. Dranca F, Oroian M (2019) Kinetic Improvement of Bioactive Compounds Extraction from Red Grape (*Vitis vinifera* Moldova) Pomace by Ultrasonic Treatment. Foods 8(8): 353. https://doi.org/10.3390/foods8080353
10. Zekun Z, Dong Y (2019) Economical and eco-friendly isolation of anthocyanins from grape pomace with higher efficiency. Food Chem *X* 10 15:100419. https:// doi: 10.1016/j.fochx.2022.100419
11. Tikhonova A, Ageeva N, Globa E (2021) Grape pomace as a promising source of biologically valuable components. In: 2021 BIO Web of Conferences 34: 6002. https:// doi: 10.1051/bioconf/20213406002
12. Musteață G, Sclifos A, Gherciu-Musteață L,Covaci E (2017) Methodological guide. Techno-chemical and microbiological control of alcoholic beverages. TUM, Chisinau, Republic of Moldova [in Romanian]
13. Covaci E, Arhip V (2020) Methodological guide. Technological operations for conditioning and stabilizing wines. TUM, Chisinau, Republic of Moldova [in Romanian]

14. Delić K, Milinčić DD, Pešić MB, Lević S, Nedović VA, Gancel A-L, Jourdes M, Teissedre P-L (2024) Grape, wine and pomace anthocyanins: winemaking biochemical transformations, application and potential benefits. OENO One 58(4). https:// doi: 10.20870/oeno-one.2024.58.4.8039
15. Serea, D (2023) The valorization of various biologically active compounds from red grapes processing by-products and the obtainment of certain value-added ingredients. PhD Thesis, Dunărea de Jos University of Galați, Republic of Romania.
16. Volf I, Ignat I, Neamțu M, Popa VI (2014) Thermal degradation of grape marc polyphenols. Food Chemistry 160: 313–320. https:// doi: 10.1016/j.foodchem.2014.03.080
17. Oancea S (2021) A Review of the Current Knowledge of Thermal Stability of Anthocyanins and Approaches to Their Stabilization to Heat. Antioxidants 10(9) :1337. https://doi.org/10.3390/antiox10091337
18. Turturica M (2018) Kinetic Behavior of Anthocyanins from Fruits during Processing in Model and Food Systems. PhD Thesis, Dunărea de Jos University of Galați, Republic of Romania.
19. Yalçınöz Ş, Erçelebi E (2017) Heat-induced degradation kinetics of monomeric anthocyanins and color of pomegranate (Punica Granatum L.) concentrate. Agriculture & Food *5*.ISSN 1314-8591
20. Khoo H, Azlan A, Tang S, Lim S (2017) Anthocyanidins and anthocyanins: colored pigments as food, pharmaceutical ingredients, and the potential health benefits. Food Nutrition Research 61:1361779. https:// doi: 10.1080/16546628.2017.1361779.
21. Pereira RN, Coelho MI, Genisheva Z, Fernandes JM, Vicente AA, Pintado ME, Teixeira JA (2020) Using Ohmic Heating effect on grape skins as a pretreatment for anthocyanins extraction. Food and Bioproducts Processing 124:320–328. https://doi.org/10.1016/j.fbp.2020.09.009
22. Castellanos-Gallo L, Ballinas-Casarrubias L, Espinoza-Hicks J C, Hernández-Ochoa LR, Nayzzel Muñoz-Castellanos L, Zermeño-Ortega MR, Borrego-Loya A, Salas E (2022) Grape Pomace Valorization by Extraction of Phenolic Polymeric Pigments: A Review. Processes 10(3):469. https://doi: 10.3390/pr10030469
23. Gordillo B, Sigurdson GT, Lao F, González-Miret ML, Heredia F J, Giusti MM (2022) Assessment of the color modulation and stability of naturally copigmented anthocyanin-grape colorants with different levels of purification. Food Research International 106:791–799. https:// 10.1016/j.foodres.2018.01.057

Citation: Botezatu, N., Covaci, E., Arseni, A. (2026). Assessment of the effects of temperature and thermal treatment duration on the stability of phenolic constituents in sweet extracts produced from Rara Neagră grape marc. *Journal of Engineering Science*. 2026, 33 (2), pp. 100-112. https://doi.org/10.52326/jes.utm.2026.33(2).08.

Publisher's Note: JES stays neutral with regard to jurisdictional claims in published maps and institutional affiliations.

Copyright:© 2026 by the authors. Submitted for possible open access publication under the terms and conditions of the Creative Commons Attribution (CC BY) license (https://creativecommons.org/licenses/by/4.0/).

Submission of manuscripts: jes@meridian.utm.md

https://doi.org/10.52326/jes.utm.2026.33(2).09
UDC 664.3:664.014:613.2

STRUCTURED OILS IN FOOD SYSTEMS: OLEOGELS AS SUSTAINABLE ALTERNATIVES TO CONVENTIONAL SOLID FATS

Viorica Bulgaru[1*], ORCID: 0000-0002-1921-2009,
Sorina Ropciuc[2], ORCID: 0000-0003-2697-5415
Iana Ciugureanu[1], ORCID: 0009-0004-1910-7833,
Olga Smerea[1], ORCID: 0009-0004-2520-439X,
Daniela Pauliuc[2], ORCID: 0000-0002-2295-1451
Natalia Netreba[1], ORCID: 0000-0003-4200-1303

[1.] *Technical University of Moldova, 168 Stefan cel Mare Blvd., Chisinau, MD-2004, Republic of Moldova*
[2.] *Stefan cel Mare University of Suceava, 13 University str., 720229, Suceava, Romania*
[3.] *Technical University of Moldova, 168 Stefan cel Mare Blvd., Chisinau, MD-2004, Republic of Moldova*
[4.] *Stefan cel Mare University of Suceava, 13 University str., 720229, Suceava, Romania*
* Corresponding author: Bulgaru Viorica, *viorica.bulgaru@tpa.utm.md*

Received: 05. 07. 2026
Accepted: 06. 12. 2026

Abstract. Nowadays, there is an increasing emphasis on the quality of dietary fats in food systems, given that the association of high consumption of saturated and trans fats with increased risks of chronic diseases. Thus, the food industry is looking for alternatives capable of reproducing the functional properties of conventional solid fats. Oleogels have emerged as a promising solution, consisting of structured liquid oils immobilized in a three-dimensional network formed by oleogelators such as waxes, monoglycerides, ethylcellulose and biopolymers. The study provides a comprehensive analysis of oleogel systems, focusing on the principles of formation, classification and structuring mechanisms. It highlights the influence of processing parameters, including cooling rate, shear and gelator selection, on the physicochemical and functional properties of oleogels. In addition, the role of different vegetable oils and extraction methods in determining gel stability and performance is discussed. Oleogels demonstrate significant potential in food applications, serving as replacements for saturated fats in products such as bakery products, confectionery, spreads and meat analogues, while improving nutritional quality. Thus, oleogels represent an innovative and sustainable strategy for the development of healthier food products with desired sensory and functional attributes.

Keywords: *fat replacement, food, oleogelator, plant-based oil.*

Rezumat: Astăzi, se pune un accent tot mai mare pe calitatea grăsimilor alimentare din sistemele alimentare, având în vedere asocierea consumului ridicat de grăsimi saturate și trans cu riscuri crescute de boli cronice. Astfel, industria alimentară caută alternative capabile să reproducă proprietățile funcționale ale grăsimilor solide convenționale. Oleogelurile au apărut ca o soluție promițătoare, constând din uleiuri lichide structurate imobilizate într-o rețea tridimensională formată din oleogelatori precum ceruri, monogliceride, etilceluloză și biopolimeri. Studiul oferă o analiză cuprinzătoare a sistemelor oleogel, concentrându-se pe principiile mecanismelor de formare, clasificare și structurare. Acesta evidențiază influența parametrilor de procesare, inclusiv viteza de răcire, forfecarea și selecția gelatorului, asupra proprietăților fizico-chimice și funcționale ale oleogelurilor. În plus, este discutat rolul diferitelor uleiuri vegetale și al metodelor de extracție în determinarea stabilității și performanței gelului. Oleogelurile demonstrează un potențial semnificativ în aplicațiile alimentare, servind ca înlocuitori pentru grăsimile saturate în produse precum produse de panificație, cofetărie, creme tartinabile și analogi de carne, îmbunătățind în același timp calitatea nutrițională. Astfel, oleogelurile reprezintă o strategie inovatoare și sustenabilă pentru dezvoltarea unor produse alimentare mai sănătoase, cu atribute senzoriale și funcționale dorite.

Cuvinte cheie: *înlocuitor de grăsimi, oleogelator, produs alimentar, ulei vegetal.*

1. Introduction

Dietary fat is a key macronutrient for health and provides more source of energy than carbohydrates or proteins [1]. In processed foods, fat enhances organoleptic characteristics. This kind of fats is generally classified into saturated fatty acids (SFA) and unsaturated fatty acids (UFA) [2]. The major problem with processed animal products is their high fat content, which is dominated by saturated fats and trans fatty acids.

In recent decades, global awareness of the adverse health effects associated with diets rich in saturated and trans fats has increased substantially. Excessive intake of these lipids has been strongly associated with a higher risk of cardiovascular diseases, obesity, type 2 diabetes, and other chronic disorders [3;4]. In response to these concerns, the World Health Organization (WHO) has launched several initiatives aimed at reducing the presence of such fats in food products. Consequently, the food industry has experienced growing pressure to develop innovative alternatives capable of replicating the technological functions of solid fats—such as texture, plasticity, and mouthfeel—while offering an improved nutritional profile [4;5]. Replacing 5% of dietary fats with polyunsaturated fats, such as those derived from vegetable and marine oils, has been reported to reduce the risk of cardiovascular diseases in humans by up to 22−37% [6]. In response to recommendations from nutrition experts and governmental regulations aimed at reducing the use of saturated and trans fats in foods, the field of oil structuring has been extensively investigated over the past decades [7;8].

In this context, oleogels have emerged as a particularly promising and innovative technological approach. Oleogels are semi-solid systems in which a large proportion of liquid oil—typically of vegetable origin and rich in beneficial unsaturated fatty acids—is immobilized within a three-dimensional network generated by a low concentration of structuring agents, commonly referred to as oleogelators [9;10]. Oleogelators, including natural waxes, glycerides, alcohols, ethylcellulose, and phytosterols, facilitate the transformation of vegetable oils into semi-solid systems by creating a structured gel network capable of entrapping liquid oil [2]. The process known as oleogelation enables the conversion of liquid oils into structures exhibiting rheological and textural properties comparable to those of conventional solid fats, such as butter, margarine, without altering the beneficial chemical composition of the oil [9]. This process is considered a nutritionally improved replacement for saturated and trans fats while maintaining the attributes desired by consumers regarding functional and sensory qualities [10]. This unique ability to “solidify” liquid oils opens up extensive opportunities for the reformulation of a wide variety of food products, including bakery and confectionery items, meat products, and spreads. Furthermore, the versatility of oleogels has attracted considerable attention in other industrial sectors. In the pharmaceutical field, oleogels are being investigated as effective delivery systems for lipophilic drugs, as they can enhance bioavailability and enable controlled release mechanisms [11]. In the cosmetic industry, oleogels provide novel textures and improved stability for creams, lotions, and other personal care formulations, while also serving as carriers for bioactive compounds [12].

Despite the rapid expansion of research in the field of oleogels in recent years, their practical application remains at a relatively early stage of development due to several existing challenges. One of the primary limitations is related to food regulations, which require the use of food-grade structuring agents and often impose restrictions on their permissible concentrations in food products. Although a wide range of oleogels has been developed using different classes of oleogelators, not all of these structuring agents are suitable for food applications [5;13]. Additional constraints include the limited understanding of the interactions between oleogels and other food components, as well as uncertainties regarding their behavior under various processing conditions associated with different food systems. Furthermore, the identification of cost-effective and readily available structuring agents remains an important challenge for the large-scale implementation of oleogels in the food industry.

Nowadays, numerous oleogels are known ffering desirable characteristics such as: thermal resistance, texture and improved structure. In addition, foods with oleogels were obtained that demonstrated that they can form textural attributes similar to products made with traditional lipid formulations, that they can improve food nutrition, have high physical and oxidative stability, and a high oil binding capacity [14].

Therefore, the objective of this review is to critically analyze current knowledge on oleogel systems, including the principles of oil structuring, the main classes of oleogelators, their physicochemical and functional characteristics, and their potential applications in food reformulation. In addition, the review highlights the main technological challenges that currently limit the large-scale adoption of oleogels in the food industry.

2. Principles of Oleogel Formation: Classification and Mechanism

The oleogels market is estimated to expand in the coming years at around 6.2% CAGR (compound annual growth rate), supported by increasing demand across the food and beverage, cosmetics and personal care, and coatings sectors. By 2035, the market value is anticipated to reach USD 1.6 billion (Figure 1).

In the food industry, the rising demand for healthier alternatives to saturated and trans fats is a key factor driving the adoption of oleogels. This trend aligns with significant shifts in consumer preferences toward functional, plant-based, and clean-label products. Owing to their favorable textural attributes, mouthfeel, and ability to enhance shelf life, oleogels represent a viable substitute for conventional fats rich in saturated fatty acids. For instance, in confectionery and chocolate applications, oleogels contribute to improved melting behavior and help prevent fat bloom. In plant-based products and processed meat analogues, they effectively replicate the structural and sensory characteristics of animal fat, delivering desirable juiciness and mouthfeel. Furthermore, oleogels can be utilized in the production of vegan cheese, plant-based meat substitutes, margarine, and butter, where they successfully emulate the spreadability, firmness, and sensory properties of traditional fat-based formulations [15].

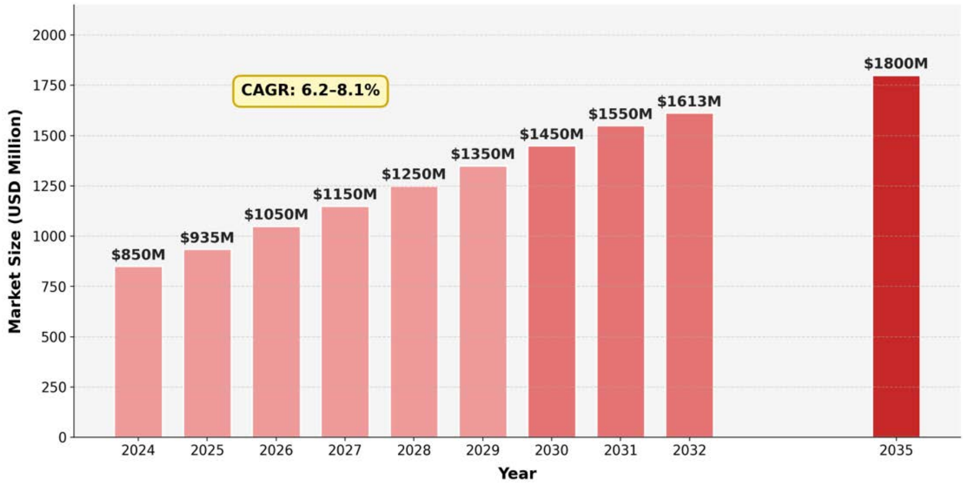

Figure 1. Global oleogels market growth projection from 2024 to 2035.

The industry framework for obtaining oleogels includes several methods categorized into 3 types of methods:

- Direct methods (direct hot method and direct cold method) - provide a process of dispersing waxes, fatty acids, monoglycerides and ethylcellulose, where they are heated until completely dissolved in liquid oil, followed by natural cooling of the mixture to refrigeration temperatures.
- Indirect methods - structured the plant material by adding a polymer to an aqueous solvent or emulsion. The freeze-drying/drying process is used to remove water in order to preserve the structure of the gel network. These methods are appreciated in the case of long-term storage of the formed oleogels because the obtained structure does not show oil removal [16].
- Semi-direct method (capillary suspension) - a small amount of immiscible liquid (usually water) is added to a dispersion of food-grade particles (such as cellulose, soy protein, or starch) in edible oil. This induces the formation of a capillary bridge between the particles, creating a strong three-dimensional network that spans space and immobilizes the oil [17;18].

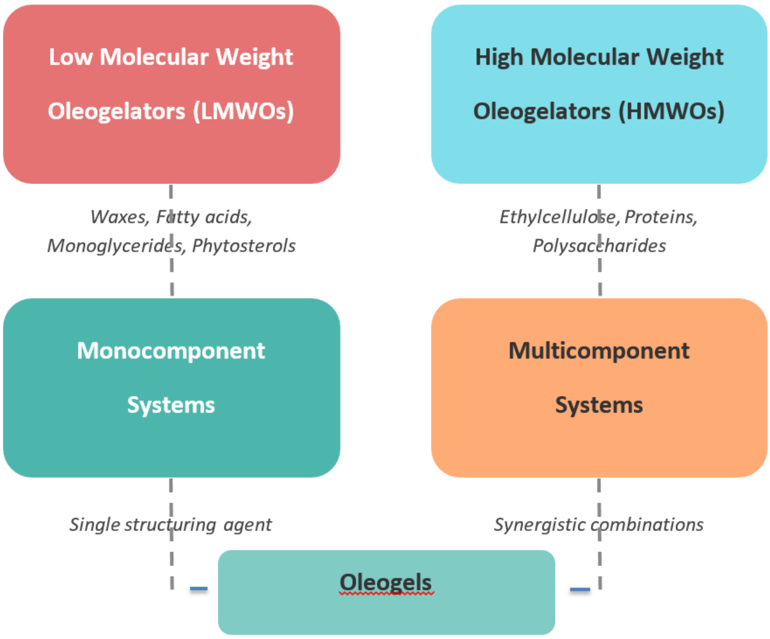

Figure 2. Oleogel classification based on oleogelator type

All of these methods allow the production of oleogels by simpler or more complex techniques. However, there are 3 factors or steps in the methods of obtaining oleogels that are critical, namely:

- Cooling rate: Adequate cooling is essential for the formation of a stable network.
- Shear: Shear applied during gelation can modify the crystal structure.
- Gelator selection: Low molecular weight gelators (LMOG) and high molecular weight gelators (HMOG).

Oleogels are primarily classified according to the chemical nature of the structuring agent, which can be a LMWO, such as waxes or monoglycerides, or a HMWO, such as ethylcellulose, (Figure 2) [19;20]. The formation of the three-dimensional network is a self-assembly process guided by non-covalent physical interactions, being a thermo-reversible phenomenon. For LMWOs, the predominant mechanism is crystallization, where the morphology of the crystals (shape, size, polymorphism) dictates the macroscopic properties of the gel [21]. The efficiency of an oleogelator is defined by its critical gelation concentration (CGC), the minimum value required to form a stable gel [22]. Understanding these fundamental mechanisms is essential for the rational design of oleogels with specific properties.

3. Oleogelators in oleogels production

The selection of the oleogelator is crucial for the functionality of the final product. A wide range of compounds has been explored, each with distinct pro and cons, as summarized in Table 1.

Table 1

Comparative analysis of common oleogelators [6;21]

Oleogelator Type	Structuring Mechanism	Key Advantages	Common Applications
Natural Waxes	Micro-crystal network	Efficient, low cost, GRAS status	Margarine, chocolate, processed meat
Monoglycerides	Lamellar crystal network	Very efficient, fine texture	Confectionery fillings, spreads
Phytosterols/Oryzanol	Nanometric fibrillar network	Health benefits, transparency	Functional foods, pharmaceuticals
Ethylcellulose	Entangled polymer network	Thermal stability, elasticity	Fat replacer in meat, frying
Proteins/Polysacchari des	Particle aggregation	Sustainable sources, clean label	Meat alternatives, vegan foods

**GRAS - Generally Recognized As Safe.*

Oleogelators are defined as the main structuring agents responsible for the development of the three-dimensional gel network, whereas “additives” refer to secondary ingredients incorporated to enhance particular properties, such as stability, oxidative resistance, or emulsifying capacity. Although certain compounds (for instance waxes or proteins) may be included in both groups, their classification is determined by the specific functional role they perform within the formulation. The appropriate selection of biopolymers plays a crucial role in achieving efficient oleogelation. In this regard, proteins and polysaccharides are especially important because of their capacity to form stable gel structures, increase oil-binding ability, and improve the mechanical and sensory characteristics of oleogels [23].

Waxes constitute a diverse group of natural esters that are insoluble in water and particularly effective as moisture barriers. The composition of wax types depends on their source and usually contains different amounts of fatty alcohols, fatty acids and hydrocarbon chains. The ratio between these components is exposed on their gelation behavior in different systems. The advantages of using natural waxes in the formulation of oleogels include good structuring capacity at low concentrations, they are available in sufficient quantities and have an acceptable price [24;25].

The properties of oleogels are influenced by the oil used, oleogelator, structuring agents and the conditions/operations of the technological processing process. These factors determine the degree of structure crystallinity, the gel strength, the oil binding capacity and the behavior of the oleogelator upon melting. Oleogelators exhibit different behaviors during processing, so by selecting and combining the right ingredients, oleogels with customized chemical and physical properties can be formed for subsequent applications in the food industry. Various plant-derived waxes have been extensively studied for their potential use in edible oleogels. Several of these waxes have been classified as GRAS by the US Food and Drug Administration [25;26].

Brykczynski et al. showed that wax esters represent an important component in the formation of the structure of wax-based oleogels, noting that the ester content could range from approximately 15% to about 90% [27].

Beeswax typically exhibited a melting point between 61 and 65 °C, providing moderate thermal stability [28]. It aws widely recognized as an effective gelator for structuring edible oils due to its ability to form gels at very low crystalline mass fractions [29].

Carnauba wax showed the highest melting point, generally ranging from 80 to 85 °C, which contributes to its remarkable thermal stability. In addition, it is capable of forming stable gels at concentrations as low as 1.5% [30].

Rice bran wax had a relatively high melting point of approximately 78–82 °C, which ensures excellent thermal stability and favorable crystallization behavior, enabling the formation of stable gel networks [31].

Sunflower wax (SW) exhibited a melting point between 74 and 77 °C, largely due to its high wax ester content, which supports the formation of stable gel structures [32].

Zhang et al. reported that oleogels structured with monoglycerides represent some of the most promising systems, as they are able to crystallize and form strong networks with good elastic properties even at low concentrations (around 3%). In hydrophobic environments, the glycerol head groups of monoglycerides self-assemble into a reverse lamellar phase, while hydrogen bonding between the hydrophilic heads promotes the crystallization of the aliphatic chains. This process leads to oil gelation and contributes to the elasticity of the resulting system [33].

A significant gap remains in the current research regarding the use of phytosterol–γ-oryzanol systems for oleogel preparation. In such complex systems, it is still unclear whether the gelator and the oil phase can interact synergistically to form a stable crystalline network capable of uniformly distributing water and liquid oil droplets. Furthermore, it remains uncertain whether an excessively dense network could hinder the melting behavior of margarine or whether multi-component crystallization may contribute to achieving the desired textural properties [34]. For instance, Pang et al. investigated the use of sterols combined with beeswax at different concentrations as oleogelators and evaluated their effects on the morphology, oil-binding capacity, texture, color, and stability of the resulting oleogels. The results indicated that, due to the longer chain structure of plant sterol ester, beeswax - plant sterol ester oleogels exhibited enhanced gelation capacity. Moreover, improved oil retention was achieved at lower concentrations, leading to the formation of more robust oleogel structures. In addition, the hardness of beeswax - plant sterol ester oleogels was significantly higher compared with other oleogel systems [35].

Ethylcellulose, a cellulose derivative, is a multifunctional polymer with application in the food industry as a non-toxic additive, as an emulsifier or stabilizer, which can easily replace synthetic additives with the same properties [36;37]. By the direct dispersion method, ethylcellulose can transform oils into oleogels [38], solid and stable, with high nutritional value. However, ethylcellulose can contribute to accelerating the processes of lipid oxidation and reducing the oxidative stability of oleogels, considering the high temperature (125-140 ºC) of dissolution of this additive in oil, in the manufacture of oleogels. Nevertheless, ethylcellulose remains an appreciated additive in the production of oleogels, with subsequent use in various branches of the food industry, due to its thermal stability, viscosity control and good binding with various vegetable oils [39].

Qiu et al. obtained ethylcellulose-olive oil oleogels, and the results showed that the oil plays a key role in the gel strength due to its influence on solvent-polymer interactions [40]. Cafuero et al. in their research reported that the quality of oleogels formulated with ethylcellulose can be improved by incorporating additional components, such as phospholipids or mono- and diglycerides. The oleogels obtained by this team based on ethylcellulose and soybean oil, were effectively adjusted in terms of their mechanical and physical properties by modifying the oil phase [41].

While oleogelators such as waxes and phytosterols have been extensively investigated, biopolymers represent relatively novel structuring agents that have been less studied but show considerable potential. These materials may provide promising alternatives due to their enhanced oil-binding capacity, improved thermal stability, and emulsifying properties.

Kirpaci et al. reported that pea protein, although less frequently used in oleogel production, exhibits a high oil-binding capacity and remains effective even at low concentrations, providing improved texture and structural stability [23]. Oleogels based on protein isolates can form strong network structures with minimal oil leakage; however, they also present certain limitations, such as the need for relatively high protein concentrations and potential allergenic effects for specific consumer groups, as highlighted by Sinha et al. [42]. It has also been demonstrated that faba bean protein shows good oil-binding capacity at optimal pH values, although it may present challenges during subsequent technological processing [43]. Similarly, whey protein isolate has exhibited a high oil-binding capacity even at low protein concentrations [44]. In addition, xanthan gum has been reported to provide higher stability, reduced oil loss, and increased gel strength in oleogel systems [45].

3. Plant-based oils used in the production of oleogels

Lipids have applications in foods such as snacks, dairy products, bakery products, and confectionery, due to the need to shape the physical and sensory attributes of these products. For example, solid fats obtained from oils by processes such as hydrogenation, interesterification and fractionation are widely used in a variety of food products. During processing, oils and fats undergo various physicochemical changes that define the product characteristics. An alternative has been considered palm and palm kernel fats, widely used in foods to replace partially hydrogenated fats. However, there are growing concerns about the use of these fats, given their high content of saturated fatty acids and sustainability issues [46]. Thus, the increasing awareness of consumers about the link between diet and health has raised concerns about these fats, especially due to the high levels of saturated and trans fatty acids. As a result, considerable efforts have been made to develop alternative approaches to produce solid fats with a reduced content of saturated fatty acids. [47]. One promising strategy involves structuring liquid oils using oleogelators to create oleogels. In this context, the usefulness of fats and oils in different food products and the modification of fats during processing involve the research of other formulations that can create food products with high nutritional and biological value without the formation of toxic compounds for the health of the consumer [48].

Oils represent about 90% of the composition of an oleogel. In accordance with the oleogel manufacturing process, vegetable oils are chosen according to certain criteria: availability, functionality, low cost, economic importance, nutritional benefits for industrial applications. Vegetable oils with wide application in this field are: soybean oil, olive oil, sunflower oil and sunflower oil with high oleic acid content [49].

The selection of oil for oleogel formulations is determined by the desired properties of the final product. Key considerations include cost, availability, regulatory constraints, and the intended application. In addition, it is essential to evaluate the compatibility and stability of the selected oil with other ingredients and additives to ensure the development of a stable and efficient oleogel system [48]. Some of the most discussed oils in obtaining oleogels are the following.

Soybean oil produced from soybean seeds, that are valued for their agronomic and quality characteristics, making them an important oil crop produced worldwide, providing a nutritionally valuable oil. The US has a soybean production of 8.24 million tons. Brazil contributes 4.28 million tons, Argentina 3.28 million tons, China 3.26 million tons and the EU approximately 2.87 million tons. Soybean oil is composed of 61% polyunsaturated fatty acids, 25% monounsaturated fatty acids and 15% saturated fatty acids [50]. The essential fatty acids are represented in a proportion of 89% by linolenic acid and 11% by α-linolenic acid. Most of the soybean oil (48%) is used in the manufacture of margarine, cooking and salad oils, and mayonnaise.

Rapeseed is characterized as being among the first crops after oil production. **Rapeseed oil** contains approximately 6% saturated fatty acids, is rich in tocopherol, has a lower stability, a property affected by its composition in compounds with high chemical reactivity. It is most often used in the food industry as a vegetable oil or in the manufacture of margarine. [51].

Sunflower oil ranks fourth as the most widely used plant-based oil and, in certain regions, is preferred over soybean, cottonseed, and palm oils. The content of saturated fatty acids does not exceed 10%, in significant quantities it is oleic acid (55-75%) and linoleic acid

(15-35%). It is commonly used for cooking, salad dressings, and margarine production; however, it is less suitable for frying due to its relatively low oxidative stability. Nevertheless, it exhibits good flavor stability [52].

Virgin **olive oil** is obtained by mechanical or other physical processes under specific thermal conditions that do not cause alterations in the oil and and is not subjected to other technological treatments specific to the field of obtaining and processing plant-based oils. It is a mixture of triacylglycerols, with some fatty acids, especially palmitic, oleic and linoleic acids. It contains approximately 71% oleic acid [53] and as minor components tocopherols or phenolic compounds with antioxidant properties [54].

Corn oil is extracted from corn kernels, which have a low oil content (3–5%), while the germ contains about 30% of oil. It has a pleasant aroma and about 15% of saturated fatty acids. The oil is characterized by very low α-linolenic acid content and high levels of polyunsaturated fatty acids. Among plant-based oils, corn oil is considered one of the most abundant sources of phytosterols (8300–25,500 ppm) and tocopherols (1130–1830 ppm). Its predominant phytosterol is β-sitosterol (63–70%), while γ-tocopherol (68–89%) represents the major tocopherol fraction. Typically obtained as a by-product of corn starch production, corn oil is widely used in margarine manufacturing, as well as for cooking and salad dressings [55].

Sesame oil is extracted from sesame seeds, that are rich in oil, about 42–56%. It has a good resistant to oxidation process and is known for its potential health benefits. This type of plant-based oil contains about 82% unsaturated fatty acids, with an equal contribution between oleic and linoleic acid. Sesame is also a rich source of minerals and vitamins, including iron, magnesium, copper, calcium, phytosterols, as well as vitamins B1 (thiamine) and E (tocopherols) [56]. Compared to other plant-based oils, sesame oil exhibits superior oxidative stability, making it suitable for use as a cooking oil. [57].

Rice bran oil is is a high-quality and versatile edible oil obtained from the outer layer of rice. It is highly valued in the food industry due to its high smoke point (around 230°C), neutral taste, and significant content of antioxidants such as gamma-oryzanol [58]. It is rich in monounsaturated fatty acids (oleic acid, 38.4%) and polyunsaturated fatty acids (linoleic acid, 34.4%), providing a well-balanced fatty acid profile [59]. It is commonly used in high-temperature processes, including frying and baking, as well as in salad dressings, and serves as a stable and healthier alternative to conventional oils in industrial food applications [58].

Linseed oil is extracted from flax seeds and is rich in unsaturated fatty acids, particularly α-linolenic acid (50%). However, its high linolenic acid content makes it highly prone to oxidation, which can quickly lead to undesirable flavors in food products. Therefore, edible linseed oil should be stored under cool, oxygen-free, and light-protected conditions, often with the addition of antioxidants to enhance its stability. This type of oil is most often used in the preparation of salad dressings, margarine, and other food products as a source of omega-3 fatty acids [60].

Pumpkin seed oil exhibits strong antioxidant, anti-inflammatory, and antibacterial properties, making it a promising candidate for various applications in the food industry [61]. It is a good source of biologically active compounds, being considered a "special oil." α-tocopherol, γ-tocopherol, α-tocotrienol and γ-tocotrienol are the phytochemical components that contribute to the formation of the antioxidant properties specific to pumpkin seed oil [62]. It is not recommended for frying or cooking over high heat because it has a low smoke point of approximately 160°C.

Research in the field has shown that the gelation reaction of different oleogel systems depends on the chemical structure of the oil, mainly on the chain length of the fatty acids and the number of unsaturated fatty acids. Tatel et al. showed that oils with a higher degree of saturation strengthen the oleogel [63]. Also, five types of oils (rapeseed, rice bran, corn, sunflower, and high-oleic sunflower oil), differing in their degrees of saturation, were analyzed to assess how fatty acid profiles affect wax-induced gel formation. The findings indicated that oils with a higher degree of saturation contributed to the formation of stronger oleogel structures [63].

Other oil characteristics, which have a strong effect on the gelation kinetics and crystallization behavior of oleogels, include the viscosity and polarity of the oil. Researchers have observed that weaker gels form in oils with higher polarity due to substantial interactions between the gelator and the solvent [64] Oils with long carbon chains and higher viscosity produce gels with higher firmness [65].

The effect on the rheological and microstructural characteristics (pore diameter) of oleogels in relation to the type of oil also are importan. For example, the results of Zetzel et al. showed that a larger pore diameter (more stable gel) was observed for rapeseed oil, and the pore diameter was reduced with increasing unsaturation of the oil component [66].

The quality, stability, and structure of the oleogel is also influenced by the method of extraction/obtaining the oil from vegetable raw materials. The extraction method influences the fatty acid composition, the presence of impurities, and the degree of oxidation in the liquid oil, all of which directly affect how the oil interacts with the oleogelator and ultimately determine its rheological behavior [66].

The extraction technique governs the fatty acid composition, impurity content, and oxidative status of the liquid oil, which in turn directly influence its interaction with the oleogelator and the resulting rheological characteristics. Oils obtained through different extraction methods contain variable amounts of minor constituents, including phospholipids, free fatty acids, and tocopherols. These components may either impede or promote the development of the oleogelator’s crystalline network, thereby affecting the textural attributes and oil-binding capacity [67;68].

Modern industry, as well as the classical one, proposes and uses three methods of extracting oil from vegetable raw materials:

1. Mechanical extraction (press);
2. Solvent extraction
3. Pre-press and solvent method [69].

Mechanical oil extraction can be performed using two main approaches: hot pressing and cold pressing. In hot pressing, the raw material is subjected to elevated temperatures generated during processing, which facilitates the extraction of a substantial proportion of the oil, typically exceeding 75%. In contrast, cold pressing relies on hydraulic systems that operate without significant heat generation, thereby preserving the natural sensory characteristics of the oil. Moreover, the absence of high temperatures minimizes protein denaturation. Although hot pressing generally yields higher extraction efficiency, it often results in reduced oil quality due to thermal degradation [70]. Consequently, cold-pressed oils are considered superior in terms of maintaining their intrinsic properties and being free from chemical alterations, which has contributed to their growing demand. Nevertheless, the efficiency of cold pressing is influenced by several parameters, including applied pressure, screw rotation speed, moisture content of the raw material, and processing temperature. Cold pressing offers several advantages, including a relatively simple technological process, ease of implementation, and economic benefits due to low capital and operating costs. However, a major limitation of this method is the relatively high amount of residual oil remaining in the press cake, which can reach up to 10–20% according to some reports [71].

Solvent extraction is commonly applied to oilseeds with an oil content below 20%, particularly in soybean processing, where it plays a key role in the oil industry. This method is highly efficient, leaving less than 1% residual oil in the meal after extraction. However, it is relatively time-consuming, as it requires adequate contact between the solvent and the oil within the seed matrix.

Particle size is an important parameter in this process, as reducing it enhances solvent penetration into the plant material and improves extraction yield. Hexane is the most widely used solvent due to its strong affinity for vegetable oils, appropriate boiling point, and relatively low latent heat of evaporation, which supports energy-efficient recovery during distillation. Additionally, hexane is non-corrosive, chemically stable under processing conditions, neutral toward the extracted oil, and economically accessible. Nevertheless, its high flammability necessitates the use of specialized equipment to ensure safe operation [72].

From the perspective of a circular bioeconomy, alternative, more environmentally friendly solvents such as ethanol, isopropanol, and certain hydrocarbons are increasingly being considered. The efficiency of solvent extraction depends on multiple factors, including the composition and moisture content of the raw material, its pretreatment, the type and temperature of the solvent, and the solvent-to-solid ratio [73].

Despite its advantages, this method has several drawbacks, including prolonged processing time, high solvent consumption, potential degradation of heat-sensitive compounds, and the formation of undesirable by-products [69;72].

The oil obtained by this method also needs to be refined. The stages of refining technology include: degumming to remove phospholipids and mucilaginous gums; removal of free fatty acids, metals and chlorophyll by neutralization; washing and drying to remove traces of water and soaps; bleaching to change the color; deodorization to remove volatile substances and carotenoids [74;75].

The **pre-pressing** followed by solvent extraction method is typically applied to oilseeds with an oil content exceeding 25%. In this approach, the initial oil content of the seeds is reduced to approximately 16–20% through mechanical pressing. The resulting press cake is subsequently subjected to solvent extraction under controlled conditions (around 50 °C for approximately 7 hours), allowing the residual oil to be recovered through solvent addition. Using this technique, the residual oil content in the meal can be reduced to below 0.5% [72]. As previously noted, each extraction method presents specific advantages and limitations. Generally, a key drawback of conventional techniques is the lower oil recovery achieved by mechanical pressing compared to solvent extraction, which may negatively impact economic efficiency. Conversely, the reliance on organic solvents in solvent-based methods, including the pre-pressing and solvent extraction approach, raises significant environmental and safety concerns [69].

Gotor and Rhazi in their work presented schematically (Figure 3) the production of sunflower oil. Subsequently, the oil obtained by this extraction method is subjected to several purification steps [76].

Oil refining after solvent extraction includes five main steps to remove minor components: degumming, neutralization, bleaching; winterization and deodorization.

Schematic representation of these stages in the oil processing process can be seen in the form of various simplified diagrams.

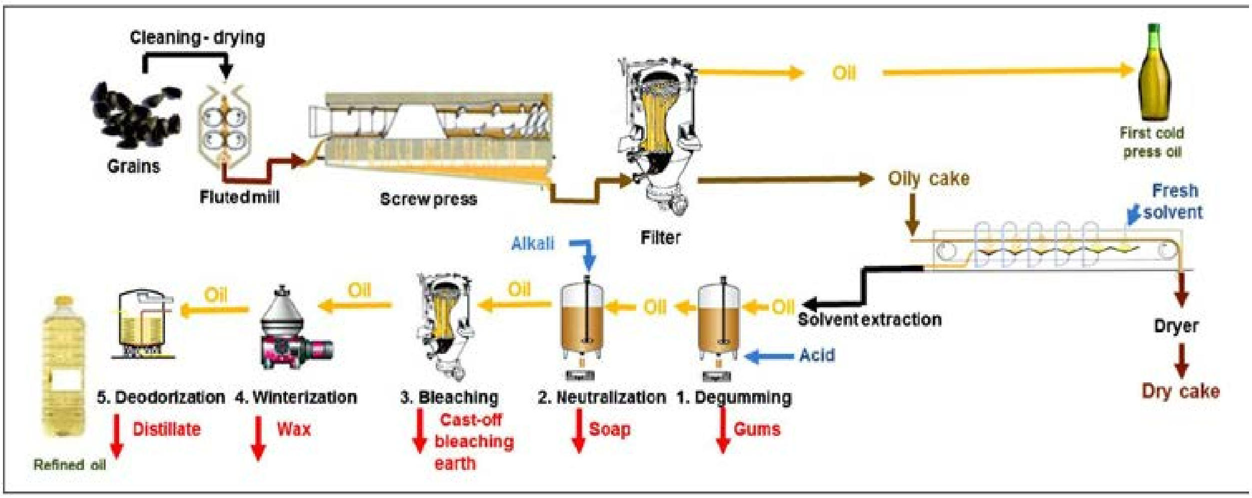

Figure 3. Extracting and refining steps of sunflower oil, [76].

The primary aim of the *degumming* step is to eliminate phospholipids, which are responsible for the dark coloration and undesirable odors of the oil. This process can be carried out using water in the case of hydratable phospholipids, or through acid pretreatment—commonly with phosphoric or citric acid—when non-hydratable phospholipids are present [77]. According to Brevedan et al., degumming can remove approximately 83% of the total phospholipids from solvent-extracted sunflower oil [78].

In addition to phospholipid removal, refining also facilitates the reduction of metal ions. Zufarov et al. reported that acid degumming decreases calcium and magnesium levels by 88% and 90%, respectively [77]. Furthermore, Kreps et al. demonstrated that the combination of degumming and neutralization can reduce free fatty acid content by up to 82% [79]. Degumming can also be carried out through enzymatic treatment. Lamas et al. demonstrated that this approach, when applied to sunflower oil, can achieve substantial reductions in impurities, including up to 97.8% removal of phospholipids, 99.4% reduction in phosphorus content, as well as decreases of 81.2% and 93% in calcium and magnesium levels, respectively [80].

Alkaline *neutralization* of oil or deacidification is an important step in the chemical refining process of edible oil with the aim of neutralizing/removing free fatty acids from the oil, using caustic soda and potassium. These treatments contribute to the transformation of fatty acids into soaps which can subsequently be decanted or separated by centrifugation. Also, this purification step allows to decrease the tocopherol content in the oil, considering that they are unstable in contact with air and alkali. For example, Alpasan et al. showed a decrease of 4.7%, Naz et al. a 16% reduction and Talal et al. a 10% decrease in sunflower oil [81;82;83]. The neutralization process allows the removal of sterols from the oil, in amounts of about 29%. For example, Ruiz-Méndez et al. confirm that a significant amount of eliminated sterols is found in the soap paste obtained from sunflower oil, arguing the influence of the alkali concentration and the temperature used during neutralization on the total content of eliminated sterols [84].

Bleaching earth is a clay-based, mineral-rich material widely used in filtration, adsorption, and decolorization processes. Within the vegetable oil refining sequence, it represents one of the key steps, where bleaching earth—being the most commonly employed adsorbent—is added to crude edible oil to remove undesirable components. This material is capable of adsorbing a wide range of impurities, including heavy metals, chlorophyll, carotenoids, hydroperoxides, free fatty acids, and various non-glyceride compounds [85]. Bleaching earths are also effective in removing residual soaps, phospholipids, and other polar lipids from the oil [71]. One of the main disadvantages of this step is that the used bleaching earth is usually disposed of in landfills, causing environmental pollution. Therefore, one of the goals of this step should include the processing of this used bleaching earth. From a technological standpoint, bleaching is considered one of the simplest stages in the refining process; however, it is not without drawbacks. During this step, oil losses of up to 2% of the total mass may occur [86]. In practice, bleaching earth is added in quantities exceeding its theoretical adsorption capacity—typically up to 5% (*w/w*) of the oil—and the mixture is agitated for a defined period. The process is commonly conducted at temperatures above 80°C. Nevertheless, studies indicate that the adsorption efficiency of bleaching earth may decline as the oil temperature increases [74].

Winterization can be generally defined as a physical fractionation process aimed at separating high-melting triglycerides. As a result, the oil is divided into two distinct phases: a viscous liquid fraction and a solid fraction. The solid phase is separated through crystal precipitation followed by filtration, under controlled conditions of temperature, time, and agitation. The crystallization of lipids proceeds through three main stages: supercooling, nucleation, and crystal growth [87]. This method also known as dewaxing, primarily aims to remove long-chain waxes and saturated triglycerides by lowering the oil temperature to approximately 6–8 °C, followed by the separation of the resulting solid fractions. This process targets compounds that crystallize at low temperatures and are responsible for oil turbidity. In the case of sunflower oil, these are predominantly waxes [88;89].

The waxes found in sunflower oil mainly consist of esters formed from long-chain fatty acids and fatty alcohols, typically containing 34 to 50 carbon atoms, with melting points ranging between 70 and 80 °C [90]. Among the refining stages, winterization has the least impact on minor bioactive compounds, particularly tocopherols; for instance, total tocopherol content in sunflower oil decreases by only about 2.4%. Furthermore, Kreps et al. (2014) reported that this process does not significantly affect chlorophyll content [79].

Deodorization represents the final stage of the vegetable oil refining process, designed to enhance oil quality and sensory attributes by removing undesirable odors. This step is both critical and mandatory, with key technological objectives focused on eliminating minor components responsible for off-flavors, including volatile aroma compounds, free and fluorinated fatty acids, and other trace constituents such as tocopherols, sterols, and pesticide residues [91].

During deodorization, the oil is exposed to high temperatures, vacuum or stripping steam, and controlled pressure for a defined period. The process is optimized to maximize the removal of unwanted substances while minimizing the loss of valuable minor components and limiting the formation of trans fatty acids or oxidation products [92]. However, excessively high temperatures can trigger chemical reactions—such as oxidation, cis-trans isomerization, cyclization, and polymerization—that degrade unsaturated fatty acids and generate hazardous contaminants, including 3-monochloropropane-1,2-diol and glycidyl esters [93].

The reduction of minor compounds in deodorized oil, typically less than 20%, partly results from their removal with the injected steam. As a consequence, valuable constituents such as tocopherols, tocotrienols, phytosterols, squalene, and hydrocarbons are concentrated in the deodorization distillate, which represents a significant by-product of edible oil refining. For instance, Naz et al. reported that sunflower oil deodorization distillates contain 13.9–14.2% sterols, 6.5% tocopherols, and 16.5% total hydrocarbons [82].

4. The correlation between the chemical composition of vegetable oils and oleogelation capacity

Vegetable oils are complex lipid systems whose chemical structure and functional properties are profoundly influenced by the nature of their fatty acids and minor bioactive compounds. In the context of oleogel development - semisolid systems obtained through structuring liquid oils - these characteristics are crucial, as they determine the mechanisms of molecular self-assembly and the stability of the three-dimensional networks formed. A comparative analysis of cold-pressed and refined oils highlights significant differences in their oleogelation behavior, rooted in their chemical composition [94].

At the molecular level, vegetable oils are predominantly composed of triacylglycerols (TAGs), esters of glycerol with various fatty acids. For instance, olive oil is rich in oleic acid (MUFA), sunflower oil contains high amounts of linoleic acid (PUFA), and coconut oil is dominated by saturated fatty acids such as lauric acid. These compositional differences directly influence the physical properties of the oils: saturated fatty acids promote ordering and crystallization, whereas polyunsaturated fatty acids increase fluidity and reduce the tendency for molecular organization [95].

In addition to the major TAG fraction, vegetable oils contain a minor fraction composed of phospholipids, phytosterols, tocopherols, and phenolic compounds. This fraction plays a critical role in oleogelation by introducing additional intermolecular interactions, such as hydrogen bonding or dipolar interactions. For example, cold-pressed sesame oil contains lignans and phenolic compounds that can stabilize supramolecular structures, while rapeseed oil contains phytosterols capable of forming fibrillar networks.

The method of oil extraction has a direct impact on the preservation or removal of these components. Cold-pressed oils, such as extra virgin olive oil, flaxseed oil, and pumpkin seed oil, are obtained mechanically at low temperatures, which preserves the minor fraction and the native TAG structure. These oils behave as complex colloidal systems in which amphiphilic compounds (e.g., phospholipids) can act as nucleation agents, facilitating the initiation of crystallization processes. Consequently, during oleogelation, these oils may exhibit an intrinsic capacity for self-structuring, generating heterogeneous three-dimensional networks without the need for large quantities of external oleogelators [96].

In contrast, refined oils, such as refined sunflower oil or soybean oil, undergo intensive purification processes that remove most minor components. The result is an almost ideal lipid system dominated by TAGs, with a reduced level of chemical heterogeneity. In the absence of polar compounds and structuring impurities, nucleation processes are limited, and oleogelation becomes dependent on the addition of external structuring agents, such as beeswax, monoacylglycerols, or purified phytosterols.

The mechanism of oleogelation essentially involves molecular self-assembly and controlled crystallization, mediated by weak intermolecular interactions. Van der Waals forces between hydrocarbon chains play a dominant role, and in the presence of polar compounds, hydrogen bonding can also occur. In oils rich in saturated fatty acids, such as coconut oil, crystallization occurs rapidly, leading to the formation of rigid networks. In contrast, oils rich in polyunsaturated fatty acids, such as sunflower or flaxseed oils, exhibit higher molecular mobility, which hinders the formation of stable structures [97].

Differences between cold-pressed and refined oils become evident in the formation of oleogels. Cold-pressed oils tend to generate more heterogeneous structures due to the presence of multiple crystallization nuclei and complex molecular interactions. These structures may be less stable over time but offer the advantage of superior nutritional functionality. Refined oils, on the other hand, allow the formation of more uniform and predictable oleogels but require precise control of processing conditions and the addition of specific oleogelators [98].

In conclusion, the oleogelation capacity of vegetable oils results from a complex interplay between chemical composition and processing method. Cold-pressed oils, such as olive, sesame, and flaxseed oils, provide a favorable environment for self-organization due to their richness in minor compounds, whereas refined oils, such as sunflower or soybean oils, require external interventions to develop comparable structures. Understanding these correlations is essential for the design of innovative food products in which structure, stability, and nutritional value must be concurrently optimized.

5. Oleogels in Food Systems: Opportunities and Challenges

Oleogels have been increasingly utilized in the formulation of diverse food products, such as spreads, baked goods, confectionery, dairy, and meat-based items. Beyond their role as substitutes for trans and saturated fats, they exhibit multiple functional properties. Specifically, oleogels can act as delivery systems for lipid-soluble bioactive compounds, contribute to the stabilization of emulsifier-free systems, improve oil retention, and enhance the thermal resistance of food products [97].

However, for all these beneficial aspects of oleogels used in the food industry to be noted in a food product, its compatibility with the food matrix must be ensured, which is currently one of the biggest challenges in the field.

The overall quality of oleogels, as well as the type and quality of the oil employed, significantly influence their characteristics, particularly the sensory attributes.

In addition, processing conditions and subsequent storage, especially exposure to temperature variations, play a crucial role in determining the textural properties of oleogels.

5. Conclusions

This review indicates that the functionality of oleogels is governed by several interrelated factors, including the nature of the oleogelator, the composition of the oil phase, and the applied processing conditions. Collectively, these parameters dictate the structural integrity, oil retention capacity, and overall behavior of oleogels in food systems. Furthermore, the incorporation of plant-based oils and naturally occurring structuring agents contributes to the development of products with a clear label, aligned with sustainability trends. Despite their significant potential, the large-scale industrial application of oleogels remains constrained by regulatory limitations, economic considerations, and an incomplete understanding of their interactions within complex food matrices. Therefore, further research efforts should be directed toward optimizing the formulation, improving oxidative stability, and improving compatibility across diverse food applications. However, oleogels represent an extremely promising strategy for developing healthier and more sustainable fat alternatives, with substantial potential to advance and redefine contemporary food formulations.

Acknowledgments: This work was supported by a grant of the Ministry of Research, Innovation and Digitization, CNCS – UEFISCDI, project number PN-IV-PCB-RO-MD-2024-0173, within PNCDI IV and NARD 25.80013.5107.25ROMD.

Contribution of authors

Viorica Bulgaru: Conceptualization, methodology, writing – original draft, writing – review & editing, investigation, project administration, supervision.
Sorina Ropciuc: Conceptualization, methodology, writing – original draft, writing – review & editing, investigation, project administration, supervision.
Iana Ciugureanu: Data curation, investigation, writing – original draft.
Olga Smerea: Data curation, investigation, writing – original draft.
Daniela Pauliuc: Data curation, investigation, writing – original draft.
Natalia Netreba: Conceptualization, methodology, writing – original draft, writing – review & editing.

Conflicts of Interest: The authors declare no conflict of interest.

References

1. Forouhi NG, Krauss RM, Taubes G, Willett W (2018) Dietary Fat and Cardiometabolic Health: Evidence, Controversies, and Consensus for Guidance. BMJ 361:k2139. https://doi.org/10.1136/bmj.k2139
2. Silva RCD, Ferdaus MJ, Foguel A, Da Silva TLT (2023) Oleogels as a Fat Substitute in Food: A Current Review. Gels 9:180. https://doi.org/10.3390/gels9030180
3. Abe A, Aiello I, Rossi C, Caputo P (2025) Oleogels: Uses, Applications, and Potential in the Food Industry. Gels 11:563. https://doi.org/10.3390/gels11070563
4. Pehlivanoğlu H, Demirci M, Toker O, Konar N, Karasu S, Sağdıç O (2018) Oleogels, a promising structured oil for decreasing saturated fatty acid concentrations: Production and food-based applications. Critical Reviews in Food Science and Nutrition, 58, pp.1330–1341. https://doi.org/10.1080/10408398.2016.1255393
5. Pușcaș A, Mureșan V, Socaciu C, Muste S (2020) Oleogels in Food: A Review of Current and Potential Applications. Foods 9:70. https://doi.org/10.3390/foods9010070
6. Kirnapci M, Aksoylu Özbek Z (2026) Emerging trends and recent innovations in oleogel-based fat substitutes for sustainable foods. European Food Research and Technology 252:52.
7. Roche HM (2005) Fatty acids and the metabolic syndrome. Proceedings of the Nutrition Society 64(1):23–29. https://doi.org/10.1079/PNS2004405
8. Hughes NE, Marangoni AG, Wright AJ, Rogers MA, Rush JWE (2009) Potential food applications of edible oil organogels. Trends Food Scientific Technology 20, pp 470–480. https://doi.org/10.1016/j.tifs.2009.06.002
9. Le Q, Fang Z, Chen H, Wu J (2025) Comprehensive Review on Oleogels Structured by Lipid-Based Compounds: From Structure Mechanisms to Nutritional Functionalities and Applications in Food Industry. Comprehensive Reviews in Food Science and Food Safety, 24. https://doi.org/10.1111/1541-4337.13345
10. Martins AJ, Vicente AA, Cunha RL, Cerqueira MA (2018) Edible oleogels: an opportunity for fat replacement in foods. Food Function 9, pp 758–773. https://doi.org/10.1039/C7FO01638H.
11. Hashemi B, Assadpour E, Jafari SM, (2026) Oleogels as novel carriers for improving the bioaccessibility of bioactive compounds: From design to applications in food products. Future Foods, 13, 100932.
12. Yaqoob N, et al. (2024). Oleogels for the Promotion of Healthy Skin Care Products. Current Pharmaceutical Biotechnology, 25, pp 2326–2336.
13. Soleimanian Y, Tanti R, Shaw N, Marangoni AG (2024) Novel strategies for structuring liquid oils, their applications, and health implications. In: Advances in oleogel development, characterization, and nutritional aspects. Springer, pp 39–76.
14. Marangoni AG, Garti N (2011) Edible Oleogels. Structure and Health Implications. First Edition. AOCS Press, Urbana. ISBN 978-0-9830791-1-8. https://doi.org/10.1016/C2015-0-02413-3

15. Transparency Market Research. Oleogels Market (2024) [cited 2026 March 24]. Available from: https://www.transparencymarketresearch.com/oleogels-market.html
16. Xu HJ, Li T, Zhang HX, Shi CH, Cao JQ, Zhang XR (2022) The application of oleogels in food products: Classification, preparation, and characterisation. Acta Alimentaria 51, pp 462–478. https://doi.org/10.1556/066.2022.00099
17. Sabet S, Pinto T, Kirjoranta S, Garcia A, Valoppi F (2023) Clustering of oleogel production methods reveals pitfalls and advantages for sustainable, upscalable, and oxidative stable oleogels., Journal of Food Engineering, 357, 111659. https://doi.org/10.1016/j.jfoodeng.2023.111659
18. Wang S, Fan Z, Huang X, Gao Y, Sui H, Yang J, Li B (2024) Preparation of Chitosan Oleogel from Capillary Suspension and Its Application in Pork Meatballs, Gels, 10,826. https://doi.org/10.3390/gels10120826
19. Tan TC, Chan ES, Manjula M, Tang TK, Phuah ET, Lee YK (2023) Production, health implications and applications of oleogels as fat replacer in food system: A review. Journal of the American Oil Chemists' Society,100. DOI:10.1002/aocs.12720
20. Qiu H, Zhang H, Eun JB (2024) Oleogel classification, physicochemical characterization methods, and typical cases of application in food: a review. Food Science and Biotechnology, 33, pp.1273–1293. doi: 10.1007/s10068-023-01501-z.
21. Patel AR (2017) A colloidal gel perspective for understanding oleogelation. Current Opinion in Food Science, pp 1–6. DOI:10.1016/j.cofs.2017.02.013
22. Perta-Crisan S, Ursachi CS, Chereji BD, Tolan I, Munteanu FD (2023) Food-Grade Oleogels: Trends in Analysis, Characterization, and Applicability. Gels 9:386. https://doi.org/10.3390/ gels9050386
23. Kırnapcı M, Aksoylu Özbek Z (2026) Emerging trends and recent innovations in oleogel-based fat substitutes for sustainable foods. European Food Research and Technology,.252:52. DOI:10.1007/s00217-025-04962-0
24. Doan CD, Tavernier I, Okuro PK, Dewettinck K (2018) Internal and External Factors Affecting the Crystallization, Gelation and Applicability of Wax-Based Oleogels in Food Industry, Innovative Food Science and Emerging Technologies, 45, pp 42–52. DOI:10.1016/j.ifset.2017.09.023
25. Dimakopoulou-Papazoglou D, Zampouni K, Katsanidis E (2025) Natural Waxes as Gelators in Edible Structured Oil Systems: A Review. Gels 11:656. https://doi.org/10.3390/gels11080656
26. Quilaqueo M, Catalán K, Millao S, Contardo I, Morales E, Rubilar M (2025) Impact of oleogelator type and concentration on the properties of food-grade bigels: a comparative study of three waxes. LWT, 238:118835. https://doi.org/10.1016/j.lwt.2025.118835
27. Brykczynski H, Till W, Floter E (2022) Revisiting pure component wax esters as basis of wax-based oleogels. Journal of the American Oil Chemists' Society, 99(11), pp 925–941. https://doi.org/10.1002/aocs.12589
28. Pakseresht S, Tehrani MM, Farhoosh R, Koocheki A (2023) Rheological and Thermal Properties of Reinforced Monoglyceride-Carnauba Wax Oleogels. Journal of the Science of Food and Agriculture, 103, pp 4184–4194. DOI: 10.1002/jsfa.12443
29. Han W, Chai X, Liu Y, Xu Y, Tan CP (2022) Crystal network structure and stability of beeswax-based oleogels with different polyunsaturated fatty acid oils. Food Chemistry, 381, 131745. https://doi.org/10.1016/j.foodchem.2021.131745
30. da Silva TLT, Arellano DB, Martini S (2019) Interactions between Candelilla Wax and Saturated Triacylglycerols in Oleogels. Food Research International, 121, pp 900–909. DOI: 10.1016/j.foodres.2019.01.018
31. Dassanayake LSK, Kodali DR, Ueno S (2011) Formation of Oleogels Based on Edible Lipid Materials,Current Opinion in Colloid & Interface Science, 16, pp 432–439.
32. Winkler-Moser JK, Anderson J, Felker FC, Hwang HS (2019) Physical Properties of Beeswax, Sunflower Wax, and Candelilla Wax Mixtures and Oleogels. Journal of the American Oil Chemists' Society, 96, pp 1125–1142. DOI:10.1002/aocs.12280
33. Zhang Y, Xu J, Tang C, Li Y (2023) Crystallization Behavior and Physical Properties of Monoglycerides-Based Oleogels as Function of Oleogelator Concentration. Foods 12:345. https://doi.org/10.3390/foods12020345
34. Li J, Hu Y, Ma Q, Zhao D, Dou X, Xu B, Liu L (2025) Phytosterol–γ-Oryzanol–Glycerol Monostearate Composite Gelators for Palm Stearin/Linseed Oil Oleogel-Based Margarine: Nutrient Enrichment, Textural Modulation, and Commercial Product Mimicry. Foods 14:1206. https://doi.org/10.3390/foods14071206
35. Pang L, Wang Y, Liu L, Cao L (2024) Potential functional oleogels based on phytosterol and diacylglycerol corn oil: Development and physicochemical characterization. LWT 198:115987. https://doi.org/10.1016/j.lwt.2024.115987

36. García-Ortega ML, Toro-Vazquez JF, Ghosh S (2021) Development and characterization of structured water-in-oil emulsions with ethyl cellulose oleogels. Food Research International, 150:110763 https://doi.org/10.1016/j.foodres.2021.110763.
37. Naeli MH, Milani JM, Farmani J, Zargaraan A (2022) Developing and optimizing low-saturated oleogel shortening based on ethyl cellulose and hydroxypropyl methyl cellulose biopolymers. Food Chemistry, 369:130963. DOI: 10.1016/j.foodchem.2021.130963
38. Millao S, Iturra N, Contardo I, Morales E, Quilaqueo M, Rubilar M (2023) Structuring of oils with high PUFA content: Evaluation of the formulation conditions on the oxidative stability and structural properties of ethylcellulose oleogels. Food Chemistry, 405:134772. DOI: 10.1016/j.foodchem.2022.134772
39. Ursachi CS, Perta-Crisan S, Tolan I, Chambre DR, Chereji BD, Condrat D, Munteanu FD (2024) Development and Characterization of Ethylcellulose Oleogels Based on Pumpkin Seed Oil and Rapeseed Oil,Gels, 10, pp.39. https://doi.org/10.3390/gels10060384
40. Qiu H, Qu K, Eun JB, Zhang H (2023) Analysis of thermal oxidation of different multi-element oleogels based on carnauba wax, β-sitosterol/lecithin, and ethyl cellulose by classical oxidation determination method combined with the electronic nose, Food Chemistry 405:134970. https://doi.org/10.1016/j.foodchem.2022.134970
41. Cafuero L, Friuli M, Waheed M, Demitri C, Sannino A, Esposito Corcione C, Lamanna L (2026) Natural Blends of Ethyl Cellulose Oleogels for Tunable Bioplastic Design, ACS Omega ,11(5), pp.8629–8636. https://doi.org/10.1021/acsomega.5c11908
42. Sinha SS, Upadhyay A, Singh A (2024) Development and optimization of oleogel made with soy protein isolate and xanthan gum using emulsion template approach and its comparison with solid fats, Heliyon 10:e25224. https://doi.org/10.1016/j.heliyon.2024.e25224
43. Mohanan A, Harrison K, Cooper DML et al. (2022) Conversion of pulse protein foam-templated oleogels into oleofoams for improved baking application, Foods 11:2887. https://doi.org/10.3390/foods11182887
44. Wang GS, Chen HY, Zhang LY et al. (2024) Facile formation of capillary whey protein oleogels with tunable mechanical and aesthetic properties and their applications as margarine alternatives. Food Hydrocolloids,154:110073. https://doi.org/10.1016/j.foodhyd.2024.110073.
45. Pan H, Xu X, Qian Z, Cheng H, Shen X, Chen S, Ye X (2021) Xanthan gum-assisted fabrication of stable emulsion-based oleogel structured with gelatin and proanthocyanidins, Food Hydrocolloids,115:106596. https://doi.org/10.1016/j.foodhyd.2021.106596
46. Tanti R, Barbut S, Marangoni AG (2016) Hydroxypropyl methylcellulose and methylcellulose structured oil as a replacement for shortening in sandwich cookie creams., Food Hydrocolloids, 61,pp.329–337. https://doi.org/10.1016/j.foodhyd.2016.05.032
47. Jimenez-Colmenero F, Salcedo-Sandoval L, Bou R, Cofrades S, Herrero AM, Ruiz-Capillas C (2015) Novel applications of oil-structuring methods as a strategy to improve the fat content of meat products. Trends in Food Science & Technology, 44(2), pp. 177–188. https://doi.org/10.1016/j.tifs.2015.04.011
48. Marangoni AG, Garti N (2011) Edible Oleogels. Structure and Health Implications. First Edition. AOCS Press, Urbana. ISBN 978-0-9830791-1-8.
49. Manzoor S, Masoodi FA, Naqash F, Rashid R (2022) Oleogels: Promising alternatives to solid fats for food applications. Food Hydrocolloids for Health, 2:100058. DOI:10.1016/j.fhfh.2022.100058
50. Nill K (2016) Soy Beans: Properties and Analysis. In: Caballero, B.; Finglas, P.M.; Toldrá, F. (eds) Encyclopedia of Food and Health. Elsevier, Oxford, ISBN 978-0-12-384947-2.
51. Zhan Y, Yuanfa L, (2023) Polyphenolic compounds from rapeseeds (Brassica napus L.): The major types, biofunctional roles, bioavailability, and the influences of rapeseed oil processing technologies on the content. Food Research International 163, 112282, https://doi.org/10.1016/j.foodres.2022.112282.
52. Jilo K, Edeo M, Hunde T, Mengistu B (2026) Fatty acid composition, oil yield, and oil content of sunflower (Helianthus annuus L.) across different pollination treatments. J. Biosci. 50. 2-8. DOI: 10.1007/s12038-025-00494-7
53. Jukić Špika M, Perica S, Žanetić M, Škevin D (2021) Virgin Olive Oil Phenols, Fatty Acid Composition and Sensory Profile: Can Cultivar Overpower Environmental and Ripening Effect? Antioxidants 10, 689, https://doi.org/10.3390/antiox10050689.
54. Jimenez-Lopez C, Carpena M, Lourenço-Lopes C, Gallardo-Gomez M, Lorenzo JM, Barba FJ, Prieto MA, Simal-Gandara J (2020) Bioactive Compounds and Quality of Extra Virgin Olive Oil. Foods 9(8):1014. https://doi.org/10.3390/foods9081014.

55. Ghazani M, Marangoni AG (2016) Healthy Fats and Oils, Reference Module in Food Science, Elsevier. https://doi.org/10.1016/B978-0-08-100596-5.00100-1.
56. Hassan MA (2012) Studies on Egyptian sesame seeds (Sesamum indicum L.) and its products 1-physicochemical analysis and phenolic acids of roasted Egyptian sesame seeds. World Journal of Dairy & Food Sciences, 7, pp 195–201. DOI: 10.5829/idosi.wjdfs.2012.7.2.1112
57. El-Beltagi HS, Maraei RW, El-Ansary AE, Rezk AA, Mansour AT, Aly AA (2022) Characterizing the Bioactive Ingredients in Sesame Oil Affected by Multiple Roasting Methods. Foods, 11:2261. https://doi.org/10.3390/foods11152261.
58. Pal YP, Pratap AP (2017) Rice Bran Oil: A Versatile Source for Edible and Industrial Applications. Journal of Oleo Science, 66(6), pp 551–556. https://doi.org/10.5650/jos.ess17061
59. Zhang H, Zheng Y, Akoh CC, Xu X (2026) Rice Bran Oil: A Critical Review on Its Chemistry, Nutrition, Processing Technology, and Application. Food Reviews International, pp 1–29. https://doi.org/10.1080/87559129.2026.2623506.
60. Shahada C, Morya S, Awuchi CG (2024) A narrative review on nutraceutical, food and industrial applications of flaxseed (Linum usitatissimum L),Cogent Food & Agriculture, 10(1), 2306017. https://doi.org/10.1080/23311932.2024.2306017.
61. Coppola F, Nazzaro F, Fratianni F, Lombardi SJ, Grazia L, Coppola R, Tremonte P (2025) Pumpkin Oil and Its Effect on the Quality of Naples-Style Salami Produced from Buffalo Meat, Foods, 14, pp 1077. https://doi.org/10.3390/foods14061077.
62. Zeynet OA, Ergönül PG (2020) Cold pressed pumpkin seed oil. In: Ramadan MF (ed) Cold Pressed Oils. Academic Press, pp 219–229. https://doi.org/10.1016/B978-0-12-818188-1.00018-9
63. Patel AR (2015) Alternative Routes to Oil Structuring. Springer International Publishing, Cham. https://doi.org/10.1007/978-3-319-19138-6.
64. de Vries A, Lopez Gomez Y, van der Linden E, Scholten E (2017) The effect of oil type on network formation by protein aggregates into oleogels. RSC Advances, 7, pp 11803–11812. https://doi.org/10.1039/C7RA00396J
65. Guo J, Cui L, Meng Z (2022) Oleogels/emulsion gels as novel saturated fat replacers in meat products: A review. Food Hydrocolloids, 137, 108313. 10.1016/j.foodhyd.2022.108313.
66. Zetzl, C., Marangoni, A.G., & Barbut, S. (2014). Microstructure of ethylcellulose oleogels and its relationship to mechanical properties. *Food Hydrocolloids*, 35, pp 60–70. DOI:10.1016/j.foostr.2014.07.002
67. Abe AA, Aiello I.; Oliviero Rossi, C.; Caputo, P. (2025). Oleogels: Uses, Applications, and Potential in the Food Industry. Gels, 11, pp 563. https://doi.org/10.3390/gels11070563
68. Zulfiqar A, Shabbir MA, Tahir F, Khan MR, Ahmed W, Yıkmış S, Manzoor MF, Abdi G, Aadil RM (2024) Development of oleogel by structuring the blend of corn oil and sunflower oil with beeswax to replace margarine in cookies, Food Chemistry X, 23, 101676. https://doi.org/10.1016/j.fochx.2024.101676
69. Bakhshabadi H, Ganje M, Gharekhani M, Mohammadi-Moghaddam T, Aulestia C, Morshedi A (2025) A Review of New Methods for Extracting Oil from Plants to Enhance the Efficiency and Physicochemical Properties of the Extracted Oils, Processes 13, 1124. https://doi.org/10.3390/pr13041124
70. Siger A, Nogala-Kalucka M, Lampart-Szczapa E (2008) The content and antioxidant activity of phenolic compounds in cold-pressed plant oils, Journal of Food Lipids, 15, pp 137–149. DOI:10.1111/j.1745-4522.2007.00107.x
71. Anderson D (2005) A primer on oils processing technology. In: Shahidi F (ed) Bailey's Industrial Oil and Fat Products. Vol 5. Wiley, New Jersey, pp 1–56. DOI:10.1002/047167849X.bio077.pub2
72. Rostami M, Farzaneh V, Boujmehrani A, Mohammadi M, Bakhshabadi H (2014) Optimizing the extraction process of sesame seed's oil using response surface method on the industrial scale, Industrial Crops and Products, 58, pp 160–165. DOI: 10.1016/j.indcrop.2014.04.015
73. Shejawale DD, Murugesh C, Rastogi N, Subramanian R (2022) Effect of feed particle size and solvent flow rate on soybean oil extraction in a percolation type extractor, Journal of Food Science and Technology, 59, pp 4723–4730. DOI: 10.1007/s13197-022-05554-6
74. Golimowski W, Teleszko M, Zając A, Kmiecik D, Grygier A (2023) Effect of the Bleaching Process on Changes in the Fatty Acid Profile of Raw Hemp Seed Oil (Cannabis sativa). Molecules, 28, pp.769. https://doi.org/10.3390/molecules28020769
75. Gharby S (2022) Refining Vegetable Oils: Chemical and Physical Refining, Scientific World Journal, 6627013.https://doi.org/10.1155/2022/6627013

76. Ayerdi Gotor A, Rhazi L (2016) Effects of refining process on sunflower oil minor components: a review, OCL – Oilseeds and Fats, Crops and Lipids, 23(2), D207. https://doi.org/10.1051/ocl/2016007
77. Zufarov O, Schmidt S, Sekretár S (2008) Degumming of rapeseed and sunflower oils. Acta Chimica Slovaca, 1, pp.321–328.
78. Brevedan MIV, Carelli AA, Crapiste GH (2000) Changes in composition and quality of sunflower oils during extraction and degumming, Grasas Aceites, 51, pp 417–423. DOI: 10.3989/gya.2000.v51.i6.460
79. Kreps F, Vrbiková L, Schmidt Š (2014) Influence of industrial physical refining on tocopherol, chlorophyll and beta-carotene content in sunflower and rapeseed oil.European Journal of Lipid Science and Technology, 116, pp 1572–1582. DOI: 10.1002/ejlt.201300460
80. Lamas DL, Crapiste GH, Constenla DT (2014) Changes in quality and composition of sunflower oil during enzymatic degumming process, LWT – Food Science and Technology, 58, pp 71–76. 10.1016/j.lwt.2014.02.024.
81. Alpaslan M, Tepe S, Simsek O (2001) Effect of refining processes on the total and individual tocopherol content in sunflower oil, International Journal of Food Science and Technology, 36, pp 737–739. DOI:10.1111/j.1365-2621.2001.00523.x
82. Naz S, Sherazi STH, Talpur F (2011) Changes of total tocopherol and tocopherol species during sunflower oil processing, Journal of the American Oil Chemists' Society, 88, pp 127–132. DOI 10.1007/s11746-010-1652-4
83. Talal Elsir M, Jiang J, Yuanfa L (2013) Chemical refining of sunflower oil: effect on oil stability, total tocopherol, free fatty acids and colour, International Journal of Engineering Science and Technology, 5, pp 449–454.
84. Ruiz Méndez MV, Aguirre-González MR, Dobarganes MC (2011) Influence of neutralization stage conditions on soapstock phytosterol content. In: AOCS (ed) World Conference on Oilseed Processing, Fats & Oils Processing, Biofuels & Applications, Turkey.
85. Machmudah S, Maulana NA, Norman AS, Nyoto VM, Amrullah I, Wahyudiono, Winardi S, Wenten IG, Goto M (2022) Oil removal from spent bleaching earth of vegetable oil refinery plant using supercritical carbon dioxide. Heliyon 8(10), e10826. https://doi.org/10.1016/j.heliyon.2022.e10826
86. Kwaśnica A, Marcinkowski D, Kmiecik D, Grygier A, Golimowski W (2022) Analysis of Changes in the Amount of Phytosterols after the Bleaching Process of Hemp Oils. Molecules 27, 7196. https://doi.org/10.3390/molecules27217196
87. Strieder MM, Pinheiro CP, Borba VS, Pohndorf RS, Cadaval TRS, Pinto LAA (2017) Bleaching optimization and winterization step evaluation in the refinement of rice bran oil, Separation and Purification Technology, 175, pp 72–78. https://doi.org/10.1016/j.seppur.2016.11.026
88. Nedić Grujin K, Lužaić T, Pezo L, Nikolovski B, Maksimović Z, Romanić R (2023) Sunflower Oil Winterization Using the Cellulose-Based Filtration Aid—Investigation of Oil Quality during Industrial Filtration Probe, Foods ,12, 2291. https://doi.org/10.3390/foods12122291.
89. Ruiz Méndez MV, Aguirre-González MR, Marmesat S (2013) Olive oil refining process. In: Aparicio R, Harwood J (eds) *Handbook of Olive Oil, Analysis and Properties,* Springer, New York, pp 772. DOI:10.1007/978-1-4614-7777-8_19.
90. Kanya TCS, Rao LJ, Sastry MCS (2007) Characterization of wax esters, free fatty alcohols and free fatty acids of crude wax from sunflower seed oil refineries. Food Chemistry, 101, pp 1552–1557.
91. Jamoussi B, Jablaoui C, Hajri AK, Chakroun R, Al-Mur B, Allaf K (2022) Deodorization process of vegetal soybean oil using Thermomechanical Multi-Flash Autovaporization (MFA). LWT 167, 113823. https://doi.org/10.1016/j.lwt.2022.113823
92. Martinčič V, Golob J, de Greyt W et al. (2008) Optimization of industrial-scale deodorization of high-oleic sunflower oil via response surface methodology. European Journal of Lipid Science and Technology, 110, pp 245–253. DOI:10.1002/ejlt.200700194
93. Abd Razak RA, Kuntom A, Siew WL, Ibrahim NA, Ramli MR, Hussein R, Nesaretnam K (2012) Detection and monitoring of 3-monochloropropane-1,2-diol (3-MCPD) esters in cooking oils. Food Control, 25(1), pp 355–360. https://doi.org/10.1016/j.foodcont.2011.10.058
94. Li L, Liu G, Bogojevic O, Pedersen JN, Guo Z (2022) Edible oleogels as solid fat alternatives: Composition and oleogelation mechanism implications, Comprehensive Reviews in Food Science and Food Safety, 21(3), pp 2077–2104.

95. Borriello A, Miele NA, Masi P, Aiello A, Cavella S (2022) Effect of fatty acid composition of vegetable oils on crystallization and gelation kinetics of oleogels based on natural wax. *Food Chemistry,* 375, 131805. DOI:10.1016/j.foodchem.2021.131805
96. Ropciuc S, Dranca F, Oroian MA, Leahu A et al. (2023) Structuring of Cold Pressed Oils: Evaluation of the Physicochemical Characteristics and Microstructure of White Beeswax Oleogels. Gels 2023, *9*(3), 216. https://doi.org/10.3390/gels9030216
97. Pușcaș Ș, Mureșan A, Socaci S, Dulf F, Muste S, Fetea F, Semeniuc CA, Bunea A, Mureșan V, Pintea A (2023) Cold pressed pumpkin seed oil fatty acids, carotenoids, volatile compounds profiles and infrared fingerprints as affected by storage time and wax-based oleogelation, Journal of the Science of Food and Agriculture, 103(2), pp 680–691. https://doi.org/10.1002/jsfa.12180
98. Grajzer M, Szmalcel K, Kuźmiński Ł, Witkowski M, Kulma A, Prescha A (2020) Characteristics and antioxidant potential of cold-pressed oils-Possible strategies to improve oil stability. Foods 9(11), 1630. doi:10.3390/foods9111630.

Citation: Bulgaru, V., Ropciuc, S., Ciugureanu, I., Smerea, O., Pauliuc, D., Netreba, N. (2026). Structured oils in food systems: oleogels as sustainable alternatives to conventional solid fats. *Journal of Engineering Science*. 2026, 33 (2), pp. 113-133. https://doi.org/10.52326/jes.utm.2026.33(2).09.

Publisher's Note: JES stays neutral with regard to jurisdictional claims in published maps and institutional affiliations.

Copyright:© 2026 by the authors. Submitted for possible open access publication under the terms and conditions of the Creative Commons Attribution (CC BY) license (https://creativecommons.org/licenses/by/4.0/).

Submission of manuscripts: jes@meridian.utm.md